



The University of  
**Nottingham**

UNITED KINGDOM • CHINA • MALAYSIA

Hybrid Carbon Fibre Architectures for High  
Performance, High Volume Applications

---

Anthony David Evans

MEng. (Hons.)

Thesis submitted to the University of Nottingham for the  
degree of Doctor of Philosophy

June 2017



## ABSTRACT

The interest in compression moulded discontinuous carbon fibre compounds is growing for semi-structural automotive applications, with target Takt times of less than 5 minutes. The main advantage of these compounds, such as sheet moulding compounds (SMC), is that they produce complex 3D geometries by using in-mould flow during compression. This results in short cycle times by eliminating preforming and infusion stages, generating low wastage by using net-weight charges and keeping costs low by minimising touch labour.

An automated manufacturing process has been developed to produce low cost carbon fibre / epoxy moulding compounds. Directed fibre compounding (DFC) uses a robot arm to direct the deposition of chopped carbon fibre bundles simultaneously with a liquid epoxy via liquid resin spray (LRS). The resulting compound can be tailored in terms of areal density, fibre length (15-75mm) and fibre volume fraction (up to 55%). The resin is chemically thickened by B-staging to prevent fibre-matrix separation, which negates using fillers that limit the fibre content of more traditional moulding compounds. The DFC material has similar tensile properties to more expensive prepreg derived carbon fibre moulding compounds.

This thesis aims to understand the effect of co-compression moulding discontinuous and continuous to form hybrid fibre architecture, offering greater mechanical properties in local regions to overcome the strength limitations of the discontinuous fibre architectures. This also enables the manufacture of complex 3D geometries with patches of local reinforcement to enhance the properties in high stress state regions without increasing the Takt time.

Mechanical testing and microstructural analysis, demonstrate that DFC produced with 100% mould coverage, 25mm long fibre bundles and 85 bar in-mould pressure can produce planar isotropic material with tensile modulus and strength values of 36.3GPa  $\pm$ 3.3GPa and 323MPa  $\pm$ 27MPa, respectively. These properties increase when the initial mould coverage area is reduced to 50% (47.6GPa  $\pm$ 5.7GPa and 480MPa  $\pm$ 58MPa), as fibres align in the direction of flow. Void content is also significantly reduced (to

~0.3%) as the charge flow increases, as the trapped air is forced out of the open flash gap, enabling lower mould pressures to be effectively used.

Adding 20% (by vol.) of unidirectional (UD) fibre to the discontinuous material increases the tensile strength and stiffness by 110% and 60% respectively, when the UD fibres are aligned in the primary loading direction. The tensile properties followed a linear relationship as the ratio of the volume of UD carbon fibre to random DFC increases. The effect of different ply layups in the transition zone from the continuous fibre plies to the discontinuous fibre material is also investigated by determining the relationships between architectural features and strain distributions (in-plane and through thickness) surrounding these joints under axial load. Results agree with both joint and ply-drop aerospace design guidelines, indicating that the continuous-discontinuous joint design requires stepping or tapering of the continuous fibre plies to achieve an interface angle of less than  $7^\circ$  in order to minimise the peel stress.

The interface between the continuous and discontinuous fibres is characterised by a double cantilevered beam test (mode-I separation). Fracture toughness values indicate that the discontinuous architecture improves the overall fracture toughness of the system by up to 23%. There was also a 37% improvement in the crack initiation load compared to the UD material, due to discontinuous 'fibre bridging' which suppresses crack development. The hybrid interfaces experience a mixture of DFC or UD failure mechanisms during mode-I separation. Therefore, although the crack initiation load increased by 15% at the hybrid interface due to fibre bridging, in comparison to UD separation as a result of fibre bridging, sudden failure of the bridged fibres momentarily increases rate of crack growth through resin rich regions at the interface and resulted in an overall reduction (11%) in mode-I fracture toughness.

A final study was conducted to understand the damage tolerance of the hybrid fibre architecture. Drop weight impact and compression after impact (CAI) testing was performed to determine the influence of the laminate layup sequence, in particular the through thickness position of the continuous plies with respects to the position of the discontinuous architecture. This was performed to determine if the multi-directional material would provide higher damage tolerance to the highly stressed load bearing UD plies, by establishing the size of the damage zones and the retained compressive

properties post-impact. The DFC material retained over 73% of its compressive strength following an impact energy of 6.7J/mm. This is high in comparison to a cross-ply UD material, which only retained 32% of the compressive strength post-impact. Hybridising the fibre architecture increased strength retention of the UD material to 39-50% depending on through thickness position of the continuous plies and the thickness of the ply stack.

## Acknowledgements

The author wishes to acknowledge his supervisors Dr Lee Harper, Prof Nicholas Warrior and Dr Thomas Turner; their advice and support received was greatly appreciated. Thanks also to Daniel Briggs, who assisted with the early stages of directed fibre compounding.

Many thanks also go to Paul Johns, Benjamin Jennison and Harry Crocker for their invaluable technical assistance.

The financial support from the Engineering and Physical Sciences Research Council (EPSRC) is also acknowledged.

Lastly, my thanks go to my family and friends for their continued support and encouragement.

# Contents

ABSTRACT.....	i
Acknowledgements.....	iv
Contents .....	v
1. Introduction.....	1
1.1 Market forces.....	1
1.2 Discontinuous fibre composites in high volume applications.....	3
1.2.1 Directed Fibre Compounding.....	4
1.2.2 Cost model.....	5
1.2.3 Commercial systems .....	6
1.2.4 Limitations .....	7
1.3 Hybrid fibre architecture compression mould compounds.....	9
1.4 Aims and objectives.....	11
1.5 Scope of Thesis.....	12
1.6 Novelty claims.....	14
2. Literature Review.....	15
2.1 Choice of material .....	15
2.2 Short fibre reinforced composites.....	16
2.2.1 Glass chopper gun .....	16
2.2.2 Directed carbon fibre preforming.....	16
2.2.3 Injection moulding .....	17
2.2.4 Sheet Moulding Compounds.....	18
2.3 Directed Fibre Compound process .....	21
2.3.1 Mould compound defect mechanisms.....	21
2.3.2 Spray path optimisation.....	26
2.3.3 Fibre bundle parameters: fibre length and tow size .....	28
2.4 One dimensional moulding compound flow .....	30

2.4.1	Characterising in-mould flow.....	30
2.4.2	Orientation characterisation .....	31
2.5	Hybrid fibre architecture and interfacial characterisation .....	32
2.5.1	Prepreg compression moulding.....	32
2.5.2	Hybrid fibre architecture .....	33
2.5.3	Layup strategy .....	35
2.5.4	Ply drop and joint design guidelines .....	36
2.5.5	Residual Stresses .....	40
2.5.6	Architectural failure mechanisms.....	40
2.5.7	Double Cantilever Beam testing (Mode-I Separation).....	45
2.6	Damage tolerance of hybrid fibre architecture .....	47
2.6.1	Fracture toughness.....	47
2.6.2	Laminate waviness .....	49
2.6.3	Notch sensitivity.....	52
2.7	Conclusions .....	53
3.	Experimentation and Methodology.....	55
3.1	Manufacturing Processes .....	55
3.1.1	Epoxy Resin .....	55
3.1.2	Directed Fibre Compound (DFC) .....	57
3.1.3	Liquid Resin Spray (LRS) fabric impregnation .....	59
3.1.4	Compression moulding .....	61
3.2	Resin analysis .....	64
3.2.1	Isothermal Differential Scanning Calorimetry (DSC) .....	64
3.2.2	Glass transition temperature.....	66
3.2.3	Rheology .....	68
3.3	Microstructural analysis .....	68
3.3.1	Density measurements.....	68

3.3.2	Microscopy.....	69
3.3.3	Out-of-plane laminar waviness measurement .....	70
3.3.4	Ultrasonic C-scan .....	72
3.4	Mechanical testing.....	73
3.4.1	Tensile properties .....	73
3.4.2	Electronic Speckle Pattern Interferometry (ESPI) .....	75
3.4.3	Flexural properties.....	77
3.4.4	Charpy impact properties .....	79
3.4.5	Double Cantilever Beam (DCB) testing.....	80
3.4.6	Drop weight impact testing .....	83
3.4.7	Compression testing .....	84
3.4.8	Compression After Impact (CAI).....	87
3.5	Analytical Model .....	88
3.6	Finite element analysis of hybrid joints.....	90
4.	Directed Fibre Compound Material Development .....	92
4.1	Introduction .....	92
4.2	Design of experiments .....	94
4.2.1	Resin selection.....	94
4.2.1.1	Mould Parameters .....	94
4.2.1.2	Mechanical testing.....	95
4.2.2	Effect of carbon fibre type and tow size .....	96
4.3	Cure cycle model .....	97
4.4	Results and discussion .....	101
4.4.1	Resin selection.....	101
4.4.2	Effect of fibre roving.....	107
4.4.3	Demoulding temperature.....	108
4.5	Summary.....	110

5.	One-dimensional flow characterisation .....	112
5.1	Introduction .....	112
5.2	Objectives .....	113
5.3	Design of experiments .....	113
5.3.1	DFC charge manufacturing .....	113
5.3.2	Benchmark materials.....	115
5.3.3	Charge strategy.....	116
5.4	Results and discussion .....	117
5.4.1	Comparison between DFC and Carbon-SMC.....	117
5.4.2	Degree of flow.....	123
5.4.2.1	Orientation tensors .....	126
5.4.2.2	In-mould pressure with flow .....	128
5.4.3	Effect of fibre length .....	129
5.4.4	Effect of moulding pressure .....	132
5.5	Summary.....	136
6.	Continuous/discontinuous interfacial characterisation .....	139
6.1	Introduction .....	139
6.2	Objectives .....	142
6.3	Design of experiments .....	143
6.3.1	In-plane mechanical testing of hybrid fibre architecture .....	143
6.3.2	Out-of-plane mechanical testing of hybrid fibre architecture .....	144
6.3.3	Joint design.....	144
6.3.4	Interfacial testing.....	146
6.4	Results and Discussion .....	147
6.4.1	In-plane properties of hybrid fibre architecture .....	147
6.4.2	Out-of-plane properties of asymmetric hybrid fibre architecture ....	151
6.4.3	Joint design: Effect of step size.....	156

6.4.3.1	Mechanical performance .....	156
6.4.3.2	In-plane strain measurement .....	163
6.4.3.3	Out-of-plane characterisation.....	167
6.4.4	Joint Design: Effect of joint geometry .....	174
6.4.5	Continuous/discontinuous interfacial Analysis.....	178
6.5	Summary.....	181
7.	Damage tolerance of hybrid fibre architecture .....	185
7.1	Introduction .....	185
7.2	Objectives .....	186
7.3	Design of Experiments .....	186
7.3.1	Cure staging.....	186
7.3.2	Compression after impact (CAI).....	188
7.4	Results and Discussion .....	190
7.4.1	Cure staging.....	190
7.4.2	Compressive performance.....	193
7.4.3	Impact testing .....	195
7.4.4	Damage zones .....	196
7.4.5	Compression after impact.....	200
7.5	Summary.....	205
8.	Demonstrator components .....	207
8.1	Demonstrator Components .....	207
8.1.1	Ribbed panel.....	207
8.1.2	Integrally stiffened pedal.....	211
8.1.3	Demonstrator conclusions .....	215
9.	Thesis conclusions .....	216
9.1	Investigation conclusions .....	216
9.1.1	Manufacturing process .....	216

9.1.2	In-mould flow characterisation .....	217
9.1.3	Hybrid carbon fibre architecture .....	218
9.1.4	Discontinuous/continuous damage tolerance .....	219
9.2	Summary of thesis conclusions .....	221
9.3	Potential future work .....	223
APPENDIX.....		225
A1 – List of Publications .....		225
A2 - Cost Model Estimation for DFC compared to other processes modelled in [6] .....		226
A3 – Determining the process to partial cure a fabric ply .....		229
A4 – Calculated and actual impact energies .....		231
REFERENCES .....		233

# 1. Introduction

This chapter outlines the scope of this thesis for determining the potential of using discontinuous fibre architecture for high performance, high volume applications, by co-compression moulding with non-crimp fabrics (NCF) to produce a hybrid fibre architecture. This thesis will primarily be concerned with developing a manufacturing process for producing discontinuous carbon fibre/epoxy moulding compounds (DFC) using low cost raw materials to significantly reduce material costs in comparison to commercially available prepreg derived compounds. The suitability of discontinuous architectures for structural applications is limited by the heterogeneous material properties. Therefore, it is proposed that the mechanical properties can be enhanced locally, by introducing some continuous fibres, without increasing Takt time and therefore maintaining the suitability of compression moulding for high volume production.

## 1.1 Market forces

Efficiency and environmental impact are increasing concerns in the automotive industry. The usage of polymer matrix composites (PMCs) is increasing for high specific strength and stiffness properties, reducing the mass of structural components where steel or aluminium would have previously been used. Reductions of approximately 20% can be made to the mass of equivalent aluminium structure designs [1].

Historically, carbon fibre was initially only used in the automotive sector in race cars, where production volumes were low and financial budgets were high. Carbon fibre chassis designs showed excellent impact resistance as a result of their high stiffness and strength. Therefore, developments have been made to reduce the costs and shorten the processing times. BMW uses carbon fibre reinforced composites for numerous models,

such as the M3 floor and roof components, while Nissan, General Motors, Toyota and Ford are aiming to achieve the same [1]. Since 2013, BMW launched the first mass produced electric car, i3, with a carbon fibre passenger cell that weighs less than steel and aluminium designs by 50% and 30% respectively. This was achieved by performing automated processes that reduce the cost by half compared to the achievable cost 10 years ago [2]. The carbon fibre reinforcement dominant BMW i3 and multi-material BMW 7 series respectively achieve production rates of 100cars/day and 300cars/day by manufacturing their carbon fibre components using wet compression moulding and high pressure resin transfer moulding (HP-RTM) [3]. To compensate for the high-energy content process, they manufacture carbon fibre at the SGL Automotive Carbon Fibers (ACF) plant in Mose Lake, USA, which is powered by hydroelectricity. The carbon fibre tows are then transported to Wackersdorf, Germany to be processed into fabric before final component production in Landshut and Leipzig, Germany [3]. This is radical long-term investment to sustainably reduce material costs for high-volume production of carbon fibre. However, this does not address the costs incurred by component manufacturing with regards to hand layup, preforming, infusion/impregnation and cure.

Although there is a light weighting benefit to using composites in the automotive industry, the rate of composite production needs to exceed 100,000ppa, or approximately 5 minute Takt times, to compete with the production rates of aluminium or steel components. The layup, preforming, infusion or consolidation times often prevent short Takt times from being achieved. Therefore, high rate manufacturing processes such as high-pressure resin transfer moulding (HP-RTM) or compression moulding are becoming increasingly popular. These methods require expensive tooling, however, this initially cost is offset by the increased production rate and long-lifetime of the tooling. HP-RTM processing still requires a preforming stage to shape the continuous fabric. Whereas compression moulding of discontinuous compounds, such as sheet moulding compounds (SMC), flow during compression to produce complex geometry without preforming. Although the strength of the short fibre composites is limited, this thesis will investigate combining discontinuous moulding compounds with high strength continuous fabrics to form high performance, complex structures without increasing Takt time.

## 1.2 Discontinuous fibre composites in high volume applications

As a result of the anisotropic nature of composite materials, there is large demand that components are stiffened by design rather than substituting as a 'black metal'. There are trade-offs between cost-effective design for manufacturing and the weight optimisation which are largely governed by global architecture and structural design. This enables the required mechanical performance to be achieved while considering the manufacturing processes for the expected annual production volumes [4].

Discontinuous fibre composites typically consist of planar random fibres which offer isotropic properties in-plane. However, the level of heterogeneity is effected by the fibre deposition process and subsequent manufacturing approaches. Discontinuous composites are often categorised by fibre length; particular (<1mm) or short fibres (<6mm) are often produced by injection moulding but have limited mechanical performance due to the fibre pull-out dominated failure, however longer fibre lengths (>6mm) are more suitable but often require Liquid Composite Moulding (LCM) or compression mould techniques.

The specific strength/modulus of different automotive materials are shown in *Fig. 1.1*. High directional strengths can be achieved with UD fabrics, however these require labour intensive hand layup or secondary forming processes prior to LCM or autoclave cure cycles. These result in large Takt times which are unsuitable for high volume production rates (>100,000ppa). Discontinuous composites such as Discontinuous Carbon Fibre Preforming (DCFP) have been developed with approximately 5 minute cycle times [5], and approximately 6 minutes for sheet moulding compounds (SMC) [6], which are 96 times faster than the hand layup and autoclave requirements of prepreg materials [6]. Additional to their suitability for high volume production, discontinuous carbon composites maintain superior specific strengths and similar specific modulus to aluminium and steel, shown in *Fig. 1.1*. Consequently, SMC is the most widely adopted material format of fibre reinforced composites within the automotive industry, accounting for 70% of composites by mass [7].

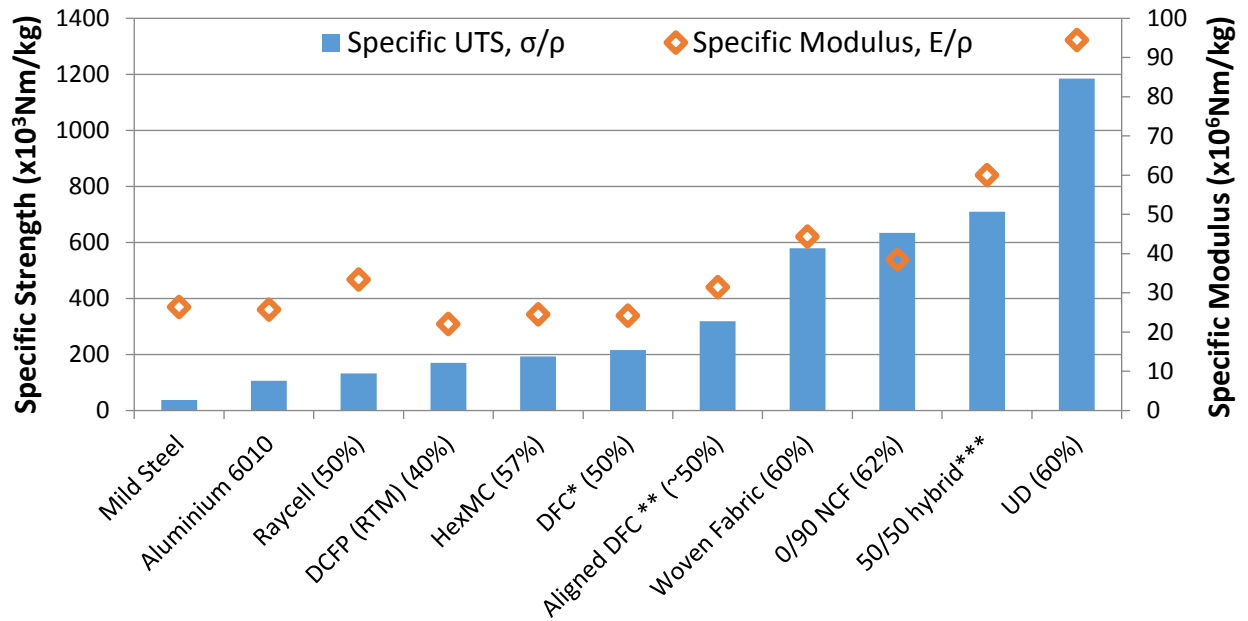


**Figure 1.1.** Specific UTS and tensile modulus between various automotive materials. Data from literature: Mild steel and aluminium [8], Raycell [9], DCFP [10], HexMC [11], Woven [12] and NCF [12]. Data from this thesis: DFC (\*25mm fibre length, net shape mould coverage), Aligned DFC (\*\*50mm fibre length, 50% mould coverage), 50/50 hybrid (\*\*\*) calculated by rule of mixtures for DFC with 50% local  $V_f$  and UD with 60% local  $V_f$  and UD carbon fibre.

### 1.2.1 Directed Fibre Compounding

Discontinuous moulding compounds such as sheet moulding compounds (SMC) are typically produced by depositing chopped fibres onto a resin paste moving on conveyor which then passes through a series of rollers to wet-out the short fibres [13, 14]. These will be discussed further in *Chapter 2*. This thesis will develop directed fibre compounding (DFC) that uses a robot arm to simultaneously deposit a chopped carbon fibre with a liquid resin spray (LRS) to produce a carbon/epoxy charge. The advantage of this is that it uses a chemical B-staging process to thicken the compound, negating the need to use filler additives that limits the fibre volume fraction, <40% (with filler) [15], allowing greater fibre content within DFC, 50-55% by volume. Directing the material deposition also allows charge geometry and fibre length to be altered without affecting the Takt time. DFC is detailed further in *Chapters 3 and 4*, however, DFC and aligned DFC have been added to **Fig. 1.1** to demonstrate how these are also capable of

achieving specific strengths that exceed automotive metals and other discontinuous composites with similar specific modulus.

The LRS system also directs a spray of epoxy resin to impregnate UD NCF. Co-compression moulding with the discontinuous compound produces a hybrid fibre architecture that will enhance mechanical properties in direction of the UD fibres. The hybrid fibre architecture (with 50% DFC and 50% UD fabric by volume) presented in this thesis but has also been added to *Fig. 1.1* to indicate how these compare to other automotive composites, bridging the gap between 0/90 fibres and pure UD.

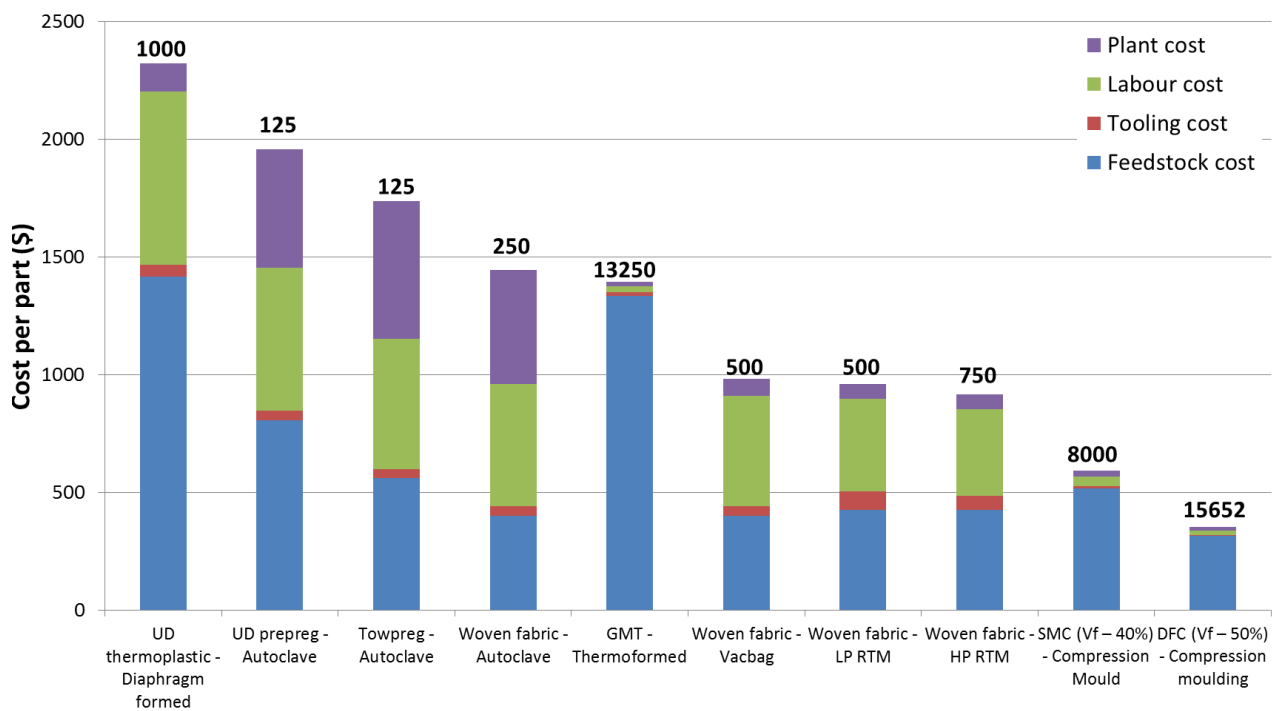


**Figure 1.2.** Cost modelling of different carbon fibre manufacturing methods for a 1m x 1m curved and ribbed part. Overlaid numbers indicate the production volumes per annum used for each material. Modelling for all manufacturing processes except DFC was performed using the methodology outlined in [6], DFC was estimated comparatively to this study, shown in Appendix A2.

## 1.2.2 Cost model

The high production rate of SMC additionally reduces the manufacturing costs per part, decreasing the impact of the high tooling costs of the compression mould. *Fig. 1.2* shows the results of a cost modelling exercise for a range of carbon fibre reinforced

composite manufacturing processes [6] with the addition of the discontinuous fibre compound process presented in this thesis. The plant and labour costs per part are 16 and 18.5 times higher, respectively, for producing the example component from UD prepreg than SMC. The high plant costs for prepreps are a result of the expensive autoclave facilities, with further increases to part cost caused by the low production rate. The labour costs arise from the long hand layup times required to prepare a mould [6].

Estimated costs for a DFC panel have been added to *Fig. 1.2* to enable comparisons between the different manufacturing methods, using the methodology outlined in [6] (see *Appendix A2*).

Understandably, for the different moulding methods shown, the cost of the tooling is influenced by the material used and the manufacturing process. Low production volume processes, such as autoclave cure, use a glass or carbon reinforced open mould tool. These are low cost compared to metallic moulds and can be used for approximately 100 pulls. For high production volumes, a metallic mould tool is required. These have a much greater cost, but long lifetime and high production volume capabilities significantly reduce the tooling costs per part [6]. Another reason for higher material costs for continuous fabrics is high amount of in-process waste. Cutting of prepreg and fabrics to a required shape can increment large amounts of wasted material, cut-offs, and can be as large as 30-40% by mass [6]. However, for DCFP, this can be as little as <3% by mass [5].

This figure shows however, that achieving high production volumes, such as by DFC, enables the overall cost per part to be significantly reduced. Also, its greater fibre volume fraction achieved reduced the volume of the component itself and would therefore reduce the mass of the component.

### **1.2.3 Commercial systems**

Advanced sheet moulding compounds (A-SMC) are carbon fibre versions of the more traditional glass-based SMCs that have been available since the 1950s. This thesis will propose DFC as a low cost alternative to current commercially available systems. More

detail on polyester or vinyl-ester systems will be given in *Chapter 2*. But the main disadvantage of glass SMC is that they use either a polyester or vinyl-ester matrix, containing thickening agents and fillers to prevent fibre-matrix separation during compression moulding [16]. Menzolit CarbonSMC 1100 is a carbon/vinyl-ester mould compound that is produced by traditional glass SMC techniques with mineral fillers [17]. A relatively low material density is achieved  $1.42\text{g/cm}^3$ , even with the inclusion of these fillers, which indicates a very low fibre volume content (approximately 45%). This is reflected by the low Young's modulus, 30GPa, and tensile strength, 130MPa. However, this fibre content is considered to be high for compounds containing fillers that are typically <40% by volume [15].

Epoxy based compounds require control of the B-stage to control the degree of thickening that prevents fibre-matrix separation during moulding. Quantum composites produced a carbon/epoxy moulding compound produced by pressing chopped fibres into a resin film on a moving conveyor to produce a compound with greater mechanical properties than the CarbonSMC 1100 (Young's modulus - 34.5GPa, and tensile strength - 265MPa) [18]. These will require suitable storage and transportation conditions to maintain a usable viscosity. However, the properties exceed the vinyl-ester based system because of a greater fibre volume fraction, 52%, and improved interfacial adhesion between the fibres and matrix. This compound later became Lamborghini's Forgeable Composite [14], pictured in *Fig. 1.3*. Alternatively, Hexcel have also developed a prepreg-based carbon/epoxy A-SMC called HexMC M77. These are derived from chopping UD prepreg and depositing randomly. Producing the prepreg ensure adequate resin impregnation is achieved and B-staging to increase viscosity. These require transporting and storage by refrigeration, however the M77 snap cure resin offers cycle times as low as 3 minutes at  $150^\circ\text{C}$  in an isothermal press [11]. This achieves a 57% fibre volume fraction and a high Young's modulus, 38GPa, and tensile strength, 300MPa [11]. However, this is an expensive product as it's derived from UD prepreg and requires a secondary cutting process.

#### **1.2.4 Limitations**

Using continuous or discontinuous fibre architecture each have their limitations. The random nature of using discontinuous fibres results in local variations with regards to

fibre volume fraction and fibre orientation [5, 19]. This results in heterogeneous material properties and size effects that reduce the mechanical performance of thinner composites. Although these materials become more homogeneous by reducing fibre length, however this reduces the area of the fibre-matrix interface and reduces the strength of the composite [20, 21]. The tow size may be reduced to increase this fibre-matrix interfacial area. However, this will significantly increase the fibre cost.



*Figure 1.3. Photo Lamborghini Huracan Performante at Geneva Motor Show 2017 featuring a large range of components produced from Forged Composites, such as the rear spoiler and diffuser [22]*

SMC requires high viscosity matrix to avoid fibre-matrix separation during moulding [23], which can be a particular problem for ribbed parts [24]. Where the low viscosity of polyester uses filler that reduces fibre content, chemical thickening of epoxy matrices is essential for minimising fibre-matrix separation during the compression moulding stage [25, 26]. Typically, the high viscosity of epoxy matrices, in comparison to traditional polyester systems, can limit macroscopic charge flow due to higher friction levels at the mould-composite interface [27], increasing the required moulding pressures. Initial mould coverage therefore tends to be high (~80-90%), inevitably increasing the amount of touch-labour required to layup and position the charge, negating some of the advantages of using a moulding compound over a prepreg system.

Sheet moulding compounds with continuous-roving (SMC C-R) are an example of hybrid carbon fibre architecture, typically with glass fibres [28]. However, SMC is not often net shape and requires flow to fill the mould of a complex geometry. Therefore, positioning of SMC C-R becomes difficult to optimise without misaligning the orientation of the continuous fibres [29].

The out-life (time at ambient temperature) of epoxy-based moulding compounds and continuous preregs are also much lower than unsaturated polyester SMC, typically less than two weeks at room temperature [30]. This is a particular problem for high volume Tier one suppliers faced with refrigerating large quantities of material increasing energy costs and transportation costs to refrigerate.

### **1.3 Hybrid fibre architecture compression mould compounds**

Hybridising the fibre architecture proposes to combine the advantages of continuous and discontinuous composites to produce a high volume, high performance material. There is very little literature for understanding the combination of discontinuous and continuous fibre architectures. Recently, preregs are being compression moulded isothermally under higher pressure, >80bar, compared to autoclave moulding which require greater preparation time and mould at a lower pressure, <8bar, and slower heating rate, 2-5°C/min, to ensure the mould tool is heated uniformly by convection. Compression moulding therefore reduces processing times while increasing strength and stiffness by reducing void content [31]. Mitsubishi Rayon have presented some minor testing of hybrid moulding compounds by combining fast cure prepreg compression moulding with carbon fibre SMC [31]. It was observed that variability of flexural properties could be improved with the introduction of preregs to SMC. They also demonstrated the production a hybrid architecture structural floor model with complex features, such as ribs and embedded inserts, using the A-SMC ability to flow during compression. However, this can produce fibre distortion and migration within the continuous ply constituents [32].

With further developments to carbon-fibre moulding compounds, detailed in this thesis, it is believed that combining carbon SMCs with carbon NCF can enable the inline production of low-cost, high performance composites. These are summarised in *Table*

*1.1*, to demonstrate how this is expected to be achieved. The cost of the material can be influenced by the constituent materials, manufacturing, volume of production and wastage. DFC uses carbon fibre tows and epoxy resin in their raw, low cost, forms. The liquid resin spray (LRS) is also used to impregnate NCF, rather than using prepreg that requires energy consuming refrigerated storage. Using the same resin for each architecture also ensures short isothermal cure cycles can be used to reduce cycle time and increase production volume. Directed fibre technologies produce little waste (<3%) [5] in comparison to the poor usage efficiency of ply cutting prepreg, which can be as little as 20-50% for complex geometries [33]. Using the in-mould flow of discontinuous material to produce complex geometries enables patches of regular shaped continuous material to be used where local stress is great, minimising cut-off waste. Additionally, the design of a component can integrally stiffen a component by isotropic features such as ribs rather than relying on planar laminate properties.

*Table 1.1. Comparison of general benefits and limitations of discontinuous fibre composites, by DFC, and continuous fibre composites, such as NCF, and expectations of hybridised DFC/NCF composites*

<b>Directed Fibre Compounding (DFC)</b>	<b>NCF fabrics</b>	<b>Hybridised DFC/NCF</b>
Low cost (no intermediates)	High material costs (stitching)	Low cost (by volume)
Short cycle time (Directed deposition)	Long cycle time	Short cycle time (Low precision layup of regular shapes)
Low wastage	High wastage	Low wastage
Highly automatable	Difficult to automate for complex geometry	Highly automatable for complex geometry
Low fibre volume fraction range (35%-50%)	High fibre volume fraction range (65%-80%)	Locally variable fibre volume fraction
Lower stiffness/strength	Higher stiffness/strength	High localised stiffness/strength
Isotropic properties	Anisotropic or orthotropic properties	Locally tailored properties
Integrally stiffened by design	Stiffness enhanced by changes to layup	Integrally stiffened by design

## 1.4 Aims and objectives

To summarise, the current problems that are faced with regards to high volume production within automotive and the usage of current discontinuous materials are:

- The difficulty to produce complex components with continuous laminates constrains preforming to hand layup techniques. This significantly increases Takt time and restricts the manufacture at high production rates suitable for automotive application. This leads to high initial tooling costs required for high production rates.
- Autoclave processing is subject to high running costs and long cure cycles, therefore out-of-autoclave processing is increasingly desirable.
- Within discontinuous composites, the ultimate strength is limited high stress concentrations that form at the ends of chopped fibres.
- Heterogeneity of discontinuous fibre bundle materials results in variations across the part in terms of fibre content and fibre orientation [5, 19]. This consequently reduces the mechanical properties for thinner composites.
- Quantification of the fibre bundle orientation distribution requires a large sample size as a result of the heterogeneity, which requires in laborious sample preparation and image processing techniques to obtain a representative distribution.
- Current SMC systems either require thickening components which restrict fibre volume content (such as polyester or vinyl-ester SMCs) [15] or expensive randomly distributed chopped UD prepreg (such as A-SMCs).
- For discontinuous materials to be used for structural components within the automotive industry, they must be capable of operating with minor damage that may arise from low velocity impacts (such as pebble strike).
- There is little understanding and literature available for materials that combine discontinuous and continuous fibres to form a hybrid fibre architecture. For the placement of a patch of localised continuous reinforcement, the transition between continuous and discontinuous material must be considered.

This thesis aims to provide a solution to these problems with the following objectives:

- Develop a low cost automated manufacturing technique to produce discontinuous carbon fibre compounds suitable for high volume manufacturing.
  - Determine the most appropriate carbon fibre tow size and matrix material for liquid resin spray deposition, without the need to use filler material that limits fibre volume content.
  - This process will use raw materials to reduce costs, rather than using materials that were subjected to secondary impregnation processes.
- Characterise the in-mould flow capabilities of the new discontinuous mould compound to understand mechanical performance and fibre orientation with respects manufacturing and moulding parameters with comparison to benchmark materials.
- Use liquid resin spray to impregnate low cost non-crimp fabrics for compression moulding.
- Characterise the mechanical performance increases when hybridising continuous and discontinuous material compared to monolithic discontinuous material.
- Understand microstructure and mechanical performance around the interface between continuous and discontinuous fibres within hybrid architecture material.
  - This will be achieved by experimentally quantifying the strain distribution in the through thickness plane.
- Establish whether the multi-directionality of random discontinuous architecture can be used to improve the damage tolerance of continuous laminates by hybridisation.
- Demonstrate the manufacture of complex features, such as ribs and metallic inserts.

## **1.5 Scope of Thesis**

This work focuses on the novel manufacturing of DFC for compression moulding and methods mechanical property enhancement via moulding process and hybridised fibre architectures. This will enable discontinuous fibre architecture to be used for structural

automotive applications which requires high performance and high-volume production capabilities. It will demonstrate how these can be obtained using low cost raw materials and NCF impregnated by LRS with no influence on Takt time and increased component complexity.

*Chapter 2* will summarise a broad literature review to provide background information and expose areas that currently lack of knowledge within the field of this research project. *Chapter 3* will detail the experimentation procedures used throughout this thesis.

The DFC manufacturing process will be developed in *Chapter 4*. The effect of resin selection, with regards to toughening and enhancing the glass transition temperature, will be determined. The elastic properties, fracture toughness and in-mould flow capabilities are assessed to help to determine the resin selected for the remainder of the thesis. A cure model is then established for the selected resin for predicting the degree of cure with time during isothermal conditions. With regards to fibre tow size, a short study determines the effect on elastic properties whilst considering the fibre cost.

With the material parameters determined, *Chapter 5* focuses on enhancing the DFC material and characterising the in-mould flow. The in-plane elastic properties of orthogonal orientations enable prediction of macroscopic orientation tensor panels produced with varying degrees of flow. Microstructural analysis is given in conjunction with in-plane elastic properties to optimise moulding parameters, such as mould pressure and fibre bundle lengths, to determine the directional property enhancement that results from the flow induced alignment.

*Chapter 6* and *Chapter 7* introduce NCF co-compression moulded with the DFC. *Chapter 6* initially investigates the relationship between the quantity of UD NCF to DFC and the mechanical performance, before characterising the interface between dissimilar architecture is then the primary objective of the investigation. This examines ply drop sequence, size and geometry of the continuous-discontinuous joint design and analyses the microstructure in conjunction to through thickness strain distribution and the influence this has on the overall performance of this joint under in-plane and out-of-plane loading. The fracture toughness of the in-plane interface between the

dissimilar architecture is also characterised with regards to the crack initiation and growth during mode-I separation.

Exploiting the superior damage tolerance and notch insensitivity of random fibre structures is the main focus of *Chapter 7*. This chapter also quantifies the ply waviness that is affected by the through thickness ply position and varying fibre volume fraction distribution within the discontinuous architecture. The hybrid architectural damage tolerance is accessed via the property degradation resulting from impact. The through thickness position of the delamination prone ply stacks was adjusted in relation to the notch insensitive DFC to determine the chopped fibres ability to protect the primary loaded continuous fibres.

## **1.6 Novelty claims**

Novel contributions from the author are summarised as follows:

- Development of a manufacturing process for the production of chopped carbon fibre composites using automatable directed techniques with the simultaneous spray deposition of liquid epoxy resins, without pre-impregnating the tows or using filler materials.
- Impregnation of continuous dry fabrics by means of directed liquid resin spray deposition using a commercially available epoxy resin without refrigeration storage requirements.
- Evaluation of tow-based discontinuous material performance and fibre orientation by orthogonal mechanical testing with comparison to benchmark materials.
- Characterisation of the performance of co-compression moulded continuous-discontinuous hybrid carbon fibre architecture.
- Experimentation to quantify strain distribution about continuous-discontinuous interface within transition zones with varying layup arrangements
- Demonstration of the ability to use discontinuous fibres to improve damage tolerance of continuous laminates for automotive structural components.

## 2. Literature Review

### 2.1 Choice of material

Within fibre reinforced composite materials, glass or carbon fibres are most popularly used. Although carbon fibre is more expensive than glass it is increasingly being adopted due to lower density and therefore higher specific strength and stiffness, shown by *Table 2.1*. A number of manufacturers have exploited the mechanical properties of carbon fibres (CF), to produce advanced SMCs that are up to 300% stiffer than E-glass derivatives [34, 35].

*Table 2.1. Fibre material properties for some types of carbon and glass fibres [36]*

		Carbon			Glass		Steel	Aluminium
		HT-T300	IM-T800	High Modulus	E-Glass	S-Glass		
Density	$\rho$ (kg/m <sup>3</sup> )	1750	1800	2170	2580	2460	7800	2600
Young's modulus	E (GPa)	230	294	385	72	87	206	69
Tensile strength	$\sigma$ (MPa)	3530	5586	3630	3450	4710	648	234
Strain to failure	$\epsilon$ (%)	1.5	1.9	0.4	4.7	5.6	4	3.5
Shear modulus	G (GPa)	23	23	20	27.7	33.5	81	25.6
Specific strength	$\sigma/\rho$ (x10 <sup>-3</sup> )	2.02	3.10	1.67	1.34	1.91	0.083	0.09
Specific modulus	E/ $\rho$	0.1314	0.1633	0.1774	0.0279	0.0354	0.0264	0.0265

Carbon fibre composites typically use epoxy rather than vinyl-ester or polyester, due to its higher interfacial strength, greater stiffness, resistance to fatigue and reduction to degradation by water [37]. Some properties have been shown in *Table 2.2* to demonstrate the greater performance of epoxy resin to unsaturated polyester with no filler materials [38, 39]. Also, shrinkage during curing is less problematic as epoxy

shrinkage is only approximately 2%, less than the vinyl-ester and polyester shrinkages around 7% [40]. However, a drawback of epoxy is higher cost, approximately double that of vinyl-ester and four times that of polyester [37].

**Table 2.2.** Typical matrix material properties for epoxy and polyester [38, 39]

		Epoxy	Unsaturated Polyester
Density	$\rho$ (kg/m <sup>3</sup> )	1100-1400	1200-1500
Young's modulus	E (GPa)	3-6	2.0-4.5
Tensile strength	$\sigma$ (MPa)	35-100	40-90
Strain to failure	$\epsilon$ (%)	1-6	<2
Shrinkage during cure	%	1-2	4-8
Water absorption	%	0.1-0.4	0.1-0.3

## 2.2 Short fibre reinforced composites

### 2.2.1 Glass chopper gun

Historically, the simultaneous deposition of chopped glass fibre has been used since the Rand Gun (a glass chopper gun) was developed in the late 1950s [41]. This deposited a spray of chopped glass rovings, typically 2 inches (50.8mm) in length, simultaneously with a spray of liquid polyester resin. This was directed by hand until the desired thickness was achieved and was largely used in the marine industry for the production of large structures using plywood core material and for repairs [42]. These composite skins were then either cured under ambient conditions or vacuum pressure was applied. This was limited however by the low fibre content, <30% by weight, of the chopped mats produced by this and therefore achieved poor mechanical performance [43].

### 2.2.2 Directed carbon fibre preforming

Directed Carbon fibre preforming (DCFP) produces a dry preform to be processed by Liquid Composite Moulding (LCM) techniques, such as Resin Transfer Moulding (RTM) [5, 19, 44, 45]. A robot arm is used to direct the spray of chopped carbon fibres into a required geometry. To handle random fibre preforms, often a powdered binder must be used. Increasing the temperature of the preform activates the binder which, once stabilised, improves the handleability to be transferred to the mould for infusion [5, 19, 44, 45]. However, it has been observed that if the binder content is too high,

>6% by weight, it could block the channels between fibres, impeding resin flow and increasing void formation [46]. Also, although the permeability tensors are often considered to be equal in every direction as a result of the random distribution [47], the localised variability of the fibre volume fraction and orientations of the random fibre bundles often cause permeability variations leading to difficulties in predicting infusion resin flow [48, 49]. **Fig. 2.1** shows the random, non-uniform nature of the flow front during RTM of DCFP.

Additionally, with LCM processes, discontinuous fibres are susceptible to moving during infusion. This is called ‘fibre washing’, where the fibres are pushed ahead of the impregnation flow front, and can affect the random orientation and areal density distributions. This limits the mould pressure and therefore potentially increases both void content and cycle time.

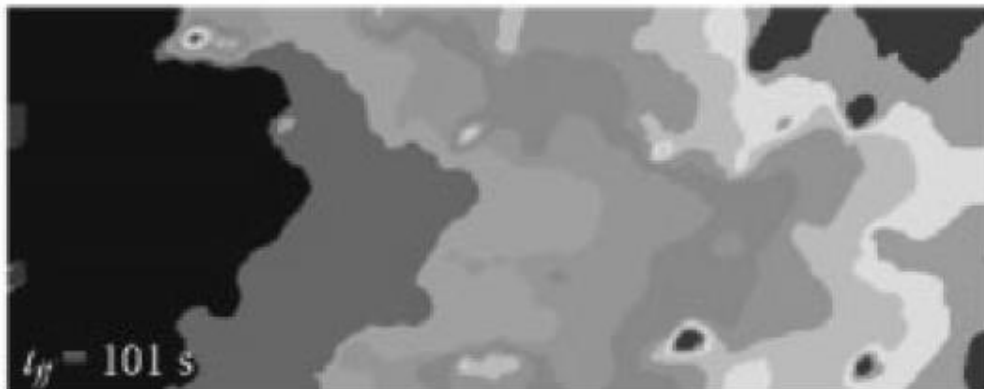


**Figure 2.1.** flow front model at regular time intervals (from left to right) showing non-uniform flow front caused by local permeability variations [49]

### 2.2.3 Injection moulding

Injection moulding is limited to short or particulate fibres, <3mm. However, although long fibre injection moulding has been attempted, by either using 10mm fibre [50] or by introducing roving directly into the extrusion barrel [51], the average fibre length within the part is reduced to <1mm as a result of fibre breakage. **Fig. 2.2** shows a typical thermoplastic injection moulding machine [52]. Glass or carbon fibres are often premixed in a reservoir of resin, this is either heated thermoplastic pellets or one component of thermoset. The fibre and resin is carried to the mould by a screw, which

is also where a hardener component is added for thermosets allowing further mixing of the matrix with the fibre. In some arrangements, the fibre may be added as a continuous roving in the screw section to chop the fibres. This damage can often cause a large degree of variability in the fibre length of the injection mould (0-10mm) [50].

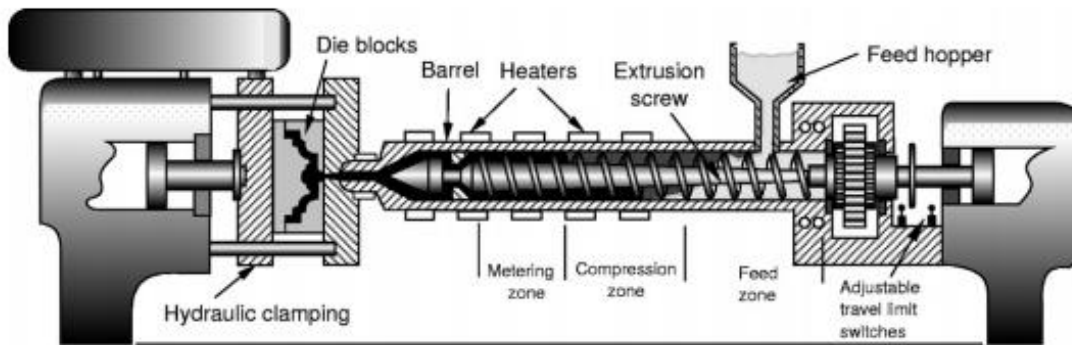


*Figure 2.2. Injection moulding schematic diagram [52]*

Injection moulding enables short cycle times ( $<2$  min [53]), depending on part volume and cooling rate, for thermoplastic composites with complex geometry. However, this is longer for thermoset matrices depending on the resin type (typically less than approximately 20 min) [52] and will result in poor mechanical properties in comparison to continuous or long fibre alternatives.

#### **2.2.4 Sheet Moulding Compounds**

Sheet Moulding Compounds (SMC) are currently used in the automotive industry for bumpers, exterior and interior panels, structural elements and even some high temperature components such as engine valve covers [54]. Carbon or glass SMCs constitute 70% of automotive composites [7]. SMC is largely manufactured by depositing chopped fibre rovings, traditionally glass fibres, onto a conveyor where it meets a measured film of resin. A second layer of resin is draped over the bed of chopped fibres. The compound is then passed through a series of rollers to press the fibre and resin mix to impregnate the fibre. The sheet material is then fed onto a roll and is delivered to customers for compression moulding following an aging process. Continuous roving can also be introduced such as in *Fig. 2.3* to produce a Sheet Moulding Compound with Continuous roving (SMC C-R) [28]. However, the initial SMC charge is often not the same shape as the tool and requires flow to fill complex

geometries. Therefore, positioning of SMC C-R becomes difficult to optimise without misaligning the continuous fibres [29].

Whilst LCM methods require resin infusion over the full geometry of the component, moulding compounds are already wetted and therefore the process is more repeatable with lower risk of large dry spots forming. With closure of the mould, heat and pressure causes the charge to flow and fill the mould. Discontinuous fibre architectures have greater flow capabilities than continuous fibre materials, as the matrix carries the shorter fibres. Generally, higher molecular weight resins can be used compared to infusion processes, which have higher toughness. The cycle time for this process/material ranges from commonly 3-45 minutes, depending on part thickness and resin type. For carbon/epoxy compounds, for example HexMC M77, cycle times are as low as 3 minutes at 150°C in an isothermal press [11]. This material is used for a number of aerospace cabin, cargo, secondary and tertiary structural component applications [55-58].

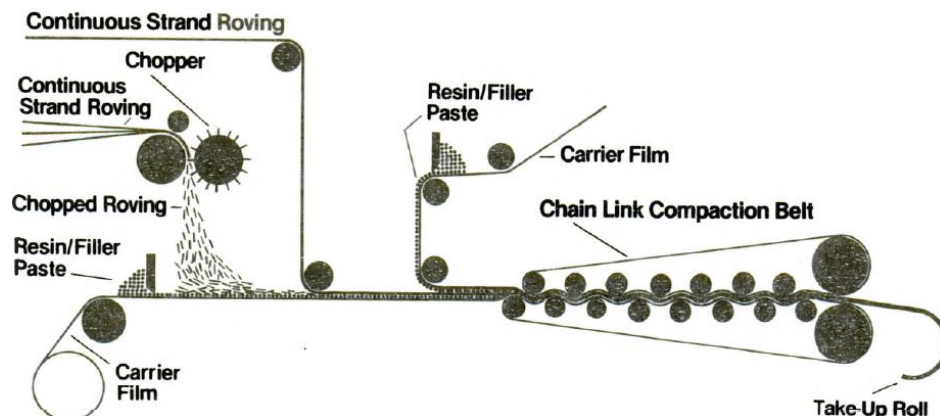


*Figure 2.3. Schematic of glass SMC C-R production, showing how continuous and random fibre architectures can be produced [29]*

Glass fibre SMCs are more established in commercial applications than carbon fibre SMCs due to their low cost. Glass SMCs mostly use vinyl-ester or polyester resins, which often require additional ingredients within the formulation [16] to give the ideal processing conditions:

- Catalysts – activated at higher temperatures to achieve a faster rate of cure.

- Filler – often calcium carbonate, CaCO<sub>3</sub>, particles sized less than 0.7 microns improve sliding capability during moulding, are used to reduce cost and decrease shrinkage during curing.
- Stretching agent – Polyurethane and urethane pre-polymers are used to further lower the shrinkage while increasing the elastic modulus and shock resistance.
- Thickening agent – ranging between 1-3% of the resin formulation, these can be used to increase/optimize the viscosity so that the SMC can fill the mould with a reproducible fibre volume fraction distribution.

Local variations in concentration of these additives can cause large differences in thickening response, which can substantially influence moisture content and fibre distribution increasing the variability in mechanical property [25, 26]. Also, the interfacial shear strength between carbon fibre and polyester or vinyl-ester are typically poor compared with carbon/epoxy systems [59, 60], limiting the mechanical performance.

Typically, when epoxy resins are used, the fibres are pre-impregnated to form a UD prepreg, before chopping into small chips to produce an Advanced Sheet Moulding Compound (A-SMC), such as, HexMC M77 [11]. Using this prepreg resin system allows the fibres to be impregnated and then stored by refrigeration before further moulding and curing, however the additional manufacturing steps increase the cost compared to glass SMC production.

Epoxies can also be thickened, but not using the same type of agents and fillers commonly used for polyesters that restrict the fibre content [15]. Many high-performance epoxies can be formulated as B-staged systems, where the reaction between the resin and the curing agent is incomplete after mixing. Chemical or thermal B-staging partially cures the epoxy, but cross-linking is only fully completed when the system is reheated at a higher temperature. The viscosity is difficult to control using B-staging, but it offers an opportunity to produce an affordable carbon fibre/epoxy moulding compound using low-cost raw materials. These are therefore capable of achieving fibre volume fractions up to 57% compared to 15-40% within polyester or vinyl-ester systems [6, 7, 61].

**Table 2.3** shows that the typical tensile properties of carbon/epoxy moulding compounds are greater than those of glass/polyester. This includes prepreg derived compounds, HexMC M77, and carbon/epoxy mould compounds produced using more traditional SMC manufacturing routes, by depositing and squeezing chopped fibres into a low viscosity resin paste, Quantum Lytex 4197 (Forged Composites) [13, 14, 18]. Additionally, it shows that carbon/epoxy SMCs have lower density to produce a greater specific strength and stiffness.

**Table 2.3.** Typical tensile properties of carbon/epoxy, glass/epoxy and glass/polyester SMCs

	Carbon/Epoxy		Glass/Epoxy	Glass/Polyester
	HexMC M77 [11]	Lytex 4197 [18]	Lytex 9063 BK-E [62]	Lytex QPC-1977 [61]
Fibre Volume Fraction (%)	57	52	45	36
Density (kg/m <sup>3</sup> )	1550	1450	1820	1700
Tensile Strength (MPa)	300	265	193	193
Tensile Modulus (GPa)	38	34.5	18	17.9

### 2.3 Directed Fibre Compound process

This section details literature with regards to considerations that must be made when developing the Directed Fibre Compounding (DFC) process. This outlines the defect mechanisms that are applicable to mould compounds such as SMC, directed fibre processing/tool path optimisation and the fibre bundle parameters, such as tow size and fibre length, that effect the areal density distribution of the carbon fibre.

#### 2.3.1 Mould compound defect mechanisms

The quality of a composite is generally determined by the abundance of defects formed during manufacture. Defects can arise from a number of scenarios depending on the type of fibres used and the manufacturing approach, and can heavily influence the mechanical properties. Due to the lack of literature on DFC, considerations of other

discontinuous composite manufacture, such as DCFP and SMC, can be used to identify the cause of potential defects. Some defect mechanisms that can occur in discontinuous architectures include:

- **Fibre agglomeration** – this can form at two levels, fibre and bundle agglomeration. The clustering of fibres has been shown to reduce the stiffness of SMC composites by 17% [63]. Bundle agglomeration forms with synchronised fibre bundle ends, resulting in greater strain concentrations. This was replicated by introducing slits into UD prepregs, which showed that high stress concentrations formed at the slit/fibre ends which decreased the properties of the prepreg laminates by approximately 40% because of the agglomeration of the fibre ends [64].
- **Void**s – a common manufacturing defect where air gets trapped within the mould and then within the composite matrix. This can also arise from gas trapped within the resin itself, or from the compression pressure being too low [65]. For every percent void content by volume, for carbon/epoxy [0/90]<sup>4</sup><sub>s</sub> laminates, the interlaminar shear strength reduces by 9.7%, the flexural strength by 10.3% and the flexural modulus by 5.3% [66].
- **Flow induced fibre content variation** – when inducing in-mould flow, the local fibre volume fraction can be influenced by the degree of flow. If the viscosity is too low or the fibre volume fraction is too high the resin may travel through the mould faster than the fibres, causing *fibre separation* that reduces fibre content at the flow front [67, 68]. A computational model of a car bonnet manufactured from glass SMC (**Fig. 2.4**) shows how the volume fraction decreases by 25% over approximately 0.5m from the initial charge position. **Fig. 2.5** shows a flow chart for how a part must be optimised for charge position to ensure that suitable mechanical properties are achieved. This suggests that a near-net shape charge, would be beneficial to improve the uniformity of the fibre volume fraction distribution. However, this is not practical for current SMC solutions, as it requires significant touch-labour to prepare the charge pack.

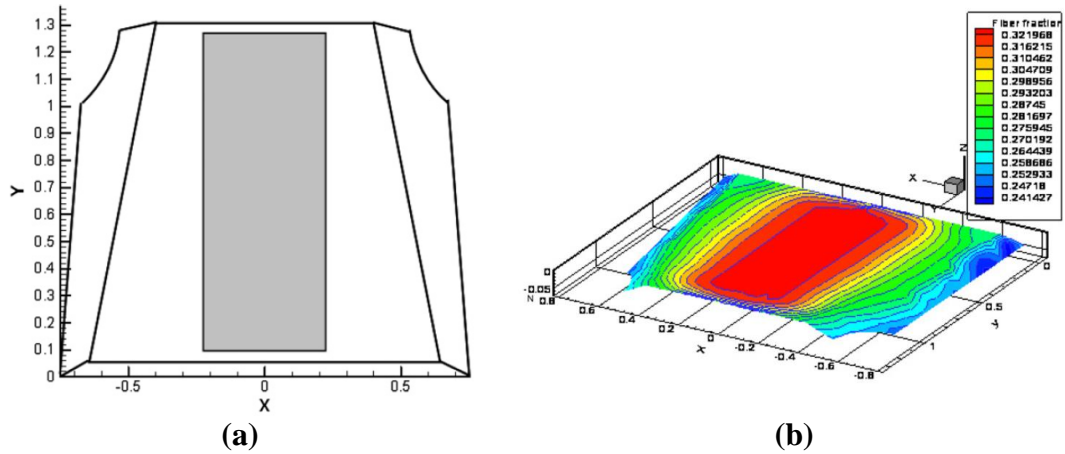


**Figure 2.4.** Flow model for a SMC car bonnet: (a) charge location (b) volume fraction distribution [67]

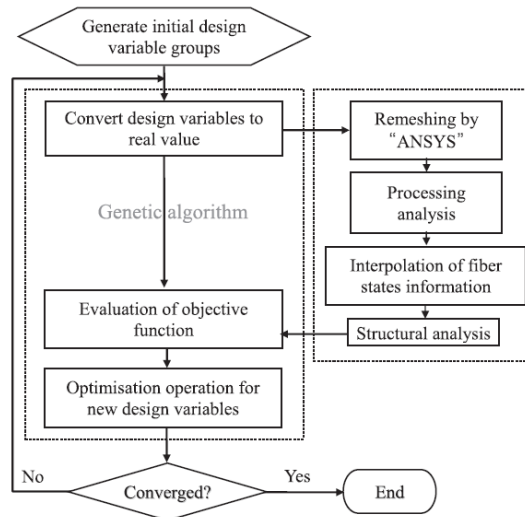


**Figure 2.5.** Flow chart for charge location and dimension optimisation [67]

Local volume fraction variations may also be caused where fibre flow is restricted by narrower sections, such as ribs used for integral stiffening. Fibres blocking other fibres from entering the narrower region (*fibre damming*) cause it to become resin rich, **Fig. 2.6.** **Fig. 2.7 (b)** however, shows how optimisation of the charge construction can be used to prevent this damming.

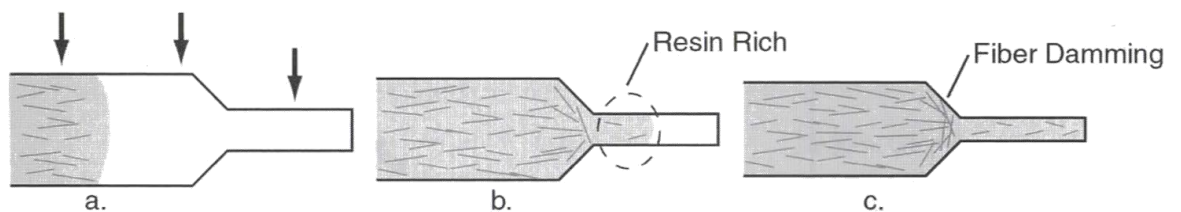


**Figure 2.6.** Fibre damming during mould filling [69]

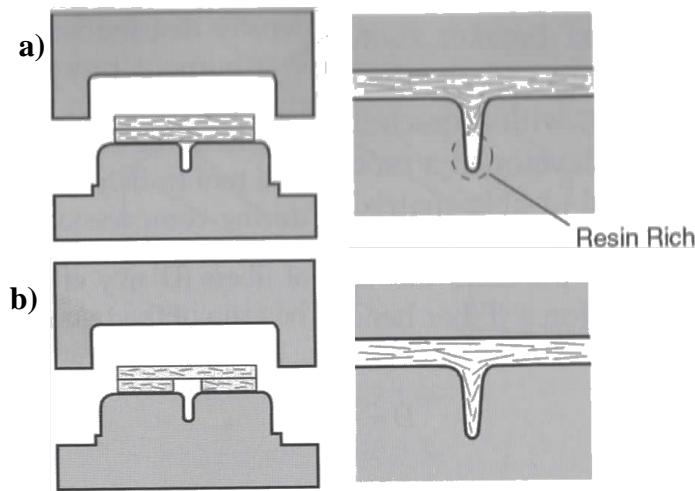


**Figure 2.7.** Alternative charge placements to improve rib filling [69]

- Fibre alignment** – as the fibres flow with the matrix, there are two mechanisms that can affect the fibre orientations: fibre-fibre interactions and flow separation. As a result of the flow separation described, fibres travelling slower than the resin, and therefore increasing in distance from the flow front, tend to rotate and align parallel to the flow direction, shown by **Fig. 2.8**. However, this same flow separation causes fibres near to the flow front to align perpendicularly to the flow direction [68]. This can result in anisotropic properties in the direction of flow travel. This suggests that alignment can be induced by optimising the charge location and shape. Alternatively, using slower closing speeds helps to achieve a uniform charge viscosity through the thickness of the compound. This produces a uniform resin flow front, *plug flow*, which decreases the amount of flow separation, reduces parallel mid-flow fibre orientations and perpendicular fibres in the flow front, reducing the risk of fibre blockages in rib regions [70].

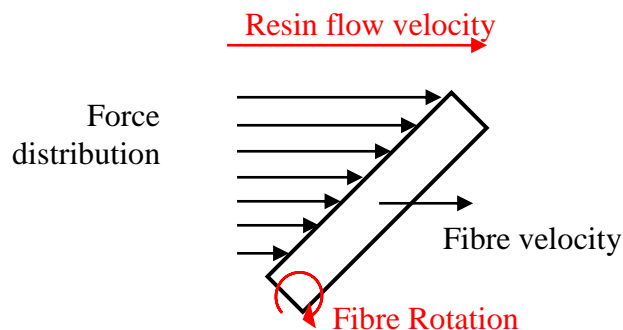


**Figure 2.8.** Alignment of fibres resulting from faster flowing resin, from flow separation

- **Knit-lines** – when multiple charges are used or the flow splits around a feature, for example a hole or insert, two or more in-plane flow fronts are produced. The separate flow fronts may have dissimilar heat distribution may cause different levels of cure or, when these flow fronts join/re-join, fibres with opposing velocity may collide [69]. This prevents interlocking between the flow fronts and subsequent alignment of the fibres, perpendicular to the flow directions, shown in **fig. 2.9**. This produces anisotropic mechanical properties and also forms a resin rich region at the knit-line, which reduces the strength and stiffness of the resulting composite.

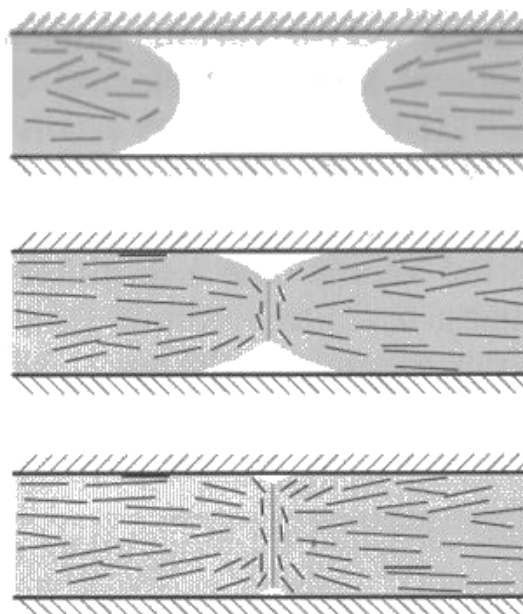


**Figure 2.9.** diagram of the formation of a 'knit-line' during compression moulding of a discontinuous fibre charge [69]

- **Edge effects** – the shape of the flow front is dependent on the rate at which heat is transferred through the compound. The closure speed of an isothermal press influences the rate of heat transfer to the charge [71]. Faster closing speeds transfer heat to the core of the compound faster, lowering the viscosity of the core. As the pressure develops in the tool, a pure shear flow velocity profile is produced, **Fig. 2.10 (a)**. Slower closing speeds transfers heat to the core slower, therefore a lower resin viscosity near the moulding surfaces compared with the core produces a more uniform flow velocity profile, **Fig. 2.10 (b)**. A slower uniform flow front velocity can also prevent flow separation.

When the flow front approaches the edge of the mould, the pressure is lower in the core of the material during pure shear, causing the fibre orientations to diverge near the edge of the mould [71]. This suggests that this *edge effect* can be reduced by lowering the closing speed to produce a more uniform flow front, similarly to preventing a perpendicular fibre flow front [70].

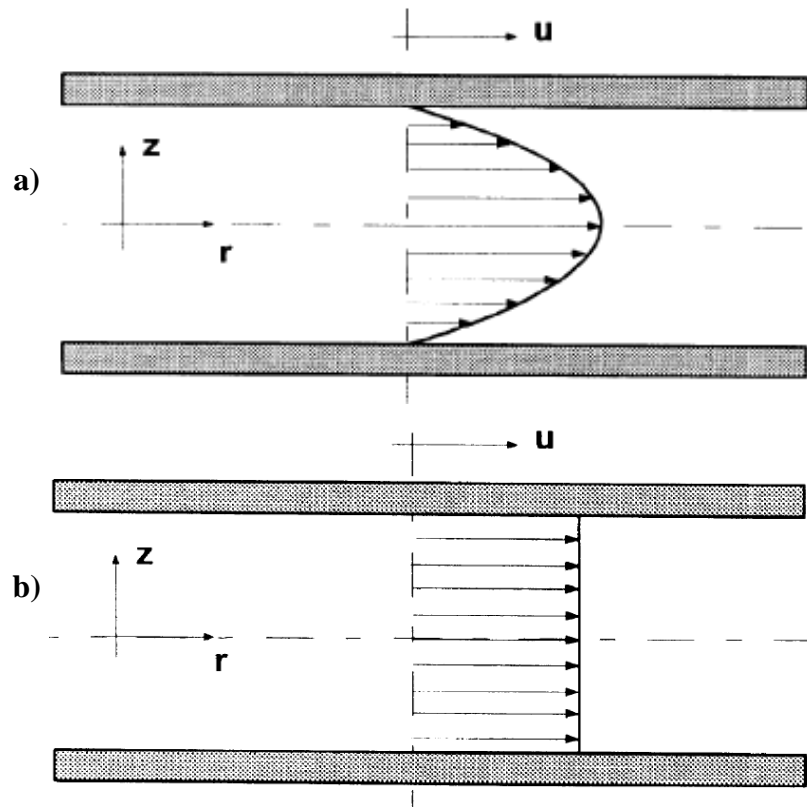


**Figure 2.10.** Velocity profiles of SMC flow fronts (a) pure shear (b) uniform [71]

### 2.3.2 Spray path optimisation

For 2D plaques, a robot program tool path has been optimised to produce a 500mmx500mm compound, which has been optimised to reduce areal mass variability, **Fig. 2.11** [19]. The rate of fibre deposition can be controlled by scaling the feed/chopper gun speeds that delivers the fibres. The volume of resin spray is controlled by the pump speed/voltage and therefore the volume fraction of the compound formed can be controlled by changing the ratio between the fibre deposition and resin spray rates.

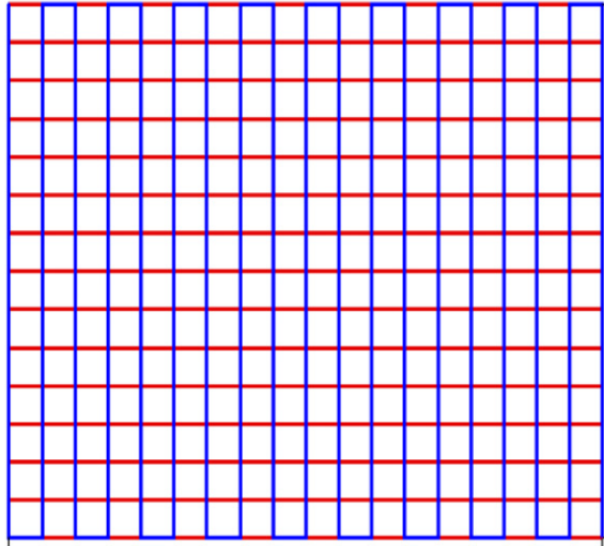


*Figure 2.11. aerial diagram of North-south/East-West tool-path used for best 2D aerial mass distribution [19]*

For 3D geometries, optimisation and generation of the tool-path is significantly more difficult as it requires the input of point-to-point coordinates until the shape is completed. This can be very time consuming and involves a lot of robot down-time to ensure that the program works correctly covering all geometry without collisions, preventing the robot from travelling out-of-reach and over rotation of any axis. Within a commercial environment, offline programming solutions can be performed to simulate and optimise the tool path from the CAD geometry of the component. It is advantageous to be able to program any new operation offline, away from the robot. Some of the benefits can be characterised as follows [72]:

- Production of previous designs can be continued until the new task/reprogramming is finalised, minimising robot down time.
- The workshop environment can be hazardous and therefore it is useful to construct the program away from the robot for a majority of the programming time.
- Simulations can allow the process to be optimized, ensuring that the robot can reach positions along the tool path and that collisions are avoided.

The initial investment for software training is relatively high, but it is important to ensure that operation can be done safely and accurately to avoid errors [72]; however,

the cost is amortised over the life of the production run and is negligible for high volume manufacture.

Attempts were therefore made to produce tool-paths using simulation software from a 3D CAD structure. MasterCAM/RobotMaster was used to simulate a milling operation to generate a toolpath usually used for removing material rather than depositing. This however enabled a tool path to be generated for a 3D CAD image, shown in **Fig. 2.12**, and generate the robot code for all 6-axes on the robot arm and 2-axes on the tilt/turn table.

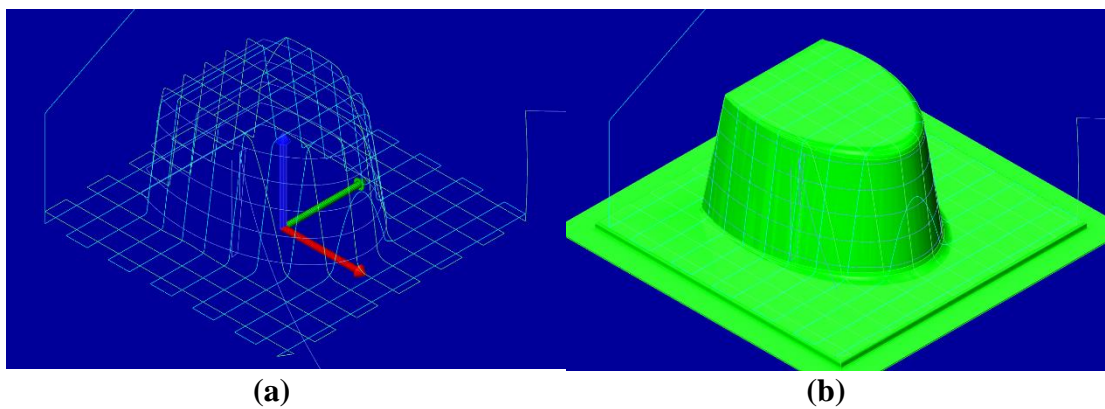


**Figure 2.12.** Example of a tool path generated with the North-south/East-West movements (a) for a 3D geometry (b) using RobotMaster

### 2.3.3 Fibre bundle parameters: fibre length and tow size

Fibre bundle architectures are influenced by the size and length of the bundles. In addition to the spray path, the size of the fibre bundles effects the areal distribution of the fibres. Reducing the fibre length will improve the uniformity of the areal fibre distribution and increases the homogeneity [19]. However, the strength of short fibre architectures is limited by the discontinuity of the fibres. This is dependent on the relationship between cross-sectional area and length of the fibre bundles. Increasing the cross-sectional area of the bundle reduces the tensile stress that that bundle exhibits, while the fibre-matrix interface exhibits shear stresses that are reduced by increasing the surface area by increasing the fibre length. Therefore, shorter the fibre lengths are more likely to fail at the interface resulting in fibre pull-out, whereas longer fibre lengths require greater loads to overcome the shear stresses at the interface and results

in greater fibre bundle breakage [45, 73, 74]. Therefore, reducing the tow size whilst maintaining fibre length prevents fibre pull-out and results in fibre breakage. For example, the tensile strength of the composite is increased by up to 55% by inducing fragmentation in 24K carbon bundles [44].

Mesoscale strain concentrations form at the end of fibre bundles due to filament end synchronisation which significantly lower failure strengths [10, 21, 75]. The magnitude of this strain concentration is influenced by the orientation of the under-lying fibre bundles. For example, if the filament ends of a longitudinal fibre bundle are positioned on top of a transverse bundle (*Fig. 2.13 (a)*), the magnitude of the fibre bundle end strain is greater than if it was positioned on longitudinal bundle (*Fig. 2.13 (b)*). Combined with the low transverse fibre strength, cracks initiate and grow in these locations as the loading is applied [76]. The frequency of this scenario is therefore influenced by the fibre length and tow size. Increasing the fibre length reduces the quantity of fibre bundle ends for a given volume, whilst reducing the tow size reduces the number of filaments with synchronised ends.

There have been additional considerations also with regards to specific energy absorption (SEA) versus fibre length one study proposes that there is little effect from changing the fibre length and that the geometry is the dominating factor for increasing the SEA of a composite [77]. However, an alternative proposal states that they experienced an increase in SEA with reducing fibre length and tow size. This was potentially due to multiple crack initiation sites, allowing uniform load distribution as a result of increased concentration of bundle end stress risers [78].

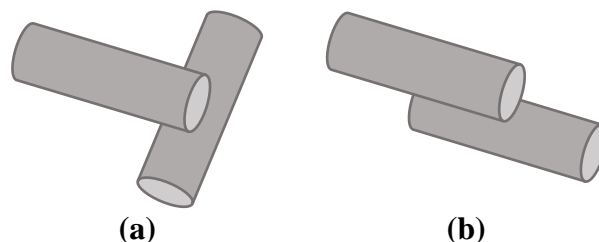


**Figure 2.13.** Schematics of transverse fibres positioned at the end of a neighbouring bundle (a) and longitudinal bundles positioned at the end of a neighbouring fibre bundle (b)

## 2.4 One dimensional moulding compound flow

### 2.4.1 Characterising in-mould flow

To exploit low cycle times of compression moulding compounds, discontinuous SMC and bulk moulding compounds flow under the compression to produce a net-shape part. The polymer rich outer layers of the moulding compound act as a lubricating layer, which shears near to the mould surface whilst the fibres deform through thickness to create plug flow [71, 79, 80], such as that shown in *Fig. 2.10 (a)*. The flowability of a moulding compound is dependent on the mould parameters, viscosity and thickening agents [24, 27, 79]. A rheological study of SMC by Guiraud et al. [27] showed the effect of mould temperature. Moulding at low temperatures to induce a higher resin viscosity, results in compressible behaviour (initial volume change) of the charge because of the high porosity levels. This compressible behaviour can be attributed to slow outgassing of entrapped air, or styrene [81]. Reducing the viscosity by elevating temperature enables incompressible behaviour and improves outgassing. Incompressibility increases the rate of flow with the degree of axial compression. The reduction in viscosity additionally reduces the friction forces within the mould and reduces the compressive load required to fill the mould [24, 27]. Alternatively, applying a slower tool closure rate enables greater heat transfer into the compound, reducing the viscosity and therefore the compressive forces required to fill the mould [71].

Fibre-matrix separation can be characterised by measuring the fibre volume fraction [67, 82] or by positioning pressure transducers [24, 80, 83] along the flow length to produce a distribution. Using a spiral flow tool enables characterisation of one-dimensional flow across great distances without the requirement of a large press [80, 83]. This applies a compressive load to a centrally located square compound, shown in *Fig. 2.14 (a)*, which forces charge flow in a near singular direction along the narrow channel. In addition to flow distance, the thickness of the mould also results in fibre-matrix separation as a result of fibre plugging or increased friction between interacting fibres [67]. *Fig. 2.14 (b)* shows an example tool with variable thickness along the flow length that measures the pressure distributions within each step [24].

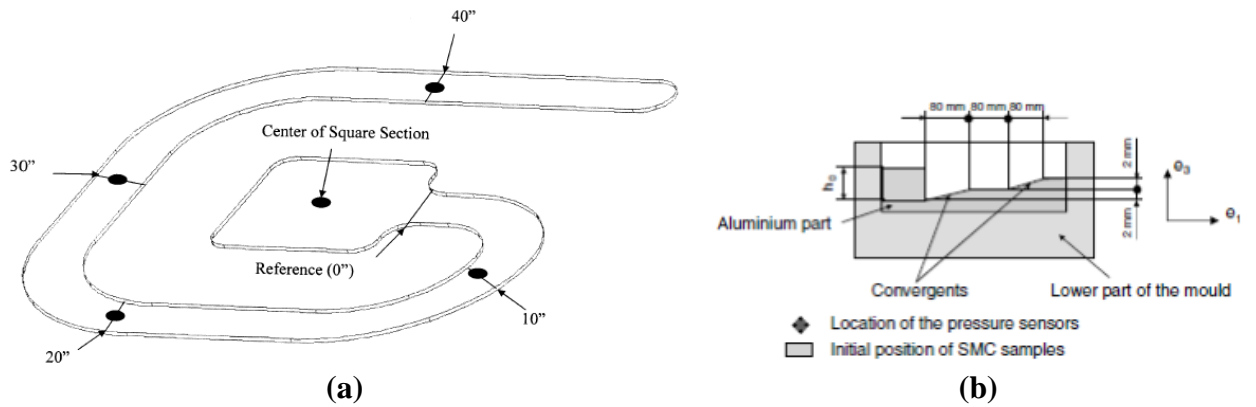


**Figure 2.14.** Example of (a) spiral flow tool [80, 83] and (b) variable thickness SMC flow tool [24]

## 2.4.2 Orientation characterisation

Fibre orientation measurements are commonly performed using optical micrographs to determine both the in-plane and out-of-plane distributions. In-plane fibre orientations are derived from the length of the major and minor axis of the filament ends on a cast cross-section of the composite. Whilst image acquisition can be automated, specimen preparation is labour intensive, only small local sections are characterised and many samples are required to achieve a representative orientation distribution. This is a particular problem for the random bundled materials studied here because it is imperative that filaments are sampled from different tows. In-plane bundle orientations therefore need to be measured at the macroscopic component level and not the microscopic filament level. Kacir et al. [84] successfully used a highly visible dye on 250 glass fibres to identify orientations using digital images. This method is clearly inappropriate for opaque carbon fibres, so burn-off studies are typically performed on dry performs to remove the binder material [85]. Whilst these macroscale methods can be successfully used to quantify bundle orientation effects, they are time consuming and accuracy can be limited.

X-ray computed tomography (X-ray CT) is one of the most common non-destructive testing techniques to obtain information on the internal structure of composite specimens. X-ray CT produces a 3D image consisting of 2D slices enabling visualisation of multiple planes within the sample that can be analysed to assess internal damage [86-88] or fibre misalignment [89, 90]. However, this requires investigation at

a microscale to quantify the orientations of individual filaments by image analysis techniques and can take up to 2 hours to generate a scan of a sample size typically less than 50mm x 50mm [89]. Although some work has been performed to quantify the fibre orientation vectors of short fibre composites [91] and microstructure of small sections of SMC [81], tow-based discontinuous compounds encounter difficulties when adopting this technique. Each individual fibre bundle will contain a filament orientation distribution which not only varies through the cross section of the bundle, but also along the length of each fibre (>25mm) [92]. This generates large localised variations which therefore requires multiple 3D scans to obtain a sample size sufficient to quantify the fibre distribution of a sample. It was therefore decided that this was beyond the scope of this thesis because of the facilities and time constraints to prepare, scan and process the number of specimens required to obtain these results.

## **2.5 Hybrid fibre architecture and interfacial characterisation**

### **2.5.1 Prepreg compression moulding**

Isothermal compression moulding is capable of achieving pressures ten times greater than in the autoclave (typically 80bar+). Compression moulding of prepregs significantly reduces processing times by using a low temperature preforming stage to reduce layup times before transferring to an isothermal tool where higher pressures are used to ensure low void content. Isothermal tooling results in uniform high heating rates by conduction, which enables the use of snap-cure resins, achieving cure times of less than 5 minutes [31, 93]. However, fibres within continuous prepregs do not flow easily during compression moulding which prevent sufficient pressure from being achieved within vertical and hollow sections of the mould. This requires advanced compression moulding techniques such as “moving wall tooling” to provide a horizontal force simultaneously with vertical compression, and particle-core moulding techniques which transfers the compression force through ceramic particles within a flexible diaphragm to induce a hoop pressure internally within a hollow region [94]. *Fig. 2.15* and *2.16* shows particle-core moulding and moving wall mould tooling.

However, to produce a mould which incorporates moving components require additional design considerations. These range from sealing the moving components, and the wear and fatigue reducing lifetime. This significantly increases the costs to

produce and maintain the mould tooling capable of incorporating a “moving wall” or particle core.

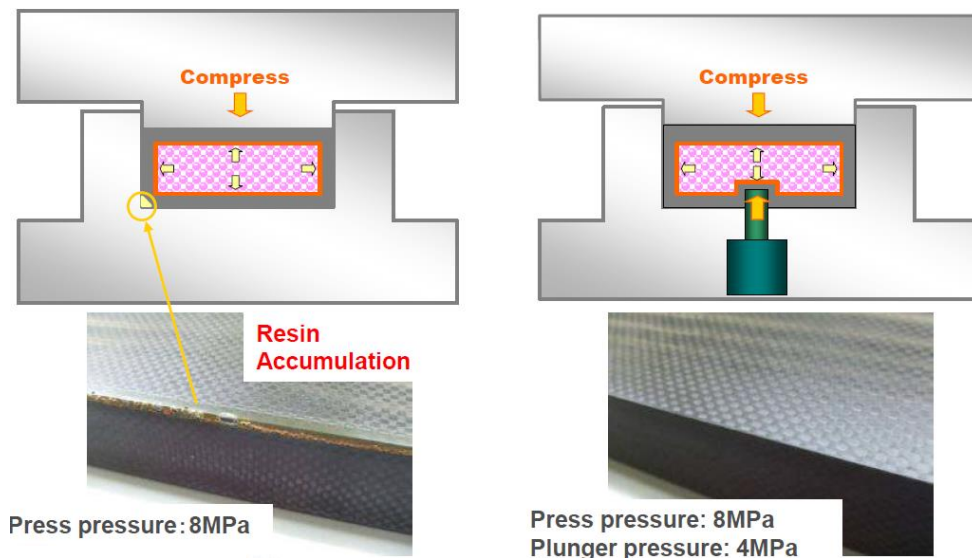


**Figure 2.15.** Compression moulding a hollow component without (left) and with (right) an internal pressure generated by Particle-core Compression Moulding [94]

### 2.5.2 Hybrid fibre architecture

It is becoming increasingly recognised that compression moulding hybrid fibre architecture has key benefits for producing complex 3D structures with tailored mechanical properties and short lead times [55, 95]. Compression moulding continuous fibres/prepregs with a discontinuous moulding compound, such as an SMC, uses the in-mould flow capabilities to improve pressure distribution within the moulding compound by generating an internal pressure, similar to particle-core compression moulding [94].

Mitsubishi Rayon Co. Ltd. [31, 94] demonstrated the potential of compression moulding hybrid fibre architecture using their advanced tooling techniques to produce ribs, embed metallic inserts and manufacture hollow sections. This is shown in **Fig. 2.17**.

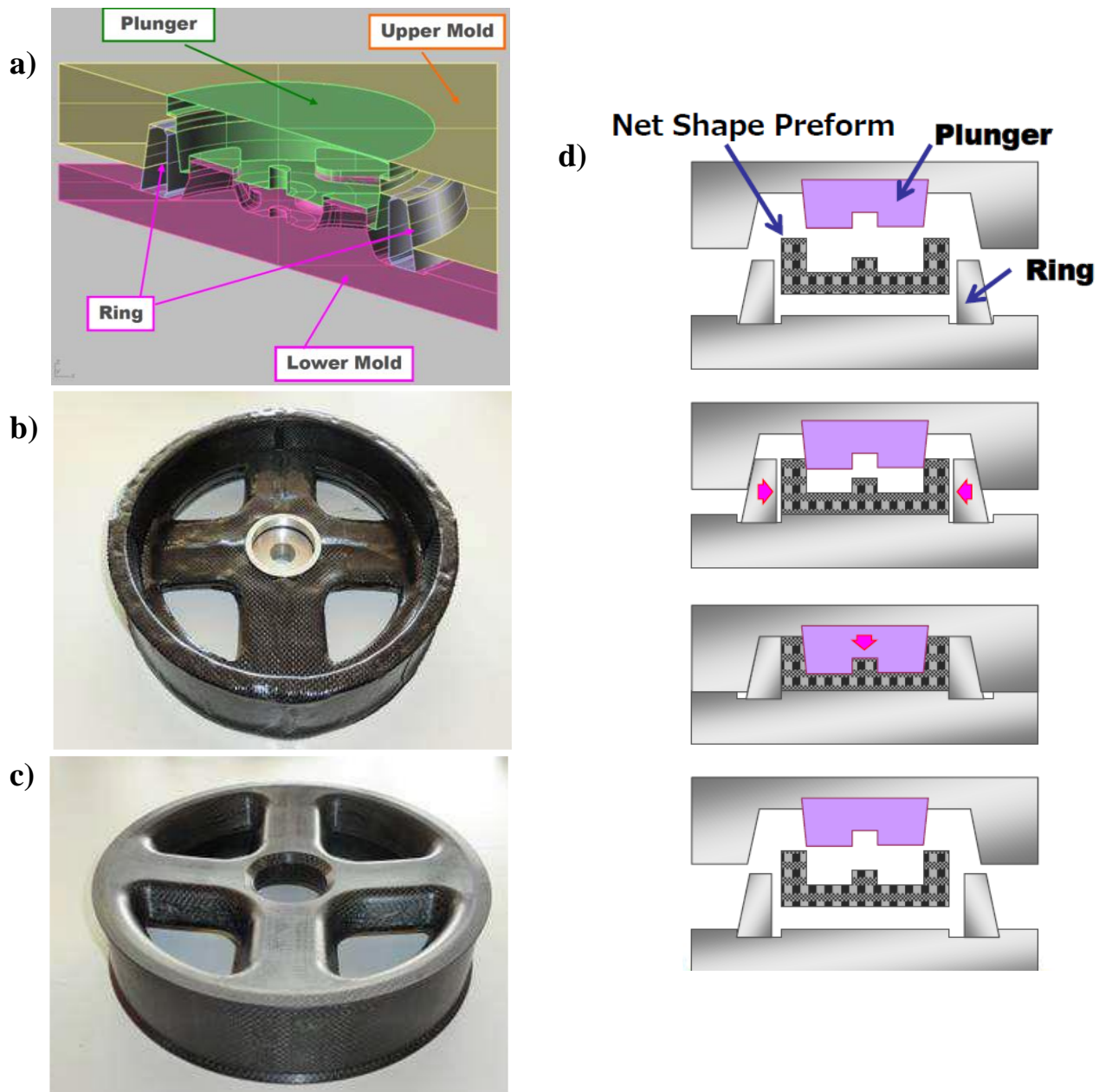
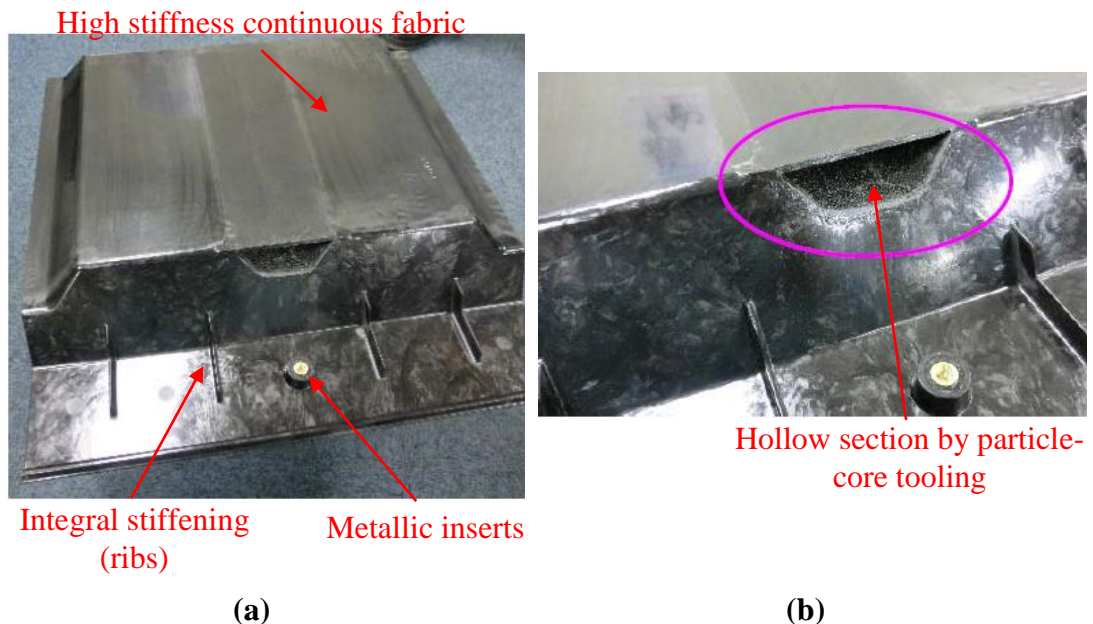


**Figure 2.16.** Compression moulding of a Carbon Fibre Wheel using moving wall tooling (a) 3D schematic diagram of the mould tool (b) warped part, without using moving wall (c) finished part using moving wall (d) flow diagram showing how the moving wall produces a horizontal force [94]

The flow of discontinuous moulding compounds within a hybrid architecture may distort the continuous plies. Corbridge et al. [32] determined that A-SMC flow in the transverse direction to the continuous fibres resulted in shearing of the laminate and in-plane waviness. Flow of moulding compounds in the continuous fibre direction resulted in ply migration. This study also demonstrated that these distortions can be reduced by advancing the cure of the continuous laminates. However, compression moulding the

cure advanced prepregs with moulding compound reduces the degree of crosslinking across an interface and results in a knock down of ILSS by up to 60% between HexPly® UD prepreg laminates.



**(a)** *Figure 2.17. (a) Floor pan application by Mitsubishi Rayon [31] demonstrating moulding features capable by compression moulding hybrid architectures and (b) using particle-core compression moulding [94]*

### 2.5.3 Layup strategy

It is difficult to automate the fabrication of complex laminates without introducing defects, due to the dexterity and precision required. One method of positioning aligned continuous fibres is to use Automated Fibre Placement (AFP), which lays a continuous roving using a robot into a net-shape, suitable for LCM. This generates little/no waste but preforming times increase depending on the level of complexity of the geometry [96].

In industry, laminate guidelines are followed to avoid warpage and to achieve good interfacial behaviour. In the aerospace industry, these can be as follows [97-99]:

- Laminates should be symmetric about the middle surface to prevent warping during cooling or thermal loading.

- Fibre orientation angles, other than  $0^\circ$  and  $90^\circ$ , should be balanced in pairs. For example, for every  $+45^\circ$  laminate there should be a  $-45^\circ$  laminate. This removes coupling between the in-plane normal and shear behaviour. This also simplifies the bending response.
- Each of the 4 basic orientations should be at least 10% of the total plies. There are variations of this rule however. If at least 20% of the plies are at  $\pm 45^\circ$ , then just 6% of  $90^\circ$  plies may be used.
- Primarily loaded plies should be internal within the laminate, improving the damage tolerance and preventing minor impacts from damaging the critical plies.
- $\pm 45^\circ$  plies on the surface maximise the buckling resistant.
- Thermal expansion should be avoided by using  $\geq 10\%$   $0^\circ$  and  $90^\circ$  plies.

#### 2.5.4 Ply drop and joint design guidelines

When stacking the continuous fabrics, the alignment of the ends of the fibre bundles must be considered. When the edge of a ply is internal within a stack, a resin rich region is formed at the ply drop (shown in *Fig. 2.18*). There are a number of design guidelines that must be adhered to when ply dropping to increase the strength before delamination [100, 101]:

- Surface plies should not be dropped
- The maximum taper angle,  $\alpha$  (*Fig 2.19*), should not exceed  $7^\circ$ . Ply drops should therefore be staggered by a minimum distance of approximately eight times the thickness of the ply.
- Ply drops should be staggered through the thickness, alternating between plies close to the surface and close to the laminate centre line
- Plies should be dropped in decreasing order of stiffness to ensure smooth transfer of load and to reduce stress concentrations. For example,  $0^\circ$  plies first and  $90^\circ$  plies last.
- The number of plies dropped at any location should be kept to a minimum to reduce the volume of resin rich regions.

Similar considerations could be used in hybrid fibre architectures when the in-plane laminate edges transition to the random phase. These ply drops effectively form a joint between the continuous and discontinuous material. **Fig. 2.19** shows some of the laminate arrangements of joints that may be suitable for in-plane change of phase between continuous and discontinuous. The single stepped lap joints showed superior flexural strength and modulus with little difference to the tensile strength [102]. This is advantageous when compression moulding hybrid fibre architectures, as stacking the double stepped lap joint and interleaved joint would significantly increase the cycle time in comparison to placing a stack of single stepped plies. The alternative would be to rely on the flow of the chopped fibre to fill between the plies in the double stepped and interleaved joint arrangement, which is likely to buckle the overhanging laminates as the matrix softens and the viscosity drops during moulding.

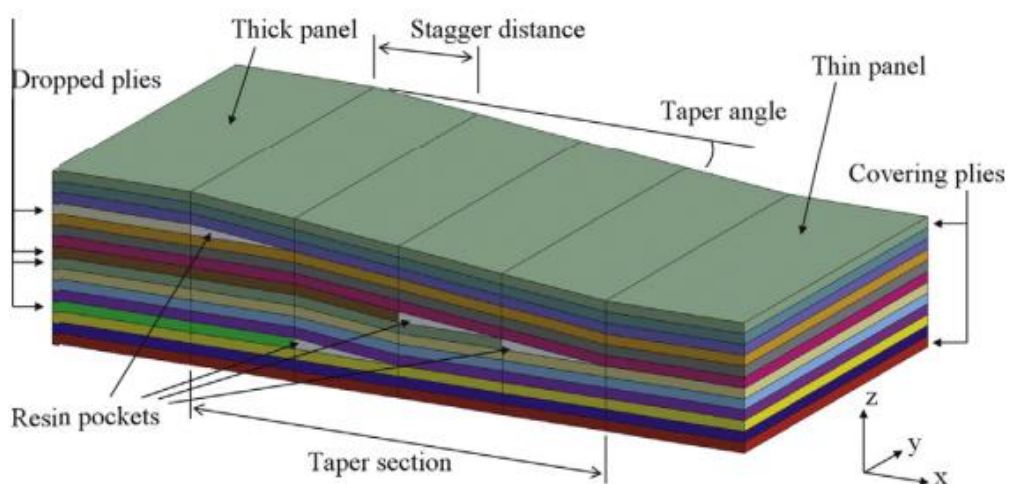


**Figure 2.18.** Schematic diagram of section with internal ply-drops [100]

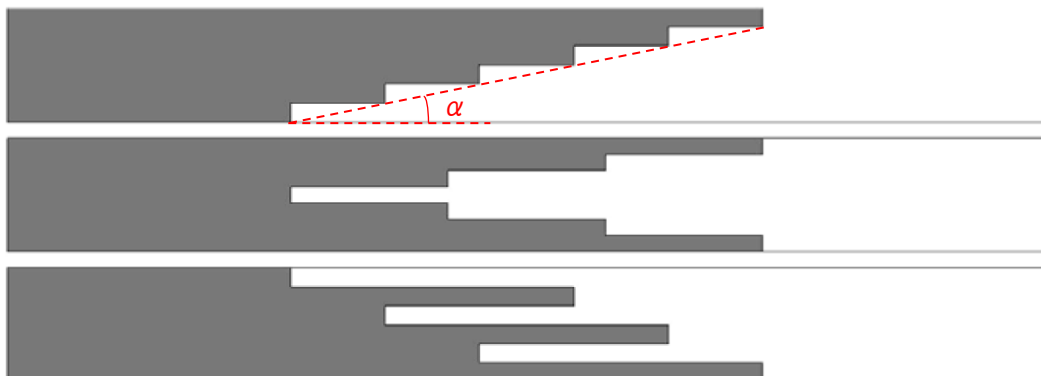


**Figure 2.19.** Joint types: (top) single stepped lap, (middle) double stepped lap (bottom) interleaved [102]

Bonded joints under a tensile load would typically experience two stresses at the adhesive interface: shear stresses about the plane of the interface and peel stresses that act in the normal direction to the interface. This results in a coupling consisting of tension and bending behaviour which is dependent on the stacking sequence within each laminate [103]. The bending-tension coupling, lower transverse stress and larger deformation of an unbalanced joint (with unsymmetrical adherend stiffness) can have a considerable effect on the adhesive stress distribution [104]. This deformation, peak and shear stresses are demonstrated in **Fig. 2.20** [105, 106], and as the stiffness imbalance ( $E_{\text{upper material}}/E_{\text{lower material}}$ ) increases, the magnitude of these stress peaks also increases [104]. Joint design guidelines for composites often suggest tapering the ends of the composite, usually by machining them to form a scarf joint if laminates cannot be stepped to minimize the peel stresses that peak near to the end of each adherend [97, 99, 107].

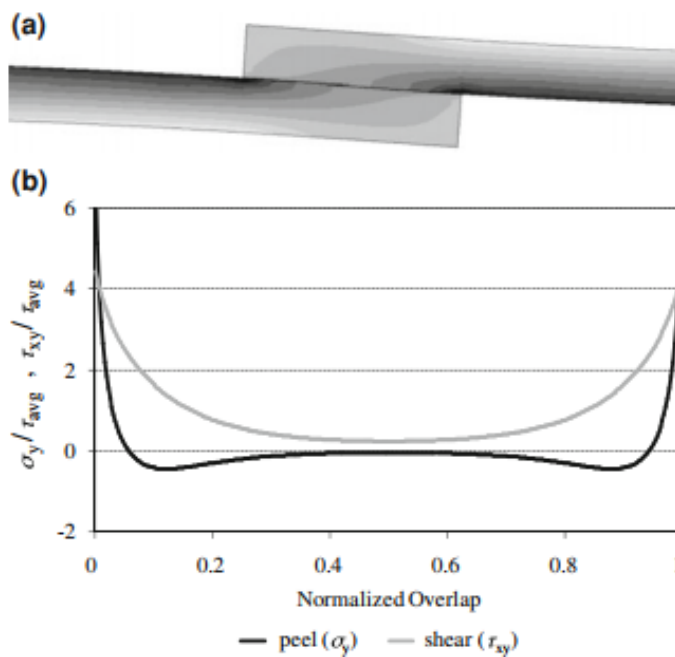


**Figure 2.20.** Deformed shape of a single lap joint (a) and peel and shear stress distributions in the adhesive bond along the overlap (b) [105, 106]

In addition to the peel and shear stresses at the interface of joints, ply drops also exhibit axial stresses in the resin rich regions at the end of each terminated ply [108]. Peaks in each stress arises at the location of the ply drop, at the end of the terminated ply and end of the resin rich region. This is shown in a finite element analysis model in **Fig.**

2.21, where the centre two plies are dropped in a 10 ply laminate [108]. This shows the axial, normal and shear stress distributions (*Fig. 2.21 (b)*) along the centre of plies (numbered in *Fig. 2.21 (a)*), 4 & 7 (either side of the dropped plies), 5 (dropped ply) and 10 (upper ply). The magnitude of these peaks is also affected by the taper angle,  $\alpha$ , by controlling the number of plies dropped at any location; increasing the number of plies dropped simultaneously, the greater the taper angle and the greater the magnitude of the stress concentrations [108]. Delamination is most likely to initiate at the end of a terminated ply, where the peaks in stresses arise. Therefore, with multiple ply drops, it is suggested that a shallower taper angle, or larger step size, will reduce the magnitude of any localised peak stresses.

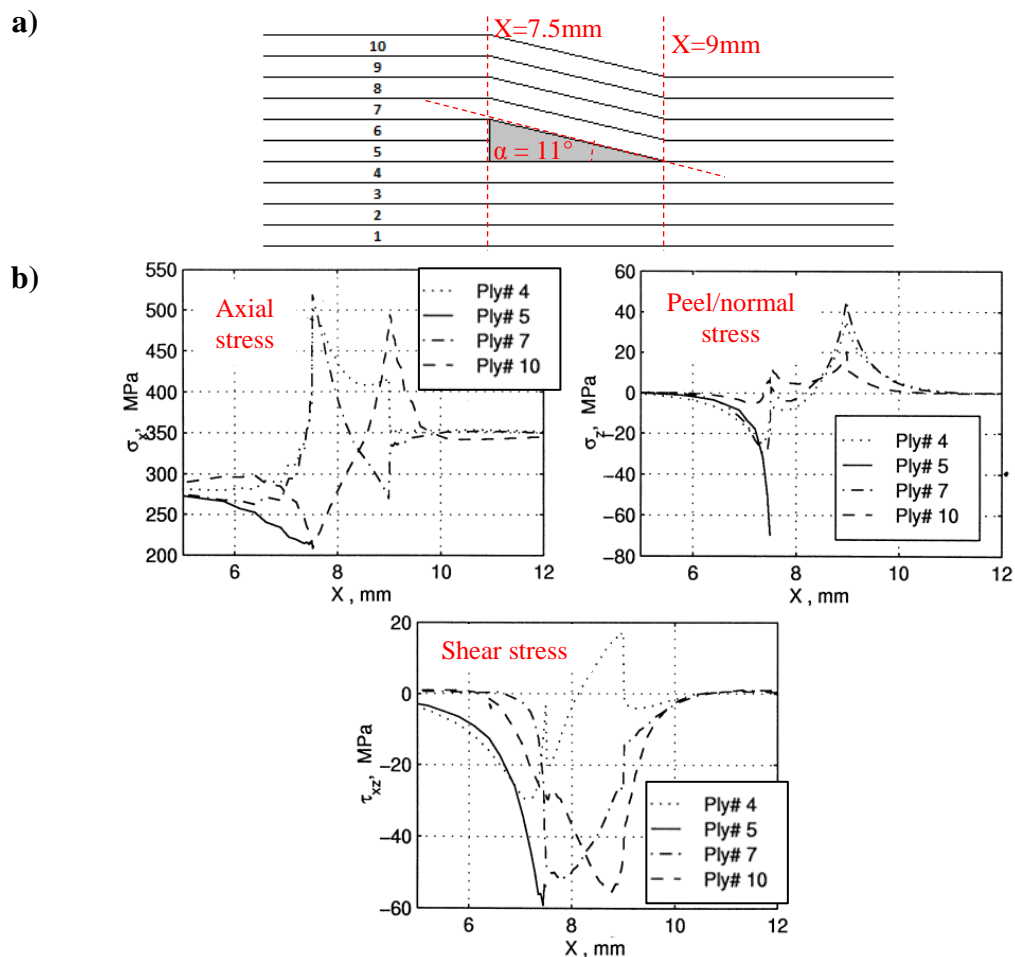


**Figure 2.21.** a schematic showing the FE analysed ply drop at the centre of a 10 ply laminate (a) and the ply stresses in the vicinity of the taper (taper angle,  $\alpha=15^\circ$ )

[108]

### 2.5.5 Residual Stresses

Residual stresses form as a result of chemical stresses, due to shrinkage and moisture content, and thermal stresses, due to the mismatch in the coefficient of thermal expansion between the fibre and the matrix [109]. The greatest cause of warpage is asymmetry about the laminate centre and the anisotropic nature of the thermal expansion mismatch [110]. This is because the matrix has a much greater thermal expansion coefficient than carbon fibre. Curing the composite at elevated temperatures results in compressive residual stress acting on the fibre which develop during cooling.

These stresses may affect the fibre performance and induce waviness which will reduce the overall strength of the composite, leading to cracking, delamination and low fatigue and fracture performance [111, 112]. At the macroscale, these stresses act anisotropically and often lead to warpage or ‘spring back’, causing difficulties during component assembly [112]. The thermal expansion is greater in the transverse fibre orientation than in the longitudinal orientation causing curvature in asymmetric panels, such as in *Fig. 2.22*, whereas symmetric plies cancel-out this curvature and result in a build-up of residual stress [112].

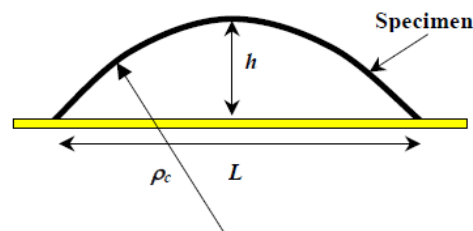


*Figure 2.22. Schematic of the curvature of an unbalanced panel [112]*

### 2.5.6 Architectural failure mechanisms

It is important to determine the failure mechanisms within hybrid composites with respect to features within the fibre architecture. For discontinuous fibre composites, stress concentrations often arise at the ends of the fibre bundles [10, 21]. For shorter fibre lengths, fibre pull-out increasingly dominates the fracture mechanism as a result of a smaller contact area with the matrix. Thus, there is more fibre breakage with longer fibre lengths since the larger fibre-matrix interface requires greater loads to overcome

the interfacial adhesion [73]. Failure within the continuous plies requires breakage of the high strength fibres and therefore requires the highest stress. Alternatively, a crack may propagate within the resin rich region between the laminates, causing delamination of the plies [1]. Unique to hybrid architecture, an additional interface is positioned between the dissimilar materials. It is therefore important to understand how stresses are transferred between the constituent materials and fibre architectures.

Inter-laminar Shear Strength (ILSS) is often used to quantify the shear strength along the neutral axis, where no longitudinal stresses are exerted as a result of the tension and compression either side of the axis [113]. This is often called the ‘apparent inter-laminar shear strength’ as it depends on the specimen geometry [113-115]. This value can be used to represent how well the stress is transferred through the thickness of a laminated composite and assess the toughness of the component to resist mode-II fracture. When hybridising the architecture, there will be a resin rich boundary between the random and continuous laminates. Good interfacial strength is therefore required to prevent delamination [1]. However, as a result of the variable nature of the random material, greatest shear stress may not arise along the planar interface between dissimilar materials and therefore the failure may not form at the same position from specimen to specimen [113]. Additionally, the ILSS is known to be influenced by the fibre volume fraction, decreasing as the fibre volume fraction increases [116]. Therefore, the variable local fibre volume fraction of discontinuous composites will prevent sufficiently repeatable results from being obtained within the small specimen geometry of short beam shear testing (20mm x 10mm [114]).

There are 3 modes of delamination fracture shown in *Fig. 2.23*:

Mode-I – tensile stresses perpendicular to the crack direction

Mode-II – laminate sliding, often caused by bending

Mode-III – in-plane tearing

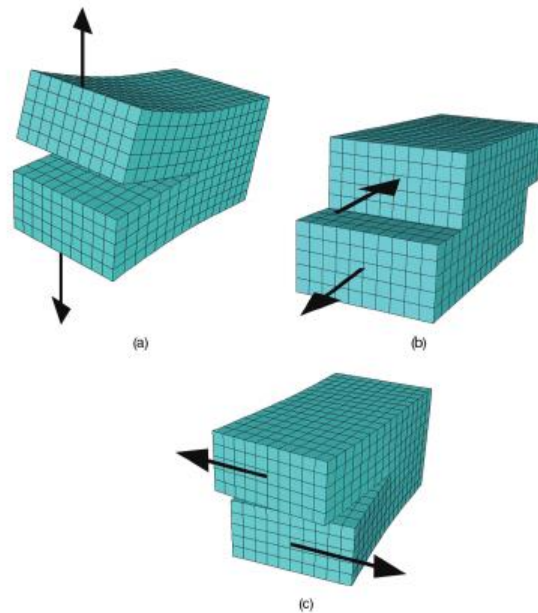


**Figure 2.23.** interfacial fracture modes (a) mode-I (b) mode-II (c) mode-III [1]

Mode-I and II are the most common and can be measured experimentally. Mode-I can be tested using Double Cantilever Beam, DCB, experiments [1], where an out-of-plane tensile force is applied to propagate a crack between the laminates. However, the non-linear fracture of discontinuous architectures can cause the crack to deviate from the laminate boundary and therefore grooves are sometime cut along the length of the specimens to direct the crack propagation, **Fig. 2.24** [73]. Asymmetric DCB can also be used to fracture away from the neutral axis to assess mode-II fracture [1]. Mode-II can also be assessed by short beam 3-point bending of End Notched Flexure specimens (see **Fig. 2.25**) [1].

Another option is to perform 4-point bending of a specimen moulded over a 90° bend, **Fig. 2.26**. This produces a through-thickness tensile stress by inducing a constant bending moment between the loading points [117]. One of the main advantages is that there is no requirement to control the direction of crack formation, which can be difficult when assessing random fibre architecture boundaries. This is because of the constant bending moment, since no direct axial tensile stress is induced [117]. However, fabrication limitations arise as it is difficult to achieve uniform fibre volume distribution about the bend.

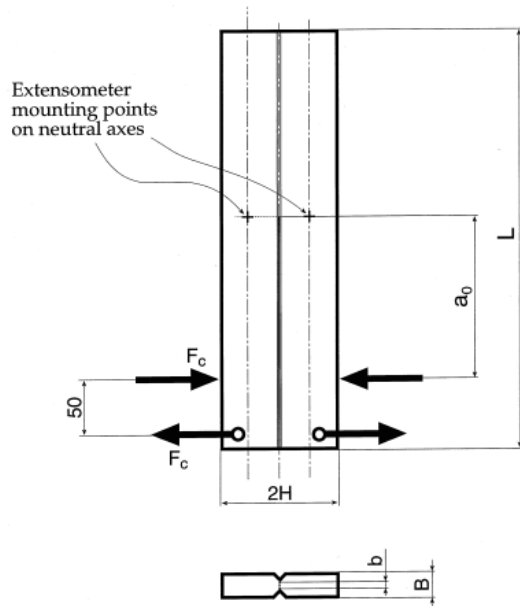


**Figure 2.24.** DCB specimen with long-length groove [73]

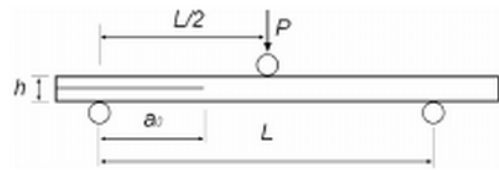


**Figure 2.25.** ENF arrangement [1]

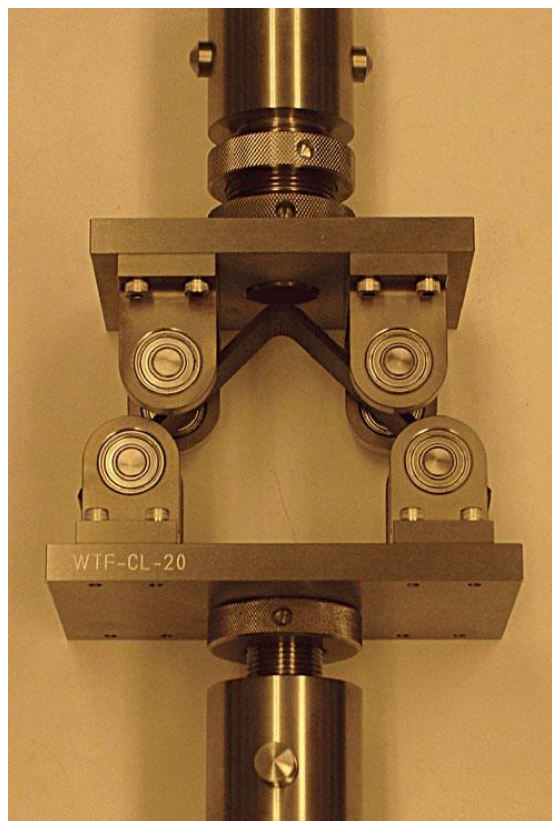


**Figure 2.26.** 4-point bend of a 90° specimen [117]

Mixed-mode fracture toughness,  $G$ , (mode-I and mode-II) can also be experimentally determined by mixed-mode bending (MMB) to simultaneously bend (mode-II) and separate (mode-I) a composite specimen [118, 119]. Apparatus for this is shown in **Fig.**

2.27. This enables the ratio between failure modes to be determined to establish the dominate fracture modes [119].

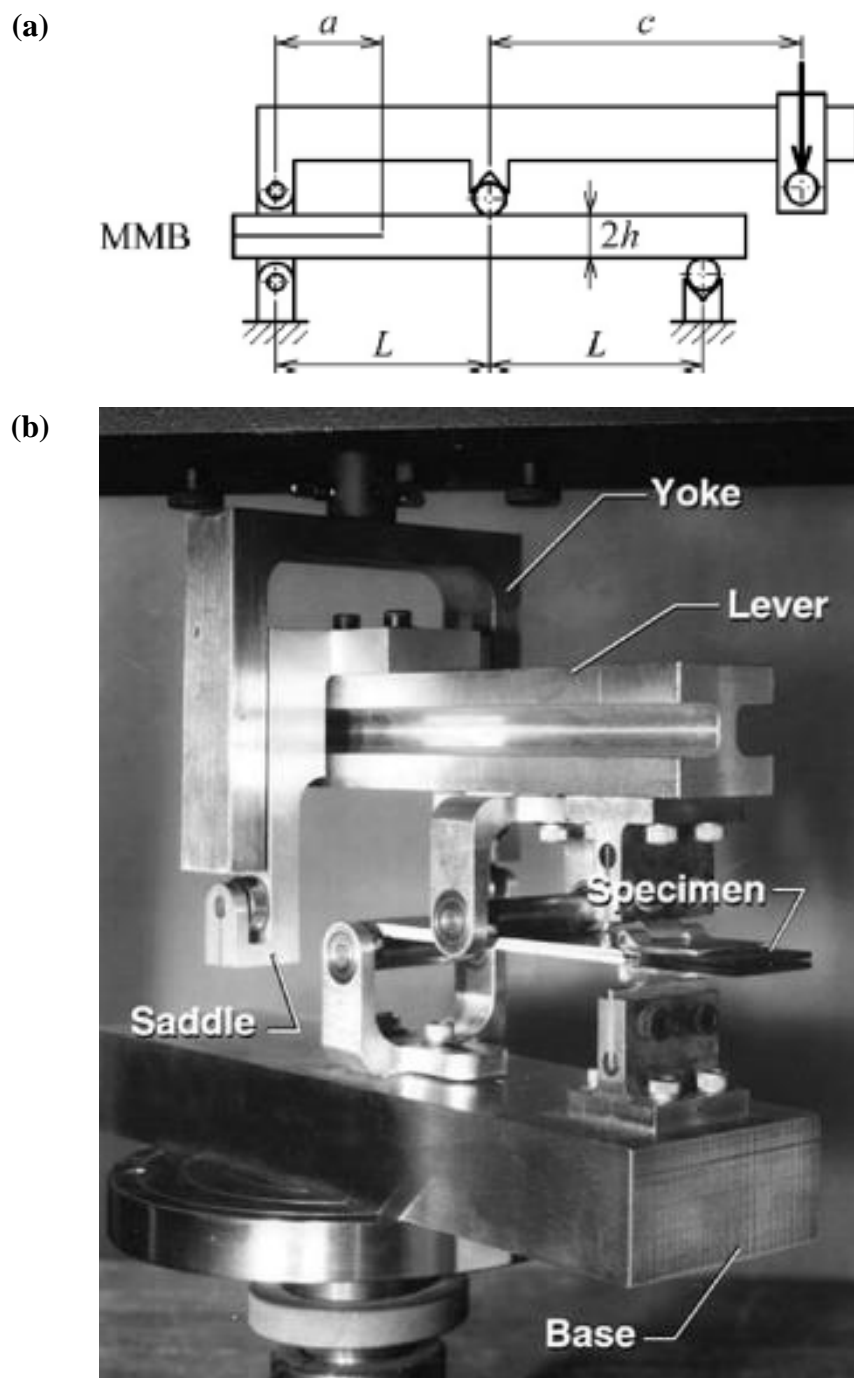


**Figure 2.27.** (a) Schematic diagram of mixed-mode bend testing arrangement [119] and (b) a photo of MMB test apparatus [118]

Although it would be useful to characterise the continuous-discontinuous interface by each mode of fracture, there are both material and manufacturing constraints that

prevent this. The random nature of the discontinuous material therefore requires investigation over a large specimen to account for the variability, whilst the geometry is required to be flat with uniform thickness as a result of the compression mould tooling. These prevent investigation of mode-II failure by tensile loads of single or double lap joints because of the small area of investigation and geometry of the specimens. Additionally, it is required for the fracture to propagate horizontally, along the interface. However, the through-thickness stress distribution of the discontinuous material during bending may result in crack deflection around fibre bundles [113] and away from the interface and into regions of high local stress. Therefore, it was deemed only suitable to investigate the mode-I separation within this thesis to enable initial understanding of a continuous-discontinuous interface to be developed. As a result, further literature investigation was made to DCB testing.

### 2.5.7 Double Cantilever Beam testing (Mode-I Separation)

Double cantilever beam (DCB) testing will be used in this thesis to determine the mode-I fracture toughness of monolithic and hybridised interfaces. During mode-I separation, delamination is induced along an interface, where a resin rich interface provides a low strength path where a crack may propagate [1]. However, load carrying fibres near to, or interleaving the interface, transfer stress across the interface producing a stress distribution surrounding the crack tip, shown by *Fig. 2.28*. Over the length of this damage zone, broken or pulled out fibres no longer contribute to stress transfer. This reduces the ability to analyse the fracture as a linear elastic fracture mechanics [73].

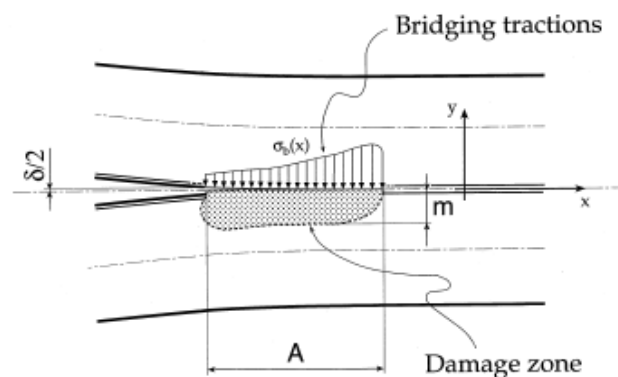


*Figure 2.28. Schematic drawing of the damage zone of a crack produced by a double cantilever beam specimen [73]*

Truss et al. [120] compared inter-laminar fracture toughness of discontinuous and continuous carbon fibre/epoxy composites. When the crack runs perpendicular to the bridging fibre direction fibre, crack deflection and blunting give excellent toughness. However, this toughness is much lower in the parallel directions to the fibre, such as delamination. Fibre bridging however still remains the most efficient mechanism in reducing the stress level at the crack by diverting the stresses through the bridged fibres [121]. Experimentation of inter-laminar DCB of the two materials showed that there was no fibre bridging for continuous plies and it was seen in the case of discontinuous fibres. This resulted in higher fracture toughness for discontinuous fibre materials (981 J/m<sup>2</sup>) compared to continuous fibre material (250 J/m<sup>2</sup>), results shown in **Fig. 2.29**, even though the fibre volume fraction of discontinuous material ( $V_f = 36\%$ ) was lower than the continuous ( $V_f = 46\%$ ).

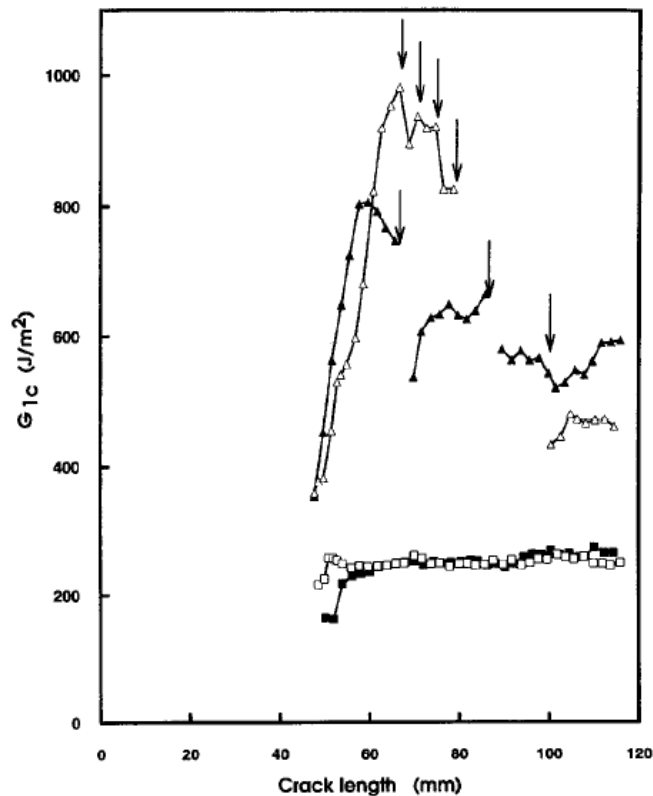


**Figure 2.29.** Interlaminar fracture toughness with respects to crack length for carbon fibre/epoxy composites, two discontinuous (▲△) and two continuous (■□) [120]

It was also noticed that the fracture toughness had to be determined as a function of crack length for discontinuous carbon fibre as the DCB testing experienced high crack

propagation rates [120]. Conversely, the inter-laminar fracture toughness against the crack length (*Fig. 2.29*) of continuous fibre architecture plateaus at the peak fracture toughness as the crack propagates at a constant rate. This can give difficulties in quantifying a global fracture toughness value for discontinuous architectures, however it should be noted that the fracture toughness at any crack length still remained greater than the peak fracture toughness of the continuous fibre architecture.

Some characterisation has been performed on dissimilar materials such as sandwich structures. The DCB test setup can induce uneven bending moments if dissimilar constituents are used to form an asymmetrical hybrid [122]. This therefore led to the development of single cantilever beam testing whereby one constituent is bonded to a rigid surface to provide horizontal bending crack propagation [123, 124]. However, this requires complex apparatus to ensure load is applied vertically to the end point of the specimen and also requires a high strength bond to the rigid surface that has a greater strength than the tested interface.

## **2.6 Damage tolerance of hybrid fibre architecture**

### **2.6.1 Fracture toughness**

An important quantity measured for composites is the fracture toughness. This dictates how much energy can be absorbed by the material without crack initiation. Once a crack is initiated, the damaged fibres can no longer contribute to stress transfer and therefore properties are significantly reduced.

The fracture toughness is often evaluated to demonstrate the resistance of the material to cracks by absorbing energy, such as performing impact tests. Two test methods commonly used are Charpy impact testing and drop-weight impact testing.

One of the problems with Charpy impact testing is that it was originally developed for metals [125] before adapting to characterise plastics [126], where the failure mechanism is through-thickness tensile failure to initiate a crack from the surface. Testing 10mm thick composite specimens, failure can be exhibited by tension, compression or shear (in and out-of-plane) or a combination of them all, dependent on the through architecture arrangement and can produce inconsistent energy absorption

measurements. This led to the development of drop weight testing [127]. Drop weight testing uses larger specimens that can be subjected to multiple impacts to assess property degradation.

A multi-impact experiment for glass fibre laminates established that delamination was the dominant failure mechanism, with the greatest energy absorption achieved in the first impact. This delamination is often characterised using non-destructive testing methods such as ultrasonic C-Scanning [128-131]. The internal damage increased with repeated impacts, along with increasing the displacement, and decreasing the force exhibited, until total failure is reached [132]. One of the benefits of carbon fibre composites is that they exhibit good impact resistance. However, energy is absorbed by failure mechanisms which may not be apparent on the surface. For example, out-of-plane impacts may cause delamination which can significantly reduce the shear strength because of the anisotropic nature for which the stresses are transferred in the fibre direction through the component and away from the impact site [130]. Delamination due to impacts were found to reduce the strength of UD carbon/epoxy laminates by approximately 16%, with further reductions to tensile stiffness and compressive strength [133].

The main load carrying fibres ( $0^\circ$  plies) would be exposed if they were positioned at the laminate surface, increasing the likelihood of damage during service. However, short fibre reinforced materials have been found to increase energy absorption by using semi-elastic failure mechanisms, such as pull-out or fibre breakage, rather than plastic deformation [134].

Random discontinuous architecture can distribute the impact stresses uniformly in-plane. This reduces the degradation experienced in the interlaminar shear strength compared to UD laminates [130]. A random discontinuous layer may be used to absorb impact energy to prevent damage to the main load carrying fibres in the continuous fabric laminate, *Fig. 2.30*. Similarly, this has been demonstrated within glass-carbon hybrid composites that show that the position of each material also influences the overall energy absorption [135]. Impacting the glass surface of a glass-carbon hybrid absorbs more energy than impacting the carbon surface. Increased fibre breakage within the low strength glass fibres increases the energy absorbed, whereas reducing the degree

of fibre breakage, by using high strength carbon fibres, dissipates the energy less effectively by delamination [135].

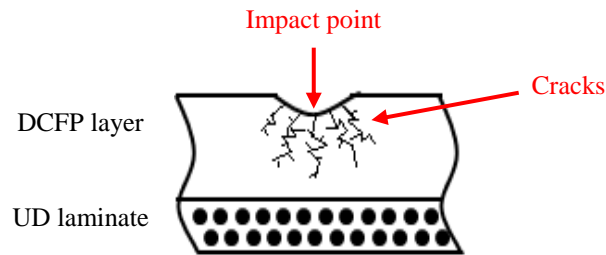


**Figure 2.30.** a schematic diagram showing how a layer of discontinuous fibres could protect the main load carrying laminate, preventing significant loss of mechanical properties.

One method for assessing the property degradation post impact is to perform Compression After Impact (CAI) testing. A specimen experiences an impact during drop-weight testing and then is subjected to an in-plane compression test. Performing CAI on directed carbon fibre preforms (DCFP), reduced the compressive strength by 48%, which is significantly less than the 81% reported for unidirectional prepregs [136]. This is because during impact, laminate structures can experience delamination which leads to buckling during compression [137]. In contrast, DCFP experiences a localised damage zone of multidirectional cracks. However, the multidirectional fibres of the fibres transfer loads around the damage zone (or notch) and therefore the fibre end stress concentrations may still be more dominant [10, 137].

### 2.6.2 Laminate waviness

Defect mechanisms often occur during the layup process and affect the mechanical properties. The most common fabric formation defects are in-plane fibre waviness and out-of-plane wrinkles:

- In-plane fibre waviness, shown by **Fig. 2.31**, is produced by accidental in-plane compression of the fabric in the fibre orientation during lamination, causing the fibres to buckle at the stitching or weave [138]

- Out-of-plane wrinkles, shown by *fig. 2.32*, form during out-of-plane compression of the laminates. This could either be misalignment in the z-plane or a complete fold of the fabric/s [138, 139].

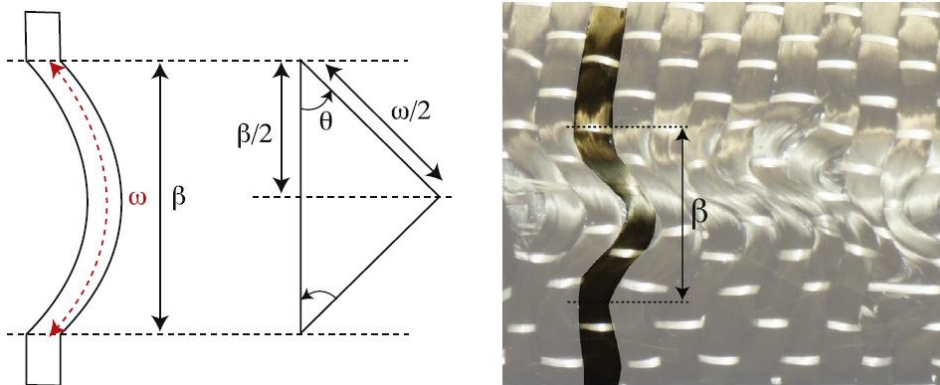


**Figure 2.31.** (a) Schematic of in-plane waviness and (b) photo, highlighting a single tow, of in-plane waviness [138]



**Figure 2.32.** (a) photograph and (b) micrograph (x32) of out-of-plane wrinkles/waviness [139]

Both misalignment mechanisms can cause significant degradation of the compressive properties. This results from microbuckling becoming the most prominent failure mechanism caused by in and out-of-plane fibre waviness [140]. The level of degradation is dependent on the size of the waviness but has been found to be negligible if the wavelength is greater than 200 times the fibre diameter [141].

One of the causes of in and out-of-plane waviness formations is due to shear mechanisms during drape forming. It is understood that woven fabric deformation mechanisms induced during drape forming are: rotation (scissoring), wrinkling, slippage and jamming [142]. These mechanisms are similar to those found for biaxial

non-crimp fabrics (NCF), however where rotation of the woven fabric is limited by the weave, the rotation of the NCF is limited by the stitching as shown by *Fig. 2.32*.

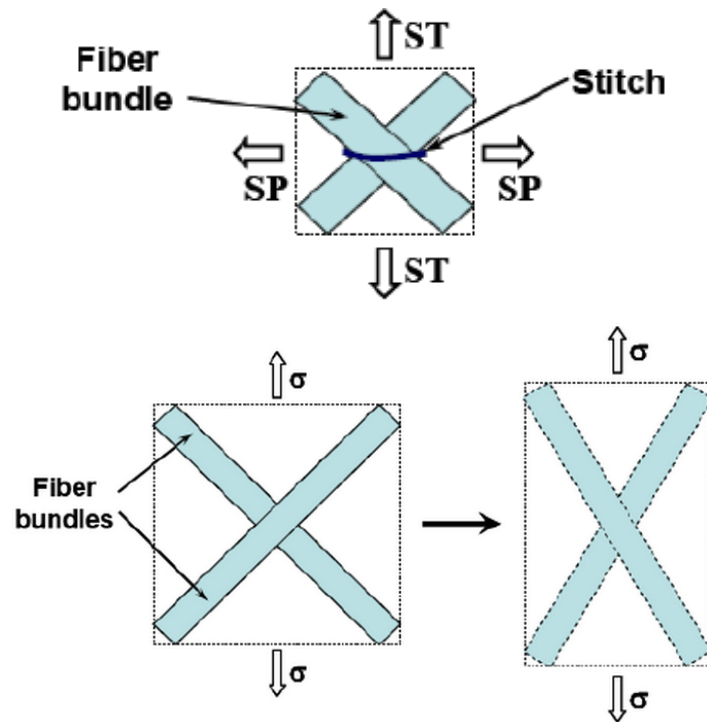


*Figure 2.33. Schematic diagram of stitching acting as a pivot point for rotation during in plane shear of NCFs [143]*

A prominent deformation mechanism of fabric laminates is waviness/wrinkles. Out-of-plane fibre waviness is likely to arise during manufacture of components consisting of hybrid fibre architectures as a result of non-uniform fibre volume fractions in the random layer. This waviness largely reduces the compressive strength as it produces buckling within the material preventing pure stress in the fibre direction [144-146].

*Fig. 2.34* indicates that waviness is experienced in continuous fibres if they are sandwiched between random fibre layers. This is likely to be a result of local volume fraction variations in the DFP material. The dominant failure mechanism during compression, is due to fibre ‘kinking’ and buckling as opposed to fibre crushing when fabric waviness is present, as shear and transverse local stresses are induced [147]. *Fig. 2.35* shows an example of failure by kinking where a failure band is visible.

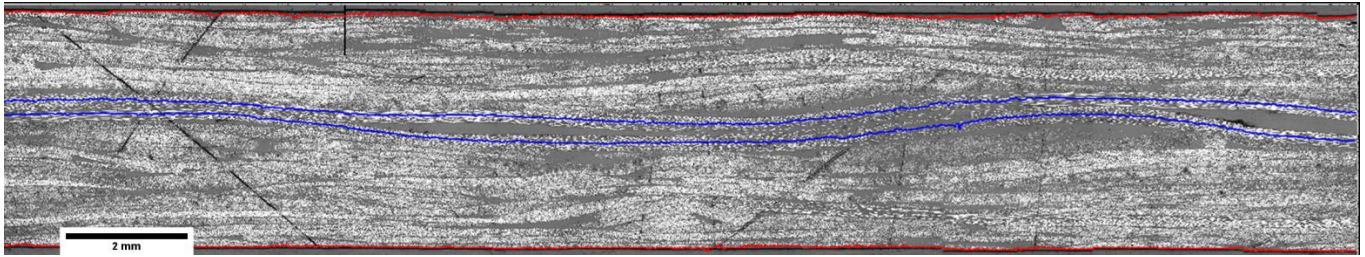


**Figure 2.34.** Micrograph showing the out-of-plane waviness of a hybridised fibre architecture carbon epoxy component  $[Random/0^\circ]_s$ . A Matlab algorithm was used to determine the upper and lower surfaces of the laminate (red lines) and to trace the centrelines of two UD plies (blue lines)

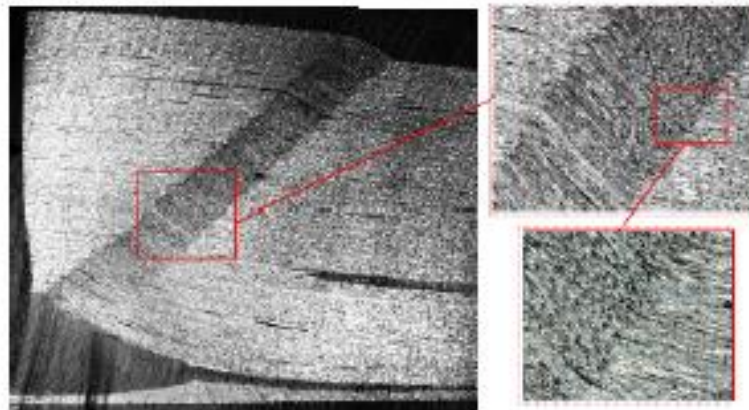


**Figure 2.35.** Micrograph of kink failure [148]

### 2.6.3 Notch sensitivity

Discontinuous fibre architectures are less sensitive to notches than continuous fibre laminates. This is because the stress concentrations at the end of the discontinuous fibre bundles are often larger than the stress concentrations that arise at a damaged/notched region [10]. Evident in **Fig. 2.36**, the fracture of a discontinuous specimen is often not located near to the equator of the notch. When determining the quality of commercial composites, non-destructive testing methods such as ultrasonic C-scan inspections are often used to identify regions of signal attenuations, or “hot spots”, which correspond to defects, such as macro-voids, fibre kinking or resin rich regions. However, notch sensitivity studies have shown that these hot spots do not always correlate to the failure location, such as notches [149]. An advantage of this is that it allows holes to be added

for inserts or fastenings without significant property degradation. A notched composite is said to be notch insensitive if it retains 85% of the unnotched strength [150].

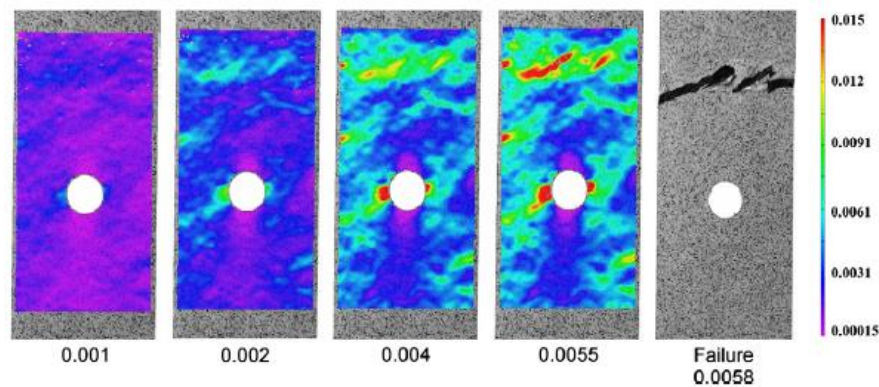


**Figure 2.36.** strain plot of a notched DCFP specimen showing greater stress concentrations away from the notch than next to it [10]

## 2.7 Conclusions

The reviewed literature provides background into the various discontinuous composites and compression moulding continuous laminates. From this review, a move towards carbon fibre moulding compounds is a logical step towards increasing the composite strength and fibre content compared to more conventional glass fibre SMCs. Compression moulding has the advantage of eliminating the problems associated with preforming and infusion, often encountered with LCM techniques with chopped fibres. The literature available for DCFP provides a base level of understanding of discontinuous architectures, with the knowledge of the range of variables that influence mechanical performance transferrable to the directed fibre moulding compound.

The flow capability of the charge is one of the main advantages of SMCs with great consideration in both the material characteristics and compression moulding parameters required for the prevention of defects. This establishes that the best methods to characterise the flow of the charge are by determining the fibre volume fraction distribution, performing microscopy and measuring directional mechanical properties to characterise fibre distribution and orientation. This overcomes the difficulty in quantifying the orientation of composites with bundle architecture, as opposed to alternative methods used to determine filament orientation distributions that are only

suitable for injection moulded filaments. The effects of tool closure rate and temperature are not considered in this thesis but could further optimise charge flow.

Very little literature is available for continuous-discontinuous hybrid fibre architectures, however laminate and ply drop design guidelines assist with the understanding of the interfaces and transition regions. Additionally, the fracture toughness is most suitable for characterising the hybrid interface. However, whilst DCB testing has been performed on monolithic structures, no literature has been found for the hybrid interface. The impact damage tolerance and notch sensitivity are also considered for using multi-directional load carrying capabilities of discontinuous fibres to protect high strength continuous fibres. Literature on CAI suggests this is a suitable method, however consideration is also made to the waviness, which would reduce compressive performance. This is influenced by the through thickness position of the plies.

# 3. Experimentation and Methodology

## 3.1 Manufacturing Processes

Plaques were produced by compression moulding DFC, Non-Crimp Fabric (NCF) or a combination of the two to produce a hybrid carbon fibre architecture. The production of DFC followed the sequence of operations shown in *Fig. 3.1*. NCF was impregnated by the same Liquid Resin Spray (LRS) system that was used during the ‘Chopped Fibre and Liquid Resin Deposition’ operation and, for hybrid fibre architecture, was introduced to DFC prior to closing the compression mould. This section will provide the details for each of these operations, for both discontinuous and continuous fibre architectures.

### 3.1.1 Epoxy Resin

An advanced epoxy resin was used throughout this work, produced by Huntsman. *Chapter 4* describes each of the components, which included Resin XU3508, Aradur 1571, Accelerator 1573 and Hardener XB3403 (100:20:3:12 by wt) unless otherwise stated. This four-part formulated prepreg system utilises two hardeners combined with a bulk epoxy resin component and an accelerator. One hardener, XB3403, is activated at 25°C over a period of 24 hours. This chemically B-stages (partially cures) the resin by ~20% of the degree of cure, obtained by differential scanning calorimetry, DSC (ISO 14322:2012). Over 24 hours this partial cross-linking within the polymer increases the molecular weight and elevates the viscosity to ~50Pas. By elevating the viscosity following compound production or fabric impregnation, this offered sufficient control over the level of staging to provide good wet-out of the fibres to achieve good adhesion between the fibres and matrix whilst the viscosity is low but, once B-staged, allowed

the compound/prepregs to be handled. It also prevented fibre-matrix separation during the compression moulding stage. In this state, the compound/prepreg can be stored at room temperature for >4weeks [151]. It is possible to accelerate the staging by substituting the XB3403 hardener for a hot maturing agent, such as XB3471 detailed in *chapter 4*. These agents have the ability to thermally B-stage the resin in ~5 minutes at 90°C [152]. However, the degree of B-stage is difficult to control thermally depending on part thickness and rate of heat transfer. To achieve full cure the second hardener must be activated by exceeding 90°C [151, 152] during moulding .

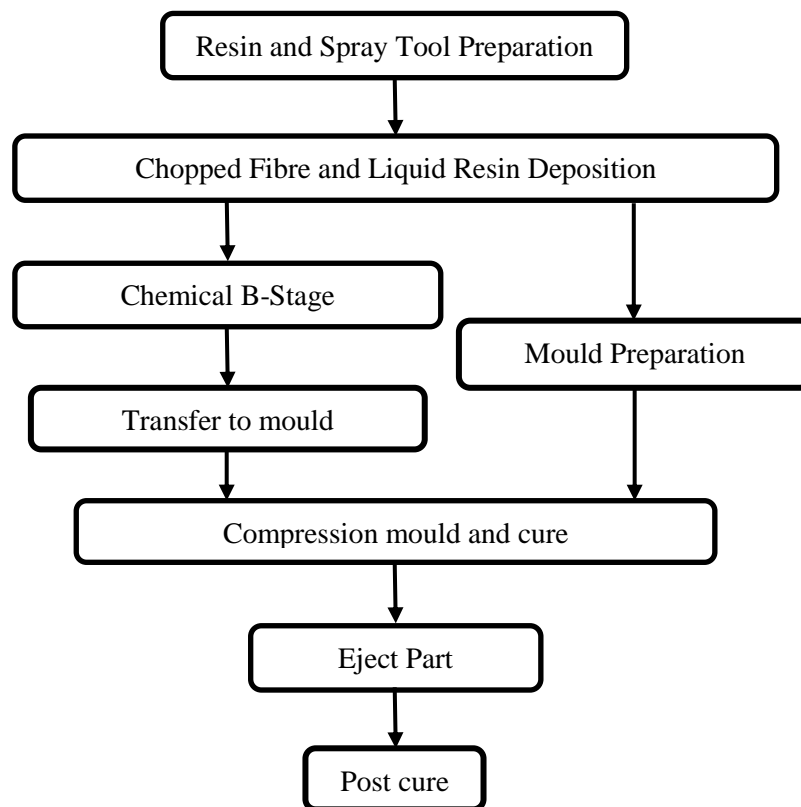


**Figure 3.1.** DFC flow chart

The resin was prepared by first weighing and mixing the high temperature hardener and accelerator components, Aradur 1571 and Accelerator 1573, using a slow propeller mixer. The bulk resin, Resin XU3508, was then weighed and added using the same mixing technique. The combination of these 3 components is referred to as the “*premix*”. It is stable at ambient temperature, enabling it to be stored in a sealed container for up to 2 weeks before processing by the addition of the B-staging Hardener XB3403.

During DFC production, the resin premix was preheated to 65°C to reduce the viscosity below 500mPas. Both the tank and the inlet hose connected to the chopper gun were heated. Once the premix viscosity reduced the Hardener XB3403 was added and stirred manually. From this point, the resin had 25-30 minutes before it gelled, therefore the system was flushed with acetone before this time. For commercial applications, it would be suitable to replace this method with high pressure resin mixing apparatus, mixing premix and hardener continuously at the chopper gun end effect to minimise the time between mixing and deposition.

### 3.1.2 Directed Fibre Compound (DFC)

The DFC process simultaneously deposits chopped carbon fibres and a liquid resin using a 6-axis robot, KUKA KR 30-3 F. This is the next generation of development to the Directed Carbon Fibre Preforming (DCFP) [5, 19, 44, 45] process for producing net-shaped carbon fibre preforms from chopped carbon fibre roving, detailed in *chapter 2*. DFC incorporates a liquid epoxy spray that was a direct progression from the Bentley–Raycell automated carbon composite charge deposition (BRAC3D) using a powder epoxy matrix for the production of structural components capable of low cost high production volumes compared to prepregs or resin transfer moulding [153, 154]. The material is deposited onto a shell tool mounted on a 2-axis (tilt/turn) table, KUKA DKP 400, to produce 2D and 3D net shaped compounds. These are both controlled by a KUKA CR-2 Controller. An end effector mounted to the 6<sup>th</sup> axis of the robot pulled roving of Toray T700-50C 12K virgin carbon fibre (**Fig. 3.2(a)**) by a feed roller shown in **Fig. 3.3**. It is guided to a four-blade chopper roller where the fibres are chopped against a freely rotating pressure roller. The feed and the chopper rollers are each driven by a servo motor, the velocity ratio between the two pairs of rollers was adjusted to control the fibre length of the chopped bundles.

The fibre tensile modulus is 230GPa and the tensile strength is 4900MPa and the roving contained 1% epoxy sizing content. The level of sizing was found to be suitable for achieving consistent fibre chopping. Lower sizing quantities (such as 0.3% on T700-

60E 12K) produced uncontrollable tow fragmentation that blocked the tow path between the feed and chopping roller.

The pre-heated resin was passed through a spiral mixer to ensure uniform distribution of the hardener and then atomised by an internal-mix nozzle. The resin was injected into a chamber where pressurised air was introduced at 1bar, controlled by an analogue output on the robot control software. The resin was atomised by the shear acting between the low flow rate resin inlet and the pressurised air. The size of the atomised resin droplets is largely dependent on the resin viscosity and the air pressure. These droplets impregnate the chopped fibre bundles individually at the tool surface to achieve good wet-out, shown in **Fig. 3.3**. The resin pump was driven by a servo motor, which controlled the resin flow rate. Changing the rate of fibre and resin deposition controls the fibre volume fraction between 30% and 55%.

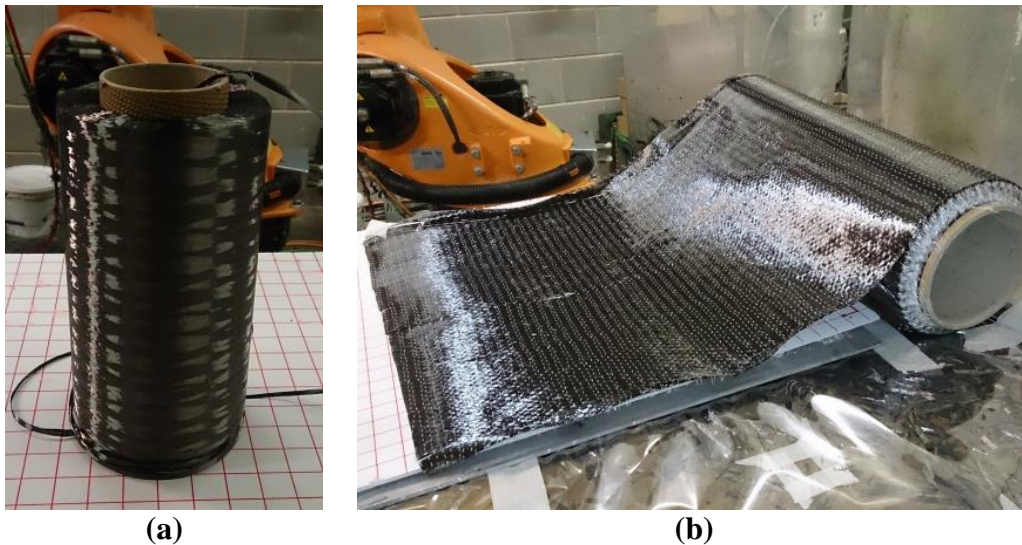


**Figure 3.2.** Photographs of Toray T700-50C 12K carbon fibre roving (a) and 200gsm stitched unidirectional carbon fibre

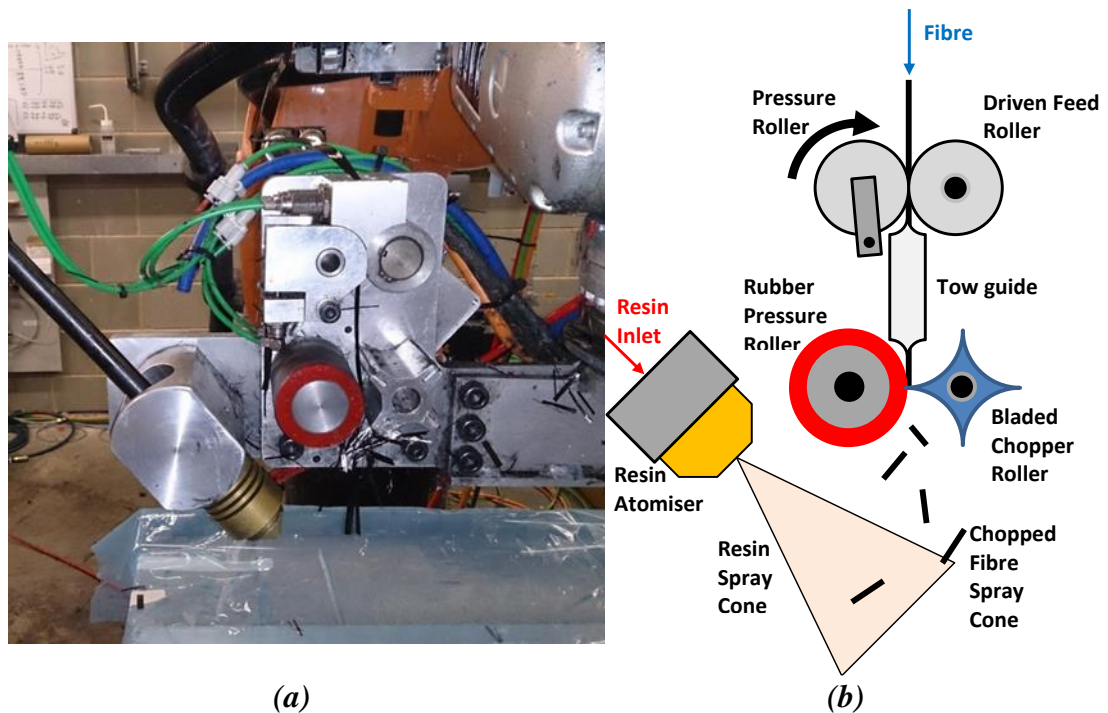


**Figure 3.3.** Photo (a) and schematic (b) of DFC end effector fitted to robot arm

Two-dimensional DFC charges were sprayed onto a layer of unperforated PTFE release film draped over a steel plate mounted to the turn table. The robot arm travelled at 0.2m/s to produce 500mm x 500mm compounds. Each compound was produced by a discrete number of layers of orthogonal, north-south/east-west, tool paths that were determined in the literature review to minimise any orientation bias from the chopping [19]. Each linear pass of the tool had a spray offset of 50mm, which was optimised to ensure uniform fibre distribution.

### 3.1.3 Liquid Resin Spray (LRS) fabric impregnation

Non-crimp fabric (NCF) was impregnated using the same liquid resin and the same hardware as the DFC. This ensured that the cure reaction and crosslinking was consistent between dissimilar architectures.

Two different types of NCF were investigated. The feasibility of producing hybrid fibre architectures was studied using a low areal mass, 200gsm, unidirectional carbon fibre, *Fig. 3.2 (b)*. The 12K tows were stitched with E-glass in the weft direction. However,

this stitch pattern created difficulties during compression moulding, as the tows sheared and moved when trying to produce ply drops with precision, **Fig. 3.4**. Therefore, a second NCF material was used – a unidirectional fibre with multiaxial stitching E-glass stitching, at  $90^\circ$  and  $\pm 45^\circ$ , shown in **Fig. 3.5**. This fabric uses 24K tows to yield an areal density of 375gsm.

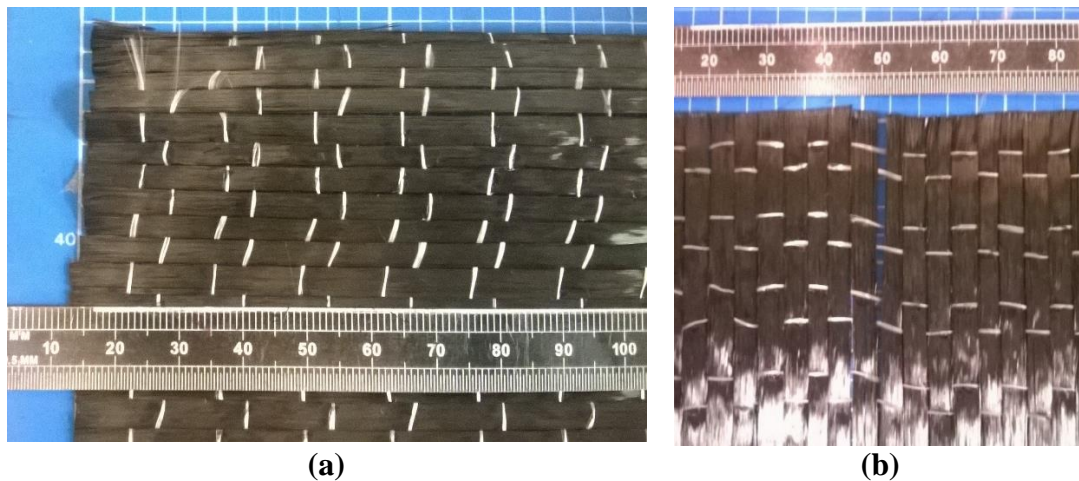


**Figure 3.4.** Unidirectional carbon with E-glass stitching in the weft direction showing tow slipping in the  $0^\circ$  direction (a) and tow spreading (b) caused by shearing

The NCF was cut to size prior to spraying. The first ply was held in position using masking tape on top of a layer of release film on the flat tool surface. This prevented movement or folding of the fabric by the air flow created by the resin spray system, **Fig. 3.6**. Masking tape was not required for subsequent layers, as the liquid resin provided sufficient adhesion. The LRS spray nozzle was adjusted to spray vertically downwards, producing a circular spray pattern of resin. Each ply was sprayed individually to minimise the resin flow distance during compression moulding to ensure good wet out of the fabric. Plies were stacked to create unconsolidated laminates immediately after spraying and were B-Staged prior to compression moulding.



**Figure 3.5.** *Unidirectional carbon fibre with multi-axial E-glass stitching*



**Figure 3.6.** *First layer of NCF on flat tool surface for impregnation by LRS*

### 3.1.4 Compression moulding

The DFC charges and NCF hybrids were ready for compression moulding once they had been impregnated and B-Staged. The edges of the DFC charges were trimmed to the required size prior to moulding, depending on the required mould coverage, **Fig. 3.7**. The cavity of the compression mould tool measures 405mm x 405mm and can produce plaques up to 15mm thick. The plaque thickness was either controlled by the quantity of material placed inside the mould cavity or by using stops located on each side of the mould. The disadvantage of using the stops is that a uniform pressure may not be achieved within the cavity if the volume of material is lower than required or the fibre distribution is heterogeneous.



(a)



(b)



(c)



(d)

**Figure 3.7.** DFC charges after trimming at 50% mould coverage (a, b) and net shape/100% mould coverage (c, d)

The tool was preheated to 130°C and allowed to soak for at least an hour to achieve uniform heat distribution across all surfaces. Before any mouldings, the tool surfaces were cleaned and 10 layers of Freekote 700NC mould release were applied using a soft cloth. Once the mould and charges were prepared, the charge was then placed into the mould, **Fig. 3.7**, and the mould was closed at a rate of 3mm per second. Some investigations will require flow to be restricted to one dimension only. These charges were placed on the left-hand side of the mould, **Fig. 3.7(b)**. Also, the orientation of the charge placement with respect to the orientation of the spray path was constant to compensate for any bias caused by the compounding or compression mould tool. The in-mould pressure was controlled by adjusting the ram pressure. This was set to generate an in-mould pressure of 85bar unless otherwise stated. Additionally, a pressure

transducer located in the centre of the upper mould tool was used to monitor and record the internal pressure.

The cure cycle was measured to be 30 minutes at 130°C, detailed in *chapter 4*. All plaques were compression moulded using this cure cycle. It was possible to mould and demould the composite at 150°C in <10 minutes, but this was impractical with the current setup due to the slow closure speed of the press advancing the cure prior to full mould closure. The compression mould tool also supports a pressure transducer located at the centre of the upper tool. It was known that at elevated temperature there was a drift in the pressure readout. Therefore, a quick trial was performed holding a flexible solid material, neoprene, at a constant mould pressure to produce a steady pressure readout at room temperature. This was then replicated at 130°C and the results, shown in **Fig. 3.8**. Following an initial overshoot, the neoprene relaxes and held a constant pressure at ambient temperature. However, at 130°C the curve demonstrates a fluctuation of  $\pm 5$ bar after the first 15 minutes. The pressures in these scenarios were very difficult to control because the trial specimens were of varied sizes and the ramp pressures was reduced as low was.

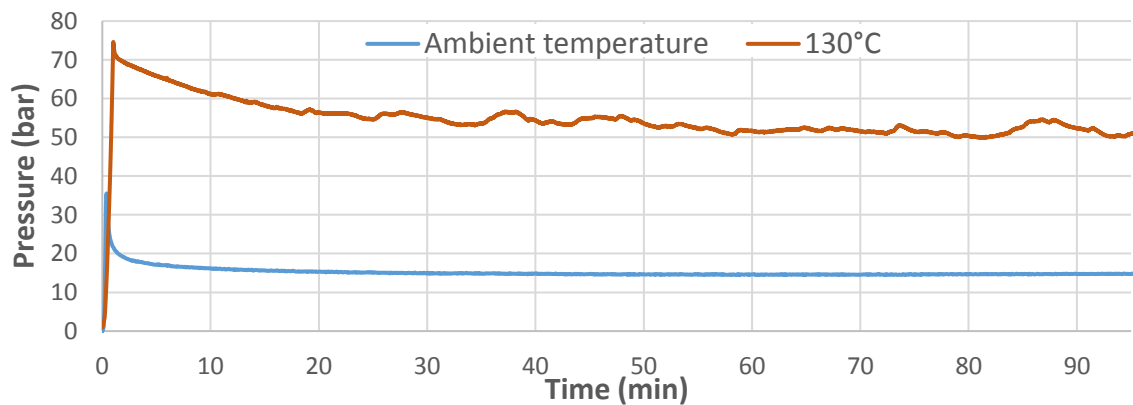


**Figure 3.8.** Pressure transducer reading during constant pressure trials at ambient temperature and 130°C

**Fig. 3.9** shows a typical pressure curve at the centre of the square mould during the 30 minute cure cycle, 130°C. The target pressure in this scenario was 85bar. Once the mould is closed, the pressure increases and stabilises. The resin then experiences a slight expansion and shrinkage as the resin then gels and cures. This shrinkage produces the decent of the moulding pressure after 5 minutes. After 30 minutes, the press was

opened and the plaques were demoulded with the mould at 130°C. This temperature is greater than the 120-125°C glass transition temperature specified in the resin datasheet [151], however this did not cause any significant distortion when demoulding simple geometry at 130-160°C.

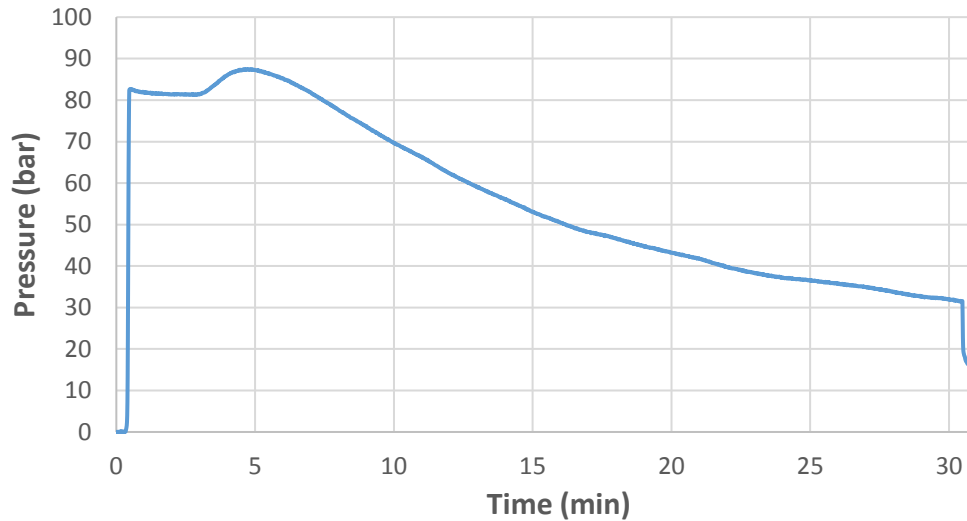


**Figure 3.9.** Pressure transducer reading during DFC cure cycle for 30 minutes at 130°C with a target in-mould pressure of 85bar

## 3.2 Resin analysis

### 3.2.1 Isothermal Differential Scanning Calorimetry (DSC)

DSC testing was conducted according to ISO 14322:2012. Testing can be divided into two sub categories, *isothermal partial cure* and *dynamic testing*. The dynamic testing was used to measure the total enthalpy of an uncured specimen,  $H_T$ , and when proceeding the isothermal stage, it was also used to determine the enthalpy remaining within a partially cured specimen,  $H_R$ . These values can then be input into *equation 3.1* to calculate the ratio of enthalpy lost over the total enthalpy. This ratio is the degree of cure,  $\alpha$ , where  $\alpha = 0$  has zero-cure and  $\alpha = 1$  is full cure.

$$\alpha = \frac{H_T - H_R}{H_T} \quad (3.1)$$

The sample size was 10-20mg, which was weighed in an aluminium pan whilst the viscosity was suitably low using a pipette. Performing this whilst the viscosity was low

was much more manageable than after the resin has B-staged. This improved the consistency sample size by preventing over and under-filling the pans. The resin sample was then B-staged for 24 hours at room temperature before testing.

#### *Isothermal partial cure*

This stage was applied to partially cure the sample. Starting at 20°C, the temperature was increased a rate of 50°C/min, the maximum capability of the TA Instrument DSC Q10. Once the specified temperature was achieved (80 – 160°C), the temperature was held in equilibrium for a specified cure time (2.5 – 120 minutes), such as the temperature profile in **Fig. 3.10**. The sample was then rapidly cooled back to 20°C, ~40°C/min, using the nitrogen purge at a constant flow rate of 50ml/min. The sample was then subjected to the dynamic testing cycle.

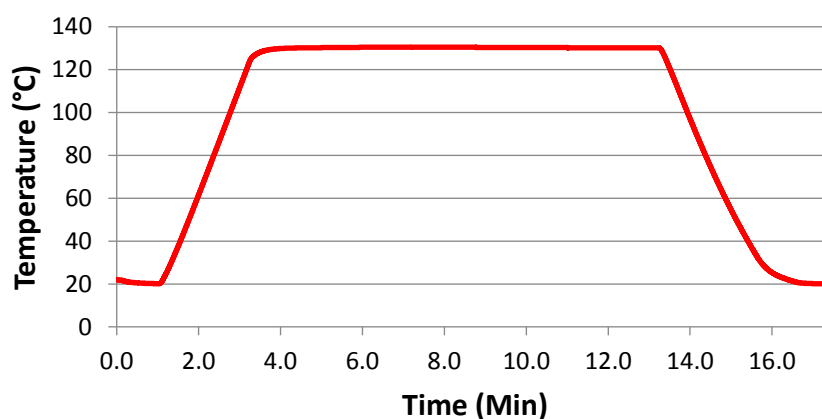


**Figure 3.10.** A temperature vs time profile for the isothermal partial cure (130°C for 10 min)

#### *Dynamic testing*

The uncured/partially cured samples were subjected to a temperature ramp of 10°C/min from 20°C to 300°C, to totally cure the specimens. The heat flow was measured during this temperature elevation. A Matlab script used to apply the trapezium rule to obtain the area of peak heat flow with respect to time for the region, shown in **Fig. 3.11**. If the sample was initially uncured, this area derived the total enthalpy of the reaction,  $H_T$ ,

and if partially cured the enthalpy remaining,  $H_R$ , was derived. These enthalpy values are inserted into *equation 3.1* to calculate the degree of cure.

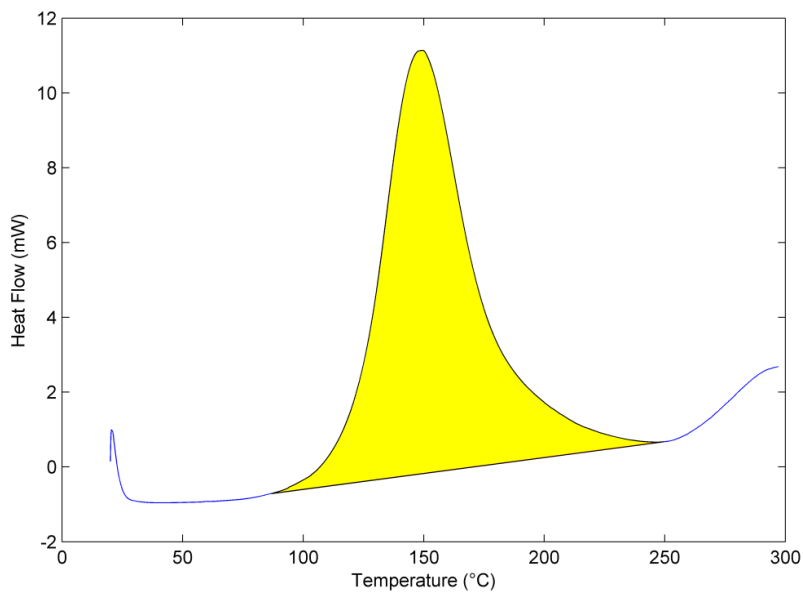


**Figure 3.11.** Heat flow vs. Temperature

The degree of cure could also be measured by obtaining the heat flow whilst the temperature was held isothermally. This was required to determine the orders of reaction necessary to model the cure cycle, discussed further in *Chapter 4*. However, during the rapid heating rates the measured heat flow is not solely the heat absorbed/emitted by the specimen. This results from heat transfer into the specimen interfering with the heat flow measurements. This prevented the start position of the peak heat flow from being determined accurately because the cure was often initiated before the heat flow stabilised, therefore errors were introduced when calculating the enthalpy.

### 3.2.2 Glass transition temperature

DSC was also used to investigate the glass transition temperature of a resin according to BS EN ISO 11357-2:2014. A sample size of 10-20mg of each resin was weighed into aluminium pans before B-staging for at least 24 hours. This B-stage was suitable to both hardeners tested, chemically and thermally activated, detailed in *Chapter 4* [151, 152]. Therefore, B-stage was applied under the same conditions, to ensure that it was completed prior to testing.

Each resin system was cured isothermally using the DSC. This was simulated by elevating the temperature of the resin from 20°C to 130°C at a rate of 50°C/min. A nitrogen purge was also applied with a flow rate of 50ml/min. The sample was held at the cure temperature for 4 hours before cooling rapidly to 20°C, ~40°C/min. A dynamic test was then performed, measuring the heat flow whilst elevating the temperature at a rate of 10°C/min.

The results were then processed using TA Universal Analysis, which uses the half-step-height method to measure the temperature at which the heat flow rate suddenly increases and decreases, creating a step in the heat flow vs temperature profile such as *Fig. 3.12*. The DSC curve is intersected by a line that is equidistant between two extrapolated baselines, indicated by a sudden change in gradient on the measured curve. This intersection point is used to quantify the glass transition temperature,  $T_g$ , as shown by the example in *Fig. 3.12*.

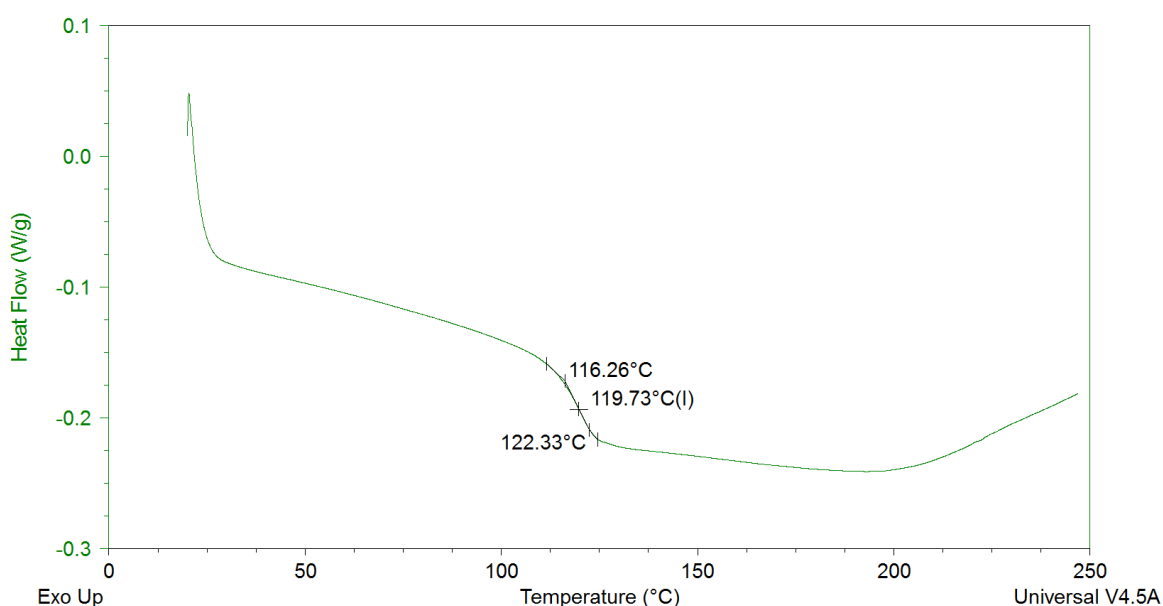


**Figure 3.12.** An example measurement of the glass transition temperature of the Huntsman resin system: Resin XU3508, Aradur 1571, Accelerator 1573 and Hardener 3403

### 3.2.3 Rheology

A Bohlin C-VOR 200 rheometer was used to measure the viscosity of the resin systems, according to ISO 3219:1995. The viscosity was determined by measuring the torque applied to rotate 40mm parallel flat aluminium plates, separated by a 500-800 $\mu$ m film of resin. The resin was tested both before B-staging to determine the spray viscosity, and after B-staging to determine the in-mould viscosity, which were both dependent on temperature. All measurements used a frequency of 1Hz and a 1% rotational strain to obtain the dynamic viscosity. Temperature ramp rates ranged between 5°C/min and 20°C/min. Exceeding this ramp rate resulted in temperatures overshooting by >10°C. Additionally, the apparatus measured the temperature of the hot air stream at the point it is introduced at the sample rather than the temperature of the sample itself. Therefore, large air temperature ramp rates were not capable of transferring heat into the sample at an equal rate. This produces an erroneous offset between the viscosity measurements and output temperature.

## 3.3 Microstructural analysis

### 3.3.1 Density measurements

A density balance was used to measure the fibre volume fraction,  $V_f$ , of 25mm x 25mm specimens. This method of obtaining the fibre volume fractions is suitable because the moulding compounds have low void content, <1%, and consist of only two constituents with known density: Toray T700-50C carbon fibre ( $\rho_{fibre}=1.8\text{gcm}^{-3}$ ) and the formulated epoxy system ( $\rho_m=1.2\text{gcm}^{-3}$ ). The areal density of the discontinuous fibre architecture is heterogeneous, therefore it is important to take a suitably large population of samples from each plaque. At least 10 repeats were performed to calculate the average fibre volume fraction. The density was measured from small 25mm x 25mm samples. This was a faster method in comparison to burn-off or acid digestion for generating many results and repetitions in a short time period. Once the density of the composite,  $\rho_c$ , was measured, *equation 3.2*, was used to calculate the fibre volume fraction.

$$V_f = \frac{\rho_c - \rho_m}{\rho_f - \rho_m} \quad (3.2)$$

The density of each specimen was obtained using the immersion method, ISO 1183-1:2012. The dry mass,  $m_{dry}$ , of each sample was measured to the nearest 0.1mg. The same balance was used to record the mass of a thin wire suspended by a frame. The temperature of a beaker of water was measured and then the water was stirred and allowed to settle to remove any trapped air bubbles. Water was used as the immersion liquid and its density,  $\rho_{water}$ , was determined from the literature depending on the temperature [155]. The wet mass,  $m_{wet}$ , was recorded by submerging the sample under the surface of the water, by suspending each specimen from the wire to completely immerse them in the water whilst preventing them from sinking. The density of the sample was calculated using *equation 3.3*.

$$\rho_c = \frac{m_{dry} \times \rho_{water}}{m_{dry} - m_{wet}} \quad (3.3)$$

### 3.3.2 Microscopy

To investigate the microstructure of the composites, optical microscopy was performed to look at the through thickness architecture. Samples were cut from the plaque at the required location and orientation of interest, 20-25mm length and ~10mm width. Specimens were encased by a clear polyester casting resin in 40mm cylindrical pots and cured overnight using Accelerator NL-49P (0.5% wt) and M50 Catalyst (1% wt). The resultant discs that were ground parallel to an approximate thickness of 15mm. The surface of interest was then polished through a series of polishing papers (400, 800, 1200, 2500 and 4000 grit). Polishing was performed for 10 minutes at each grit size, using a Struers DAP-7 orbital polisher. A final polish was performed for a further 10 minutes using 1 $\mu$ m alumina powder. Upon completion, the remaining alumina was washed away with water and the sample was dried with a soft cloth.

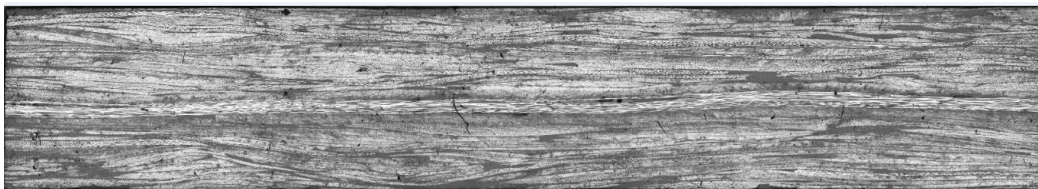
A series of optimal microscopic overlapping 1392 x 1040 pixel images are then taken using a Zeiss® Axiolab optical microscope fitted with a monochrome Q-Imaging camera at 5x magnification with a pixel size 0.9 $\mu$ m/pixel. This was performed using ImagePro software that then tiles the image together, whereby the overlapping regions are matched and aligned by the software to generate the full field image of the specimen.

### 3.3.3 Out-of-plane laminar waviness measurement

Following the production of the hybrid carbon fibre architecture, the variability in local fibre volume fraction within random fibre architecture produces out-of-plane waviness within the continuous plies. A Matlab algorithm was produced quantify this waviness behaviour from the microscopy images generated. The centreline of fabric laminates was traced to produce x and y coordinates that corresponds to the pixel location. From this, the waviness characteristics by wavelength and amplitude can be quantified.

The steps taken by the algorithm are:

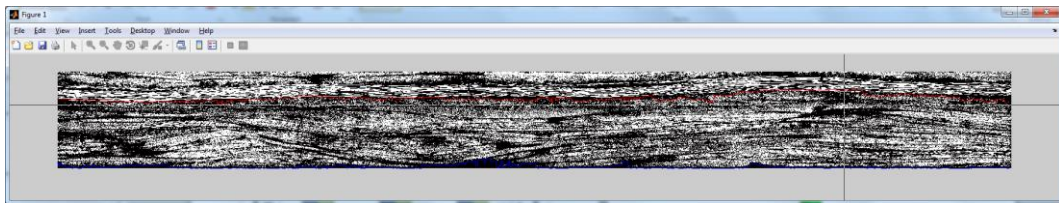
1. Load image



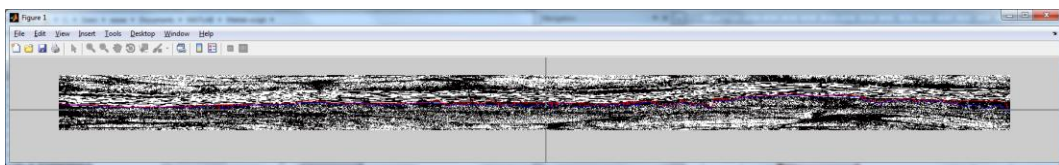
2. Crop the width of the image to a multiple of the 'step size'. This is the number of columns of pixels observed collectively at any one time. Cropping the image to a width equal to a multiple of the step size ensures that all steps are equal size.
3. Apply 'erosion' and 'dilation' to the image to remove noisy pixels
4. Convert the image to a binary image by applying a threshold to the greyscale values of the image and assigning each pixel either a 0 or 1 to produce a black and white image. The threshold value was manually determined for each image depending image brightness and quality. This is used to distinguish between the two constituent materials in the micrograph. Pixels representing voids and resin regions have a greyscale value greater than the threshold value and are assigned as 0 (black) in the binary image. The pixels containing fibre have a greyscale value below the threshold value and are assigned as 1 (white) in the binary image.



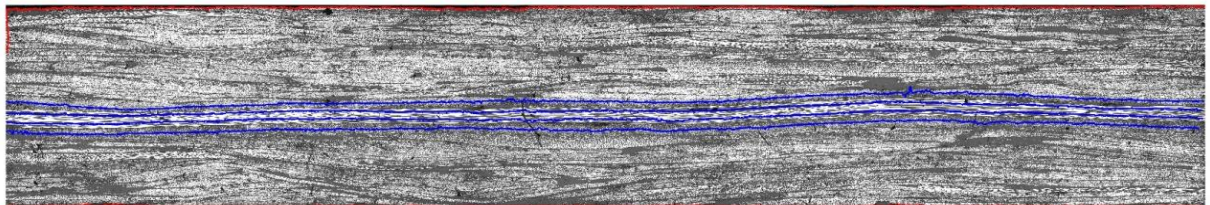
5. Starting from the bottom left corner of the image, an algorithm determines for a step size of 30 horizontal pixels whether there are any fibres present. These are indicated by a white pixel. This indexes in the rows above until the first fibre is found. Once determined, the process is then repeated for the next 30 pixels, until the full border of the bottom laminate is determined.
6. The user is then requested to select the resin region above the bottom ply, but below the next laminate up.
7. Like step 5, the algorithm then steps from left to right by step sizes of 30 horizontal pixels and indexes up or down to determine the upper ply surface of the bottom ply. The algorithm accounts for wrinkles by incorporating vertical steps indexing left or right if necessary and also to click to magnify and correct sections that the algorithm cannot determine.



8. Once the right-hand side of the image is reached, the step repeats to find the lower surface of the next laminate.



9. Steps 6-8 repeat until all ply upper and lower surfaces are traced.
10. A separate algorithm then finds the average point between the upper and lower traces to determine the centreline laminate coordinates.



11. From this, a linear line of best fit can be applied to determine the neutral axis of the waves

### 3.3.4 Ultrasonic C-scan

Non-destructive testing (NDT) was used to determine internal through-thickness damage of the composite plaques following out-of-plane impact loading. This was performed using an Olympus Omniscan MX2 and the data was processed using the OmniPC software. This uses 4 apertures, each with 16 elements, to emit ultrasound through the thickness of the composite and echoes off the back-wall or when there is a sudden change in density, the response time and amplitude of the return signal determine variations internally within the specimens. **Fig. 3.13 (a)** shows a peak at amplitude of the echo signal at a location of the specimen that receives from the back-wall of the composite. **Fig. 3.13 (b)** shows how the peak shifts to the left after the echo signal at a location where a sudden change of density was exhibited near the mid plane. This was caused by a defect such as a void or delamination. The scanner interprets this information and produces a 2D distribution of the amplitude of the return signals into a planar view of the composite, C-scan, **Fig. 3.14**.

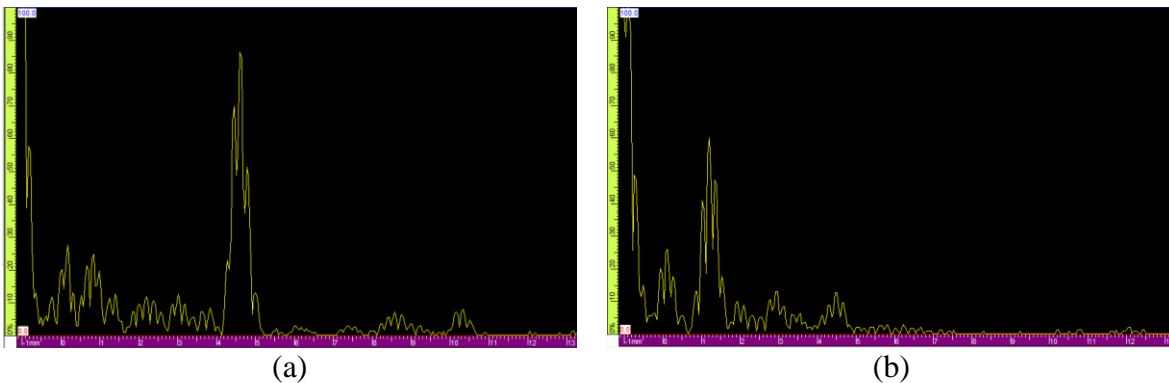


**Figure 3.13.** Amplitudes of ultrasound against the depth of the echo signal showing a spike at the back-wall (a) and delamination at a central laminate (b)

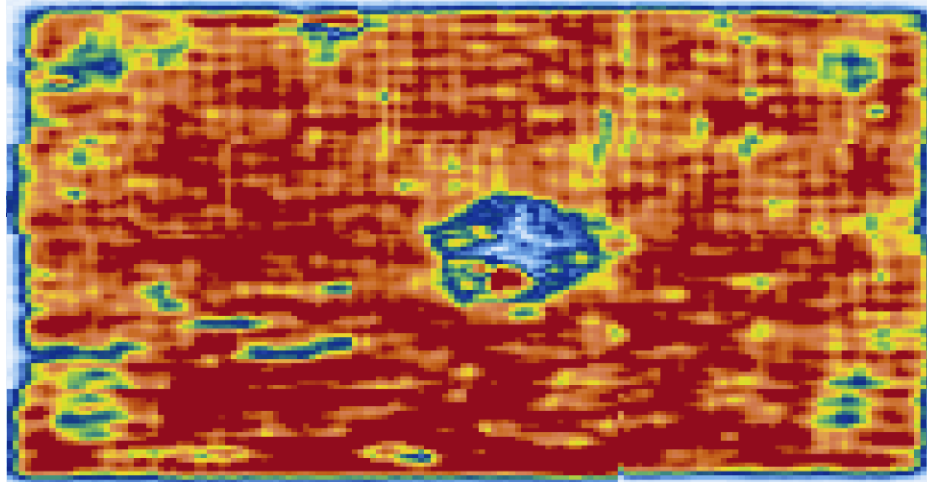


*Figure 3.14. C-scan of a drop weight impacted 150mm × 100mm hybrid carbon fibre architecture panel*

### 3.4 Mechanical testing

#### 3.4.1 Tensile properties

The tensile properties are investigated in *Chapter 4, 5 and 6*. This investigates the mechanical responses: Young's modulus and tensile strength when subjected to pure axial loading. This was used in *Chapter 4* to compare the effects of material choices in terms of changing matrix material and fibre bundle tow size. *Chapters 4 and 5* determine the moduli,  $E_1$  and  $E_2$ , to characterise the directionality of the fibres. *Chapter 5* also measures the tensile properties to compare the material response of DFC to benchmark moulding compounds. Finally, the tensile properties are also investigated in *Chapter 6* which investigates the material response to hybridising the fibre architecture in comparison to the monolithic DFC and UD-NCF composites.

Tensile testing was conducted according to ISO 527-4:1997 and ISO 527-5:2009, using an Instron 5969 universal testing machine shown in *Fig. 3.15*. Specimens were cut to 200mm long and 25mm wide, *Fig. 3.16*. The thickness,  $h$ , and width,  $b$ , of each specimen were measured using Vernier callipers to the nearest 0.01mm at four locations. These values were then averaged to calculate the average cross-sectional area ( $A = bh$ ). The specimen gauge length was 100mm and 50mm long tabs were applied at each end to prevent premature failure in the grips. For discontinuous fibre architectures, coarse emery tape tabs were sufficient to prevent damage in the grips.

Aluminium tabs were bonded to the NCF and hybrid specimens using Araldite and a slow hardener.

Testing was conducted at an extension rate of 2mm/min. A 50kN or 250kN load cell was used to measure the force applied to the crosshead, F. The tensile strength,  $\sigma$ , was calculated using *equation 3.4*. An extensometer with a 50mm long gauge length was used to measure the extension from 0-0.3% strain. The stress at  $\varepsilon_1= 0.05\%$  strain,  $\sigma_1$ , and stress at  $\varepsilon_2= 0.25\%$ ,  $\sigma_2$ , was used to calculate the Young's modulus, E, using *equation 3.5*.

$$\sigma = \frac{F}{A} \quad (3.4)$$

$$E = \frac{\sigma_2 - \sigma_1}{\varepsilon_2 - \varepsilon_1} \quad (3.5)$$

*Fig. 3.17* shows a typical specimen cutting plan to obtain longitudinal and transverse tensile properties and to account for fibre bundle orientation bias in the random architecture.



*Figure 3.15. Photo of tensile test of DFC with clip-on extensometer*

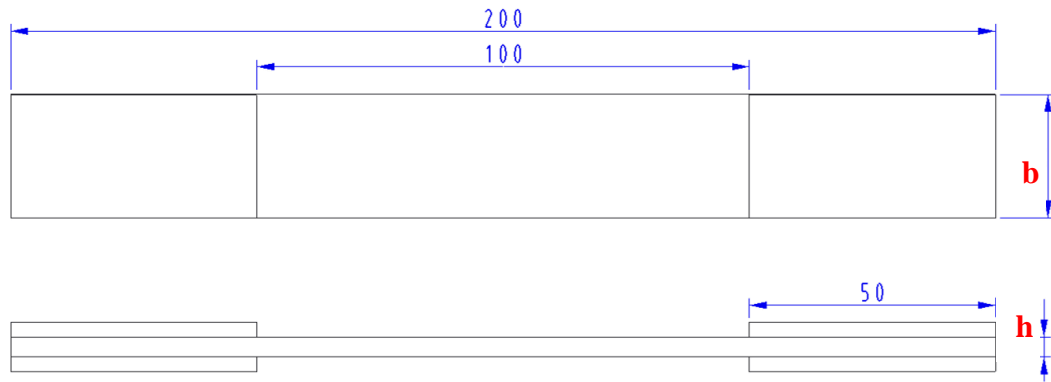


**Figure 3.16.** Schematic diagram of tensile test specimen

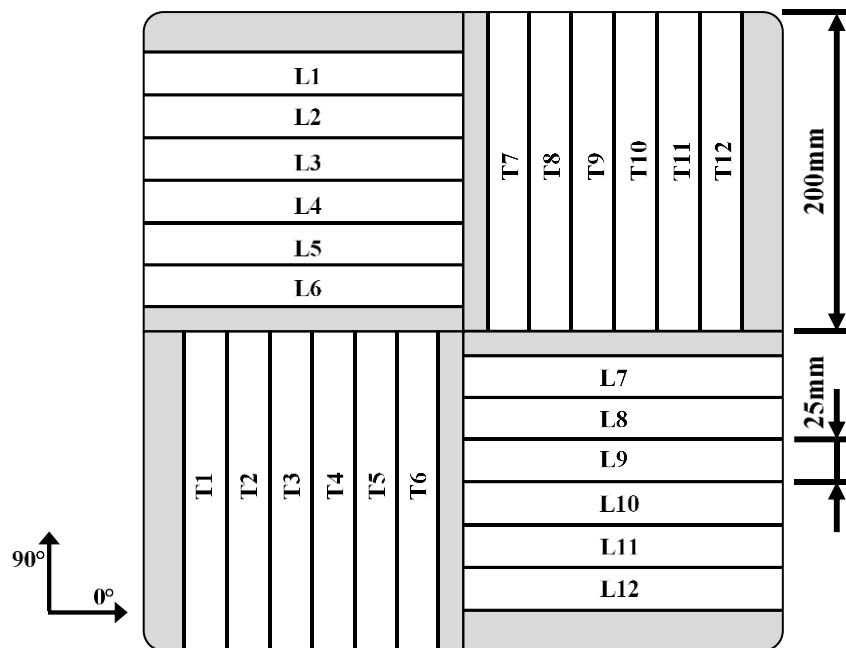


**Figure 3.17.** Cut plan for tensile and flexural test specimens from 405mm x 405mm plaques

### 3.4.2 Electronic Speckle Pattern Interferometry (ESPI)

Electronic Speckle Pattern Interferometry (ESPI) was used to measure local strain distribution during tensile testing. This was used to observe the in-plane (x-y plane) and out-of-plane (y-z plane) strains for specimens with hybrid fibre architectures. Out-of-plane strains were determined by rotating the specimen edge-on and measuring surface strains of the y-z plane. The specimen was painted matt white to provide a monochromatic optically rough surface. A laser light was then reflected off the surface which produced a subjective speckle pattern that was detected by the video detector. The speckle pattern changes as a load is applied, which can be used to quantify the

strain distribution. The laser and video detector assembly was mounted to an Instron 5569 universal testing machine, shown in **Fig 3.18 (a)**, which moved at half of the rate of the applied tensile extension, 1mm/min. This ensured that the centre point of the detector image followed a fixed point of the specimen to negate the relative movement from affecting strain readings. The tensile test paused momentarily every 200N load, up to 5kN, whilst the detector captured an image of the speckle pattern.

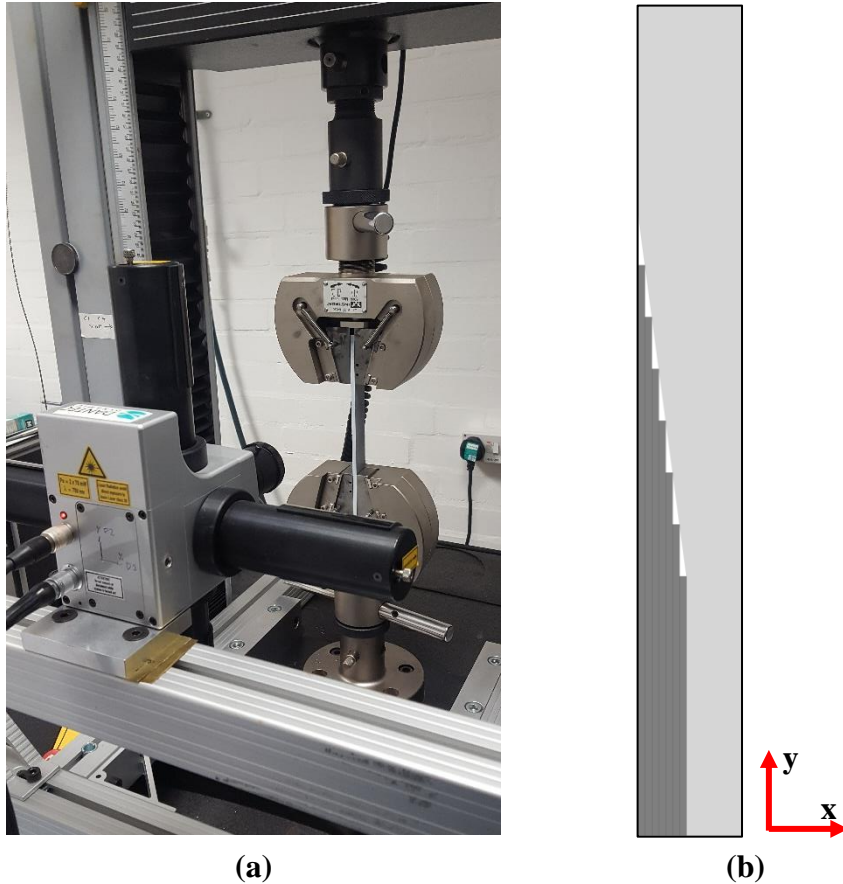


**Figure 3.18.** Photograph of the ESPI setup looking at the through thickness of a tensile specimen (a) and the coordinate system for a hybrid fibre architecture joint (b)

The difference from one image to the next produced a series of black contours called ‘fringes’. These fringes are then used to calculate the transverse strain ( $\epsilon_x$ ), axial strain ( $\epsilon_y$ ) and shear strain ( $\gamma_{xy}$ ) using *equations 3.6-3.8*. Where  $\partial u$  and  $\partial v$  are the extensions in the x and y directions respectively, and  $\partial x$  and  $\partial y$  are the original length in their respective directions. **Fig. 3.18 (b)** shows the orientation of a specimen investigating the joint between a continuous fibre fabric and DFC, (taken from *chapter 6*). **Fig. 3.18 (b)** indicates the coordinate system used. The camera lens had a resolution

0.24mm/pixel and a field of view of 60mm of the specimen and the full width or thickness.

$$\varepsilon_x = \frac{\partial u}{\partial x} \quad (3.6)$$

$$\varepsilon_y = \frac{\partial v}{\partial y} \quad (3.7)$$

$$\gamma_{xy} = \frac{\partial u}{\partial y} + \frac{\partial v}{\partial x} \quad (3.8)$$

### 3.4.3 Flexural properties

The flexural properties have been investigated in *Chapter 6*. This investigates the structural responses to asymmetric layup strategies as well as varying the ply drop sequence with the transition zone between continuous and discontinuous fibre architectures. The specimen dimensions in each investigation remains constant to prevent undesired structural differences from effecting the results when varying UD content within hybrid architectures and when comparing the effects of step size and ply drop strategy within hybrid joints.

The flexural properties were characterised by a three-point bend test, using ISO 14125:1998+A1:2011 standards. An Instron 5969 universal testing machine was fitted with Ø5mm load and support rollers and a 50kN load cell to measure the applied central load,  $F$ , shown in **Fig. 3.19**. The load roller travelled at a rate of 2mm/min. Specimens were cut 25mm wide and 200mm long using the cut pattern shown in **Fig. 3.17**. A low bending strain was determined using a Linear Variable Differential Transformer (LVDT) gauge to measure the beam mid-point deflection,  $s$ , **Fig. 3.19 (a)**. The flexural strain,  $\varepsilon_f$ , was calculated in real-time using *equation 3.9*, where  $L$  is the span between the two support rollers. The bending was stopped when the LVDT recorded 0.3% strain to prevent damage to the specimen. The flexural modulus,  $E_f$ , was then calculated using the difference in load,  $\Delta F$ , and difference in beam mid-point deflection,  $\Delta s$ , from  $\varepsilon_f' = 0.05\%$  and  $\varepsilon_f'' = 0.25\%$ , *equation 3.10*.

$$\varepsilon_f = \frac{6sh}{L^2} \quad (3.9)$$

$$E_f = \frac{L^3}{4bh^3} \left( \frac{\Delta F}{\Delta s} \right) \quad (3.10)$$

Once the undamaged specimens were unloaded, the LVDT gauge was removed, **Fig. 3.19 (b)**, and specimens were tested to failure using the measured load to calculate the flexural stress using *equation 3.11*

$$\sigma_f = \frac{3FL}{2bh^2} \quad (3.11)$$

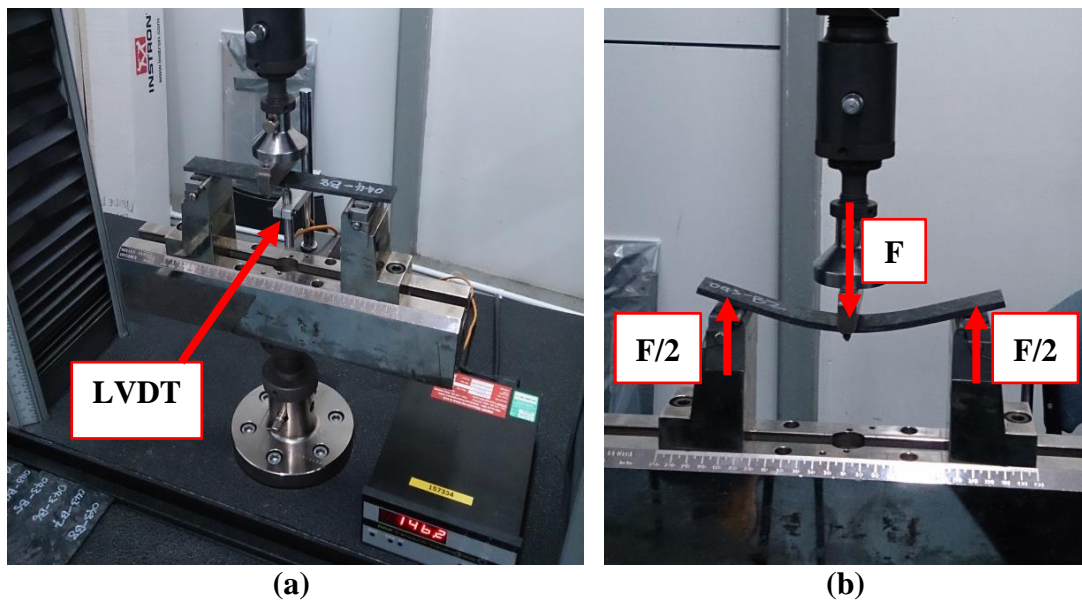


**Figure 3.19.** 3-point bending set up with LVDT for flexural extension measurements (a) and without LVDT to determine maximum flexural stress (b)

The test standards recommend a dissimilar span between the support rollers depending on the fibre architecture,  $40h$  for unidirectional fibres and  $16h$  for discontinuous. There is also no suggested span for hybrid fibre architecture. Thus, it was decided that the span length would be held constant for all fibre architectures. **Fig. 3.20** shows the effect of span length against the flexural modulus for 3 different architectures, where  $h = 3\text{mm}$ . Agreeing with the standards, it shows that the flexural properties of the discontinuous architecture, DFC, plateau at a much lower span length,  $\sim 60\text{mm}$  ( $20h$ ), than it does for unidirectional carbon fibre,  $>100\text{mm}$  ( $33h$ ). The hybrid architecture, 40% UD and 60% DFC, showed a similar plateau to DFC. Therefore, from this it was decided that  $120\text{mm}$  span length will be used for all specimens. The flexural properties

at this span length are stable for all fibre architectures, and it is equivalent to the 40h recommended for unidirectional carbon fibre architectures.

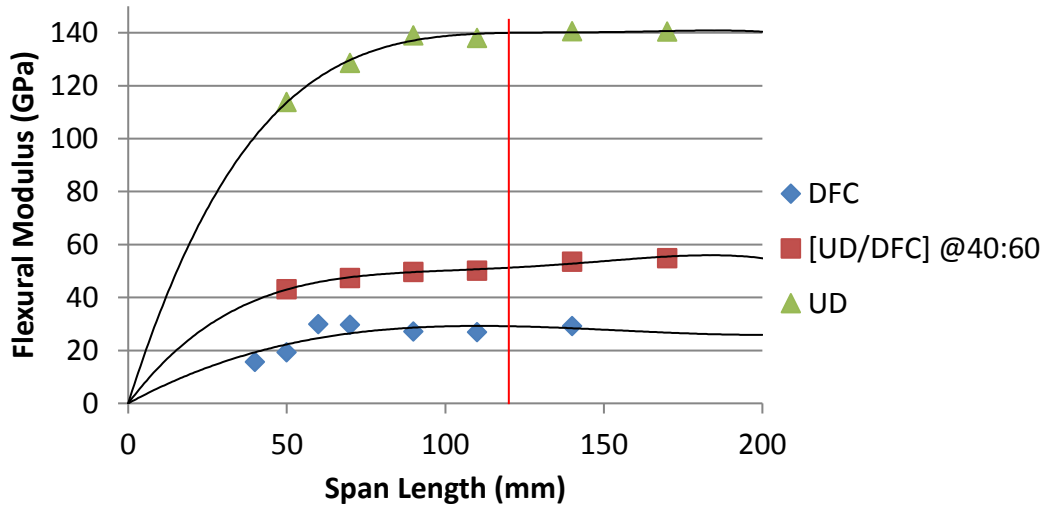


**Figure 3.20.** Flexural modulus of three carbon fibre architectures,  $h=3\text{mm}$ , with respect to the span length. Vertical red line shows 120mm span length that was selected as a result of this experiment

#### 3.4.4 Charpy impact properties

The Charpy impact strength of the composites was assessed to quantify the energy absorption of the composite during fracture. This was performed using an Avery Charpy impact tester, **Fig. 3.21**, following ISO 179-1:2010. Specimens were produced from plaques 3mm thick plaques, which were cut 10mm wide,  $b$ , and 80mm long,  $l$ . The specimen was placed on supports 60mm wide, on its edge, so that it was loaded flatwise. The impact energy of the axe was 15J, as a 2.5kg impactor was used with a strike velocity of 3.46m/s. This energy level was sufficient to cause total failure of the specimen, to determine the remaining energy in the axe. By measuring the height of the swinging axe after impact, the potential energy of the axe at this point is equal to the residual remaining. The difference between the impact energy and the residual energy was the energy absorbed by the specimen,  $E_c$ . The Charpy impact strength,  $a_c$ , was then calculated using *equation 3.12*.

$$a_c = \frac{E_c}{bh} \quad (3.12)$$



*Figure 3.21. Avery Charpy impact testing apparatus*

### **3.4.5 Double Cantilever Beam (DCB) testing**

Double cantilever beam (DCB) tests were performed in *Chapter 6* to characterise the critical strain energy release rate, or mode-I interlaminar fracture energy,  $G_{IC}$ , of laminate interfaces. This was used over shear testing, as mentioned in *section 2.5.6*, as to maintain horizontal crack propagation along the material interface rather than through-thickness as the shear may result in crack deflection around the discontinuous fibre bundles. The ISO 25217:2009 standard was used to apply a mode-I opening load to DFC, hybrid fibre architecture or NCF specimens. Aluminium load-blocks were bonded to the specimen surface to provide a location for load pins. A jig was used to align the load-blocks during bonding. The specimens were cut from plaques, 25mm wide,  $b$ , and 200mm long,  $L$ . A layer of Melinex® polyester sheet, 100 micron thick, was coated in Freekote 700NC and inserted at the interface of interest prior to compression moulding. This initiated a crack length 50mm from the centre line of the load pins,  $a_0$ , as shown in *Fig. 3.22*. This interleaf film was taped to the edge of the mould to prevent movement during compression moulding. All test samples were produced from net-shaped compounds to prevent flow from distorting the crack initiator.

The edges of each specimen were painted white and pen markings were applied every 5mm from the end of the initiated crack to provide a real-time reference for crack growth during testing. The cross head travelled at a rate of 5mm/s and a video camera was used to film the crack growth in relation to the applied load, **Fig. 3.23**.

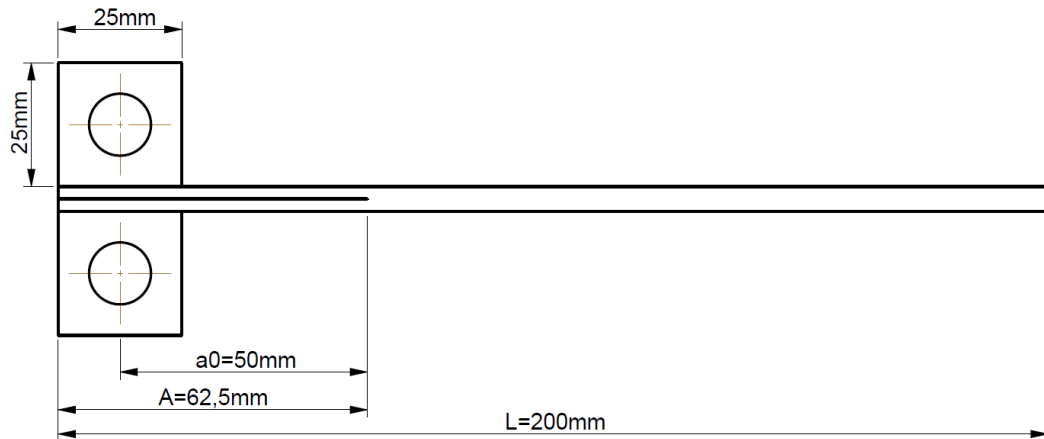


**Figure 3.22.** Dimensions of the DCB test specimen

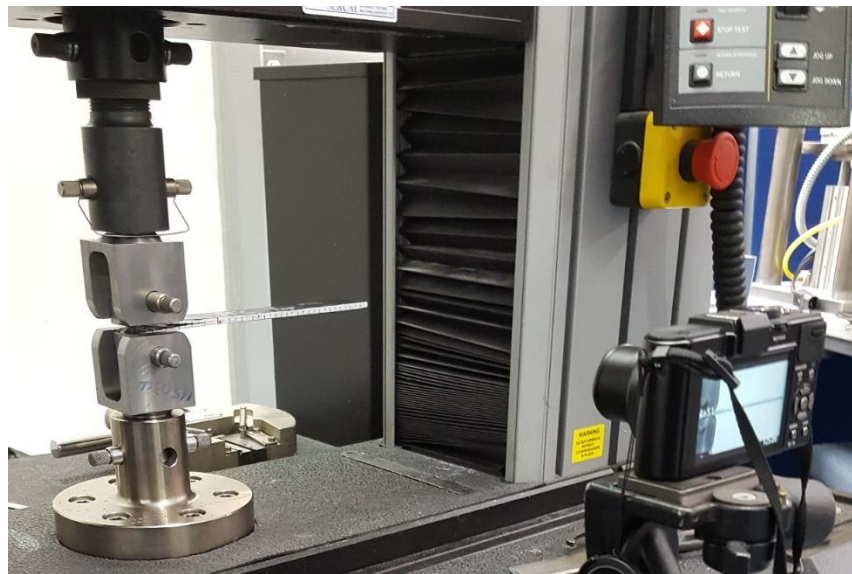


**Figure 3.23.** Setup of the DCB test apparatus and video camera

Three fibre architectures were tested, each with 4 repeats. The DFC architecture, had a target fibre volume fraction of 50% and was produced from two stacked charges to enable the crack initiator to be positioned in the centre. The UD architecture was produced from 10 layers of 375gsm carbon NCF. These were prepared and impregnated by LRS with a target fibre volume fraction of 60% in stacks of 5 layers to place the

crack initiator at the mid-thickness. The hybrid carbon fibre architecture was investigated to examine the mode-I fracture toughness of the interface between discontinuous and continuous architecture. These were produced by compression moulding a stack of 5 layers of UD-NCF, longitudinal orientation, and one mould compound of DFC. It should also be noted that when investigating the interface surface of a pre-cured UD was dulled with wet and dry paper and cleaned with acetone to remove any mould release applied during the first mould. The bending stiffness, EI, was calculated using *equations 3.13-3.15*, which was kept constant for each architecture to ensure equal bending and horizontal crack propagation, **Fig. 3.24**.

$$E_{DFC}I_{DFC} = E_{UD,1}I_{UD} \quad (3.13)$$

$$E_{DFC} \left( \frac{bh_{DFC}^3}{12} \right) = E_{UD,1} \left( \frac{bh_{UD}^3}{12} \right) \quad (3.14)$$

$$h_{DFC} = \sqrt[3]{\frac{E_{UD,1}}{E_{DFC}} h_{UD}^3} \quad (3.15)$$

The thickness of the 5 layers of UD was known,  $h_{UD} = 1.5\text{mm}$ . The Young's moduli of DFC ( $E_{DFC} = 36.3\text{GPa}$ ) and UD ( $E_{UD,1} = 147.4\text{GPa}$ ) are measured in *chapter 4* and *chapter 6*, respectively. This resulted in a thickness of 2.4mm for the DFC,  $h_{DFC}$ .



**Figure 3.24.** DCB tested hybrid fibre architecture investigating interface between 5 layers of UD NCF (top) and DFC (bottom)

Due to the sporadic nature of the crack growth in DFC specimens, detailed in *chapter 6*, the average mode-I fracture toughness (critical strain energy release rate),  $G_{IC}$ , was calculated over a 100mm crack propagation length using *equation 3.16*. The change in crack length,  $\Delta A$ , is 100mm, and the energy, E, is the area under the load-deflection

curve from the initial crack length, 62.5mm, to 162.5mm. This was calculated using the trapezium rule within Microsoft Excel.

$$G_{Ic} = \frac{E}{\Delta Ab} \quad (3.16)$$

### 3.4.6 Drop weight impact testing

Damage tolerance was accessed by a combination of drop weight impact, NDT analysis (section 3.3.4) and compression after impact (CAI). A dropped weight produced a low velocity impact to hybrid fibre architecture composite panels in the normal direction following the ISO 18352:2009 standards. Panels with dimensions shown in **Fig. 3.25 (a)** were cut from plaques shown in **Fig. 3.25 (b)**.

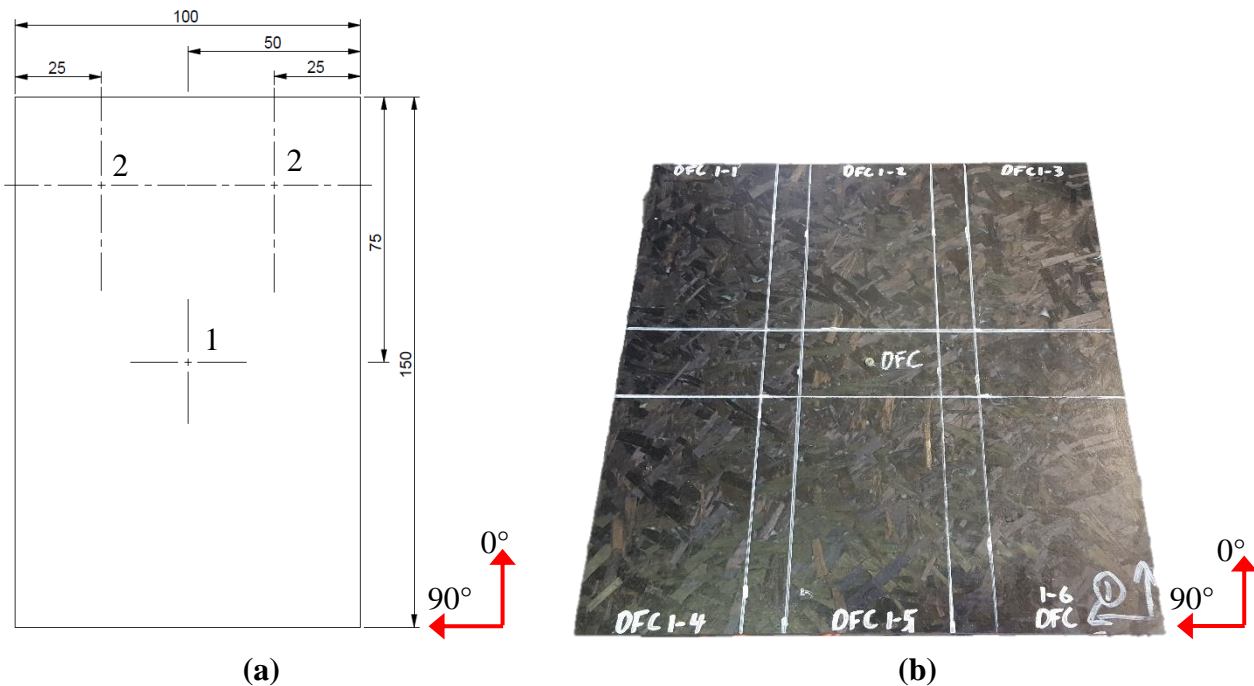
The panels were placed beneath the drop tower, held in place by rubber bushes at the corners above a 125mm x 75mm window. A steel hemispherical impactor was then dropped on the centre of the panel, location 1 in **Fig 3.25 (a)**. The drop height of the impactor governs the impact energy (the mass of the impactor,  $m$ , was 8.641kg). Two impact energies,  $E_c$ , were tested: 4.5J/mm and 6.7J/mm. The target thickness of the panels,  $h$ , was 5mm  $\pm$ 1mm but the actual thickness was measured using Vernier callipers. *Equations 3.17-3.18* were then used to calculate the drop-height,  $h_{drop}$ , where  $E_{impact}$  the impact energy.

$$E_{impact} = E_c h \quad (3.17)$$

$$h_{drop} = \frac{E_{impact}}{mg} \quad (3.18)$$

The impact velocity,  $v_{impact}$ , and force of the impact were measured. The impact velocity and mass of the impactor was used to verify the impact energy by equation 3.19. The impact damage was then assessed by NDT and CAI.

$$E_{impact} = \frac{1}{2} m v_{impact}^2 \quad (3.19)$$



(a) (b)  
**Figure 3.25.** Drop weight and CAI specimen dimensions with the position of the impactor, location 1, and the strain gauges, location 2, (a) and the plaque cutting plan (b)

### 3.4.7 Compression testing

Compression tests were performed to determine the in-plane compressive behaviour within continuous, discontinuous and hybrid carbon fibre architectures. Testing followed the ISO 14126:1999 standards and was performed using an Instron 5581 Universal Testing Machine with a 50kN load cell. The IITRI compression test was used, whereby load was applied to the specimen by shear to the in-plane surface or through trapezoidal fixtures that grip the specimen under compression with a gauge length of 12.7mm, shown in *Fig. 3.26 (a)*. *Fig. 3.27* shows the spacers used to maintain this gauge length whilst adhering aluminium tabs. The target thickness of the test specimens was 5mm and the specimens were all cut to 150mm in length. DFC specimens were 25mm wide, equal to the fibre bundle length, and untabbed because the damage sustained from the grips was not substantial enough to deter failure from the gauge region, *Fig 3.26 (b)*. When compression testing continuous architecture or hybrid carbon fibre architecture, the clamping force was found to damage the load bearing fibres and affect the ultimate compressive strength of the composite. 1.5mm thick aluminium end tabs were bonded to the specimens to prevent damage to the surface

fibres. Spacers were used to maintain a constant gauge length and ensure that the edge of the tabs were perpendicular to the load direction, **Fig. 3.26**. Also, the strength of these fibre architectures was greater than for the discontinuous specimens. Therefore, 15mm wide specimens were used to reduce the ultimate force acting to cause failure, **Fig. 3.26 (c)**.

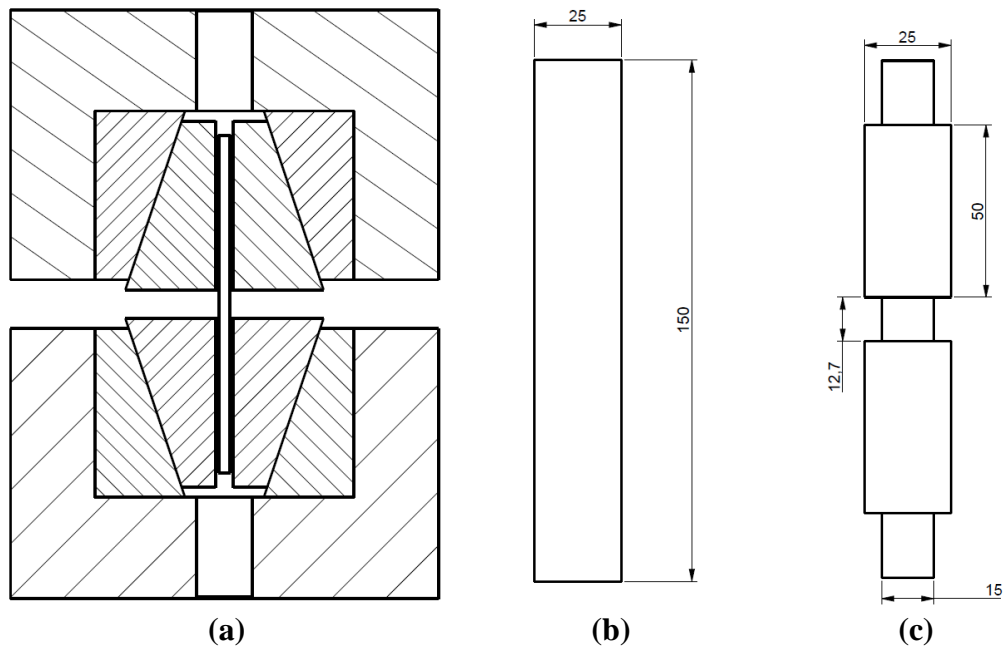


**Figure 3.26.** Schematic drawings showing the compression testing apparatus used (a), the geometry of the untabbed DFC specimens (b) and of the tabbed specimens continuous or hybrid fibre architecture (c)

A test rate of 1mm/min was used, using a video gauge to measure the strain,  $\epsilon$ , on the front surface of the specimen whilst the load cell recorded the applied force,  $F$ , as shown in **Fig. 3.28**. The specimens were tested to failure, and the failure mode was observed to ensure that the specimens didn't fail by buckling, which happens if the specimen bends during compressive load. This was performed as it was unfeasible to apply strain gauges to the surfaces of each specimen with small view windows and high number of repeat results. The compressive stress,  $\sigma_c$ , was determined using *equation 3.20*. The compressive modulus,  $E_c$ , was calculated using *equation 3.21*, using the compressive stresses at a strain of  $\epsilon_1 = 0.05\%$ ,  $\sigma_{c,1}$ , and  $\epsilon_2 = 0.25\%$ ,  $\sigma_{c,2}$ .

$$\sigma_c = \frac{F}{A} \quad (3.20)$$

$$E_c = \frac{\sigma_{c,2} - \sigma_{c,1}}{\varepsilon_2 - \varepsilon_1} \quad (3.21)$$

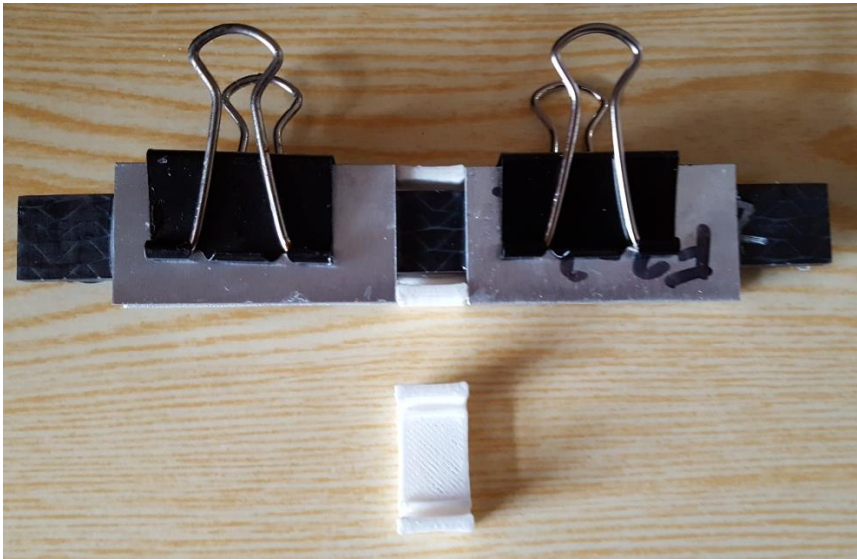


*Figure 3.27. Photo during the tab bonding process of compression specimen using spacers to maintain the 12.7mm gauge length*

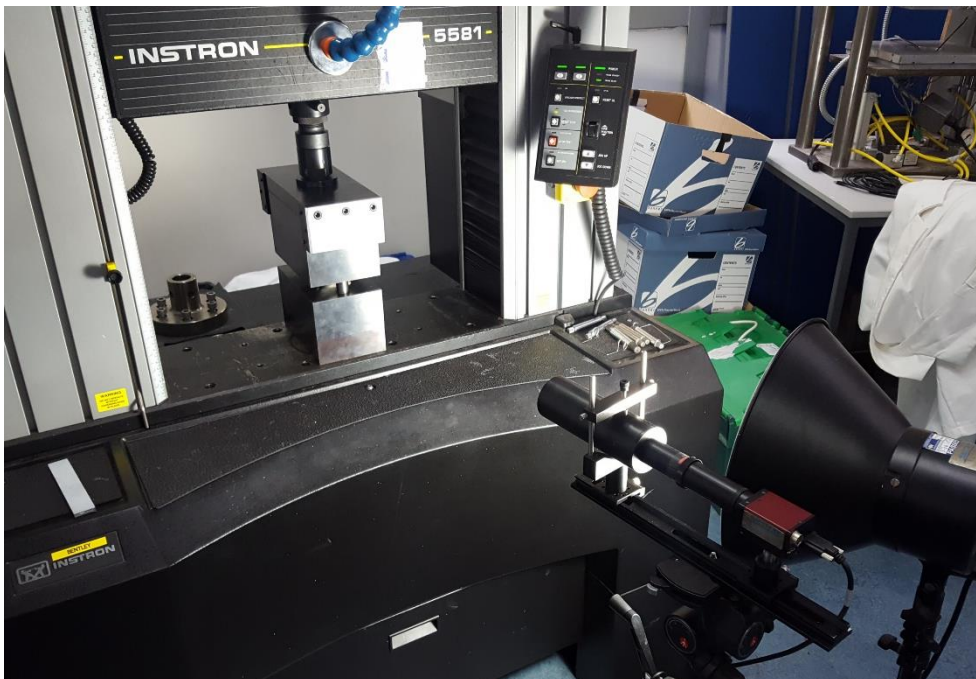
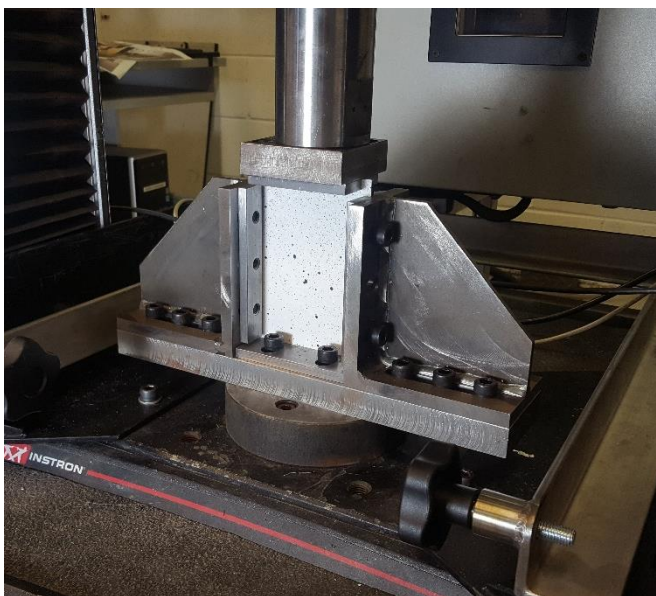


*Figure 3.28. Compression testing arrangement using IITRI fixtures and a video gauge*

### 3.4.8 Compression After Impact (CAI)

Proceeding the drop weight impact testing, specimens were compressed in the  $0^\circ$  direction to understand the influence of the impact damage on the mechanical performance of the composites. The results are compared to the compression tests performed on undamaged specimens, using the method detailed in *section 3.4.7*. This was performed using an Instron 5989 testing machine following ISO 18352:2009. The geometry of the specimens is the same as the geometry used during impact testing, *Fig. 3.25 (a)*. Compression was performed using the rig shown in *Fig. 3.29 (a)* at a rate of 1mm/min.



(a)



(b)

**Figure 3.29.** CAI test rig for compression of plates impacted by the drop weight testing (a) and the tracking locations of the video gauge strain measurements (b).

The four edges of the plates were constrained to prevent out-of-plane movement and bending of the specimen, ensuring that the load was applied purely in-plane. Three repeats were performed using four strain gauges (two on the front, two on the back) positioned at the locations shown in *Fig. 3.25 (a)*. This was to confirm that the specimens were not bending during compression in the fixtures used. At least four repeats were performed on damaged specimens using a video gauge to measure strains at three discrete locations in the loading direction by tracking a speckle pattern on the specimen surface, *Fig. 3.29 (b)*. During compression, the 250kN load cell measured the

compressive force, which then enabled the compressive strength and compressive modulus to be calculated using *equations 3.20 and 3.21*. The failure modes were also inspected to understand the damage caused by the impact and to ensure that failure was not due to bending.

### 3.5 Analytical Model

An analytical model, provided by Harper [5, 45], was used to reverse engineer the orientation distribution tensors from the in-plane stiffness values. This has been previously used for the prediction of the tensile stiffness.

This inclusion model was used to predict the elastic constants and to determine the fibre orientation state for plaques manufactured for the charge coverage study. The closed-form expressions of the Mori Tanaka method [156] were reformulated by Qiu and Weng [157] to include the effects of anisotropic constituents, such as carbon fibre. Using the methodology outlined by the authors in [19], the Qiu and Weng model has been applied at 2 stages to firstly establish bundle properties, and secondly to predict unidirectional ply properties. Orientational averaging was applied at a third stage using the tensor approach of Advani and Tucker [158], to distribute the UD sub-units from Stage 2 according to a 3D spatial distribution.

The elastic properties of the bundles were calculated at Stage 1 using the elastic constants for carbon and epoxy taken from [157]. A tow volume fraction of 60% was assumed, similar to [19]. The fibre length was taken to be 25mm and the fibre diameter was assumed to be 7 $\mu$ m. The transversely isotropic bundle properties from Stage 1 were then used to calculate UD ply properties at Stage 2, assuming the UD sub-unit had a volume fraction of 75% to account for the matrix material contained within the bundles. This yielded a global volume fraction of 45% to correspond with the experimental study.

The spatial orientation of a single bundle can be described by the Cartesian components ( $p_1, p_2, p_3$ ) of a unit vector  $\mathbf{p}$ . A representative element of the present material contains many bundles of a constant length but different orientations, which can be described generally by the probability density function  $\psi(\theta, \phi)$ .  $\phi$  describes the in-plane bundle

orientations (in radians between  $-\pi/2$  and  $\pi/2$ ), which can be summarised by a double exponential distribution:

$$f(\phi) = \alpha \left( \frac{\exp\left[-\left(\frac{|\phi|-\mu}{2\beta}\right)\right]}{2\beta} \right) \quad (3.22)$$

where  $\mu$  is the location parameter,  $\beta$  is the shape parameter,  $\alpha$  is the normalisation constant. This was previously used by the authors in [159] to describe the in-plane bundle orientations from a preforming process using similar spray deposition equipment. The in-plane fibre orientations are random in the 1-2 plane when  $\beta$  tends to infinity, and are aligned in the 1-direction when  $\beta$  tends to zero.

$\theta$  summarises the out-of-plane orientations (in radians between 0 and  $\pi/2$ ), using a trigonometric function in the form of:

$$f(\theta) = a \sin^{2(b-1)} \theta \quad (3.23)$$

where  $a$  is a normalisation constant and  $b$  controls the shape of the out-of-plane distribution. This function was previously used in [19] to describe the out-of-plane orientations for a discontinuous carbon fibre material with 14mm long bundles. All of the fibres are aligned in the 1-2 plane when  $b$  is infinity. When  $b$  is unity the fibres are 3D random in space and when  $b$  is zero all of the fibres are aligned in the 3-direction (i.e. all fibres are out of the laminate plane).

The second and fourth order orientation tensors can be calculated by substituting the probability distributions from *equations 3.22 and 3.23* into *equations 3.24 and 3.25* respectively:

$$\alpha_{ij} = \langle p_i p_j \rangle \equiv \int_0^{2\pi} \int_0^\pi (p_i p_j \psi(\theta, \phi) \sin \theta) d\theta d\phi \quad (3.24)$$

$$\alpha_{ijkl} = \langle p_i p_j p_k p_l \rangle \equiv \int_0^{2\pi} \int_0^\pi (p_i p_j p_k p_l \psi(\theta, \phi) \sin \theta) d\theta d\phi \quad (3.25)$$

where  $\langle \rangle$  denotes the orientational average.

Limited material availability prevented a destructive method from being used. A sensitivity analysis has been performed to establish the second and fourth order orientation tensors required to yield similar mechanical properties to those determined experimentally. Values of  $\beta$  and  $b$  have been adjusted until the longitudinal stiffness  $E_{11}$  was within 0.5% of the experimental value and the transverse stiffness  $E_{22}$  was within 5%.

### 3.6 Finite element analysis of hybrid joints

To further understand the relationship between joint design and the stress distributions within *Chapter 6*, a simple 2D finite element analysis model was produced using Abaqus/CAE. This model neglects the variability in the DFC material and assumes each material to be homogeneous. The through-thickness (x-z) plane of continuous-discontinuous hybrid joints were investigated for synchronised ply ends (*Fig. 3.30 (a)*) and stepped arrangements (*Fig. 3.30 (b)*). The hybrid specimens consisted of 7 plies, 0.3mm ply thickness, with a 4mm overall thickness and gauge length of 100mm was used. The plies used were UD carbon fibre oriented in the x-direction ( $0^\circ$ ) and the remainder of the material was DFC. The UD material had elastic engineering constants:  $E_1 (E_x) = 147.3\text{GPa}$  and  $E_2 (E_z) = 10\text{GPa}$  determined in *Chapter 6*, and a shear modulus of 5 GPa, Poisson's ratio of 0.3 and density of  $1.56\text{g/cm}^3$  were used. The DFC material was given an isotropic Young's Modulus ( $E = 37\text{GPa}$ ) determined experimentally, Poisson's ratio of 0.3 and density of  $1.5\text{g/cm}^3$ . The boundary conditions fixed the nodes on the left hand side, with zero displacement and rotation and an axial displacement of 0.5mm to the nodes on the right hand side to generate a global strain of 0.5%. A mesh of 0.05mm square elements was used. The axial, peel/normal and shear stress distributions were determined along the centre line of each of the plies, from  $X=20\text{mm}$  to  $X=80\text{mm}$  with the centre of each joint located at  $X=50\text{mm}$ .

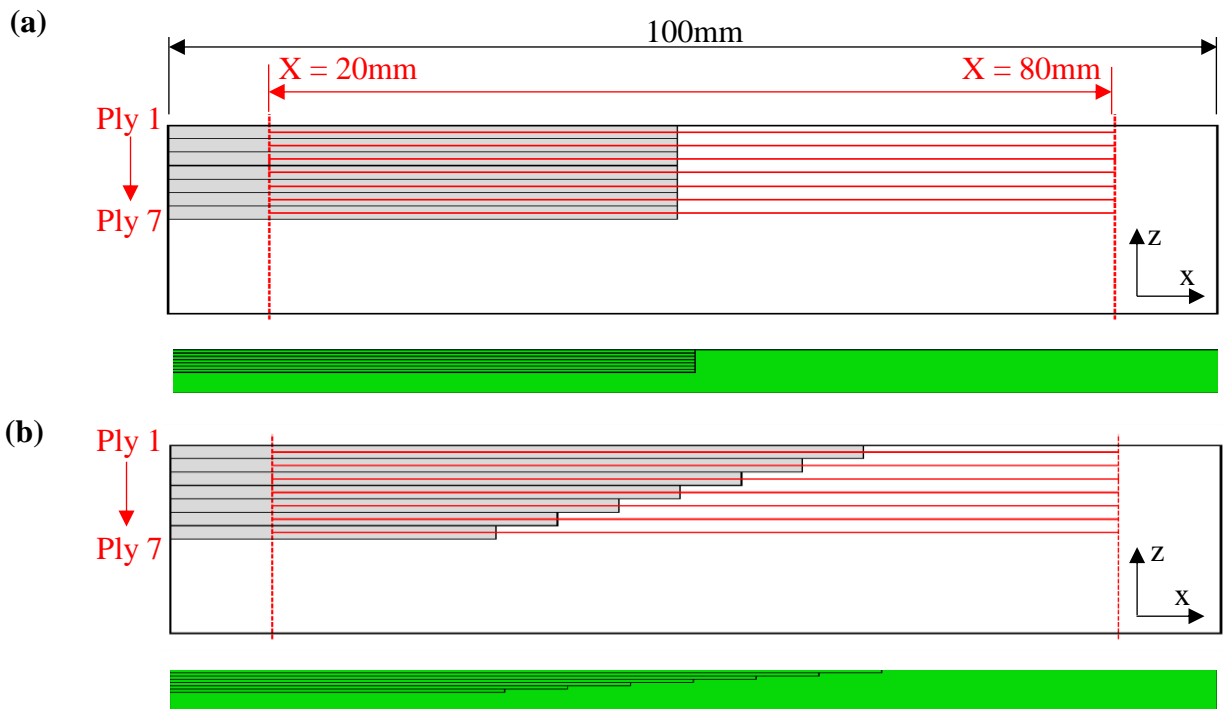


**Figure 3.30.** Schematics of the dimensions and paths used to measure the stress distribution along UD plies in each 2D FE model of a continuous-discontinuous hybrid joint: (a) synchronised ply ends and (b) stepped joint (Step size to ply thickness ratio – 20:1)

# 4. Directed Fibre Compound

## Material Development

### 4.1 Introduction

SMCs manufactured from glass/polyester are well established and the manufacturing route is highly optimised, shown in *Chapter 2*. However, developing this process to produce carbon fibre/epoxy compounds is not without difficulty. During cutting and handling of the carbon fibres, their high strength and low failure strain may result in fibre damage prior to chopping may lead to fibre blockages within the chopping apparatus [44]. Additionally, the low density of the carbon increases the risk of disruption during deposition by the atomising air stream used by the liquid resin spray. *Chapters 1 and 2* detail the difficulties in using an epoxy matrix. These include the ability to control the degree of B-stage to control viscosity, storage of high volumes of epoxy with necessary refrigeration to prevent aging and risk of exothermic reaction. The resin requires a low viscosity to achieve good fibre wet-out but needs to be increased following the deposition stage to prevent the fibre and matrix separating under compression. This is also achievable by using polyester or vinyl-ester resins and introducing fillers to increase the viscosity. However, these lack the adequate interfacial properties with the fibres and limited fibre content.

This chapter presents the process optimisations steps during the development of the Directed Fibre Compound (DFC) process for the production of discontinuous carbon fibre/epoxy moulding compounds. DFC exploits the chemical thickening ability of commercially available epoxy formulated systems. Many high-performance epoxies can be formulated as B-staged systems, where the reaction between the resin and the curing agent is incomplete after mixing. Chemical or thermal B-staging partially cures the epoxy and cross-linking is only fully completed when the temperature is elevated

and the curing process is completed. This offers a low-cost alternative to prepreg-derived carbon fibre moulding compounds, such as HexMC.

The objective is to determine an optimised process for producing a short carbon fibre/epoxy moulding compound by means of DFC. This considers the effect of fibre tow size and the choice of an appropriate epoxy resin to provide fundamental DFC plaque manufacturing criteria that was used throughout the duration of this project. Considerations were also made to their practicality within high volume production volumes. Experiments were performed to understand mechanical effects of fibre roving and resin selection. This chapter also aims to determine the optimal cure cycle for both the lab scale DFC platform and high-volume production capabilities by outlining how it can achieve cycle times of less than 5 minutes. A cure model is also produced to understand the isothermal cure times that haven't been tested by DSC.

The main focus of this chapter is to select a suitable epoxy resin to enable the viscosity of the charge to be controlled via B-staging, avoiding the use of thickening agents which reduce the maximum fibre volume fraction. These resin systems have been investigated with regards to their manufacturability with reference to spray temperature and glass transition temperature. The optimum spray temperature was determined as a function of the resin viscosity, ensuring the resin could be sprayed through the atomising nozzle at the exit of the spray head. A required viscosity of less than 1000mPas was achievable by preheating with sufficient resin stability at this temperature to prevent damage of the apparatus by premature gelation. The glass transition temperature,  $T_g$ , was obtained to understand the composite behaviour during hot demould following compression moulding. If the glass transition temperature is too low, then demoulding at higher temperatures could result in warping and bending of the part during this stage. All resin systems investigated use the same high-temperature hardener, Aradur XB1571. Therefore, cure cycles are expected to be very similar. Higher glass transition temperatures enable the components to be moulded at higher temperature which reduces cure time. The mechanical properties of DFC compounds produced using these resin systems were also determined. In-plane properties were evaluated by tensile testing plaques produced from moulding net-shaped compounds and composites that exhibited one-dimensional flow during the mould process. These charges were produced with 50% mould coverage. Finally, the Charpy impact strength was obtained

to determine the difference in fracture toughness between the resin systems. This is desirable for composites that are going to be used in the automotive industry as they must be able to withstand low velocity impacts, such as pebbles striking the body panels, without inducing structural damage.

## **4.2 Design of experiments**

### **4.2.1 Resin selection**

#### **4.2.1.1 Mould Parameters**

In this section, each DFC plaque used a constant fibre type: 12K Toray 700 50C carbon fibre chopped to 25mm length bundles. Plaques were moulded without using rigid stops in the compression mould tool. The plaque thickness was controlled by the quantity of material within the press. Flat plaques were produced with dimensions of 405mm x 405mm with approximate weight of 740g with a 3mm target thickness and target 50% fibre volume fraction. Four formulated epoxy resin systems with the option for B-staging were considered for DFC, detailed in **Table 4.1**. Each system was prepared by creating a “*premix*”. First, the Aradur and Accelerator components were blended together, before adding the resin component and mixing for a second time. When thoroughly mixed, it was poured into the heated resin tank in the LRS system. The temperature of this tank was set to achieve a resin viscosity of less than 1000mPas, which was determined by rheometry. These temperatures are shown in **Table 4.1**. This viscosity enabled the resin to atomise during the spray deposition, providing good wet-out of the fibre bundles. The hardener was added once the “*premix*” reached the optimum operating temperature. The maximum working time for resins were approximately 30 minutes.

The four resin systems are referred to as T-Ch, T-Th, N-Ch and N-Th; where T and N indicate whether the resin component is toughened (epoxy resin XU 3508) or non-toughened (epoxy resin XB 50021A), respectively, and Ch and Th indicate chemical or thermal B-staging. Resin systems A (T-Ch) and C (N-Ch) were B-staged chemically over 24 hours at ambient temperature, whilst systems B (T-Th) and D (N-Th) were B-staged thermally at 90°C for 6 minutes [151, 152]. The non-toughened epoxy resin was designed, by Huntsman, for higher glass transition temperature,  $T_g$ , increasing

demoulding temperature. Each were moulded at 130°C for 30 minutes in the compression mould with 85bar in-mould pressure applied. A freestanding oven then completed a post cure at 130°C for 3.5 hours.

**Table 4.1.** Huntsman formulated epoxy prepreg resin systems with suitable spray deposition and B-staging requirements for DFC and compression moulding

			Components	Parts by weight	Spray Temp (°C)	B-staging mechanism	B-staging Temp (°C)	B-stage time
A	T-Ch	Pre-mix	Resin XU 3508 Aradur 1571 Accelerator 1573	100 20 3	65	Chemical	25	24 hours
		Hardener	XB 3403	12				
B	T-Th	Pre-mix	Resin XU 3508 Aradur 1571 Accelerator 1573	100 20 3	60	Thermal	80	17 min
		Hardener	XB 3471	12				
C	N-Ch	Pre-mix	Resin XB 50021A Aradur 1571 Accelerator 1573	100 20 3	56	Chemical	25	24 hours
		Hardener	XB 3403	12				
D	N-Th	Pre-mix	Resin XB 50021A Aradur 1571 Accelerator 1573	100 20 3	48	Thermal	80	17 min
		Hardener	XB 3471	12				

#### 4.2.1.2 Mechanical testing

Specimens were then produced for tensile testing and Charpy impact testing to compare the effect of each resin system on mechanical performance. The tensile performance was also measured for two mould coverages, 50% and 100%, to ensure that each resin system was capable of flowing during moulding without fibre-matrix separation. Flow was restricted to one dimension so that the flow direction was known in relation to the tensile performance in that direction, longitudinal, and perpendicular to the flow direction, transverse. This was performed by placing the charge on the left-hand side of the mould tool, as shown in *Fig. 4.1*, and thus flowing towards the right. *Fig. 4.2* shows the cut plans used for each of the plaques. 25mm x 25mm samples were also taken from the ends of each tensile specimen from the 50% mould coverage plaques to measure their fibre volume fraction via density measurement. The glass transition temperature

was also measured for the resin systems hot-demoulding ability by DSC standards BS EN ISO 11357-2:2014.

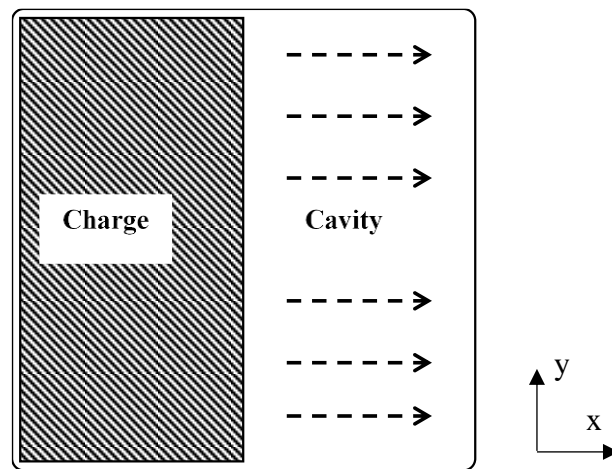


**Figure 4.1.** In-mould charge placement within a 405mm x 405mm flat tool to produce 50% mould coverage exhibiting one-dimensional flow

#### **4.2.2 Effect of carbon fibre type and tow size**

Three types of carbon fibre tow were trialled for producing DFC compounds: 3K (Texex-E E13 200tex), 12K (Toray 700 50C) and 24K (Tenax F13 1600tex). These demonstrate a simplistic range of tow sizes and types of carbon fibre roving available. The 3K and 12K roving each contained 1% epoxy sizing. This was the minimum required for the roving to pass through the feed rollers on the chopping device without fragmentation. The 24K tow roving contained 1.3% epoxy sizing. The fibre bundles were chopped with 25mm fibre length and the target fibre volume fraction of the compounds was 50%. These were moulded with 100% mould coverage using the compression mould stops to control the thickness of the plaques to prevent excess resin bleed off that was discovered during the moulding that resulted in variable fibre volume fractions experienced in the resin selection experiments. This was also found to improve uniformity of the thickness as this prevented tilting of the top mould tool during closure of the mould. Tensile testing was performed in the x (longitudinal) and y (transverse) orientations to ensure that the fibre bundles were randomly distributed before averaging the tensile strength and modulus results regardless of orientation.

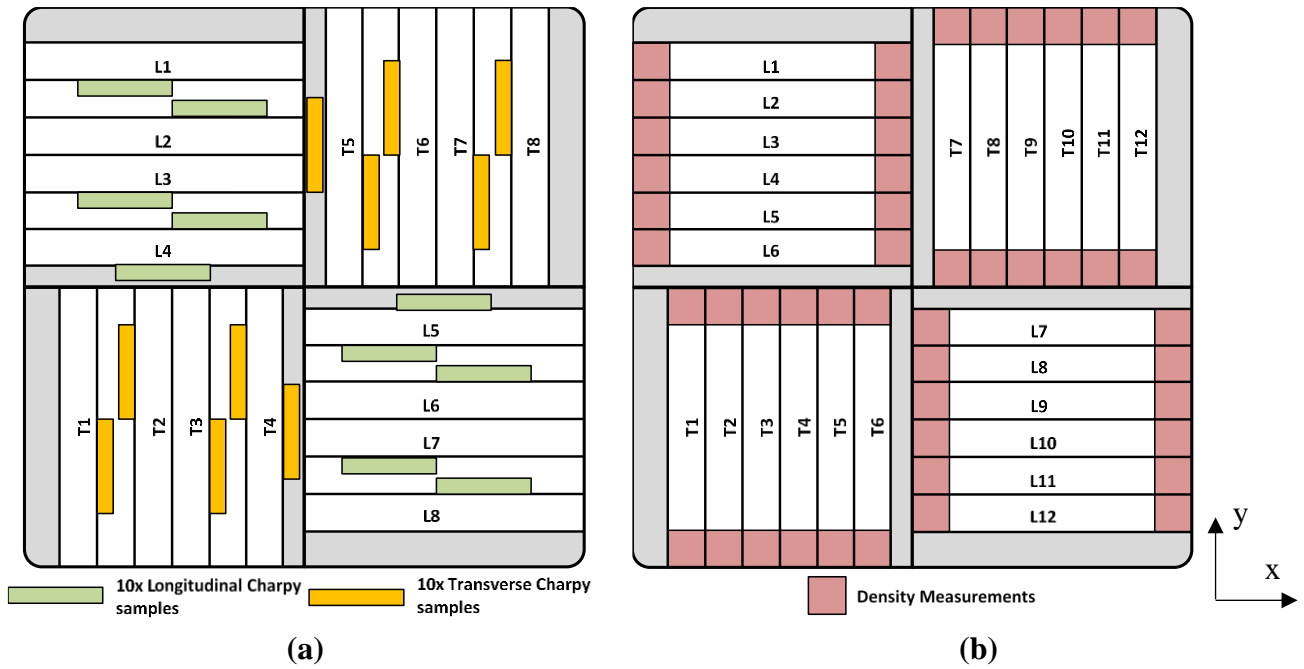


**Figure 4.2.** Cutting plan of 405mm x 405mm plaques produced with 100% mould coverage (a) and 50% mould coverage (b)

### 4.3 Cure cycle model

The cure cycle of resin system A modelled to characterise the degree of cure with time. DSC testing was therefore performed to produce this. Prior to testing, a 10 to 20mg sample was B-staged for 24 hours in an aluminium DSC testing pan. **Table 4.2** shows the set of cure times and temperatures that have been investigated with at least two repeats in each case.

**Table 4.2.** List of DSC test specimens

Isothermal temperature (°C)	Isothermal cure time (min)
N/A (Dynamic testing only)	0
80	20, 40, 60, 120
100	20, 40, 60, 120
115	5, 10, 20, 40, 60
130	2.5, 5, 10, 20, 40
150	2.5, 5, 10, 20
160	1, 2.5, 5, 10

The data obtained from DSC experimentation was used to determine the kinetic parameters for modelling the degree of cure, or percentage of conversion, of the cure reaction [160, 161]. Prior work by several authors details cure kinetic models for

different polymerization reactions. Work by Flory [162] and Stevenson [163] developed mechanistic models based on the amine-epoxy reaction and the concept of free radical polymerization. Stevenson [163] developed a simplified free radical based model by applying restrictions to rate coefficients. This improves the convenience of analytical solution under isothermal conditions and accounts for the effects of type and concentration of initiators and inhibitors suitable for simulating compression moulding of SMC. However, mechanistic models require a large number of kinetic parameters, leading to high complexity when predicting and interpreting the curing reactions of thermosetting polymers [161].

The degree of conversion,  $\alpha$ , was calculated using a rate law whereby the reaction rate,  $\frac{d\alpha}{dt}$ , is a proportional relationship between the temperature dependent Arrhenius rate constant,  $k(T)$ , and a function dependent on the degree of conversion,  $f(\alpha)$  [160, 161, 164]:

$$\frac{d\alpha}{dt} = k(T)f(\alpha) \quad (4.1)$$

For epoxy systems, the function,  $f(\alpha)$ , usually takes the form of either  $n^{\text{th}}$  order reaction kinetics or autocatalytic cure [160, 161]:

$$n^{\text{th}} \text{ order reaction:} \quad f(\alpha) = (1 - \alpha)^n \quad (4.2)$$

$$\text{Autocatalytic cure:} \quad f(\alpha) = \alpha^m(1 - \alpha)^n \quad (4.3)$$

Where  $m$  and  $n$  are orders of reaction.

This uses the data obtained by isothermal DSC for at least two repeats to achieve full cure at 4 temperatures, 115°C, 130°C, 150°C and 160°C. The temperature was initially ramped up rapidly at 50°C/min, to replicate the heat transfer to the charge during the closure of the mould tool. The percentage conversion was calculated and the rate of reaction with respect to time was also determined. From this the natural logarithm of the autocatalytic cure kinetics equation was used:

$$\frac{d\alpha}{dt} = k(T)\alpha^m(1 - \alpha)^n \quad (4.4)$$

$$\ln\left(\frac{d\alpha}{dt}\right) = \ln(k(T)) + m \ln(\alpha) + n \ln(1 - \alpha) \quad (4.5)$$

The Arrhenius rate constant and reaction orders, m and n, were determined by solving *equation 4.5* in Matlab. The Arrhenius rate constant is temperature dependent, so replicates were averaged at each temperature. The orders of reaction are dependent on the reactants used, which were constant throughout all of the tested temperatures. These were therefore averaged by solving *equation 4.5* for each of the isothermal temperatures. These results are presented in **Table 4.3**:

**Table 4.3.** Kinetic parameters determined by Isothermal DSC

	Average (x10 <sup>-3</sup> )	Standard deviation (x10 <sup>-3</sup> )	CoV (%)
m	0.187167	0.071667	38.29%
n	0.691981	0.022895	3.31%
k(T = 115°C)	0.992	0.0291	2.94%
k(T = 130°C)	2.493	0.2343	9.40%
k(T = 150°C)	5.403	0.6870	12.71%
k(T = 160°C)	7.441	0.2438	3.28%

This also indicated that activation of the hardener was not initiated until the temperature had exceeded 80°C. At a cure temperature of 100°C, DSC results showed that there was an initial zero rate of cure for approximately 24 minutes which affected the modelled result for this temperature. This is indicated by the initial offset in **Fig. 4.3** for the 100°C cure temperature. These results and models demonstrate that cure times can be significantly reduced by elevating the temperature. At 160°C, the cure time can be reduced to less than 5 minutes, which is the target for automotive applications where production volumes of 100,000ppa are required. However, a longer cure cycle was selected for laboratory trials, 30 minutes at 130°C, due to restrictions with the closure speed of the press. This slower cure cycle ensured that the material didn't prematurely cure before the mould tool has been closed and pressure was applied.

When increasing the mould temperature above the glass transition temperature to improve the cycle time, such as 5 minutes at 160°C, this may result in warpage when

demoulding complex geometry without cooling. Additional consideration must be made when moulding isothermally at these higher temperatures to ensure there is no thermal decomposition of the matrix, which would reduce the molecular weight of the epoxy and therefore degrade the mechanical performance. The melt temperature, normally indicated by a peak in the heat flow vs temperature curves beyond the glass transition temperature, is greater than the maximum temperatures investigated (>200°C). The resultant heat flow measurements in the fully cured specimens is caused by thermal decomposition [165]. However, when comparing the dynamic DSC of specimens cured for 30 minutes at 130°C and 5 minutes at 160°C, there was no distinguishable difference in the magnitude of heat flow during the temperature ramp. Any differences were difficult to observe because of the variability between specimens.

It was beyond the scope of this project to optimise the resin blend for cure cycle and thermal degradation as a result of the in-depth experimentation required to investigate their effects on mechanical properties. Therefore, moulding with a 5 minute cycle time at 160°C example has been used only to demonstrate feasibility of this target cycle time.

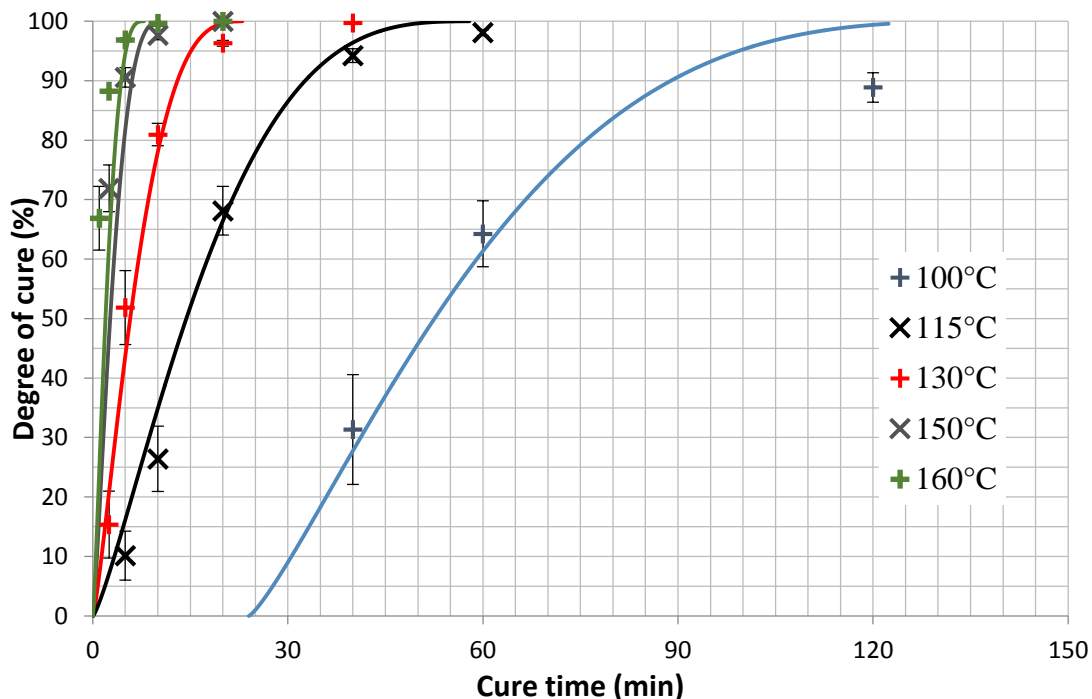


**Figure 4.3.** Cure cycle of resin system A (T-Ch) obtained by isothermal DSC for different temperatures and cure times. Graph contains experimental results (points) and modelled results (lines)

Within high production volume applications, automation techniques will consistently control the rate of charge placement and mould closure (1-10mm/s) to ensure cure doesn't arise prematurely. Further techniques are already in operation for producing composites from glass SMC whereby the upper and lower moulding surfaces are held at dissimilar temperatures [79]. In this case, the lower mould tool is held at a lower temperature than the upper mould tool. This slowly transfers heat from the lower tool into the compound after charge placement and rapidly elevates the rate of heat transfer from the upper tool once the mould is closed and pressure is applied.

## **4.4 Results and discussion**

### **4.4.1 Resin selection**

#### *100% mould coverage (zero flow)*

Moulding plaques using a net-shaped charge prevented any in-mould flow. The mechanical results in this section are therefore dominated by the DFC manufacturing process. The tensile properties of the 100% mould coverage were obtained from 8 specimens from each plaque, and the average values are shown in **Fig. 4.4. Table 4.4** shows a summary of all the mechanical testing results obtained from plaques using each of the resin systems. There was no statistical difference between the properties at different test orientations and therefore the material is assumed have near isotropic behaviour when the charge coverage is 100% of the tool. Results have been averaged to obtain the overall mechanical properties. The tensile strength for DFC composites produced using the toughened resin system, A (T-Ch), was statistically higher than the non-toughened systems, C (N-Ch) and D (N-Th), ( $p < 0.01$ ). A reduction of 24% was demonstrated from resin system A (T-Ch) to C (N-Ch), using the same B-staging mechanism. The large error bars are a consequence of the heterogenous nature of tow-based discontinuous material increasing variability between specimens. However, the 16 repeats (8 in each orientation) was sufficient that there was no overlap between error bars of the tensile strength of using resin system A (T-Ch) and that of systems C (N-Ch) and D (N-Th). However, there is slight overlap between the error bars of the tensile strengths of B (T-Th) and C (N-Ch). However, there was no statistical difference between the tensile modulus of these systems. This was because the tensile modulus was dominated by the fibre content and the local orientations, which were similar

between each of the plaques produced as a result of controlling the mass of material and using stops to control the mould thickness.

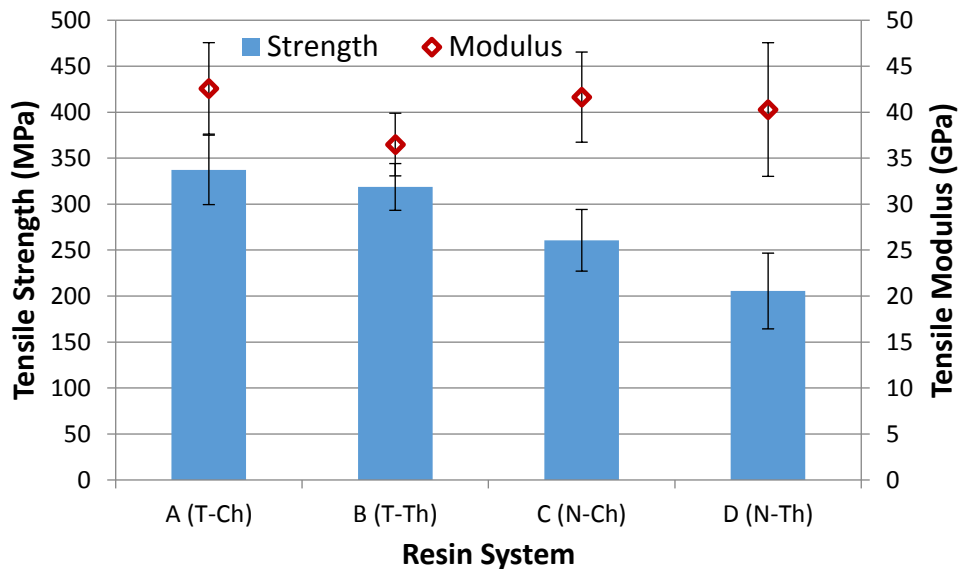


**Figure 4.4.** Tensile properties of 100% mould coverage plaques for each resin system

Statistically, the tensile strength of the chemically B-staged plaques was greater than those thermally B-staged ( $p < 0.05$ ). Plaques using resin B (T-Th) exhibited a 5% reduction in tensile strength compared to the chemically B-staged system A (T-Ch). This difference was greater for the non-toughened resin system, showing that the thermally B-staged system, resin D (N-Th), had a tensile strength that was 21% lower than its chemically B-staged alternative, resin C (N-Ch).

The Charpy impact strengths were also measured for each of the resin systems, testing 10 repeats in the longitudinal and transverse orientations, **Table 4.4**. These were averaged once results showed no statistical difference between Charpy impact strength for each orientation, **Table 4.4**. It was deemed to be statistically significant that the toughened resin systems, resins A (T-Ch) and B (N-Ch), were greater Charpy impact strength as a result of this resins superior fracture toughness than that of systems C (N-Ch) and D (N-Th). Large standard deviations in the results causes cross over between results and their errors. However, 20 repeats of each Charpy impact result produces strong statistical significance to support this statement. The four P-values are all less than 0.005 to support that the Charpy impact strength of A (T-Ch) and B (T-Th) are greater than C (N-Ch) and D (N-Ch). This large variability in the results is caused by

the small aspect ratio between specimen width and fibre bundle length. A sample width smaller than the fibre bundle length increases the proportion of fibre bundles that are cut during sample preparation. This effectively increases the distribution of fibre bundle lengths within the samples. However, the large variations result in no noticeable differences between the type of B-staging mechanism; i.e. resin A (T-Ch) compared to B (T-Th), and resin C (N-Ch) compared to D (N-Th).

**Table 4.4.** Tensile testing results (a) and Charpy impact strengths (b) with respect to their orientations and isotopically for compounds moulded using four resin systems and 100% mould coverage

(a)

Resin System	Modulus (GPa)				UTS (MPa)			
	A (T-Ch)	B (T-Th)	C (N-Ch)	D (N-Th)	A (T-Ch)	B (T-Th)	C (N-Ch)	D (N-Th)
Longitudinal	43.28	37.76	41.38	41.67	348.36	317.13	264.30	203.81
St. Dev	4.47	3.60	3.48	7.73	37.19	26.40	30.63	43.11
CoV (%)	10.34%	9.54%	8.41%	18.55%	10.68%	8.33%	11.59%	21.15%
Transverse	41.90	35.20	41.90	38.91	326.19	320.25	257.07	207.24
St. Dev	5.65	2.86	6.27	7.01	37.40	26.08	37.96	42.13
CoV (%)	13.49%	8.13%	14.95%	18.01%	11.46%	8.14%	14.77%	20.33%
Average	42.59	36.48	41.64	40.29	337.28	318.69	260.69	205.53
St. Dev	4.97	3.41	4.91	7.27	37.81	25.40	33.52	41.21
CoV (%)	11.68%	9.35%	11.78%	18.04%	11.21%	7.97%	12.86%	20.05%

(b)

Resin System	Charpy impact strength (kJ/m <sup>2</sup> )			
	A (T-Ch)	B (T-Th)	C (N-Ch)	D (N-Th)
Longitudinal	112.95	105.10	92.22	74.16
St. Dev	19.95	18.97	18.59	20.43
CoV (%)	17.66%	18.05%	20.16%	27.54%
Transverse	121.06	113.22	82.02	76.25
St. Dev	16.70	19.40	24.59	13.60
CoV (%)	13.80%	17.13%	29.98%	17.84%
Average	117.00	109.16	87.12	75.21
St. Dev	18.38	19.14	21.85	16.92
CoV (%)	15.71%	17.53%	25.08%	22.50%

50% mould coverage (one-dimensional flow)

Tensile testing results were obtained for a preliminary investigation demonstrating an advantage of in-mould flow-induced alignment of the fibre bundles, during

compression. This enhanced the mechanical properties in the flow direction, whilst reducing the properties perpendicular to the flow. **Fig. 4.5** and **Table 4.5** show the tensile properties of DFC compounds moulded with one-dimensional flow, 50% mould coverage. It is expected that the only factor that causes the change in performance between longitudinal and transverse directions is the result of flow-induced alignment. Therefore, the degree of this alignment has also been indicated in **Table 4.6** showing the ratio between the longitudinal and transverse tensile modulus and strength.

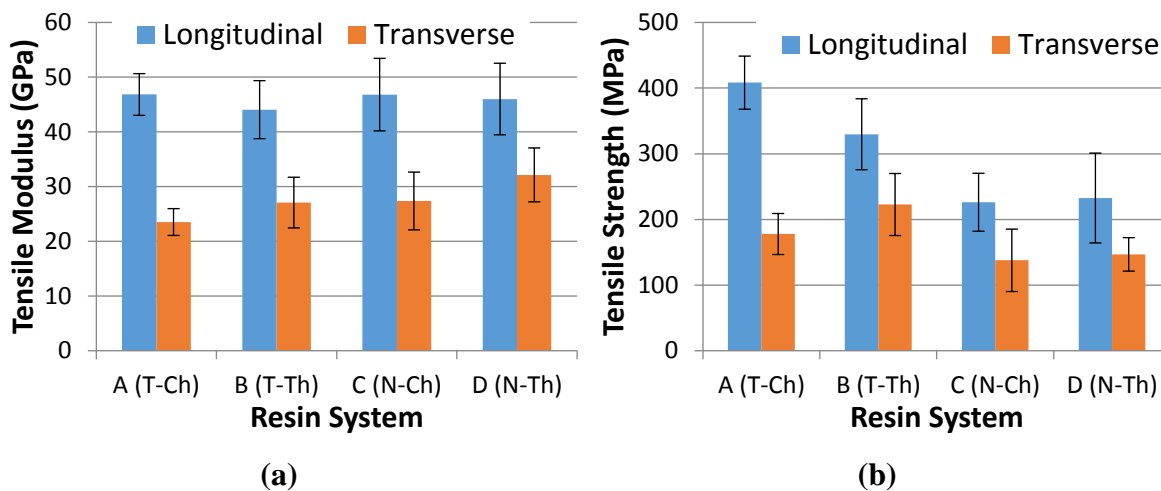


**Figure 4.5.** Longitudinal and transverse tensile modulus (a) and strength (b) for DFC composites with each resin system using 50% mould coverage.

The greatest enhancement in tensile strength from this test was experienced by resin system A (T-Ch), showing a 21% increase in the longitudinal direction ( $408.29\text{MPa} \pm 40.46\text{MPa}$ ) compared to 100% mould coverage ( $337.28\text{MPa} \pm 37.81\text{MPa}$ ). Although, there is an overlap between the standard errors in these values, because of the heterogeneity of the material, the large number of repeats (50% mould coverage plaque - 12 repeats in each direction, 100% mould coverage plaque – 16 repeats total) produces statistical significance in agreeing with the increase in strength in the longitudinal direction ( $p < 0.001$ ). The high number of repeats also shows that the tensile modulus for resin system A (T-Ch) increases from  $42.59\text{GPa} \pm 4.97\text{GPa}$  (100% mould coverage) to  $46.83\text{GPa} \pm 3.81\text{GPa}$  in the longitudinal direction (50% mould coverage) ( $p < 0.05$ ). No difference in longitudinal moduli was seen between the different resin systems exhibiting flow with 50% mould coverage. However, the tensile strength shows the large variation between each of the resin systems. The toughened resin systems continue to show the greatest tensile strength in the longitudinal direction. This also

indicates that this exhibited the greatest degree of fibre alignment producing the greatest ratio between longitudinal and transverse tensile modulus and strength, shown in **Table 4.6**.

**Table 4.5.** Tensile properties of 50% mould coverage plaques in orthogonal orientations.

Resin System	Modulus (GPa)				UTS (MPa)			
	A (T-Ch)	B (T-Th)	C (N-Ch)	D (N-Th)	A (T-Ch)	B (T-Th)	C (N-Ch)	D (N-Th)
Longitudinal	46.83	44.06	46.81	46.00	408.29	329.72	226.20	232.59
St. Dev	3.81	5.30	6.63	6.55	40.46	54.04	44.11	68.45
CoV (%)	8.13%	12.04%	14.17%	14.23%	9.91%	16.39%	19.50%	29.43%
Transverse	23.53	27.08	27.37	32.13	177.77	222.71	137.69	146.77
St. Dev	2.45	4.64	5.28	4.92	31.23	47.24	47.53	25.47
CoV (%)	10.41%	17.13%	19.30%	15.32%	17.57%	21.21%	34.52%	17.35%

The B-staging characteristics of resin A (T-Ch) achieve a more optimal in-mould viscosity for carrying the fibres during flow, preventing fibre-matrix separation. This is evident by the lowest variability between each of the resin systems of the tensile modulus and strength results macroscale within the plaque (<10%). Additionally, to further establish the fibre carrying capabilities of each of the resin systems, the fibre volume fraction,  $V_f$ , was measured at 24 locations within each plaque to study the distribution of the fibre content. Initial observations during compression moulding showed that the quantity of resin flash that escaped from the mould was significantly greater when using the non-toughened resins C (N-Ch) and D (N-Th), than for the toughened resin, resins A (T-Ch) and B (T-Th). This suggests that the in-mould viscosity reduced further in the non-toughened resin at 130°C than in the toughened resin. This increased resin flow therefore reduced the overall quantity of the resin that remained within the mould cavity. Therefore, the average fibre volume fraction over the entire plaques using resin systems C (N-Ch) and D (N-Th) were greater than plaques produced using the toughened resin systems. This is reflected in the  $V_f$  values presented in **Table 4.7**, which shows that although the DFC plaques were manufactured with the same parameters, those produced with resins C (N-Ch) and D (N-Th) had higher fibre volume fractions 56.8% and 56.4%, respectively, compared to the fibre volume fractions for plaques A (T-Ch) and B (T-Th), 44.9% and 47.2%, respectively.

**Table 4.6.** Ratios of longitudinal tensile modulus and strength to the transverse properties

		Longitudinal/Transverse Ratio	
		Modulus	Strength
Resin system	A (T-Ch)	1.99	2.30
	B (T-Th)	1.63	1.48
	C (N-Ch)	1.71	1.64
	D (N-Th)	1.43	1.58

**Table 4.7.** Summary of plaque fibre volume fraction determined over the 24 density measurements performed for each plaque produced with 50% mould coverage

Plaque	Toughened resin	Average Vf (%)	St. Dev	CoV	Vf Range (%)
A (T-Ch)	Yes	44.92%	2.11%	4.70%	8.27%
B (T-Th)	Yes	47.21%	6.40%	13.55%	25.08%
C (N-Ch)	No	56.81%	9.21%	16.22%	36.17%
D (N-Th)	No	56.44%	6.19%	10.97%	25.13%

In addition to the average global fibre volume fraction, the distribution was visualised by plotting the fibre volume fractions with respect to sample distance from the left side of the mould, which represents the flow distance. **Fig. 4.6** shows that resin system A (T-Ch) had very little variability over the length of the flow distance. This also results in the lowest coefficient of variation of average fibre volume fraction for each resin system and the smallest range between the maximum and minimum fibre volume fraction values obtained, **Table 4.7**. The other resin systems, especially those that use the untoughened resin systems (C and D) with a lower in-mould viscosity experienced a high level of variability. This was a result of the matrix flowing at a faster rate, independent of the fibre bundles that flow slower. This is known as fibre-matrix separation and is caused by the resin viscosity dropping too low when the temperature is elevated by the heated compression mould tool. This could be avoided by reducing the moulding temperature, however this would consequently increase the cycle time.

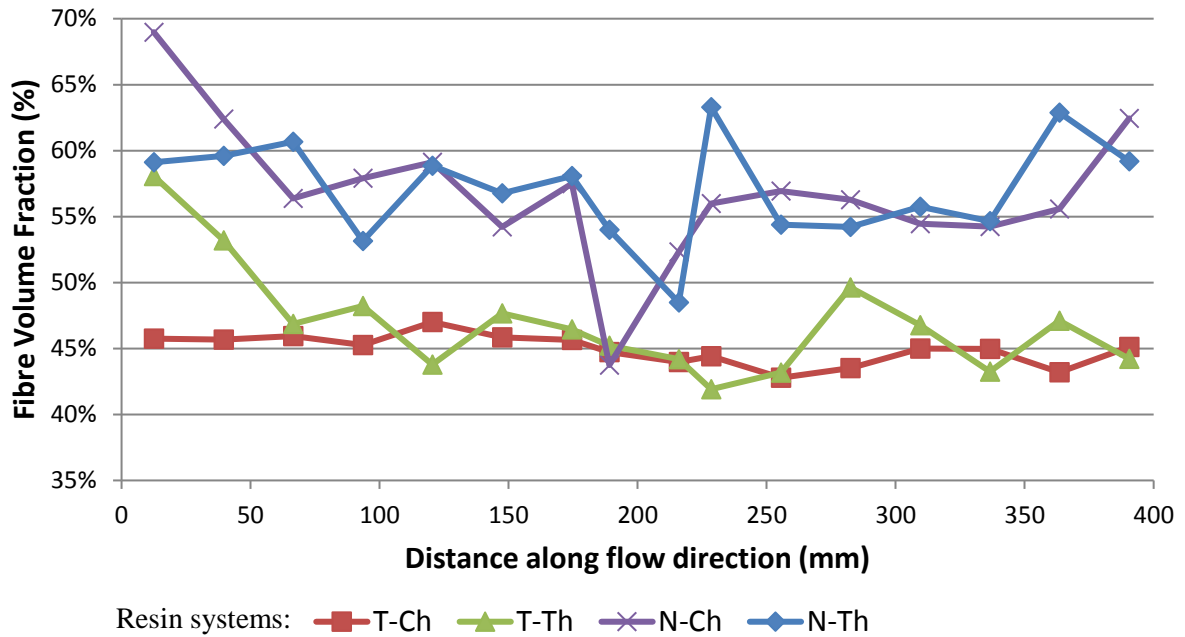


**Figure 4.6.** Fibre volume fractions measured by density measurements of samples taken along the length of the flow direction of the plaques produced from 50% mould coverage

#### 4.4.2 Effect of fibre roving

It was expected from the literature that the smaller tow size exhibits smaller stress concentrations within the resin regions that form at the end of each fibre bundle [10, 21, 75]. However, fibre roving with a lower filament count are significantly more expensive than larger industrial grade tows. For example, 12K tows are estimated to be approximately \$16/lb, however 3K and 1K are estimated to be 125% and 900% greater than this, respectively [166]. Therefore, it is desirable to use the greatest tow size available without significant performance degradation.

It is seen in **Fig. 4.7** that the tensile properties of the 12K roving have no statistical difference to the 3K bundles. These fibres however are less than 50% of the cost and can be deposited at four times the rate than 3K fibres. The similar performance to 3K tows is achieved by the 12K roving. This is because a large degree of fragmentation induced by the chopping was observed for the 12K fibres that wasn't apparent for 24K. This reduced the actual size of the fragmented fibre bundles once chopped relative to the tow size of the roving fed into the chopper. However, increasing the tow size further

to 24K was the cause of a large decrease in tensile strength as a result of the large stress concentrations that form at the end of the large fibre bundles. These large stress concentrations are therefore frequently effected by the stress concentrations that form around neighbouring fibre bundles producing a plane of weakness.

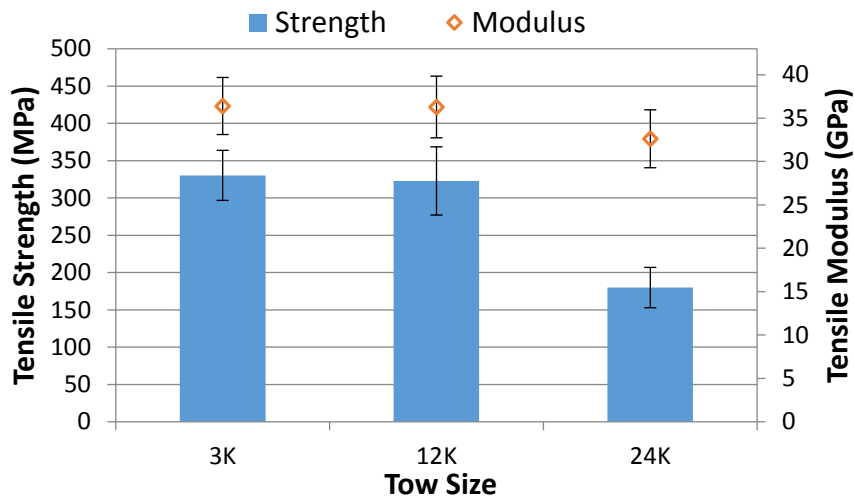


*Figure 4.7. Tensile strength and modulus of three types carbon fibre roving*

#### 4.4.3 Demoulding temperature

Compression moulding is typically an isothermal process, therefore the component is hot demoulded at the end of the cure cycle. The glass transition temperature,  $T_g$ , determines whether the part can be successfully removed from the tool without inducing warpage or other defects. *Fig. 4.8* shows the measured heat flows for the 4 candidate resin systems during the dynamic stage of the DSC program, following the 130°C isothermal cure for 4 hours. The glass transition temperatures have been indicated for each resin system.

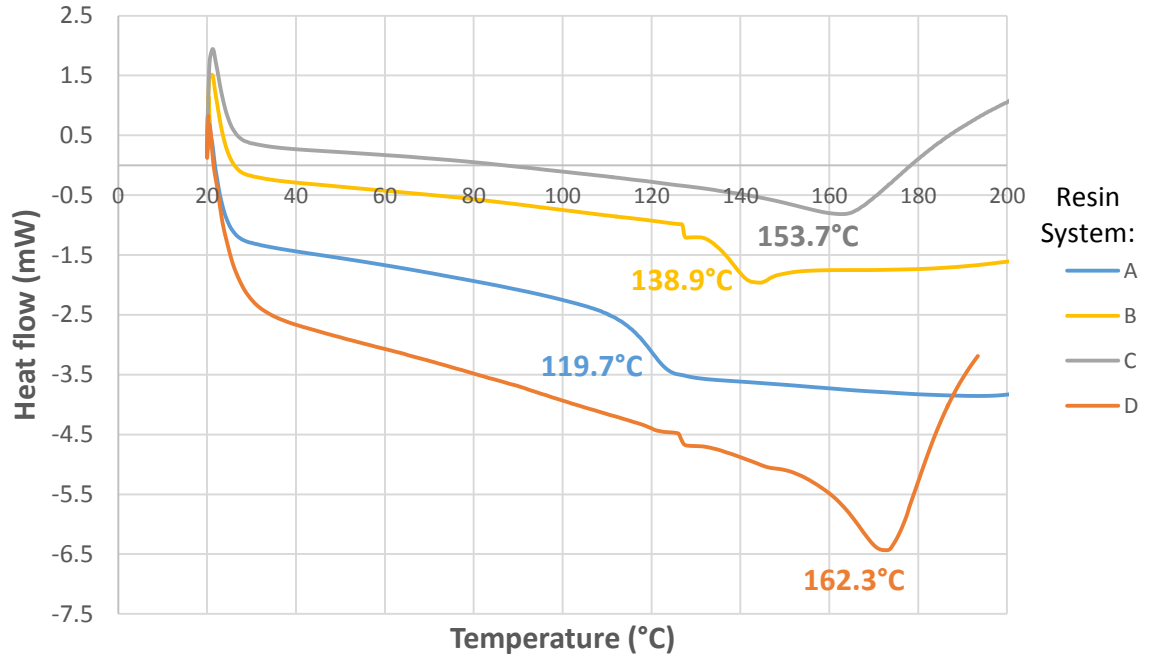


**Figure 4.8.** Heat flow measured by DSC for each resin system formulation for determining the glass transition temperature

The toughened resin system, systems A and B, show a lower T<sub>g</sub> than the non-toughened resin system, resins C and D. The values of the toughened resins are similar to those stated in the datasheets, however the non-toughened resin had no available datasheet. It is also shown that for both resin systems B-staging them using the thermally activated hardener, resins B and D, achieve greater glass transition temperatures than their comparative chemically B-staged systems, resins A and C respectively.

For the production of 2D panels, demoulding can be achieved with little stresses being induced by demoulding above the T<sub>g</sub>. However, for more complex structures, the thermal expansion and demoulding stresses must be considered to prevent warpage when demoulding above the T<sub>g</sub>. It is possible however adjust the quantities of hardener and accelerator to reduce the cycle time [151]. However, this was beyond the scope of lab scale production and requires further developments to improve to the mixing capabilities of the liquid resin spray system to account for the reduction in resin work life.

## 4.5 Summary

The fibre and resin system that were selected in this chapter are used throughout the duration of remainder of this thesis. The chosen carbon fibre roving was the Toray 700 50C with a tow size of 12K. This was shown to exhibit a tensile strength 80% higher than an equivalent 24K material, but costs were less than 50% than the smaller 3K tow size. 12K carbon fibre was also capable of production times four times faster than the 3K tow size. The 1% epoxy sizing was also on the lower limit that allowed chopping of the fibres at a rate that was limited by the mechanical performance of the chopping blades and the chopper assembly. This sizing level enabled fragmentation of the carbon fibre bundles to be induced by the chopper at the tested bundle length, 25mm. This fragmentation increases the distribution of the tow sizes, <12K. This reduction in bundle filament count reduces the size of the resin regions that form at the ends of the fibre bundles as a result of the reduction in the cross-sectional area of each bundle. During in-plane mechanical testing this effectively reduces the size of the localised stress concentrations that form at the ends of each fibre bundle. Collectively, this enhances the global in-plane properties of the plaques produced compared to using larger tow sizes. This enhanced the mechanical properties of plaques produced by 12K fibres, to achieve properties equivalent to using a 3K fibre.

The selected resin for the remainder of this thesis was the toughened resin system using chemical B-staging, Resin System A: Resin XU3508, Aradur 1571, Accelerator 1573 and Hardener XB3403. This resin offers the greatest mechanical performance to demonstrate the potential of the DFC manufacturing process. These tensile modulus and strength, 42.6GPa and 337MPa respectively, are greater than 38GPa and 300MPa, respectively, for HexMC [11]. It is also predicted that the cost of approximately material cost £16.50 (€19) per kg of DFC (based on 50% Vf, €22 per kg euros roving cost and £12 (€13.70) per kg supplier cost for resin) is significantly cheaper than the cost to produce and chop UD preregs. The larger chemical B-staging time, 24 hours, is suitable for the lab scale DFC arrangement whereas this would be depending on storage space and design for higher production volumes in industry. However, as compounds can be stored for >4 weeks at ambient temperature as a result of the long shelf life of the resin [151]. However, directing the tows directly into a mould geometry enables online manufacturing of the compound suitable for “Just-in-time”

manufacturing. This negates storage of large material volumes requirements, risk of exothermic reaction and refrigeration costs that would result.

This tensile strength of this resin system was 29% greater than the untoughened resin using the same chemical B-staging hardener and 6% greater than the same toughened resin using the thermally activated B-staging hardener. One-dimensional flow showed that this resin system also exhibited the greatest degree of flow induced alignment allowing the mechanical properties to be enhanced in the flow direction with the least variability in the fibre volume fraction across the flow distance. This suggests that the in-mould viscosity does not reduce too low that the fibre and matrix separate during flow, and not too high that the flow distance is restricted to short distances.

This chapter has also successfully produced a model for the cure cycle of this resin and fitted with the experimental data. For lab-scale DFC production, a 30 minute cure cycle at 130°C will be used. Without using automation techniques to consistently achieve a constant time between the compound placement and mould closure, a cure time was selected that was long enough to prevent premature cure from occurring before mould closure was completed and the pressure was applied. It was possible to reduce the cure time to less than 10 minutes by elevating the mould temperature to greater than 150°C. However, this temperature is significantly greater than the glass transition temperature of the selected resin, ~120°C, and would therefore require cooling to avoid warping the composite during demoulding. This is avoided by either using a resin system with a higher glass transition temperature or by increasing the accelerator content to reduce the cure time at lower moulding temperatures. The datasheets state that the gelation time would reduce as the accelerator content is increased [151]. However, this has not been investigated by this study because the reduction in gelation time increases the risk of blockage within the heated resin hoses between the LRS pump and chopper assembly on the robot.

# 5. One-dimensional flow characterisation

## 5.1 Introduction

An important requirement of any moulding compound is its ability to flow during compression moulding. The flow characteristics of typical industrial grade carbon fibre moulding compounds are optimised for lower tool coverage (80-100%). This is beneficial for incorporating features such as ribs and fasteners into complex geometries. Consequently, this simplifies the production process for forming complex shapes from a weighed quantity of charge, which does not require the same level of precision required during hand layup of a carbon fabric. This allows for rapid automated deposition techniques to be used for high volume production whilst obtaining the desired stiffness requirements by integrating stiffening mechanisms by its geometry, such as ribs and embossing. As a result, it is important to understand the effects that flow has on the microstructure and mechanical properties of carbon fibre moulding compounds. As discussed in *Chapter 2*, a number of commercial ASMCs have been produced using polyester or vinyl-ester matrices. However, the interfacial shear strength between carbon fibre and vinyl-ester is typically poor compared with carbon/epoxy [59, 60], limiting the mechanical performance.

This chapter investigates DFC's capability to flow with <80% mould coverage for producing low cost carbon fibre/epoxy SMCs. DFC was compared to other carbon fibre moulding compounds produced by alternative techniques. These included Press-Formed Compounds (PFC) under development at the University of Exeter, and commercial materials HexMC M77 and Menzolit Carbon SMC 1100. The mechanical properties were assessed to understand degree of flow induced alignment of the fibre bundles and to determine its repeatability. This would enable the design of a CF-SMC

component to be optimised locally to enhance the properties in a desired orientation, by controlling the charge geometry determined by the spray path, and placement to govern the flow direction and magnitude. The flow in this chapter has been restricted to one-dimension only to isolate the relevant variables and quantify them in relation to the known flow direction.

## 5.2 Objectives

The aim of this chapter is to understand the potential of DFC to flow during compression moulding and characterise their mechanical performance. The objectives were:

- To compare the tensile properties from one-dimensional flow of DFC and alternative CF-SMCs. The effect of flow induced alignment of the fibre bundles was characterised by measuring the in-plane properties.
- Integrating these tensile properties into a previously developed analytical model, detailed in *chapter 3.5*, to reverse engineer an orientation tensor to describe the fibre bundle orientation distribution from the in-plane properties.
- Investigating the effect of fibre bundle length to understand its effects on charge flow and tensile properties. This uses microscopy to observe the microstructure and void content effects of the flow and fibre lengths.
- The mould pressure was also adjusted to observe the effects on microstructure and void formation.

## 5.3 Design of experiments

### 5.3.1 DFC charge manufacturing

Each DFC charge was sprayed as a series of discrete layers, split into two orthogonal passes with a constant 50mm offset. The spray path was optimised to ensure uniform fibre distribution and to minimise any orientation bias from the chopping device [5, 19]. An initial study was conducted to understand the influence of in-mould flow on the local fibre volume fraction, to assess fibre-matrix separation. *Table 5.1 (a)* shows the DFC parameters used to produce moulding compounds with 40%, 60%, 80% and 100% mould coverages. The target fibre volume fraction, fibre length and linear robot travel

speed remained constant at 45%, 25mm and 0.2m/s respectively. The carbon fibre tow feed rate, chopping rate, resin pump speeds and number of spray layers were adjusted to produce the required target areal mass of material for each mould coverage scenario.

**Table 5.1.** DFC and moulding parameters for charge size study (a) and fibre length versus moulding pressure study (b)

(a)

Target Vf (%)	45			
Mould coverage (%)	40	60	80	100
Fibre length (mm)	25			
Robot speed (m/s)	0.2			
Feed rate*	0.94	1.00	0.94	1.00
Chopping rate*	0.94	1.00	0.94	1.00
Resin pump speed*	0.94	1.00	0.94	1.00
No. of spray layers	8	5	4	3
Charge areal mass (gsm)	6480	4320	3240	2592
Initial charge area	162mm x 405mm	243mm x 405mm	324mm x 405mm	405mm x 405mm
Mould pressures (bar)	85			
Closing speed (mm/s)	1			

\* Speeds normalised to 100% mould coverage (45% Vf, 25mm fibre length), highlighted red

(b)

Target Vf (%)	50											
Mould coverage (%)	50				75				100			
Fibre length (mm)	15	25	50	75	15	25	50	75	15	25	50	75
Robot speed (m/s)	0.15	0.2	0.2	0.2	0.15	0.2	0.2	0.2	0.15	0.2	0.2	0.2
Feed rate**	0.75	1.00	1.00	1.00	0.60	0.80	0.80	0.80	0.75	1.00	1.00	1.00
Chopping rate**	1.25	1.00	0.50	0.33	1.00	0.80	0.40	0.27	1.25	1.00	0.50	0.33
Resin pump speed**	0.75	1.00	1.00	1.00	0.60	0.80	0.80	0.80	0.75	1.00	1.00	1.00
No. of spray layers	6				5				3			
Charge areal mass (gsm)	5760				3840				2880			
Initial charge area	202.5mm x 405mm				304mm x 405mm				405mm x 405mm			
Mould pressures (bar)	20 and 85				85				20, 60 and 85			
Closing speed (mm/s)	1											

\*\* Speeds normalised to 100% mould coverage (50% Vf, 25mm fibre length), highlighted red

The DFC machine parameters used for producing plaques to study the effects of fibre length and moulding pressure are shown in **Table 5.1 (b)**. For this study, the target fibre volume fraction was constant at 50%. A range of fibre lengths were investigated (15mm, 25mm, 50mm and 75mm) for different mould coverage levels (50%, 75% and 100%). The fibre feed rate, chopping rate, resin pump speed and number of spray layers were adjusted according to the required charge size (see values in **Table 5.1 (b)**). The

chopping rate was adjusted relative to the fibre feed rate to control the fibre length. The robot speed was constant (0.2m/s) for all fibre lengths greater than 25mm, but was reduced to 0.15m/s for the 15mm fibre length due to the gear ratio in the chopping device.

### **5.3.2 Benchmark materials**

A carbon fibre sheet moulding compound developed at the University of Exeter uses the same carbon fibre and epoxy constituents as DFC, but was produced using a modified glass SMC production facility. Carbon rovings were chopped and then distributed onto a resin film, which was then squeezed through the fibres. A charge pack was cut from the sheet material before compression moulding. This was provided to show the effectiveness of the liquid resin spray used by DFC to wet-out the fibre bundles rather than pressing the fibres into a resin film. This material shall be referred to as Press-Formed Compound, PFC throughout.

A comparison was also made against two commercial CF-SMCs: HexMC M77 and Menzolit CarbonSMC 1100. HexMC M77 is a carbon fibre moulding compound that has an epoxy matrix and shall be referred to as EP-SMC. The EP-SMC is derived from UD prepreg chopped into 50mm × 8mm chips, which are deposited randomly to form a sheet compound with a fibre volume fraction of 57% [11]. It uses AS4 carbon fibres with a tensile modulus of 230 GPa and tensile strength of 4400 MPa. The epoxy resin is a snap curing resin system which can be moulded in 3 minutes at 150°C and is suitable for automotive applications. A T<sub>g</sub> of 125°C enables parts to be hot demoulded. Menzolit CarbonSMC 1100 has a vinyl-ester matrix and thickening agents, such as calcium carbonate, that typical of some glass SMCs. This shall therefore be referred as VE-SMC. It is produced by conventional glass compounding methods; using carbon fibre bundles with a tensile stiffness of 244 GPa and a tensile strength of 4068 MPa. Carbon fibres are chopped to 25mm and the matrix system has a continuous service temperature of 170°C, making it compatible with the E-coat process commonly used in the automotive industry. The fibre volume content of the VE-SMC is 40% ± 2% [17]. Although these systems are not directly comparable to DFC, they are two common systems that are already used by the automotive industry. These therefore provide a suitable benchmark for DFC.

### 5.3.3 Charge strategy

Plaques were moulded in a 405×405mm square compression mould tool with a peripheral flash gap of 0.25mm. A tool closure speed of 1 mm/s was used throughout to minimise fibre disruption around the edge of the plaques [71]. DFC plaques were moulded isothermally at 130°C for 30 minutes, followed by a 3.5 hour freestanding post cure in an oven. This moulding temperature was consistent for all DFC and commercial SMC moulds. The cure times for the EP-SMC and VE-SMC were 6 minutes and 30 minutes respectively, followed by a 3.5 hour free standing post cure. The mould pressure was 85 bar unless otherwise stated and was determined by the pressure transducer located at the centre of the mould. Hard stops were used to avoid plaques tapering under non-uniform charge placement and to maintain constant plaque thickness. Plaques were produced from the VE-SMC and DFC materials using two charge coverage levels; 50% and 100%. EP-SMC was moulded at 80% coverage according to the manufacturer's recommendation.

Mould coverage was adjusted as a percentage of the total area mould coverage and was constrained to one-dimension by placing the DFC and SMC charges on the left-hand side of the mould. This allowed flow in only one direction from left to right, as shown previously in *Fig. 4.1*. The mould coverages used for preliminary fibre investigation into degree of flow were 40%, 60%, 80% and 100%, shown in *Fig. 5.1*. These have a charge width of 162mm, 243mm, 324mm and 405mm respectively, adjusting the charge thickness to maintain a constant volume to investigate fibre-matrix separation at these mould coverages. Further experiments investigating fibre length and moulding pressure use 50%, 75% and 100% mould coverages to induce one-dimensional flow. These have a charge width of 202.5mm, 303.75mm and 405mm respectively.



**Figure 5.1.** Initial charge position and cutting plan for the 405mm x 405mm plaques. Locations for tensile coupons, density measurements and micrograph shown.

## 5.4 Results and discussion

### 5.4.1 Comparison between DFC and Carbon-SMC

A comparison of tensile properties is presented in **Fig. 5.2** and **Table 5.2** for all of the moulding compounds investigated. The red dotted line indicates the average of the longitudinal and transverse properties for the 100% coverage DFC plaque. The average tensile stiffness and strength was  $36\text{GPa} \pm 3.3\text{GPa}$  and  $320\text{MPa} \pm 27\text{MPa}$  respectively, at a moulded fibre volume fraction of 50%. This scenario has been used as a reference, as it avoids any uncertainty associated with flow induced alignment and makes future comparisons with published data more viable.

There is approximately 3% variation between the longitudinal and transverse properties for the 100% DFC material, and error bars are small ( $<10\%$ ) confirming that the material is generally homogeneous and isotropic when moulded net shape (100%

charge coverage), using the current specimen cutting plan (*Fig. 5.1*). The longitudinal properties increase for smaller charge sizes (50% charge coverage), indicating flow induced alignment. The error bars remain low however, indicating good levels of fibre dispersion during flow.

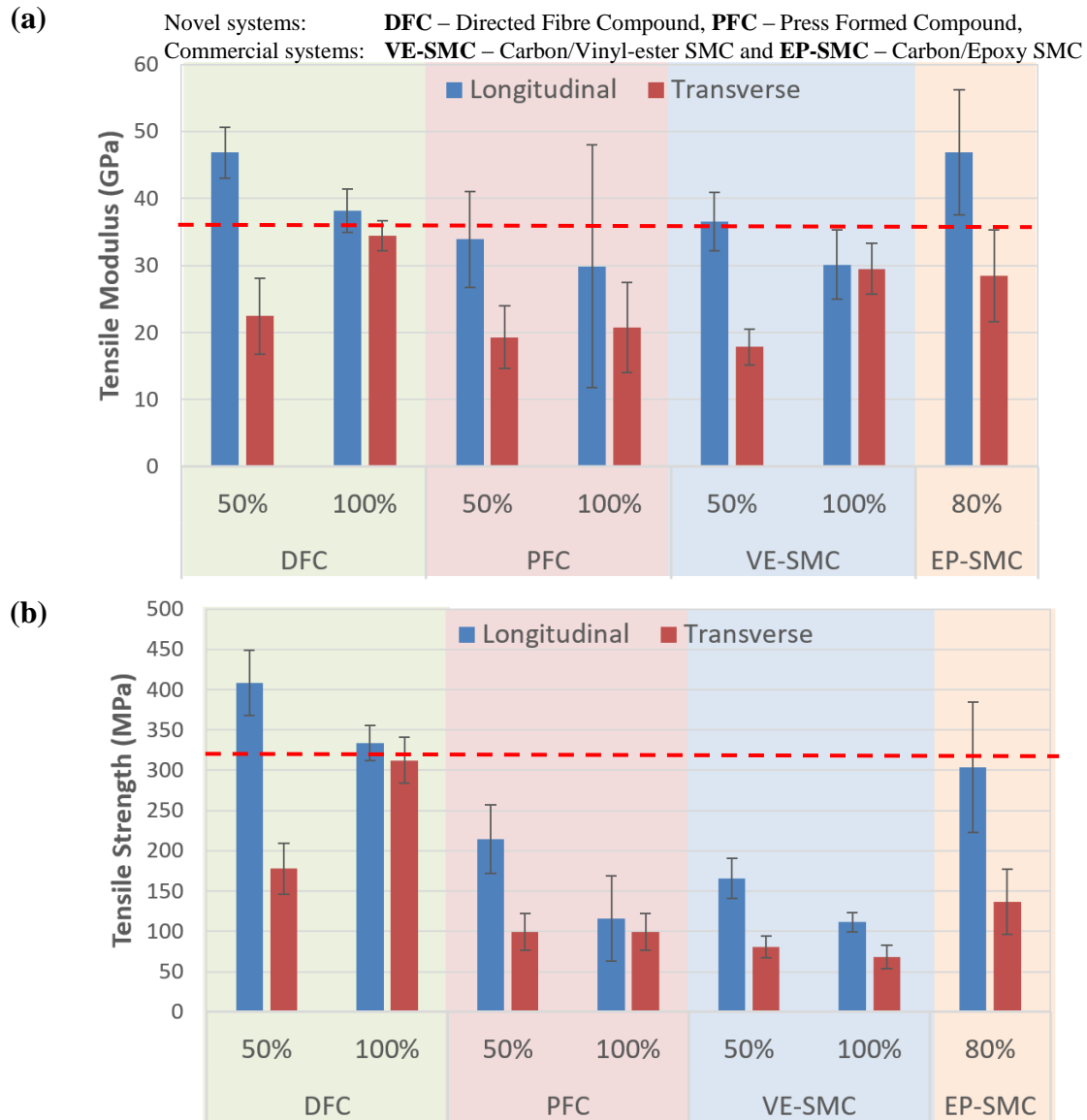


**Figure 5.2.** Tensile modulus (a) and tensile strength (b) as a function of mould coverage. All materials moulded at 85 bar. The red dotted line represents the average of the longitudinal and transverse properties of the 100% coverage DFC material.

The properties of the DFC material are competitive against the commercial systems. The tensile modulus of the 100% DFC is comparable to the prepreg derived EP-SMC material, accepting there has been some fibre alignment in the commercial material due

to the 80% initial charge. The modulus of the 100% DFC is ~20% higher than the stiffness of the 100% VE-SMC as a result of the higher fibre volume fraction (50% for DFC compared to 40% for VE-SMC) and 40-45% higher than the 100% PFC material. There is slight overlap between the error bars of the moduli of DFC (100% mould coverage) and the VE-SMC (100% mould coverage) as a result of their heterogeneity created by their discontinuous nature of the materials. However, the high number of repeats (12 in each orientation), results in statistical agreement that the difference in moduli is significant ( $p < 0.001$ ). Furthermore, the strength of DFC (100% mould coverage) is significantly higher than the PFC and VE-SMC materials. The strength of DFC (100% mould coverage) is similar to the longitudinal strength of EP-SMC (80% mould coverage) however the transverse strength of the DFC is 128% greater than that of EP-SMC. For 100% charge coverage, the average ultimate strength for the VE-SMC material is  $90\text{MPa} \pm 25\text{MPa}$ , 72% lower than DFC ( $323\text{MPa} \pm 27\text{MPa}$ ). This can be attributed to the lower fibre strength ( $4068\text{MPa}$ ) for the VE-SMC compared to the DFC ( $4900\text{MPa}$ ) and the poor interfacial bonding between the vinyl-ester matrix and the carbon fibre. However, although the constituents of PFC are the same as those used for DFC, pressing the chopped fibres into a resin film failed to fully wet-out the fibre bundles. PFC therefore has reductions of 67% and 30% for tensile strength and stiffness respectively compared to DFC.

**Table 5.2.** Tensile modulus and strength as a function of mould coverage for all materials moulded at 85 bar. Results are given in terms of the tested orientation.

Mould Coverage:		DFC		PFC		VE-SMC		EP-SMC
		50%	100%	50%	100%	50%	100%	80%
Longitudinal	Modulus (GPa)	46.83	38.18	33.89	29.88	36.60	30.14	46.85
	St. dev (GPa)	3.81	3.24	7.12	18.07	4.35	5.14	9.32
	CoV (%)	8.13%	8.50%	21.01%	60.47%	11.88%	17.05%	19.89%
	Strength (MPa)	408.29	333.42	214.47	115.98	165.84	111.37	303.50
	St. dev (MPa)	40.47	21.76	42.84	53.05	25.32	12.41	80.56
	CoV (%)	9.91%	6.52%	19.97%	45.74%	15.27%	11.14%	26.54%
Transverse	Modulus (GPa)	22.48	34.41	19.30	20.78	17.85	29.48	28.53
	St. dev (GPa)	5.64	2.25	4.65	6.76	2.64	3.79	6.84
	CoV (%)	25.09%	6.53%	24.07%	32.56%	14.76%	12.86%	23.98%
	Strength (MPa)	177.77	312.29	99.11	99.11	80.84	68.62	136.65
	St. dev (MPa)	31.23	28.54	22.84	22.84	13.54	14.34	40.53
	CoV (%)	17.57%	9.14%	23.05%	23.05%	16.75%	20.90%	29.66%

The *orientation ratio* between the longitudinal and transverse strength ( $\sigma_1/\sigma_2$ ) and stiffness ( $E_1/E_2$ ) were calculated and are shown in **Fig 5.3**. This demonstrates the degree of flow induced alignment reflected in the in-plane mechanical properties. When DFC is moulded with 100% mould coverage, it shows similar performance irrespective of orientation. This is indicated by a strength and stiffness orientation ratio near to 1. When it is moulded with 50% mould coverage, these properties are enhanced in the longitudinal direction whilst reducing in the transverse direction. This achieves strength and stiffness performance in the flow direction that is more than twice as high as in the transverse direction. This can be observed in each of the moulding compounds tested, except for EP-SMC where there was insufficient material available to test multiple mould coverages.

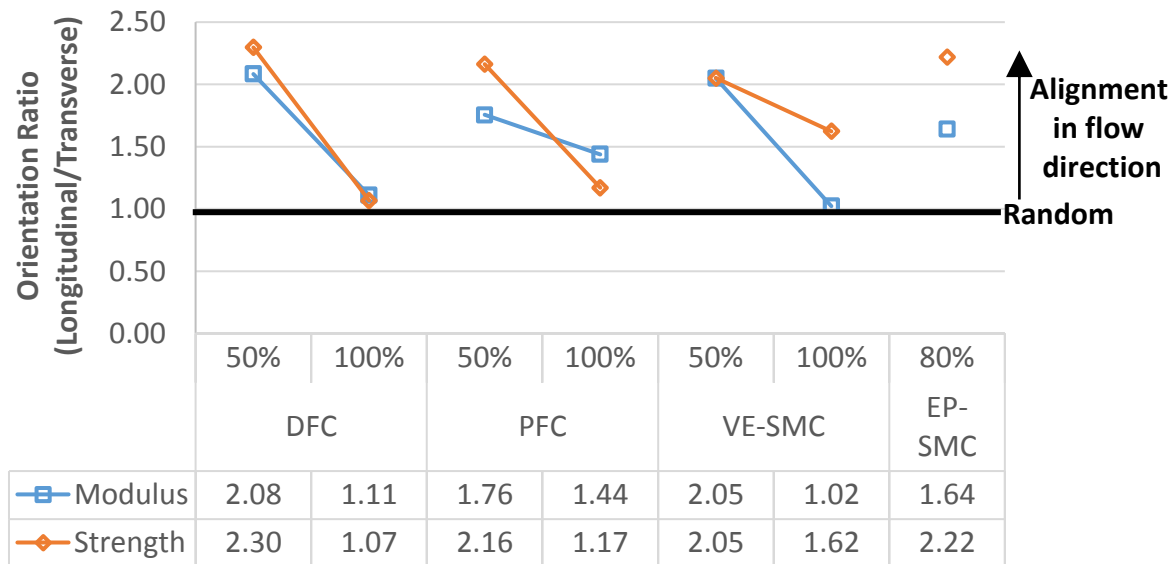


**Figure 5.3.** Ratios between longitudinal and transverse tensile strength ( $\sigma_1/\sigma_2$ ) and stiffness ( $E_1/E_2$ ) for all materials moulded at 85 bar.

The PFC however experiences greater orientation ratio values with 100% mould coverage. This suggests that there is an orientation bias as a result of the hand deposition of the carbon fibre bundles, as opposed to the automated technique used for the production of DFC. **Table 5.3** provides a combined average of the longitudinal and transverse tensile results and assumes that all moulding compounds are isotropic when moulded with 100% mould coverage. These values support the ratios in **Fig. 5.3**. DFC shows the lowest coefficient of variation (CoV) in the combined average of strength and stiffness, <10%. This suggests DFC is both the most repeatable of the tested

moulding compounds and has the least biased orientation distribution as a result of the multidirectional material deposition paths. PFC has the greatest CoV, >40%, supporting the conclusion that this has the greatest orientation bias. VE-SMC has both a low CoV, 14.86%, and a ratio close to 1 for the modulus. This indicates that the fibre orientation distribution is random. However, the elevated ratio for strength, 1.62, and increase in CoV, 28.30% suggests that the filler material was not evenly distributed throughout the compound and reduces its repeatability.

**Table 5.3.** Tensile modulus and strength for DFC, PFC and VE-SMC moulded at 85 bar and 100% mould coverage. Results are averaged assuming fibre orientation distribution is perfectly random generating planar-isotropy. These results are also compared to the datasheet values of the EP-SMC[11].

	DFC	PFC	VE-SMC	EP-SMC*
Modulus (GPa)	36.29	25.33	29.81	38
St. dev (GPa)	3.34	14.26	4.43	-
CoV (%)	9.20%	56.30%	14.86%	-
Strength (MPa)	322.86	115.51	89.99	300
St. dev (MPa)	27.06	48.26	25.47	-
CoV (%)	8.38%	41.78%	28.30%	-

\* EP-SMC values obtained from datasheet [11]

Fracture sites for each material have been captured in **Fig. 5.4**. The fracture site for the 100% DFC coupons is relatively straight and perpendicular to the applied tensile load, **Fig. 5.4 (a)**, indicating a fibre-dominated failure. This is because there is a strong fibre-matrix interface. This was observed for both longitudinal and transverse coupons, due to the high level of isotropy. Flow induced alignment in the 50% DFC coupons resulted in a combination of interface and fibre-dominated failures, depending on the orientation of the specimen relative to the flow direction. Cracks at the interface propagated along the length of bundles at a lower stress than required to break the fibres, resulting in a matrix-dominated failure for specimen's transverse to the flow direction, **Fig. 5.4 (b)**. However, fibre-dominated failure was experienced when the load was applied in the flow direction, longitudinal.

**Fig. 5.4 (c)** shows intact fibre bundles at the failure site for PFC, indicating that cracks propagated around the fibre bundles. This was evident across all PFC specimens and

suggests that failure was matrix dominated as a result of its poor fibre wet-out. Similar failures were also observed for VE-SMC, *Fig. 5.4 (d)*. This can be attributed to the poor interfacial bonding between the vinyl-ester matrix and carbon fibre.

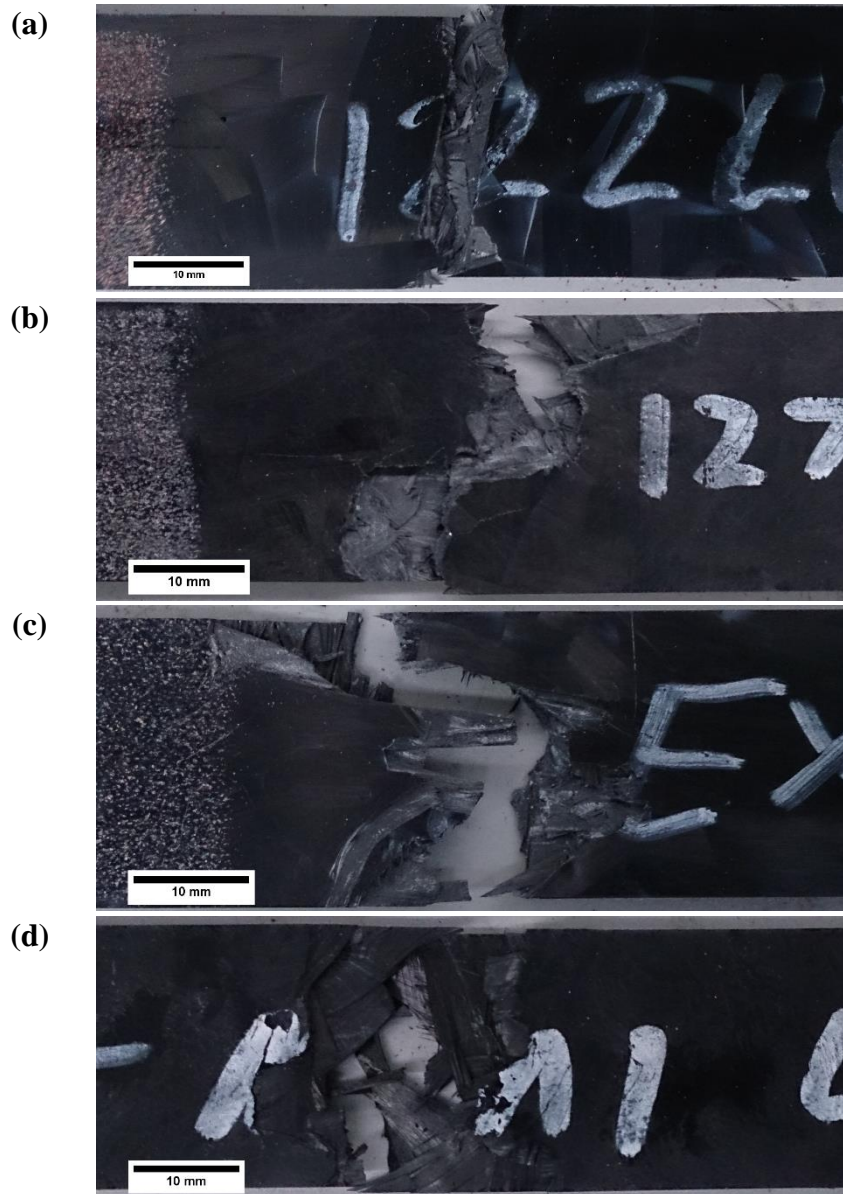


**Figure 5.4.** Typical failure mechanisms experienced during tensile failure of longitudinal specimens of (a) net-shape DFC, (b) 50% mould coverage DFC, (c) net-shape PFC and (d) net-shape VE-SMC.

## 5.4.2 Degree of flow

There is a limit to the distance that compounds can flow during moulding before fibre-matrix separation occurs, as fibre agglomerations and entanglements prevent the matrix from carrying the fibres. The local fibre volume fraction variation has been measured across the width of each plaque in the flow direction. In general, **Fig. 5.5** indicates that the fibre volume fraction varies by approximately  $\pm 5\%$  across all plaques tested, including plaques with initial charge coverage as low as 40%. There is therefore no evidence of major fibre-matrix separation for the plaques tested.

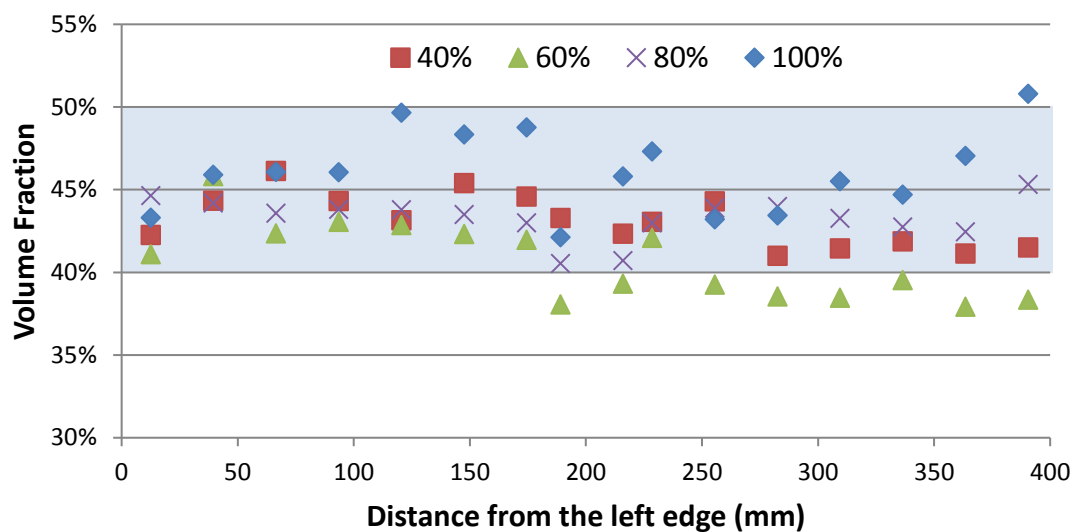


**Figure 5.5.** Fibre volume fraction measurements at positions from the left plaque edge ( $x = 0\text{mm}$ ), to the right edge ( $x = 400\text{mm}$ ) for different percentage mould coverages. Initial charge placement was on the left and flowed in one dimension to the right.

In-mould flow of the DFC moulding compound causes the discontinuous fibre bundles to rotate and align in the flow direction. This causes a disparity in mechanical properties between the longitudinal (parallel to flow direction) and transverse (perpendicular to flow) directions. The level of flow is dependent on the initial size and shape of the DFC charge and therefore the mechanical properties can be tailored to some extent by encouraging charge flow, as shown in **Fig. 5.6**. There is a clear linear trend between tensile stiffness and initial mould coverage, for both the longitudinal and transverse coupon directions. At 100% mould coverage, the material can generally be considered

to be isotropic, with an average Young's modulus value of 34.3GPa for a fibre volume fraction of 45%. As the mould coverage is reduced to 40%, the longitudinal stiffness increases to 42.0GPa  $\pm$  3.3GPa and the transverse stiffness reduces to 21.8GPa  $\pm$  2.8GPa. There is no measurable increase in coefficient of variation in tensile modulus, indicating a homogeneous distribution of fibre across the plaque.

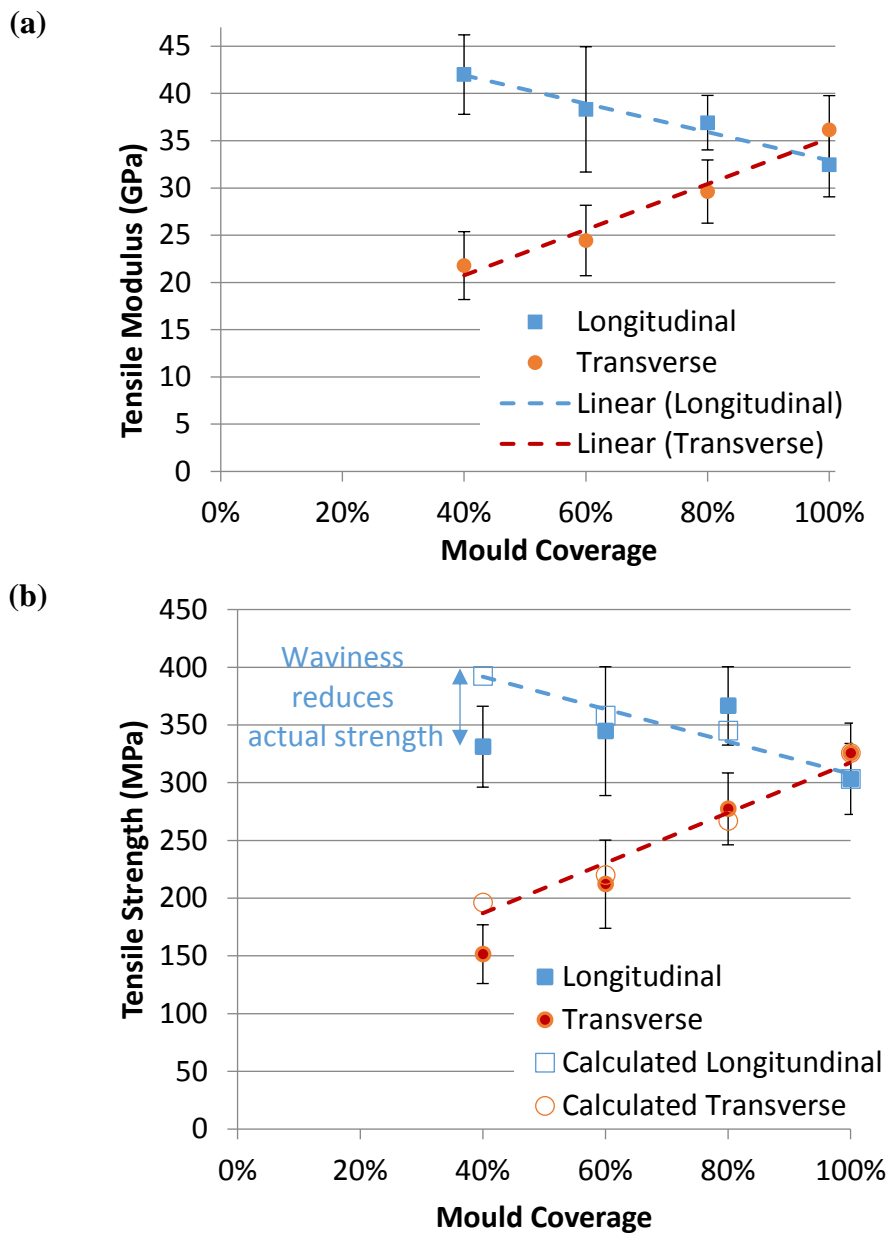


**Figure 5.6.** (a) Tensile modulus and (b) strength of DFC plaques (25mm fibre length, 45% Vf)

The tensile strength, *Fig. 5.6 (b)*, exhibits a similar general trend, increasing longitudinally and decreasing transversely as the mould coverage decreases. The calculated values have been determined from the strengths for the 100% mould coverage, assuming the same percentage changes for the smaller charges as observed for the stiffness. The calculated values are within the experimental standard deviation values for all data points except the 40% coverage plaque. The strengths for the low coverage plaque (40%) were lower than expected, which can be attributed to an increase in out-of-plane fibre waviness with increased flow. Waviness was mostly observed in the boundary regions of the plaque, approximately one fibre length (25mm) from the edge, as shown in *Fig. 5.7*. However, further analysis of the data showed no clear trend between the position of the test coupon (*Fig. 5.1*) and the failure strengths recorded, as the ends of the specimens taken from the plaque edge were located in the jaws of the testing apparatus rather than the gauge section. The highest degree of waviness can be observed in the 40% mould coverage specimens, *Fig. 5.7 (a)*, which tends to decrease as the level of in-mould flow decreases. The fibre bundles in the 100% mould coverage plaque are relatively planar, *Fig. 5.7 (d)*. These micrographs also confirm that the filaments remain in bundle form during flow and there are no matrix rich regions caused by fibre-matrix separation.

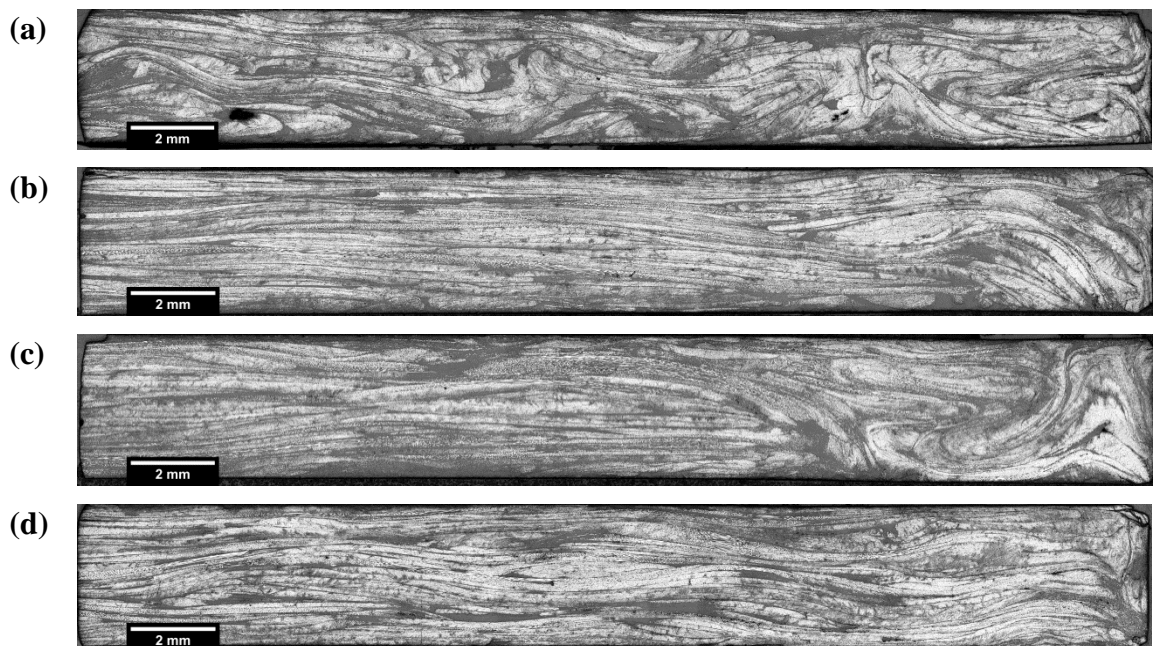


*Figure 5.7. Micrographs (5x magnification) of the right-hand edge, end of flow, for (a) 40%, (b) 60%, (c) 80% and (d) 100% mould coverages. All images are parallel to the flow direction*

### 5.4.2.1 Orientation tensors

The influence of charge size, and hence increasing levels of flow, has been studied analytically, using the Qiu and Weng inclusion model [157] and an orientation averaging approach [158] to predict the in-plane elastic constants. **Fig. 5.8** shows the influence of changing values for the in-plane shape parameter,  $\beta$ , and out-of-plane shape parameter,  $b$ , on the longitudinal ( $E_{11}$ ) and transverse ( $E_{22}$ ) moduli. These parameters control the shape orientation distributions in each plane, if  $\beta$  or  $b$  tend to 0 this implies the fibres are aligned in the 1 or 3 directions, respectively. As  $\beta$  and  $b$  increase, the two in-plane moduli converge, as the fibre distribution tends towards being random in the 1-2 plane. The solid data points represent the experimental values and the percentages indicate the initial charge coverage values. Different values of  $b$  indicate changes in the out-of-plane orientation distribution. It is clear that each experimental data point corresponds with a different  $b$  value curve, indicating that the level of out-of-plane waviness changes in the experimental values, due to the reduction in charge size.

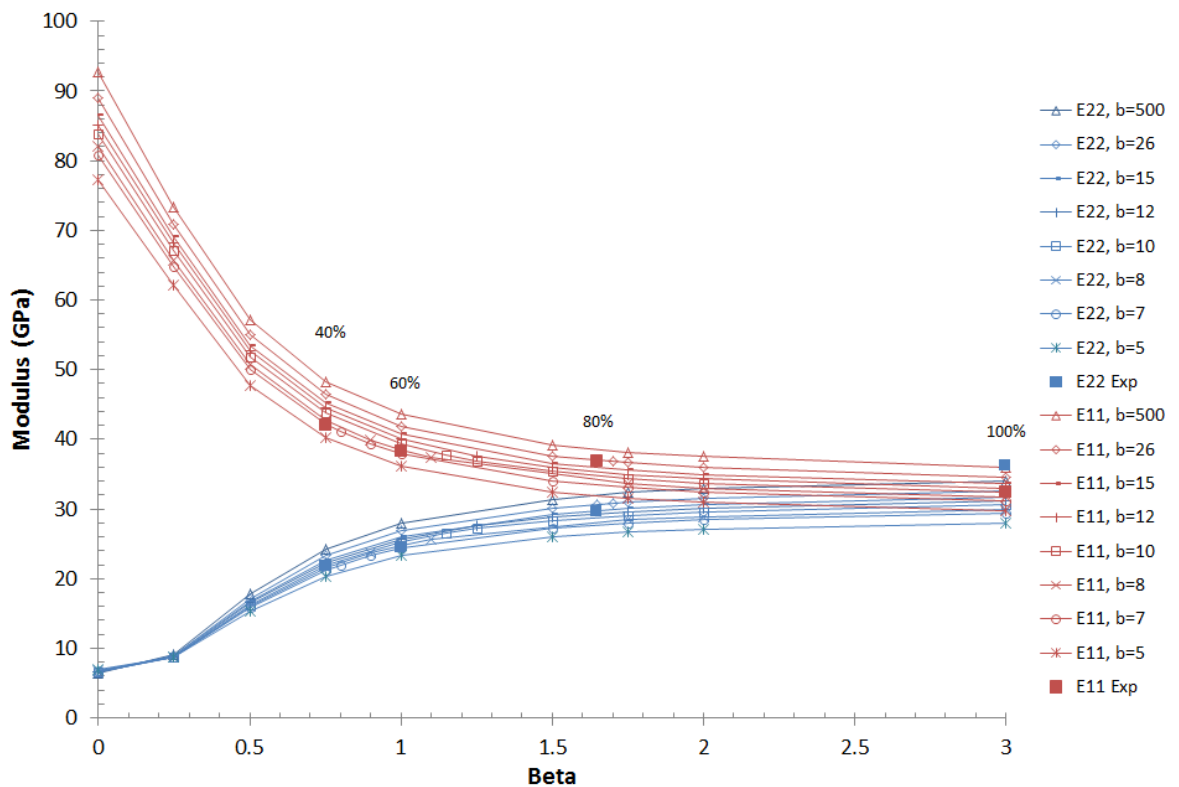


**Figure 5.8.** Effect of  $\beta$  on the tensile modulus for a range of  $b$  values. Percentage values indicate the level of charge coverage

This can be seen more clearly from **Table 5.4**, which summarises the tensor components required to yield equivalent tensile stiffnesses to the experimental values. Both the  $a_{33}$  and  $a_{3333}$  components increase as the charge size decreases, indicating greater levels of out-of-plane fibres. This observation corresponds with the micrographs shown in **Fig. 5.7**, which confirm that the fibres become wavy as the flow distance increases.

**Table 5.4.** Summary of tensor components for DFC plaques with decreasing initial charge coverage. Corresponding stiffnesses are presented from the Qiu and Weng model and compared against the experimental values. Tensors for 2D random and 2D UD are included for reference.

	2D Random	100%	80%	60%	40%	2D UD
$\beta$	100000	3	1.65	1	0.75	1E-07
$b$	500	500	26	8	7	500
$a_{1111}$	0.375	0.323	0.404	0.430	0.476	1.000
$a_{2222}$	0.375	0.404	0.323	0.252	0.205	0.000
$a_{3333}$	0.000	0.000	0.001	0.009	0.012	0.000
$a_{1122}$	0.125	0.124	0.118	0.105	0.099	0.000
$a_{1212}$	0.125	0.124	0.118	0.105	0.099	0.000
$a_{1133}$	0.000	0.000	0.010	0.030	0.036	0.000
$a_{2233}$	0.000	0.000	0.008	0.020	0.019	0.000
$a_{1313}$	0.000	0.000	0.010	0.030	0.036	0.000
$a_{2323}$	0.000	0.000	0.008	0.020	0.019	0.000
$a_{11}$	0.500	0.449	0.532	0.565	0.610	1.000
$a_{22}$	0.500	0.532	0.449	0.376	0.323	0.000
$a_{33}$	0.000	0.000	0.019	0.059	0.067	0.000
$E_{11}$ (GPa)	34.92	33.94	36.99	38.50	42.14	92.70
$E_{22}$ (GPa)	34.92	36.06	30.70	24.71	21.22	6.47
$G_{12}$ (GPa)	13.10	13.02	12.47	11.36	10.83	2.32
$\nu_{12}$	0.33	0.32	0.28	0.22	0.18	0.02
Experimental $E_{11}$ (GPa)		32.45	36.91	38.32	42.00	
Experimental $E_{22}$ (GPa)		36.16	29.62	24.44	21.79	
Error $E_{11}$		4.40%	0.23%	0.48%	0.34%	
Error $E_{22}$		-0.28%	3.52%	1.09%	-2.67%	

The tensor components for the 100% random case indicate that there may have been some preferential alignment during the fibre deposition phase, as  $a_{11}$  and  $a_{22}$  are different (yielding different values for  $E_{11}$  and  $E_{22}$ ).  $E_{22}$  is larger than  $E_{11}$  for the 100% coverage case, where the 1-direction was the expected flow direction ( $E_{22} = 36.06$  GPa,  $E_{11} = 33.94$  GPa). The tensor components for this case were established using the  $E_{22}$  value, which is why the error between the experimental  $E_{11}$  value and the analytical prediction is higher than that for  $E_{22}$ .

#### 5.4.2.2 In-mould pressure with flow

The in-mould pressure during the compression moulding cure cycle was also monitored for each flow condition. A reduction of the in-mould pressure can be expected during the moulding cycle due to resin cure shrinkage. Using a pressure transducer positioned at the centre of the mould, the magnitude of the pressure reduction during cure increased where compounds experienced large degrees of flow, **Fig. 5.9**. It was discussed in *chapter 3* that the pressure transducer displays a  $\pm 5$ bar fluctuation after logging the first 15 minutes of data. However, the differences in pressure drop-off experienced for each mould coverage were significant enough to remain uninfluenced by this fluctuation. For 100%, 80%, 60% and 40% mould coverages, the pressure reduction in 30 minutes was approximately 59%, 66%, 76% and 100%, respectively. This is a consequence of increasing the fibre orientation imbalance, by decreasing mould coverage, influencing the level of mould shrinkage in the principle direction [167]. In addition, the orientations of the resin macromolecules are also reoriented as a result of partial curing during flow. Local variations in the direction of shrinkage then further imbalance the residual stresses may result in warpage [168].

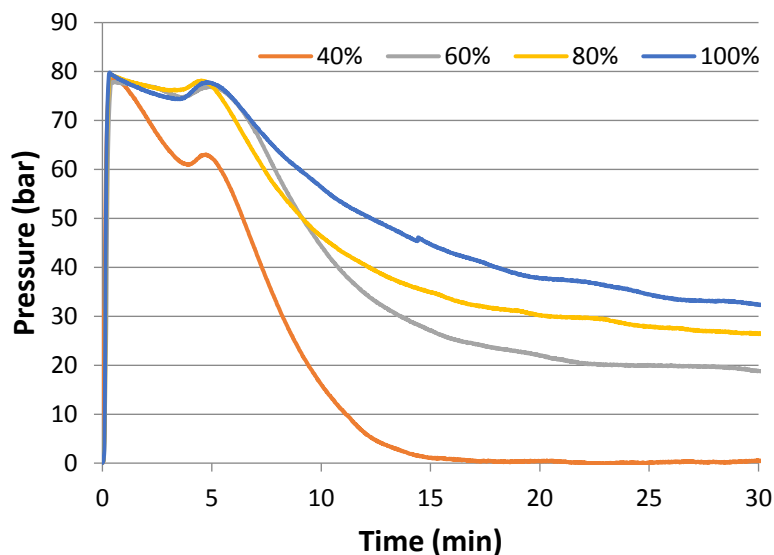


**Figure 5.9.** In-mould pressure profile over the duration of the 30-minute cure cycle for different mould coverages

### 5.4.3 Effect of fibre length

DFC plaques with fibre lengths ranging from 15mm to 75mm were manufactured at a fibre volume fraction of 50%, using 100% charge coverage. It is difficult to establish a trend between the tensile properties and increasing fibre length due to the high coefficient of variation. *Fig. 5.10* indicates that 25mm is the optimum fibre length for 100% mould coverage, yielding the highest tensile stiffness and strength. However, all other data points are within one standard deviation, so the statistical significance of this trend is low. There is however, an increase in the coefficient of variation as the fibre length increases. This can be attributed to size effects [169], as a constant width test coupon was used for all fibre lengths according to ISO 527-4: 1997. Other studies in the literature have shown that increasing the specimen width relative to the fibre length would increase the tensile modulus but decrease the tensile strength [10, 170]; since the tensile modulus is a volume averaged property whereas the strength is dominated by critical flaws. The probability of a critical flaw increases as the volume of the coupon increases, hence the ultimate strength is lower for larger coupons.

The effect of fibre length becomes more pronounced as the charge coverage decreases and the level of flow increases. *Fig. 5.10* indicates that the ratio between longitudinal and transverse properties generally increases as the fibre length decreases for smaller mould coverages. Shorter fibres are more susceptible to flow induced alignment than longer (75mm) fibres, particularly for smaller initial charges (50% compared with 100%). This has been previously discussed in terms of the Reynolds number [171], a measure of the inertial forces in the fluid, which is proportional to the fibre length. Long fibres cease to rotate when the Reynolds number is above a critical value and instead drift monotonically towards the shearing plane. However, compounds manufactured using 15mm long fibres did not flow as expected, as large dry patches formed. Chopping fibre bundles shorter increased the level of natural bundle fragmentation, as shown in *Fig. 5.11*, effectively reducing the filament count per fibre bundle [19]. This consequently increased the loft (bulk factor) of the compound, increasing the compression forces required to close the mould tool [44] and reducing the permeability of the fibre architecture [49]. The number of fibre-fibre interactions also increases with shorter fibre lengths, increasing the frictional forces between the fibres, causing fibre bundle agglomeration and preventing fibre flow [67]. This can also result in large void

formations of net shaped compounds because of the large fibre volume fraction regions restricting fibre packing under compaction, *Fig. 5.12*.

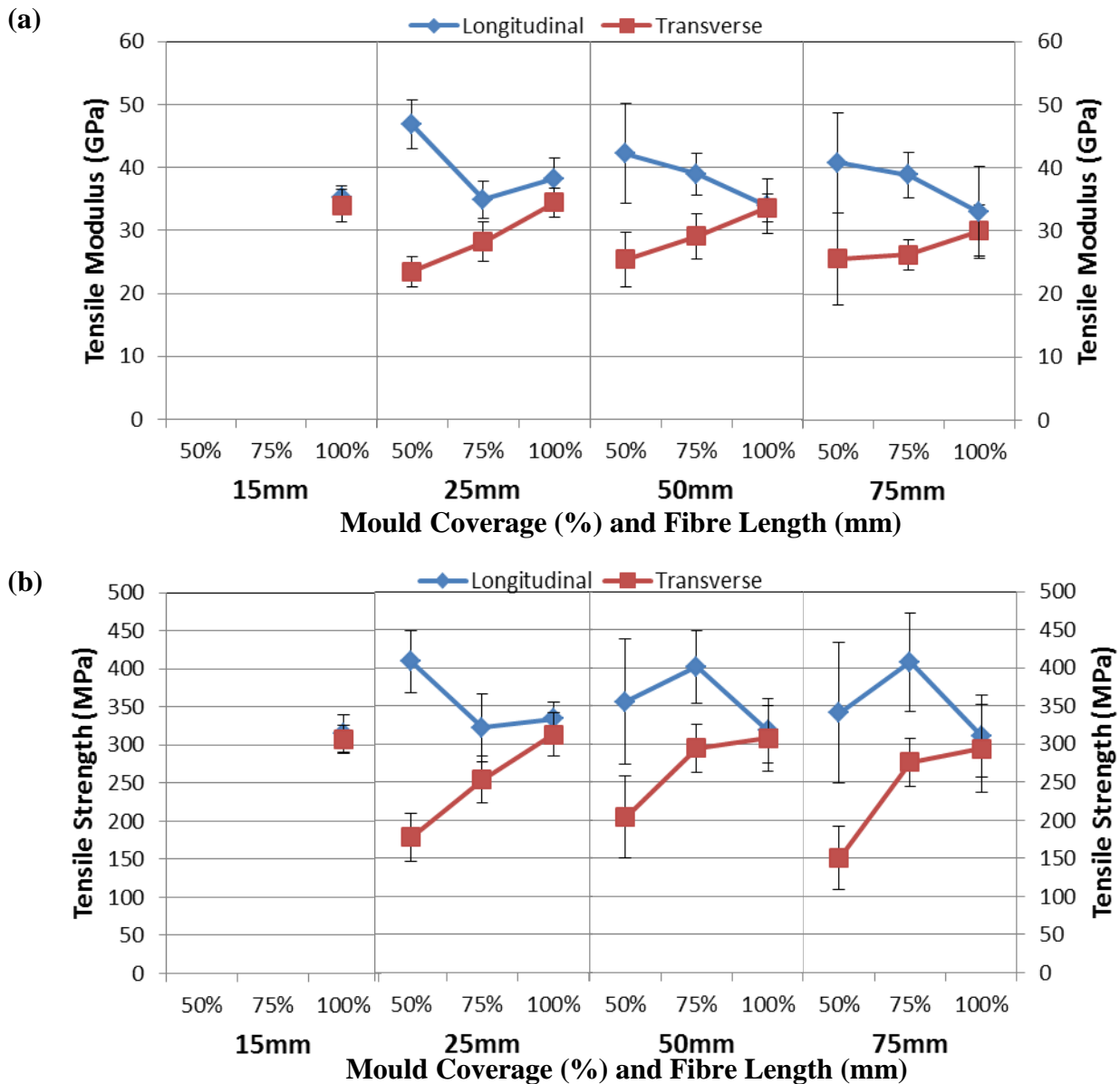


**Figure 5.10.** Effect of fibre length on tensile modulus (a) and tensile strength (b) for DFC compounds with 50%, 75% and 100% mould coverages (50% Vf).

According to *Fig. 5.10 (b)*, the highest strength for the 50mm and 75mm fibre lengths is achieved when selecting a 75% charge size, compared to 50% charge for the shorter 25mm fibre length. This can also be attributed to fibre waviness. The longitudinal strengths of the 50mm and 75mm fibre length (50% coverage) plaques are superficially low, as the ultimate strength is limited by the degree of out-of-plane waviness, as

previously shown in *Fig. 5.7*. This is supported by the trend observed for the transverse strength, which consistently decreases with decreasing charge size.

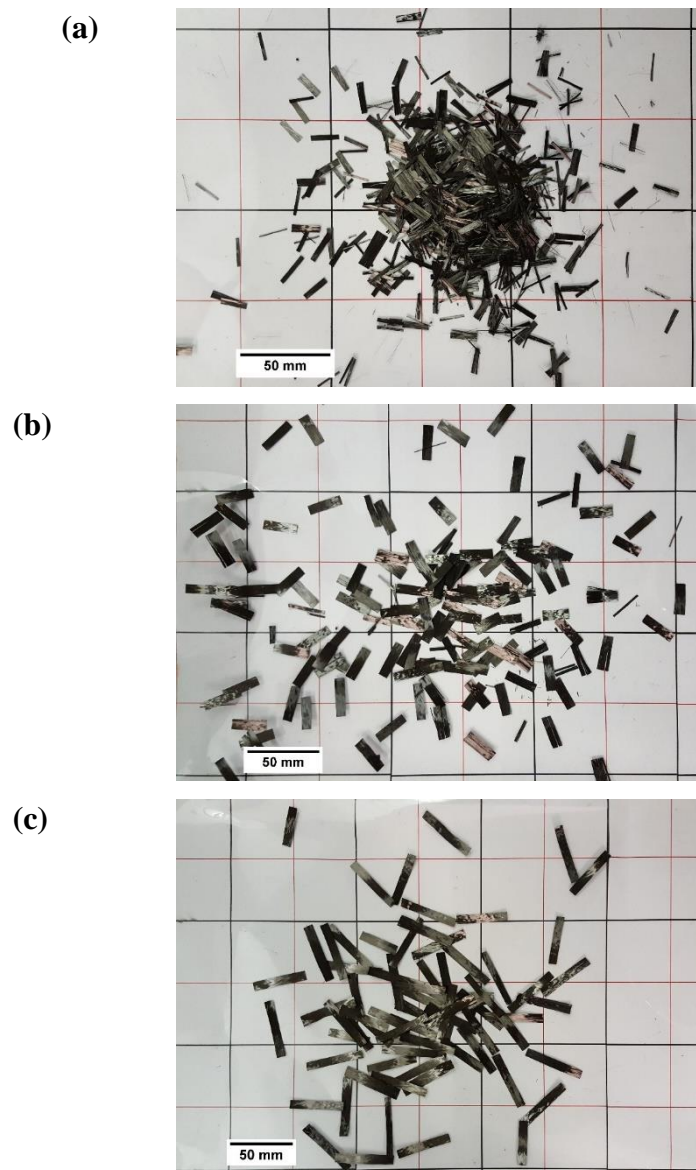


*Figure 5.11. Dry deposition of (a) 15mm (b) 25mm and (c) 50mm fibre lengths, showing increasing levels of tow fragmentation for shorter bundle lengths.*

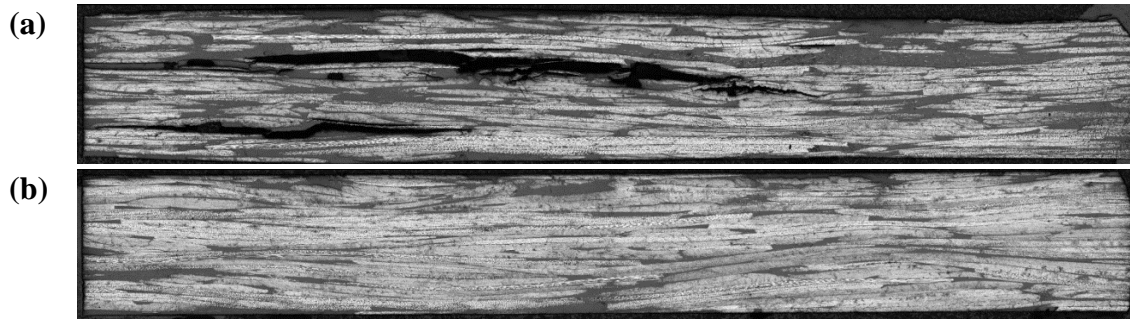


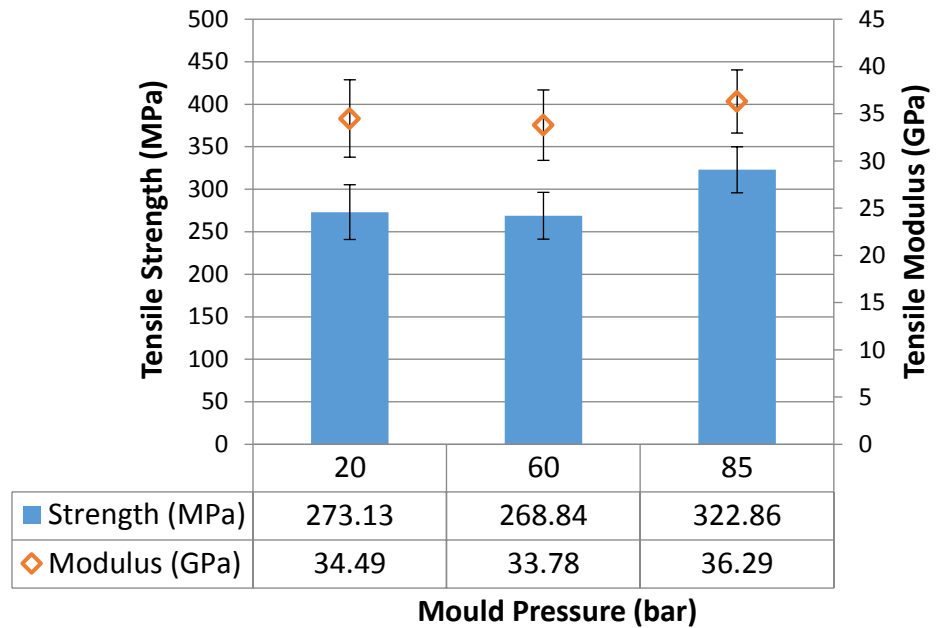
**Figure 5.12.** Void formation as a result of poor fibre packing in net-shaped 15mm fibre length compounds (a) compared to fibre packing of net-shaped 25mm fibre length (b)

#### 5.4.4 Effect of moulding pressure

Plaques for this study were initially manufactured using 100% charge coverage to isolate the effects of moulding pressure from fibre flow. **Fig. 5.13 (a)** shows that there was a reduction in both tensile stiffness and strength when the pressure was reduced from 85 bar to 60 bar. No further reduction in properties was observed when the pressure was reduced to 20 bar, however. Reducing the moulding pressure influences the void content. **Fig. 5.13 (b)** confirms that the void content is higher (1.5%) for plaques moulded at 20bar, compared with those moulded at 85bar (1.0%). This directly influences the tensile strength, which decreases by 15% when the pressure is reduced from 85 bar to 20 bar. There are three requirements to achieve complete dissolution of trapped air: 1) high pressure, 2) high (local) flow rate and 3) low initial gas concentration [172]. During compression moulding of net-shaped compounds, the flow is negligible and the gas concentration is uncontrolled as a result of the atomisation stage of the liquid resin. Therefore, moulding pressure is the most influential factor controlling the level of voids, with higher pressures required to collapse any pockets of air.

A second study was conducted to understand the influence of moulding pressure for charge packs where flow was anticipated (i.e. less than 100% charge coverage). In addition, a range of different fibre lengths was also investigated during this study to understand the combined effects of fibre length and mould pressure. Unexpectedly, tensile properties presented in **Fig. 5.14** and **Table 5.5** show that both the stiffness and strength are generally higher for 50% coverage plaques moulded at 20 bar, compared

(a)



(b)

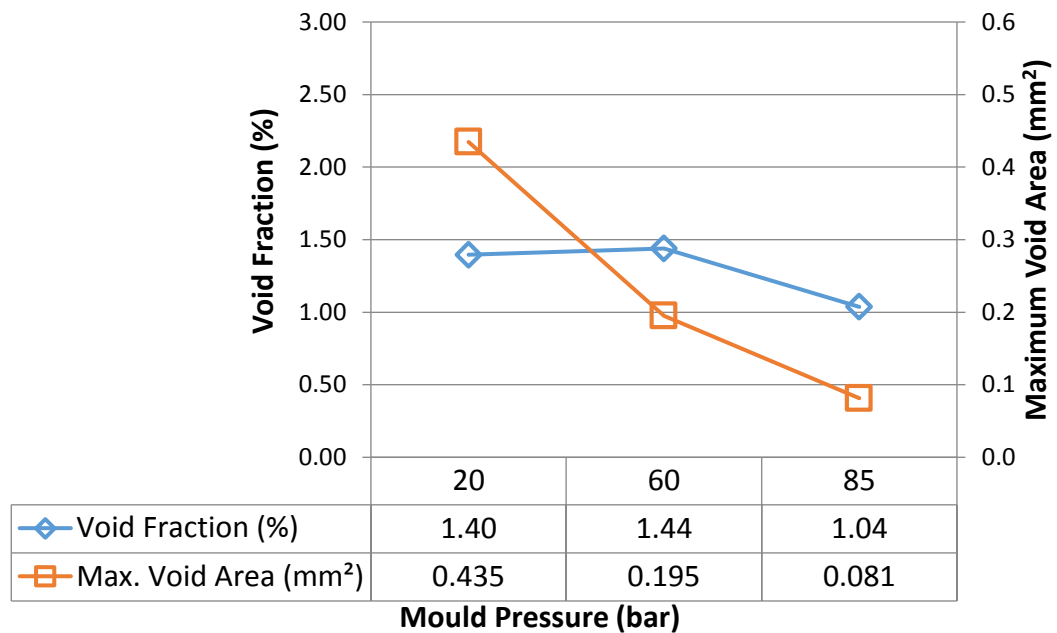


*Figure 5.13. The effect of mould pressure on tensile properties (a) and void content (b) for 100% net-shaped compounds*

with similar plaques moulded at 85 bar. This is more pronounced for the longer fibre lengths, as the longitudinal strength increases by 33% for the 50mm fibres when the pressure is reduced from 85 bar to 20 bar and by 40% for the 75mm long fibres. Furthermore, the tensile moduli were also found to increase by 11% and 17% for the 50mm and 75mm fibre lengths respectively, when the pressure was reduced from 85 bar to 20 bar. Micrographs, such as those shown in *Fig. 5.15*, indicate an increase in

fibre waviness for the longer fibre lengths, but there is also the possibility of increased fibre breakage due to increased fibre-fibre interactions, which increase at higher moulding pressures. It is also shown that for the larger fibre lengths, 50mm and 75mm, moulding at a lower pressure reduces the coefficient of variation, from 17-29% to 10-17%, in the tensile modulus and tensile strength results in both orientations. This can also be attributed to the reduction in fibre waviness.

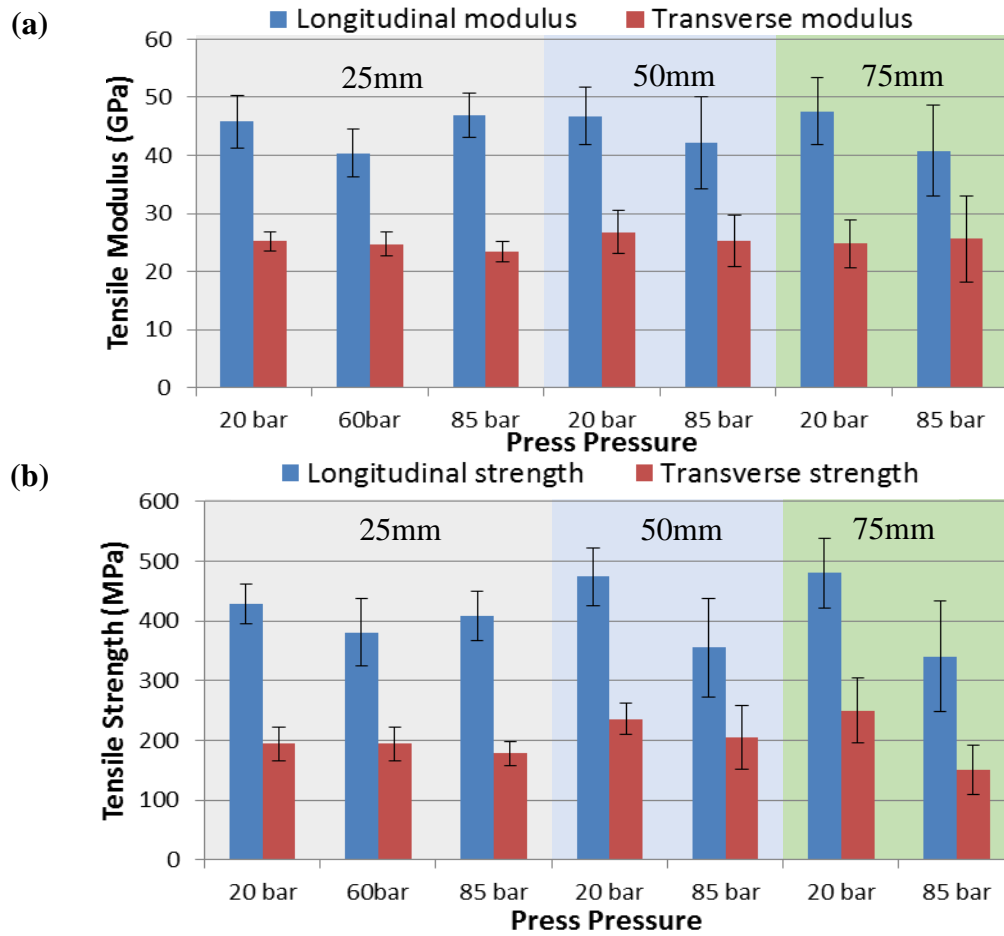


**Figure 5.14.** Tensile modulus (a) and strength (b) of different fibre length DFC compounds with 50% mould coverage and 50%  $V_f$ , varying the moulding pressure.

**Table 5.5.** Tensile modulus and strength of different fibre length DFC compounds with 50% mould coverage and 50% Vf, varying the moulding pressure.

Fibre Length (mm)		25mm			50mm		75mm	
Mould Pressure (bar)		20	60	85	20	85	20	85
Longitudinal	Modulus (GPa)	45.81	40.36	46.83	46.77	42.23	47.57	40.78
	St. dev (GPa)	4.58	4.12	3.81	4.89	7.95	5.74	7.88
	CoV (%)	9.99%	10.20%	8.13%	10.45%	18.83%	12.07%	19.33%
	Strength (MPa)	427.85	380.45	408.29	474.26	355.41	479.64	340.56
	St. dev (MPa)	32.75	55.95	40.47	48.13	82.49	57.97	92.23
	CoV (%)	7.65%	14.71%	9.91%	10.15%	23.21%	12.09%	27.08%
Transverse	Modulus (GPa)	25.23	24.73	23.45	26.74	25.36	24.78	25.59
	St. dev (GPa)	1.60	2.13	1.76	3.70	4.42	4.20	7.32
	CoV (%)	6.36%	8.62%	7.49%	13.84%	17.42%	16.95%	28.62%
	Strength (MPa)	194.56	194.56	177.77	236.09	204.14	250.13	150.16
	St. dev (MPa)	28.00	28.00	21.02	25.22	53.40	54.91	41.24
	CoV (%)	14.39%	14.39%	11.83%	10.68%	26.16%	21.95%	27.46%

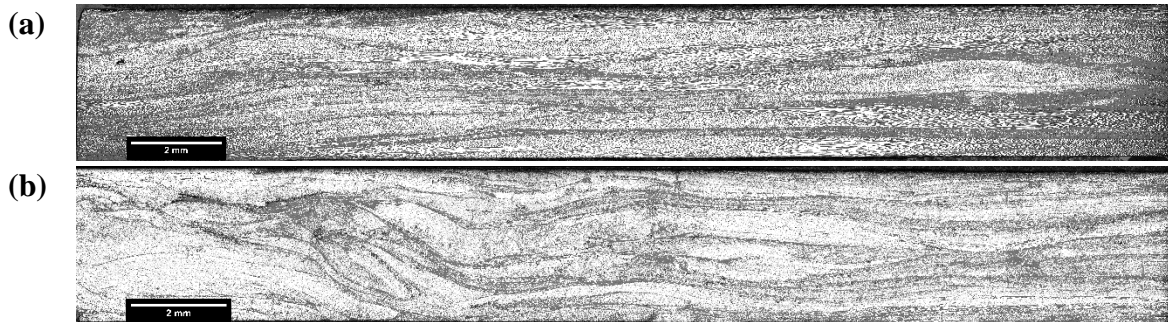


**Figure 5.15.** Micrographs of plaques produced with 50% mould coverage and 75mm fibre length. Images taken perpendicular to the flow directions showing reduction in out-of-plane waviness when moulded at 20bar (a) than moulded at 85bar (b)

According to the results shown in **Fig. 5.16**, charge flow improves the likelihood of air removal. The void content is lower for the 50% charge coverage plaques than the 100% net-shape plaques, for all fibre lengths tested at a given pressure. In addition, **Fig. 5.16** also indicates that the void content is lower for plaques moulded at 20bar when the charge size is 50% (0.3%), compared with plaques moulded at 85bar with 100% coverage (1.0%). This also has the added benefit of reducing fibre waviness, as reported above.

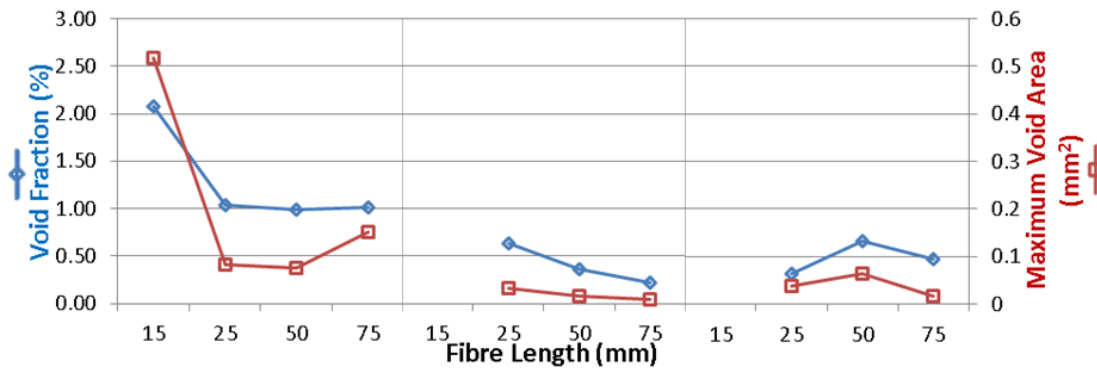


**Figure 5.16.** Void content for varying fibre lengths for 100% charge coverage at 85 bar (left), 50% charge coverage at 85 bar (middle), and 50% charge coverage at 20 bar (right)

## 5.5 Summary

The production of DFC carbon fibre moulding compounds has successfully been characterised in comparison to existing commercially available CF-SMCs and alternative manufacturing techniques. It has also investigated the mechanical properties of DFC, showing that the properties can be tailored by using flow induced alignment to enhance them in the flow direction. This is achieved by changing the moulding size and position of the charge. It does this without effecting the cycle time maintaining its suitability for high volume compression moulding.

Directed Fibre Compounding (DFC) overcomes the challenges of producing carbon fibre/epoxy moulding compounds using conventional compounding routes, to produce a structural material directly from low cost carbon fibre tows and liquid epoxy resin. It eliminates the need for secondary manufacturing stages such as chopping UD prepreg, such as for HexMC M77, intimately coating each fibre bundle with an epoxy spray to ensure that the fibre bundles are suitably wet out during moulding. The resin spray is necessary to achieve this and using this method has shown superior mechanical performance compared to pressing the fibre bundles into a resin film, such as PFC. It has also been shown that the DFC fractures with greater levels of fibre breakage than PFC, which exhibited matrix-dominated failure during in-plane testing. The PFC experienced similar mechanical performance to the carbon fibre/vinyl-ester moulding compound. These were manufactured by using the more traditional SMC

manufacturing approach, and therefore exhibited matrix-dominated fracture as a result of poor fibre-matrix interfacial strength. The DFC and EP-SMC therefore demonstrated greater tensile strengths because of their improved fibre-matrix bonding. Net-shape charge packs can be produced if no charge flow is required, which is of particular interest for the following chapters where DFC may be combined with LRS impregnated fabric and co-compression moulding to produce a hybrid architecture. Using the same resin system components for the dissimilar architecture ensures that the resin cure rate is homogeneous and crosslinking is complete throughout the composite.

The DFC process enables the charge to be specifically tailored for the intended application. The shape and position of the charge can be refined to encourage flow induced fibre alignment to enhance local material properties. Tensile stiffness and strength values of 36 GPa and 320 MPa are reported for isotropic DFC materials, which increase to 46 GPa and 408 MPa with flow induced alignment (50% charge coverage at 50% fibre volume fraction). A novel feature of the DFC material is that charge packs covering just 40% of the mould tool can be successfully used to produce plates with homogeneous fibre distribution. Analysis of local fibre volume fraction confirms that high levels of flow can be achieved without experiencing fibre-matrix separation. This has been made possible by using a B-staged epoxy, where the viscosity changes according to the degree of chemical conversion. Initially, a low viscosity during fibre/matrix deposition ensures high levels of bundle impregnation, whilst a higher viscosity after staging ensures fibre mobility during the compression moulding stage.

One of the outcomes however of encouraging flow to the moulding compound is an increase in the degree of out-of-plane waviness of the fibre bundles. The analytical inclusion model reverse engineered the experimental modulus results to generate an orientation tensor. The result of this showed an increase of  $a_{33}$  with flow distance and suggested the presence of out-of-plane waviness, agreeing with the micrograph observations. This was found to restrict the tensile strength of the composites, especially for the larger fibre length, >50mm. However, this was found to be controllable by adjusting the moulding pressure of the compression mould tool. Combining the introduction of in-mould flow (50% mould coverage), increasing fibre length to enhance the mechanical performance of aligned composites (from 25mm to

75mm) and reducing the moulding pressure (from 85 bar to 20 bar) the tensile stiffness and strength were increased to 48 GPa modulus and 480 MPa strength, respectively.

Furthermore, it has been shown that there are two dominant mechanisms for minimising porosity. Higher moulding pressures are required for net-shape (100% coverage) charges to collapse entrapped air, due to the lack of resin flow. Conversely, encouraging charge flow (smaller charge coverage) allows additional air to escape through the flash-gap, potentially enabling the moulding pressure to be reduced to achieve a high-quality laminate. Lower moulding pressures also lead to reduced fibre waviness, particularly for longer fibre lengths, yielding higher tensile properties. There are clearly significant interactions between the variables studied here and it is therefore worth noting that increasing mould coverage, fibre length and moulding pressures concurrently does not necessarily produce the highest mechanical properties for these carbon moulding compounds.

# 6. Continuous/discontinuous interfacial characterisation

## 6.1 Introduction

This chapter will characterise the change in mechanical performance that is achieved by co-compression moulding UD-NCF with chopped fibre moulding compounds. Following the successful production of carbon fibre moulding compounds using the liquid resin spray (LRS), this chapter investigates impregnating dry unidirectional fabrics using the same methodology. The benefits of this have been recognised for SMC/prepreg co-compression moulding [55]; enabling composites to be produced with short cycle times, taking advantage of in-mould flow of the moulding compound, combined with the localised reinforcement of NCF regions for managing higher stresses. The relationship between the ratio of chopped random to unidirectional carbon fibre is therefore established to demonstrate that the in-plane properties are directly proportional to this ratio.

It is impractical to cover large areas of the compression mould tool with continuous fibres for complex components because of the increase in charge preparation time, so hybridising offers additional local reinforcement using highly optimised fibre architectures. Consequently, this introduces a complex stress state between the two architectures at the transition point. This effectively forms a joint from one material to another, which can lead to large reductions in mechanical performance. This chapter therefore also investigates the design of such joints, in terms of step size and geometry.

Various design considerations are made when dropping plies to reduce part thickness of continuous laminate composites or when joining laminates. When the end of a ply is positioned internally within a stack, a triangular resin rich region is formed at the ply

drop, introducing a potential failure initiation site. There are a number of design guidelines that must be adopted when dropping plies within laminates to maximise strength before delamination [97, 99-101]:

- Surface plies should not be dropped
- The maximum taper angle,  $\alpha$ , should not exceed  $7^\circ$ . Ply drops should therefore be staggered by a minimum distance of approximately eight times the thickness of the ply.
- Ply drops should be staggered through the thickness, alternating between plies close to the surface and close to the laminate centre line.
- Plies should be dropped in decreasing order of stiffness to ensure smooth transfer of load and reduce stress concentrations. For example,  $0^\circ$  plies first and  $90^\circ$  plies last.
- The number of plies dropped at any location should be kept to a minimum to reduce the volume of resin rich regions.

When joining laminates, there is a large amount of literature detailing experimentation and modelling the design [97, 102, 107]. However, as there is no literature on joining continuous laminates with chopped fibre bundles. Therefore, a number of assumptions are used based on the joint design of laminates. The most significant variable affecting the performance of a joint is the distance between each step [100]. The optimal number of plies ending at any particular step should be just one, as increasing this number significantly reduces the tensile and flexural performance [102]. Other joint design guidelines for composites often suggest tapering the ends of the composite, usually by machining the end of the moulded laminate to form a scarf joint, if the laminate cannot be easily stepped during the layup. This minimises the magnitude of the peel stresses at arises at the end of the joining component [97, 99, 107]. The peel stress is a function of the thickness of each joint constituent [173]. A shallower taper angle, or larger step size, will minimise the thickness distribution along the joint length and therefore minimise the peel stress at the thinnest point, where delamination is most likely to initiate.

Failure within hybrid composites can occur within three distinct regions; the continuous fibre plies, the discontinuous fibre material and the interface between plies or

architectures. Failure within the continuous plies requires breakage of the high strength fibres and therefore requires the highest stress. Within discontinuous fibre composites, stress concentrations often arise at the ends of the fibre bundles [10, 21]. For shorter fibre lengths, fibre pull-out increasingly dominates the fracture mechanism as a result of a smaller contact area with the matrix. Thus, there is more fibre breakage with longer fibre lengths since the larger fibre-matrix interface requires greater loads to overcome the interfacial adhesion [73]. Failure at the interface in the form of delamination, is dominated by the performance of the resin between the plies or architectures. During mode-I separation, delamination is induced along an interface, where a resin rich interface provides a low strength path where a crack may propagate [1]. However, load carrying fibres near to, or interleaving the interface, transfer stress across the interface producing a stress distribution surrounding the crack tip. Over the length of this damage zone, broken or pulled out fibres no longer contribute to stress transfer. This reduces the ability to analyse the fracture as a linear elastic fracture mechanism [73].

Commonly for discontinuous fibre architectures, cracks propagating perpendicular to a fibre bundle result in crack arresting or non-linear crack growth, as it deviates around the high strength fibres. The crack deflection produces fibre bridging across the interface which gives excellent toughness during mode-I separation [120]. However, cracks propagating parallel to a fibre experience less crack deflection and bridging. This prevents load transfer across the interface and therefore reduces toughness. Fibre bridging remains the most efficient mechanism for reducing the stress level at the crack, by transferring the stress through the bridged fibres across the interface [121]. A study by Truss et al. [120] demonstrates that fibre bridging leads to higher fracture toughness for discontinuous fibre materials ( $981 \text{ J/m}^2$ ) compared to continuous fibre material ( $250 \text{ J/m}^2$ ). This is despite the fibre volume fraction being much lower (36% for the discontinuous material compared to 46% for the continuous fibre material). It was also noted that the fracture toughness had to be determined as a function of crack length for the discontinuous fibre material, as the DCB testing experienced rapid crack advance [120].

## 6.2 Objectives

The objectives of this chapter are to investigate the design characteristics that require consideration when producing continuous/discontinuous hybrid carbon fibre architecture. The discontinuous fibre architecture will be manufactured by Directed Fibre Compounding (DFC) and the UD-NCF will be impregnated using the LRS system.

This chapter initially aims to quantify this mechanical enhancement by tensile performance of symmetric composites to determine the influence of the volume ratio of UD to DFC within symmetric arrangements (UD/DFC/UD) is determined. Asymmetric arrangements (UD/DFC) will also be characterised in terms of flexural properties whilst observing the warpage formation during freestanding that proceeds hot demoulding.

The main focus of this chapter is then to understand the effect of the laminate design in the transition zone between these dissimilar architectures, in terms of ply step size and the ply drop strategy. These are investigated in terms of the bending and tensile performance of the joint. The microstructure of these joints will be analysed to establish the conformity between the materials with varying step size and joint geometry. Electronic speckle pattern interferometry (ESPI) then generates through-thickness multidirectional strain distributions of axially loaded continuous-discontinuous joints.

Finally, this chapter will characterise the interfacial mode I fracture toughness of hybrid carbon fibre architecture by means of DCB testing. The fracture toughness of discontinuous and continuous carbon fibre/epoxy composite benchmarks are also investigated in addition to the hybrid architectures to highlights the dominate fracture mechanisms during mode-I separation. The benefit of compression moulding hybrid laminates rather than pre-curing the continuous plies prior to compression moulding is also demonstrated.

### 6.3 Design of experiments

#### 6.3.1 In-plane mechanical testing of hybrid fibre architecture

The tensile performance was used to compare the material response of DFC and UD carbon fibre compounds within hybrid carbon fibre architecture. This was performed by adjusting the quantity of DFC and UD fabric in each of the hybrid carbon fibre architecture compounds with the structure:  $[0_n/DFC]_s$ . The UD plies were positioned at the upper and lower tool surface (UD/DFC/UD) to minimise the out-of-plane ply waviness and to ensure a thicker DFC central section compared to dividing the DFC material into a DFC/UD/DFC sandwich configuration. This helped to reduce any potential size effects previously observed when moulding thin discontinuous fibre architectures [5]. This arrangement, shown in *Fig. 6.1*, also provided symmetrical specimens that did not warp.

To maintain a constant composite thickness of 3mm, *Table 6.1* shows the target thickness of the central DFC region sandwiched between the layers of UD fabric. These were verified by microscopy, by measuring the thickness of the UD and the thickness of DFC. For each of the hybrid carbon fibre architecture composites, four micrographs were obtained (2 longitudinal and 2 transverse) to verify that the volume of UD and DFC is correct by measuring the thickness of each constituent at 6 locations in each micrograph.

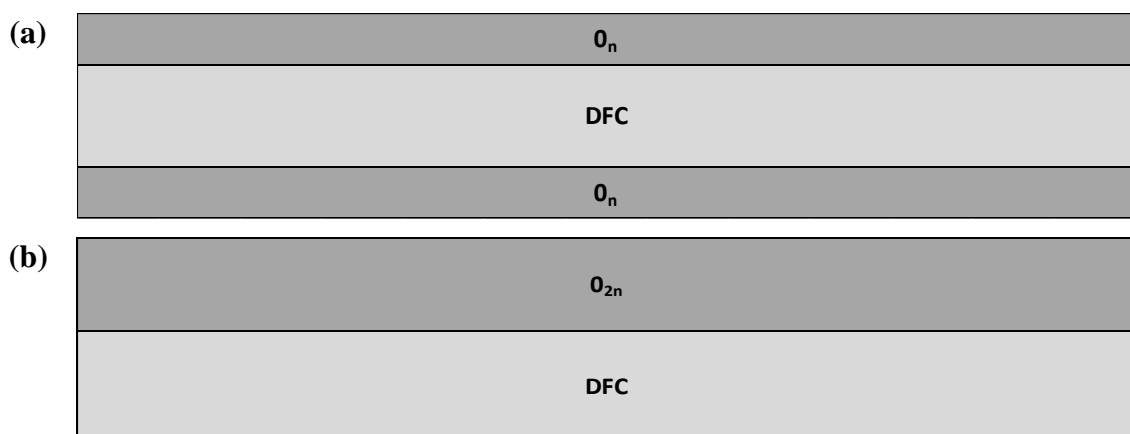


*Figure 6.1. Hybrid fibre architecture schematics with symmetric (a) and asymmetric (b) arrangements, where the number of UD plies,  $2n$ , and thickness of DFC are altered to achieve each ratio of UD material by volume*

**Table 6.1.** Details of each of the symmetric hybrid fibre architecture specimen to vary quantity of UD whilst maintaining constant thickness

Ratio of UD (by vol)	0%	20%	40%	60%	80%	100%
Ratio of DFC (by vol)	100%	80%	60%	40%	20%	0%
Number of UD plies, 2n	0	2	4	6	8	10
Thickness of UD material (mm)	N/A	0.6	1.2	1.8	2.4	3
Thickness of DFC material (mm)	3	2.4	1.8	1.2	0.6	N/A
Number of DFC layers	3	3	2	2	1	0
Adjustment to quantity of DFC material deposited per layer	100%	80%	90%	60%	60%	N/A

### 6.3.2 Out-of-plane mechanical testing of hybrid fibre architecture

In the event of using a patch of fabric placed onto the surface of DFC to provide location of localised mechanical enhancement, it will be difficult to align an equally sized patch on the opposing surface. Therefore, tests were performed to quantify the structural response of asymmetric hybridised specimens,  $[0_{2n}/DFC]$ . These arrangements are shown in **Fig 6.1 (b)**, with more details included in **Table 6.1** with target DFC to UD ratios as those performed during in-plane testing. This was achieved by 3-point bend testing, with a span length of 120mm, as described in *Chapter 3*. To fully understand the effect of the asymmetric architectural arrangement, this testing was performed in both positive bending (i.e. UD on the upper surface and DFC on the lower surface) and negative bending (i.e. DFC on the upper surface and UD on the lower surface). Further observations were also made to understand other effects of moulding asymmetric hybrid architectures, noting warping and curvature to the flat specimens with respects to the ratio of UD to DFC (by volume).

### 6.3.3 Joint design

The joint design was divided into two studies: step size and ply drop arrangement. First, the effect of step size was considered for a *stepped* geometry, **Fig. 6.2 (a)**. Stepped joints were arranged so that each ply was incrementally shorter than the surface ply. The step length was increased from 0 mm (all ply ends synchronised) to 1.5mm, 3mm, 6mm and 12mm. This step sizes are shown in **Table 6.2** as a function of the ply thickness,  $h=0.3\text{mm}$ . A second study was conducted using two additional types of joint

design to investigate the effect of the ply drop arrangement, shown in **Fig. 6.2**. These were *tapered* and *alternating* joints. Tapered joints had the longest UD ply positioned at the interface with the discontinuous fibres, which encased the ends of each of the other UD plies. The alternating arrangement had the longest ply positioned at the tool surface, which was a combination of a stepped and tapered joint. The step size for all three geometries was kept constant at 6mm (20 times the ply thickness). Each of these joints were configured with 7 plies of  $0^\circ$  UD fabric, shown in **Fig. 6.3** which were placed on top of a DFC charge with uniform areal density covering 100% of the tool surface. This was to minimise the level of charge flow in the vicinity of the transition zone.

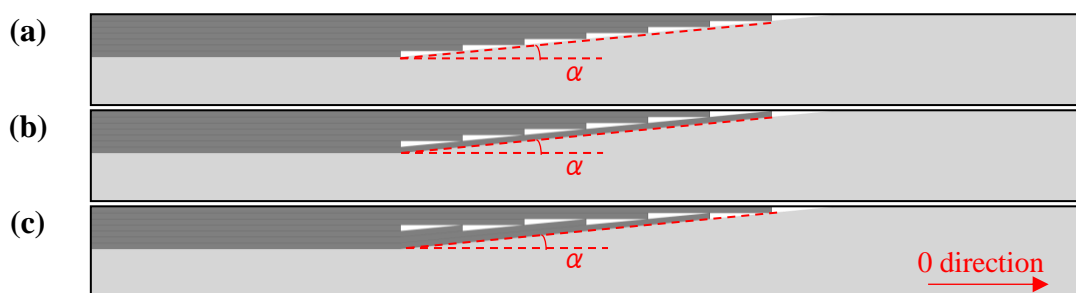


**Figure 6.2.** Schematic of the joint geometries between continuous UD laminates in the zero orientation (dark grey) and random DFC (light grey): stepped (a), tapered (b) and alternating (c)

**Table 6.2.** The step sizes investigated for the ‘stepped’ joint geometry

Step size (mm)	Step size as a function of ply thickness
0	0h
1.5	5h
3	10h
6	20h
12	40h

The in-plane and out-of-plane mechanical performance were characterised during both studies by performing tensile and three-point bending at the centre of each joint. The tensile testing results were averaged from 12 repeats. The three-point bend tests were performed in both the positive and negative bending directions, with 6 repeats in each direction, as shown in **Fig. 6.4**. It was important to ensure that the testing position of the joint was constant between repeats. During tensile testing, the grips were positioned 50mm each side of the centreline of the joint. This ensured that the same volume of UD

fabric was between the grips for each test. Additionally, the grips of the extensometer were positioned equally each side of the joint centreline. The centreline of the joint also provided the loading location during the three-point bend tests to ensure that the volume of UD fabric and random material between the two support rollers were constant with each step size and joint geometry.

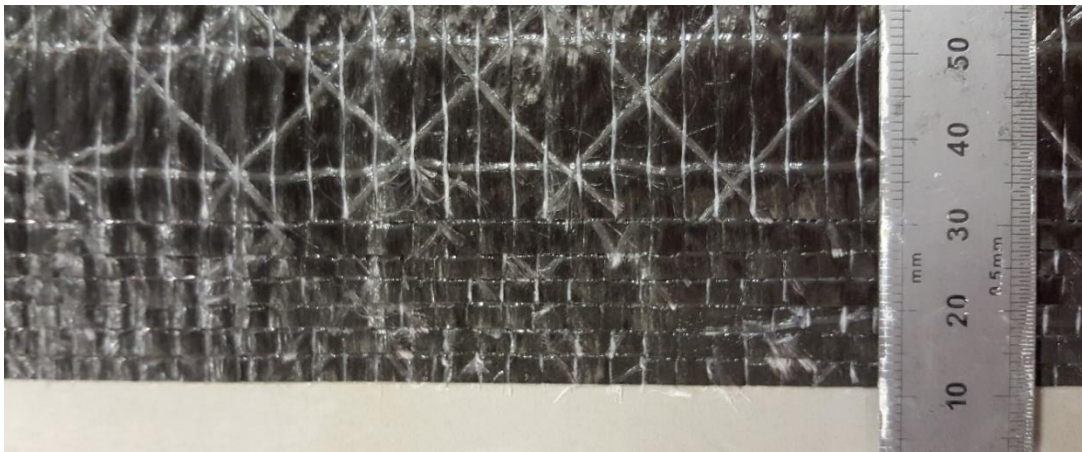


**Figure 6.3.** Stacked UD plies for producing a stepped joint with a step size of 3mm

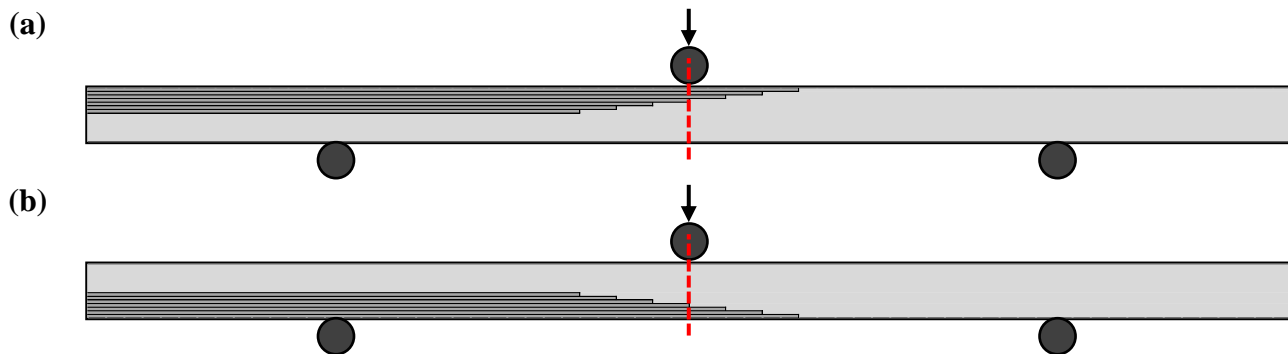


**Figure 6.4.** Schematic of the location of the load roller during 3-point bend when testing in the positive bending direction (a) and the negative bending direction (b)

### 6.3.4 Interfacial testing

A double cantilevered beam (DCB) test was used to measure the mode-I fracture toughness of both the DFC and UD materials (independently) and the hybrid fibre architecture [0<sub>5</sub>/DFC], separated at the planar interface between the dissimilar material. Two variations of the hybrid architecture interface were investigated. The first was produced by co-compression moulding the continuous and discontinuous components, using 100% tool coverage for both materials. The second was produced by pre-curing the UD plies in an oven under vacuum pressure before compression moulding with the

DFC, preventing matrix crosslinking at the interface. Four repeats were performed for each of these architectures. The thickness of the DFC component was chosen to give an equal bending stiffness to the UD element, to ensure that delamination occurred horizontally at the interface between the two materials, as detailed in *Chapter 2*.

## 6.4 Results and Discussion

### 6.4.1 In-plane properties of hybrid fibre architecture

Hybrid composite plaques were manufactured with an increasing percentage of unidirectional carbon fibre. The tensile stiffness and strength results, shown in *Fig. 6.5* and *Table 6.3*, both follow strong linear relationships in the longitudinal and transverse orientations. Consequently, there is good agreement between the experimental data and rule of mixtures predictions. The tensile modulus and strength in the direction  $i$ ,  $E_i$  and  $\sigma_i$  respectively, are given in *equations 6.1 and 6.2*, determined by the sum of the product between the property and the volume fraction of discontinuous,  $V_{disc}$ , or continuous material,  $V_{cont}$ . Fitting each of the experimental data points to the rule of mixtures equations generates  $R^2$  values close to 1, *Table 6.3*, indicating sufficient goodness of fit. The baseline strength of 333MPa  $\pm$ 22MPa for the near-isotropic DFC material (0% UD) increases by more than 110% with only 20% UD content, but the corresponding transverse strength reduces by just 25%.

$$E_i = V_{disc}E_{disc,i} + V_{cont}E_{cont,i} \quad (6.1)$$

$$\sigma_i = V_{disc}\sigma_{disc,i} + V_{cont}\sigma_{cont,i} \quad (6.2)$$

Spraying NCF fabric from one side only semi-impregnates the fibres through the thickness. This effectively applies a resin film to the fabric surface, with some flow required through the thickness during the moulding step. If there is insufficient flow, resulting from a locally low pressure or a high resin volume fraction, then resin rich regions may form it is unable to flow into fibres, as shown by *Fig. 6.6 (a)*. It was also observed from the micrographs in the transverse orientation that large resin rich regions form in regions with stitches between fabric tows, shown by *Fig. 6.6 (b)*. Examples of the micrographs of the hybrid carbon fibre architecture are shown in *Fig. 6.7* where the

UD positioning, in contact with the upper and lower surface, results in a negligible amount of out-of-plane waviness.

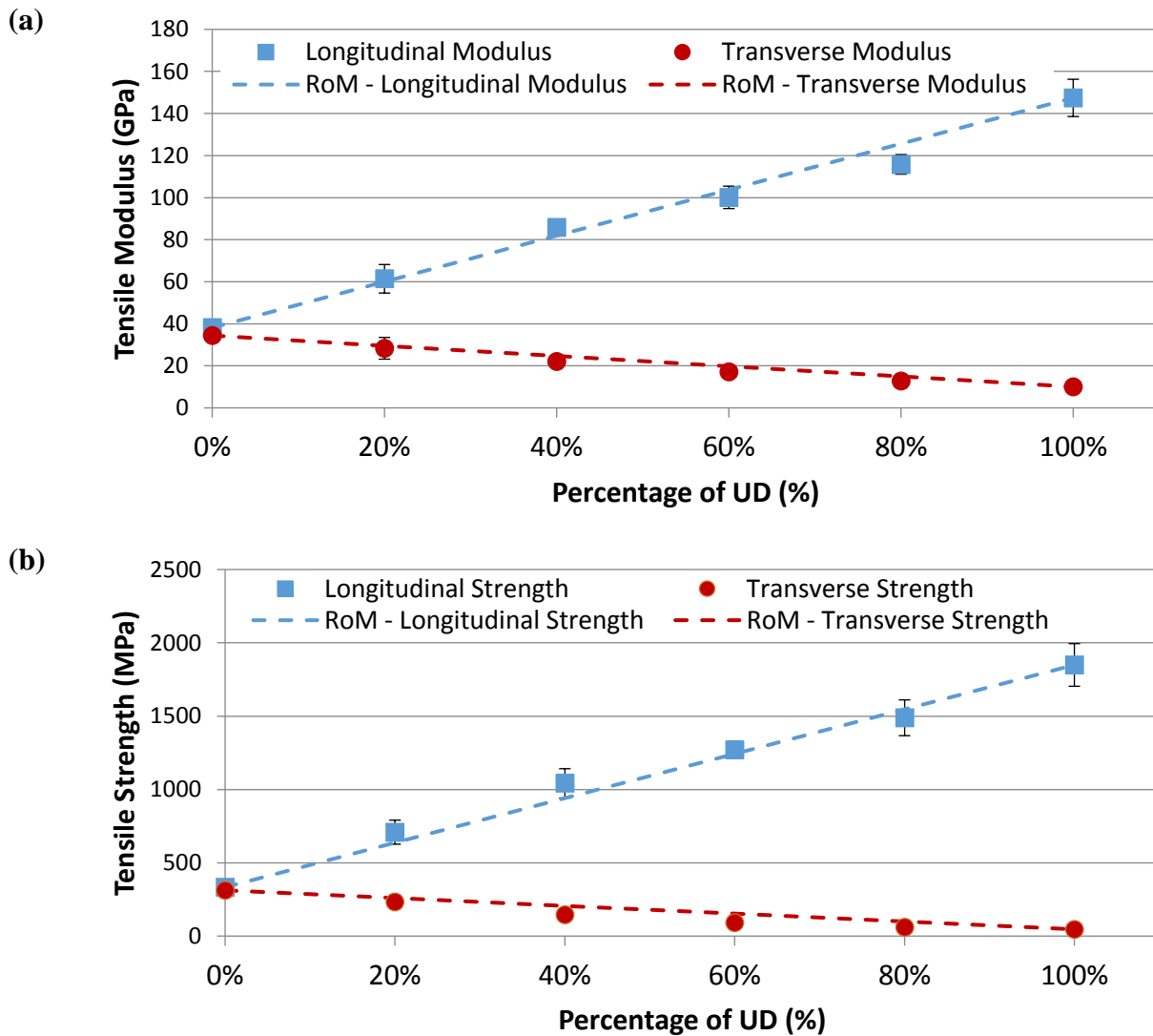


**Figure 6.5.** Tensile modulus (a) and strength (b) of UD/DFC hybrid carbon fibre architecture with increasing percentage of UD fabric by volume, thus decreasing percentage of DFC. Charts include linear lines for properties calculated by rule of mixtures (RoM)

By analysing the fractured specimens, it was found large, sudden delaminations along the interface between DFC and UD fabric propagated from the failure location, shown in **Fig. 6.8 (a)**. This indicated that the strain imbalance between the different architectures produced an out-of-plane shear stress between the fabric and DFC. Additionally, one specimen exhibited waviness within the UD fabric. This was caused

by the small degree of flow as the DFC compresses under high moulding pressures inducing in-plane shear in the fabric. This waviness produces a localised weak point that failed at low stresses, **Fig. 6.8 (b)**. This result was excluded from the average values presented in **Fig. 6.5** and **Table 6.3**.

**Table 6.3.** Tensile properties of UD/DFC hybrid carbon fibre architecture with increasing percentage of UD fabric by volume, thus decreasing percentage of DFC in each tested orientation. Table includes the  $R^2$  values for goodness of fit for each experimental data point in relation to the rule of mixtures equations

Percentage of UD (by volume)		0% (DFC only)	20%	40%	60%	80%	100% (UD only)	$R^2$ values
Longitudinal	Modulus (GPa)	38.18	61.41	85.80	100.12	115.80	147.43	0.97
	St. dev (GPa)	3.24	6.78	3.82	5.33	4.66	8.86	
	CoV (%)	8.50%	11.05%	4.45%	5.33%	4.02%	6.01%	
	Strength (MPa)	333.4	708.5	1041.8	1270.9	1489.1	1849.3	0.96
	St. dev (MPa)	21.8	82.0	99.8	57.7	122.0	145.3	
	CoV (%)	6.52%	11.57%	9.58%	4.54%	8.19%	7.86%	
Transverse	Modulus (GPa)	34.41	28.34	22.09	17.13	12.80	10.03	0.85
	St. dev (GPa)	2.25	5.16	2.55	2.21	1.20	0.10	
	CoV (%)	6.53%	18.22%	11.52%	12.91%	9.41%	0.99%	
	Strength (MPa)	312.3	232.7	144.4	90.1	60.7	46.2	0.75
	St. dev (MPa)	28.5	45.4	32.3	14.3	6.1	1.6	
	CoV (%)	9.14%	19.52%	22.37%	15.83%	10.03%	3.49%	

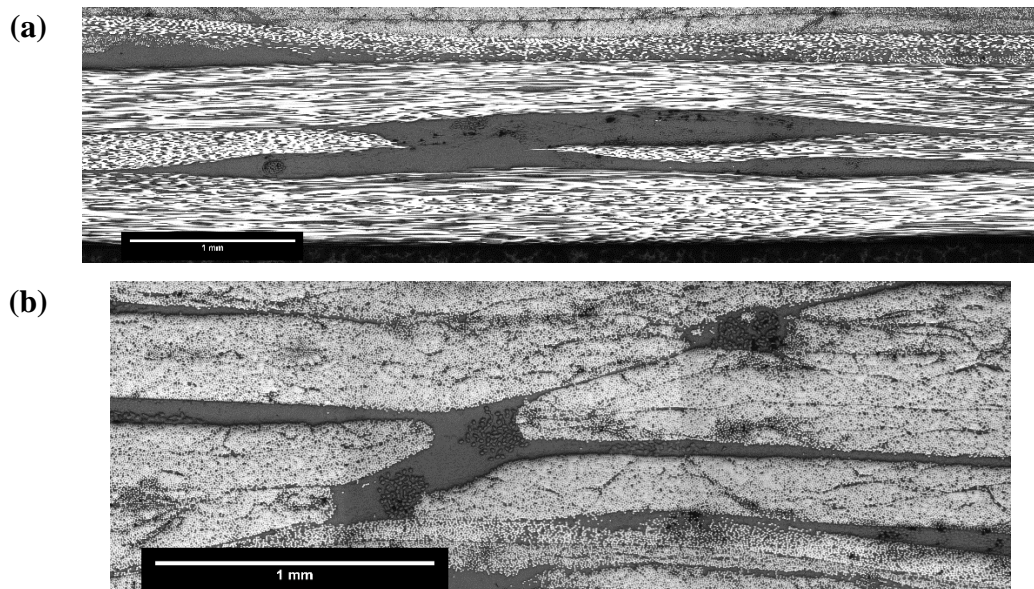


**Figure 6.6.** Examples of resin rich formations between layers (a) and at the stitching between NCF tows (b)

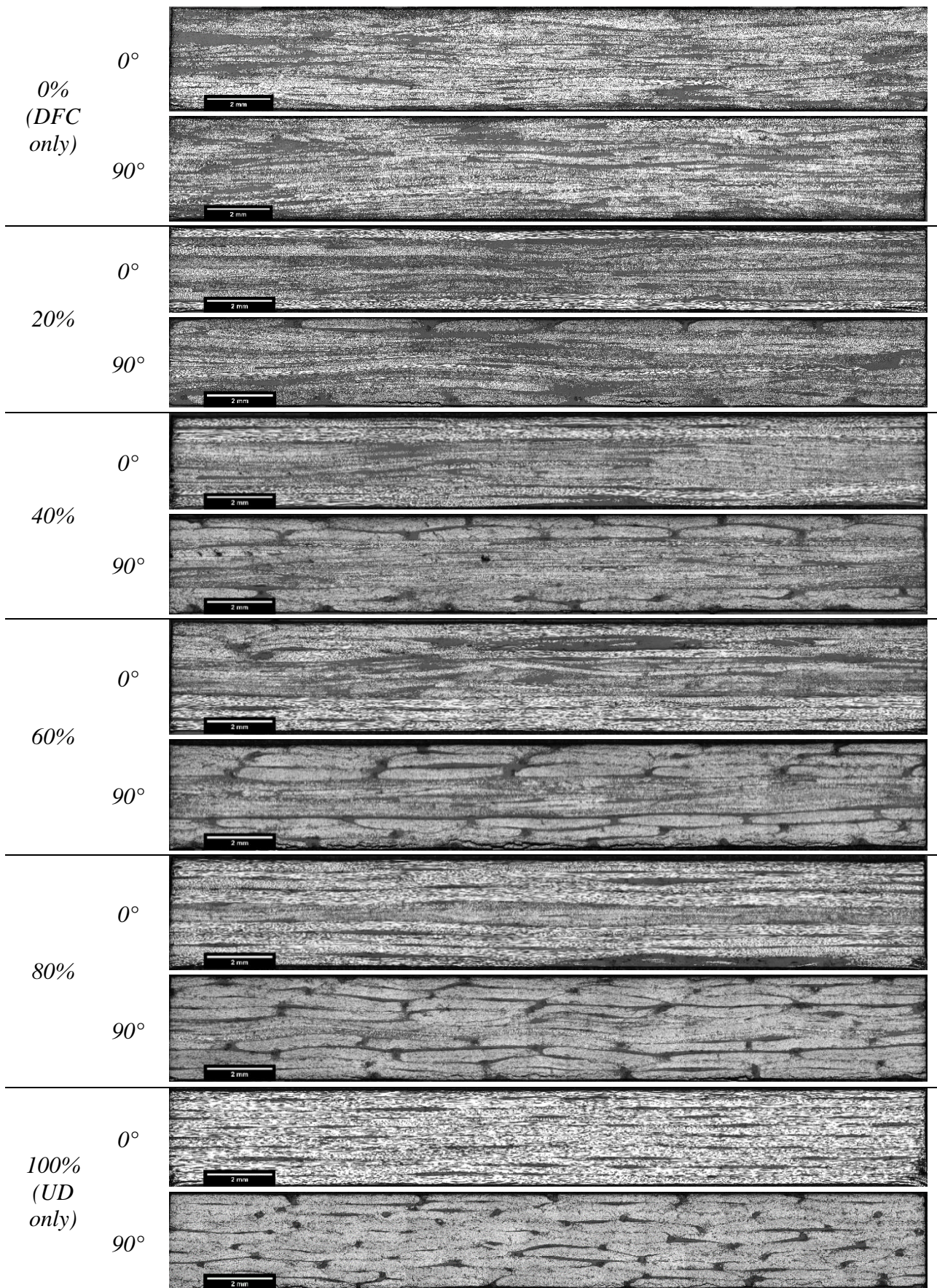


**Figure 6.7.** Example micrographs of the cross section of hybrid fibre architecture with varying quantity of UD fabric

#### 6.4.2 Out-of-plane properties of asymmetric hybrid fibre architecture

Hot demoulding the plaque from the flat compression mould tool removes the constraints during cooling. The thermal expansion coefficient of the UD fabric is greater in the transverse direction than in the longitudinal direction. Combined with the asymmetry of the hybridisation, this imbalance results in flat plaques becoming curved during cooling [110]. This curvature was measured with a ruler, taking the peak height from the horizontal plane. Increasing the height of these 405mm x 405mm panels is representative of the decreasing radius of its curvature. The results, shown in *Fig. 6.9*, suggest that the greatest curvature found at approximately 60%. This is greater than 50% volume of UD material because the thermal expansion coefficient of UD fibre in the transverse direction,  $\alpha_{UD,T}$ , is greater than that of random chopped fibre,  $\alpha_{Rand}$ , which is greater than UD fibres in the longitudinal direction,  $\alpha_{UD,L}$ :

$$\alpha_{UD,T} > \alpha_{Rand} > \alpha_{UD,L} \quad (6.3)$$



*Figure 6.8. Delamination of hybrid fibre architecture specimen with 40% UD content (a) and failure resulting from the waviness of the UD fabric, 60% content (b)*

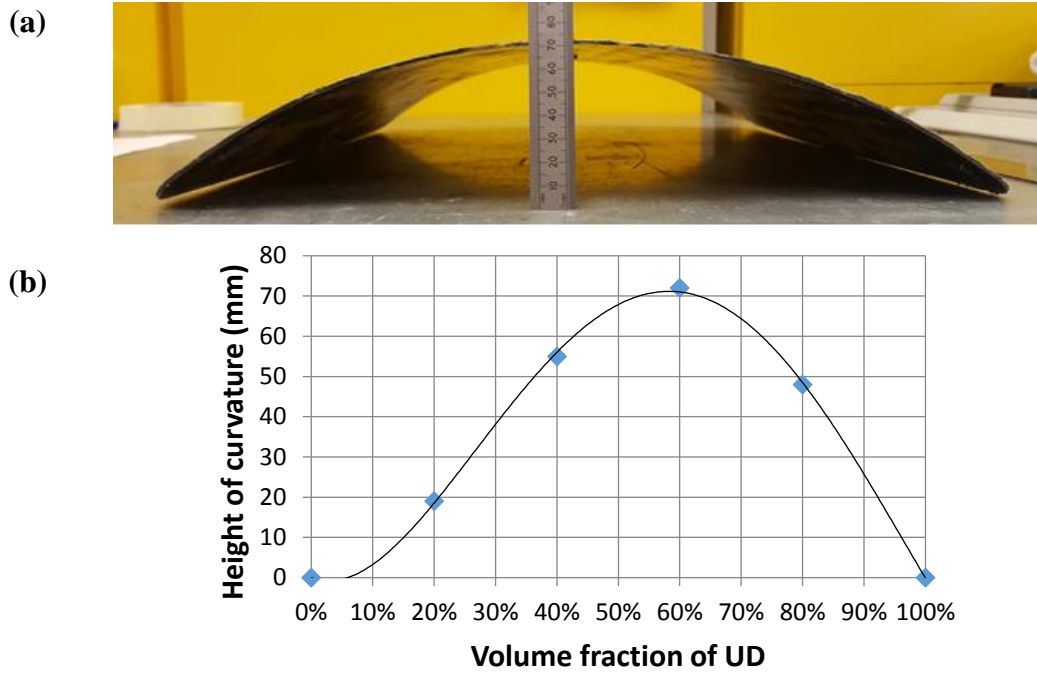


**Figure 6.9.** (a) Photograph of 405mm x405mm plaque warped during cooling following hot demould and(b) the height of each curved panel from flat surface to the bottom surface at the peak of the panel

Three-point bend tests were performed on the asymmetric hybrid architecture composites with varying quantity of UD fabric. This was performed in both the positive (UD fabric under compression, DFC in tension) and negative bending directions to understand the structural response of the asymmetric architecture. When measuring the modulus of transverse specimens, the LVDT gauge required repositioning to account for specimen curvature and maintain contact with the specimen at zero strain. Also, a pre-load of approximately 130N was applied to reduce the level of curvature to ensure that the specimens were entirely supported by the rollers and not interfered with by the fixtures as shown by *Fig. 6.10*.

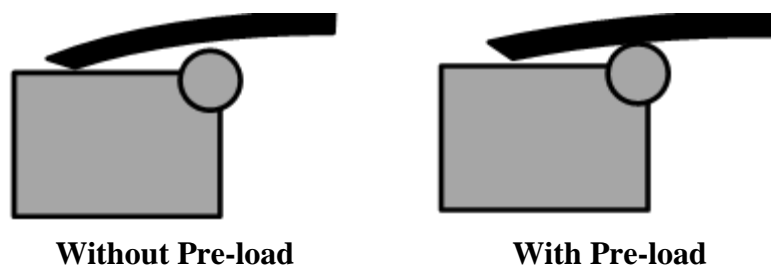


**Figure 6.10.** Schematic showing the effect of curvature against the three-point bend fixture.

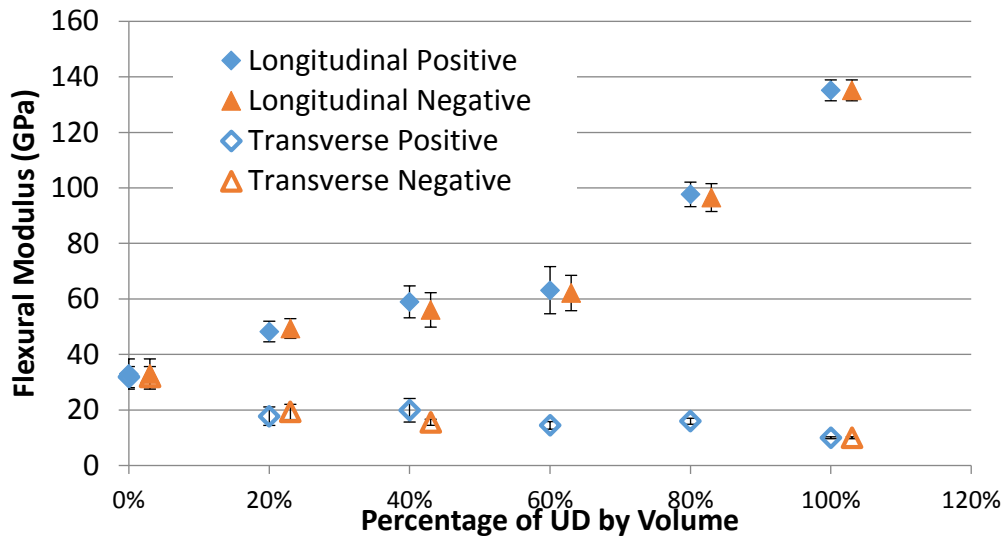


**Figure 6.11.** Flexural modulus of asymmetric UD-DFC hybrid architecture under positive and negative bending (offset +3%). Varying the percentage of UD by volume, with the remainder DFC

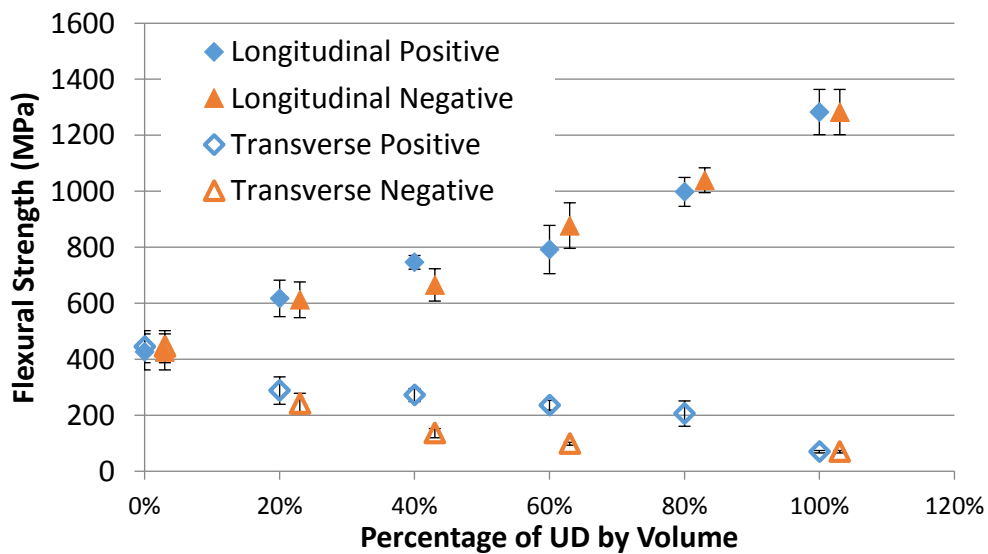


**Figure 6.12.** Flexural strength of asymmetric UD-DFC hybrid architecture under positive and negative bending (offset +3%). Varying the percentage of UD by volume, with the remainder DFC

The flexural moduli and flexural strength are shown in **Fig. 6.11** and **Fig. 6.12**, respectively. Although there was no statistical difference between positive and negative bending strengths, there were visible differences in the failure mechanisms experienced for each:

- In positive bending, a linear flexural stress/strain curve is observed (*Fig. 6.15*), with the peak coinciding with the sudden tensile failure of the DFC material on the tensile surface, *Fig. 6.13*. The crack propagates through-thickness before traveling along the interface with the continuous fabric.

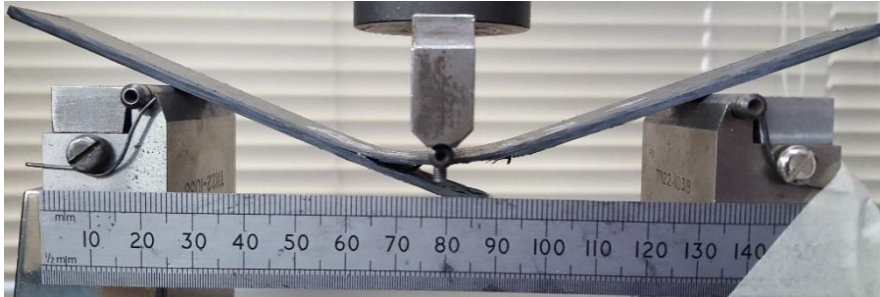
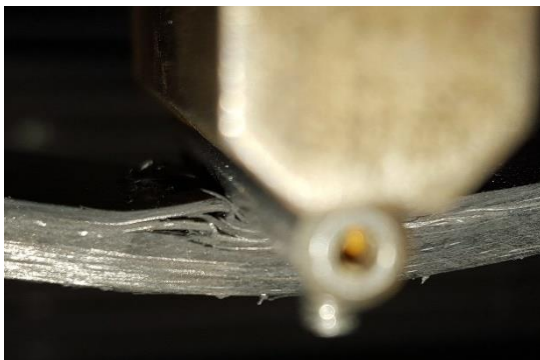


**Figure 6.13.** Tensile failure of the DFC material during positive three-point bend testing of asymmetric hybrid fibre architecture with 40% UD content

- The flexural stress/strain curve in negative bending also showed linearity, such as in *Fig. 6.15*. At the peak of this curve, an initial crack forms within the DFC under compression failure. The DFC fibre bundles buckle under the compression of the bending, as shown in *Fig. 6.14*. As the fibre bundles buckle, the crack propagation is much slower than if they were in tension and results in more progressive failure than in positive bending.



**(a)**



**(b)**

**Figure 6.14.** Compressive failure of DFC within asymmetric hybrid fibre architecture (40% UD content) experiencing negative bending

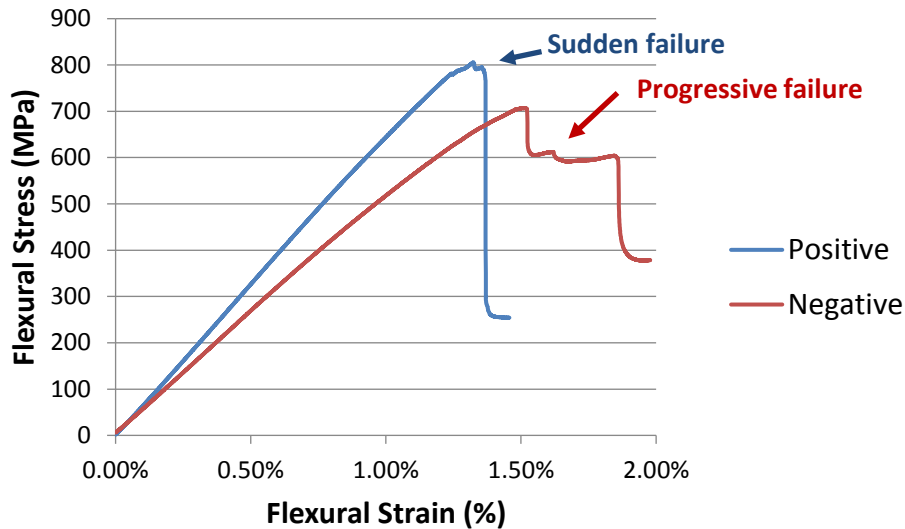


**Figure 6.15.** Examples of flexural stress/strain curves for three-point bend tests of hybrid fibre architecture (40% UD content) in the longitudinal direction for positive and negative bending

For hybrid architectures with UD content between 40% and 60%, the transverse flexural properties are different between positive and negative bending. This is also a result of different failure mechanisms:

- In positive bending, fibre buckling was observed on the continuous surface. The transverse fabric appears to weak spots within the resin rich regions between each tow for delamination to initiate, such as in **Fig. 6.16**. Final failure was sudden and under tension in the DFC region.

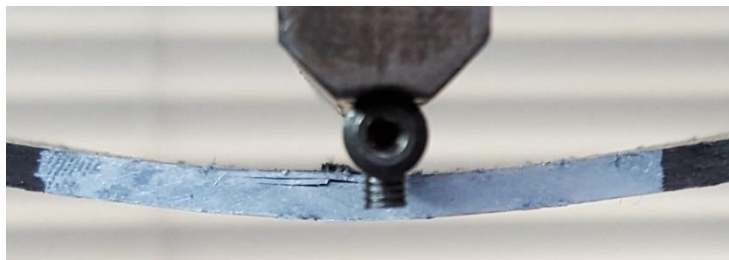


**Figure 6.16.** Buckling of the transverse UD fibres within hybrid fibre architecture (40% UD content) exhibiting positive bending

- In negative bending, cracks initiated at the surface in the resin rich regions between the transverse tows at the surface, **Fig. 6.17**. This is attributed to the low fracture toughness in the transverse direction. Cracks initiated at a much

lower strain than in positive bending, and resulted in very progressive failure under tension. This is shown in the flexural stress/strain curves in *Fig. 6.18*, which indicate that fracture initiates at a lower stress than the maximum stress.

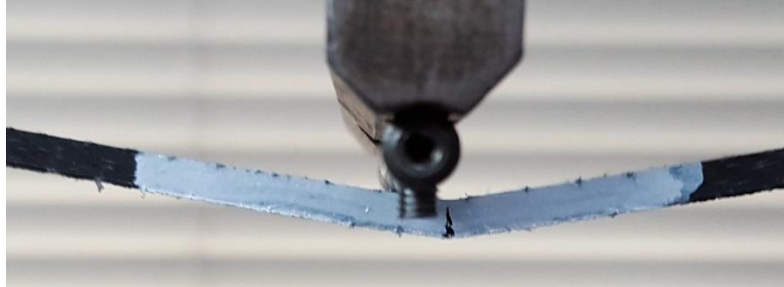


*Figure 6.17. Failure of the transverse UD fibres under tension within hybrid fibre architecture (40% UD content) exhibiting negative bending*

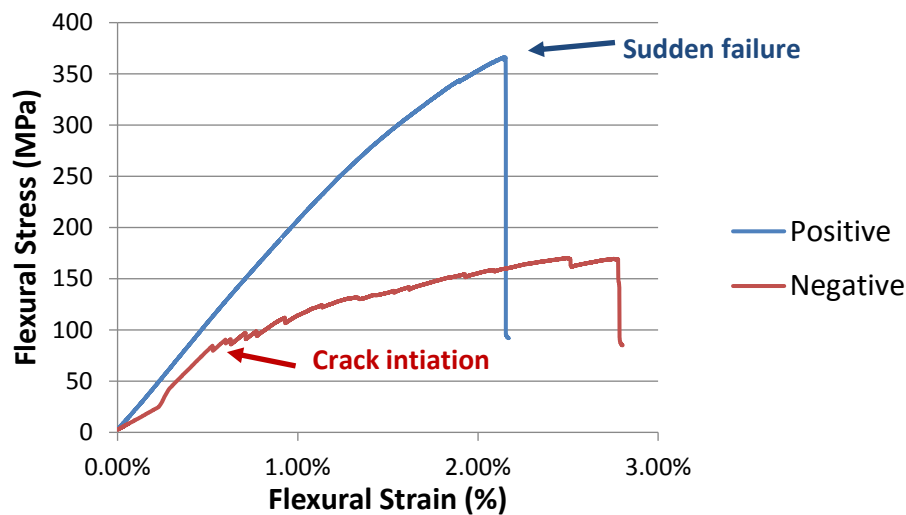


*Figure 6.18. Examples of positive and negative flexural stress/strain curves for three-point bend tests of hybrid fibre architecture (40% UD content) in the transverse direction.*

### 6.4.3 Joint design: Effect of step size

#### 6.4.3.1 Mechanical performance

Micrographs for varying step sizes (*Fig. 6.19*) show the through-thickness interface between the unidirectional plies and the discontinuous DFC. There is significant ‘swirling’ of the discontinuous fibres for a UD step size of 0mm, *Fig. 6.19 (a)*, which results in varying fibre content within the discontinuous region. The discontinuous

material is initially thicker and therefore experiences higher compressive forces at a shorter stroke during the compression stage. This results in DFC material flowing towards the thicker sections of the compound (from right to left in the micrographs). Similar swirling was also observed in *Chapter 5* when the charge coverage was reduced to just 40% of the tool area, but it is exacerbated here as the discontinuous fibres are encouraged to flow over a steep change in gradient at the end of the UD ply stack. This gradient is reduced as the step size increases, therefore this reduces the observed levels of turbulence in the DFC material, as shown in *Fig. 6.19 (b-e)*.

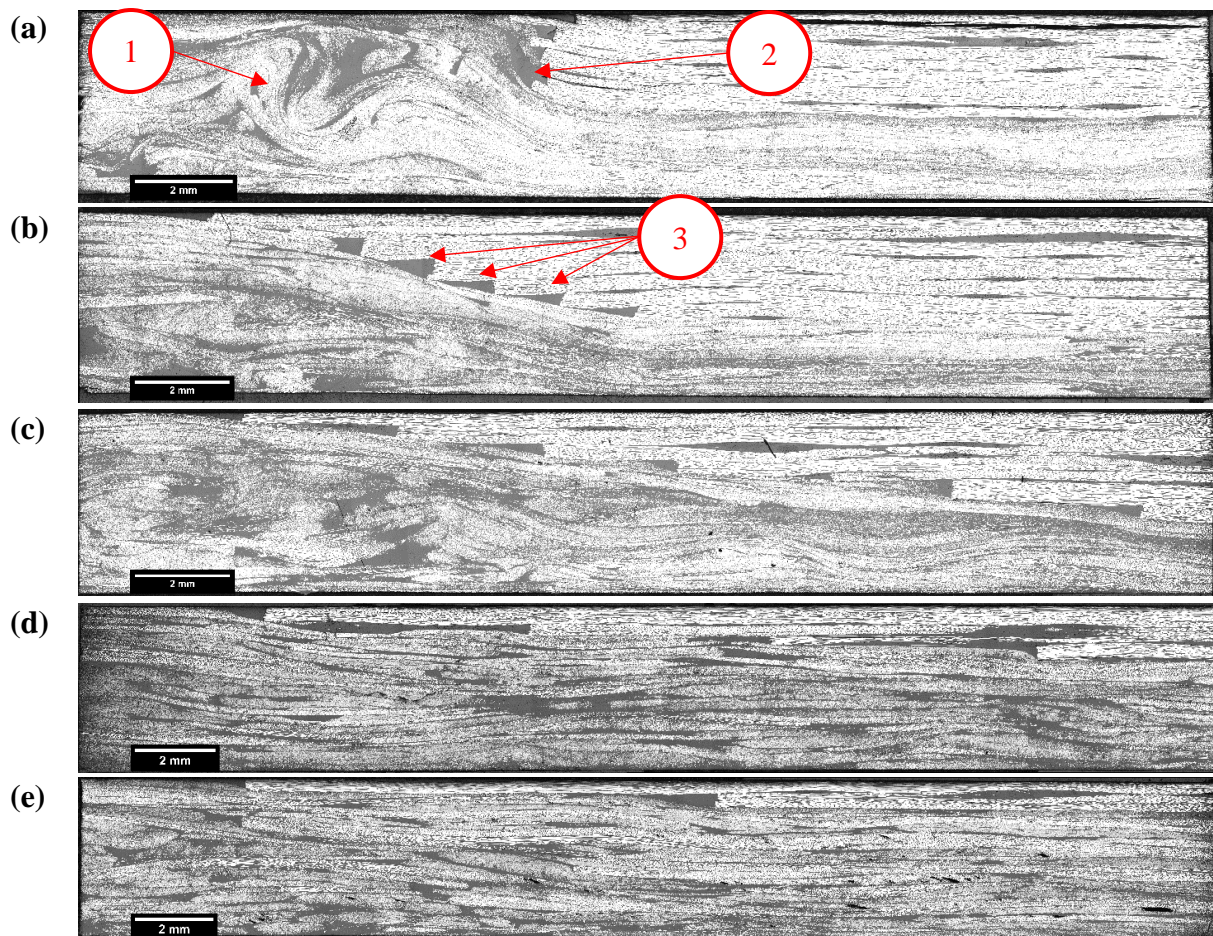


**Figure 6.19.** Micrographs (5x magnification) of stepped unidirectional/discontinuous carbon fibre joints produced by co-compression moulding: (a) 0mm, (b) 1.5mm, (c) 3mm, (d) 6mm and (e) 12mm step sizes. Point 1 indicates the fibre swirling and Points 2 and 3 indicate some locations of resin richness at the end of each ply drop.

A resin rich region was also noted at the end of each ply drop. The shape of the resin rich region varies depending on the orientation of the discontinuous fibre bundle that bridges the end of the continuous fibre ply. Where fibre bundles are parallel to the flow

direction along the joint a large, triangular resin rich region forms in the enclosed area, shown in *Fig. 6.20 (a)*. Step sizes shorter than the fibre bundle length (25mm) will experience a greater frequency of these larger triangular resin rich regions because each longitudinally orientated fibre bundle encloses multiple ply ends. These are less frequent when the step size is increased because the fibre bundles compact parallel to the ply direction. Perpendicular fibre bundles to the flow direction over the joint have a significantly smaller resin rich region as the fibre bundle is pushed closer to the ply end, *Fig. 6.20 (b)*. Although the size of the resin rich region is reduced, this is still an area of weakness due to the transverse orientation of the fibres. Steeper joint gradients, with a shorter step size, also contain a greater number of fibre bundles that enclose multiple ply ends, shown in *Fig. 6.20 (c)*.

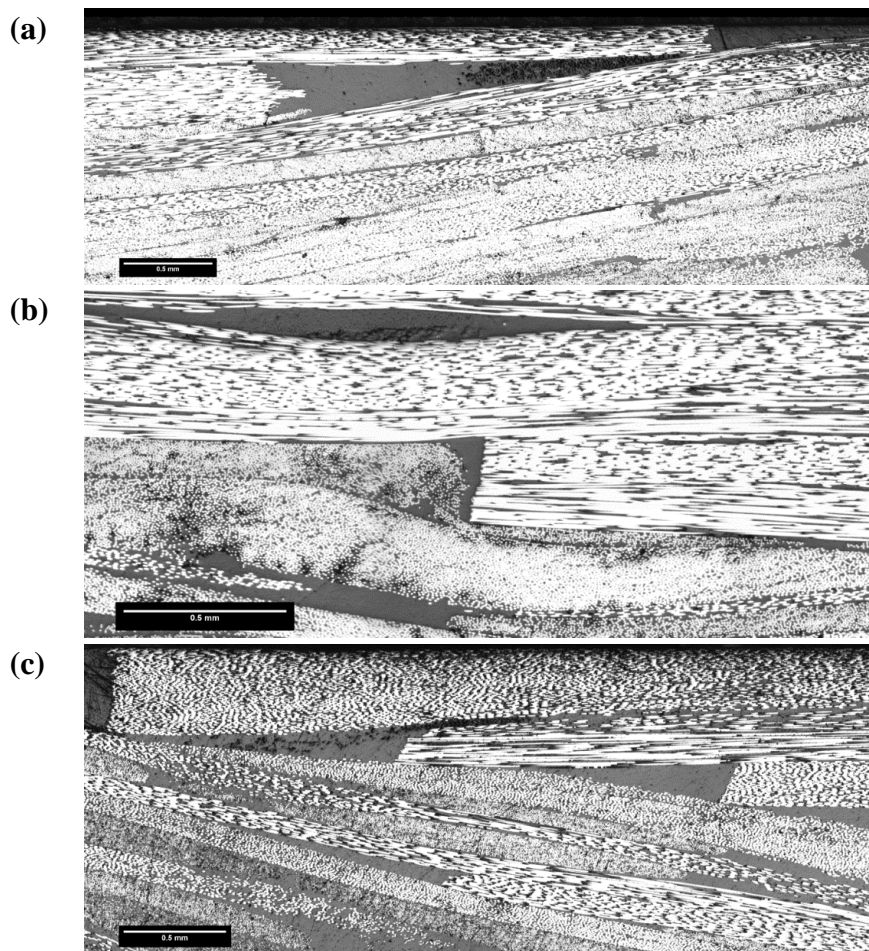


*Figure 6.20. Varying size and shape of ply end resin rich regions where bridging fibre bundles are orientated parallel to the flow direction (a), perpendicular to the flow (b) and enclose the ends of multiple plies around a joint with a shorter step size (1.5mm) (c).*

Flexural properties of the stepped joints have been compared to the baseline DFC. These are shown by *Fig. 6.21* and *Table 6.4*. The flexural modulus increases linearly with increasing step size. The ratio of step size to ply thickness (S-T ratio) needs to be greater than 5:1 (step length of 1.5mm), to maintain a higher flexural modulus than the DFC material. However, the flexural strength required an S-T ratio greater than 20:1 (step length of 6mm) to exceed the baseline flexural strength of the DFC.

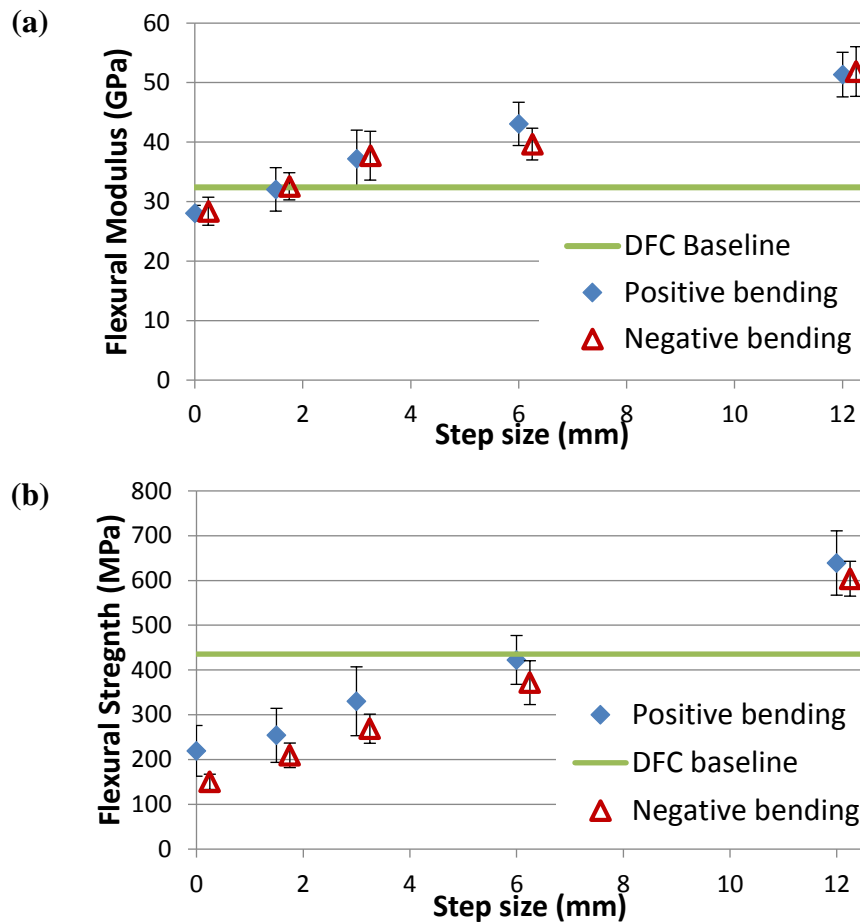


**Figure 6.21.** Flexural properties of UD/DFC stepped joints in positive and negative bending directions for varying step size. N.b. negative bending points are offset by +0.25mm for clarity. DFC baseline at 32.4GPa  $\pm$ 4.6 modulus and 435.5MPa  $\pm$ 60.4 strength.

Although there was no significant difference between the positive and negative bending directions in terms of flexural modulus, the flexural strengths were affected due to a change in failure mechanism, *Fig. 6.21 (b)* and *Table 6.4*. During positive bending, the UD fibres on the upper surface were in compression and failure occurred due to tension

in the DFC material. For shorter step sizes, < 6mm, it was observed that most failures occurred away from the joint because of the non-uniform bending moment caused by the asymmetric laminate, shown in **Fig. 6.22 (a)**. As the step size increased, the failure region moved closer to the load point, exhibiting buckling in the UD laminates and some delamination, as seen in **Fig. 6.22 (c)**. However, in negative bending tension in the UD fibres increased the stress in the resin rich region at the end of the surface laminate. As this resin rich region fails, the crack propagates along the boundary between the continuous and discontinuous fibres, as can be seen in **Fig. 6.22 (b) and (d)**. This change in failure mechanism reduced the flexural strength by approximately 50MPa in the negative bending direction compared to the positive direction.

**Table 6.4.** Flexural properties of UD/DFC stepped joints bent about the centre of the length of the joint during three-point bend testing in the positive and negative bending directions

Step size:Ply thickness Ratio		No Steps	5:1	10:1	20:1	40:1
Step size (mm)		0	1.5	3	6	12
Positive bending	Modulus (GPa)	28.06	32.06	37.23	43.06	51.35
	St. dev (GPa)	1.31	3.65	4.79	3.63	3.75
	CoV (%)	4.66%	11.39%	12.86%	8.44%	7.30%
	Strength (MPa)	219.5	254.1	330.2	422.5	639.0
	St. dev (MPa)	56.6	60.4	76.9	54.6	71.8
	CoV (%)	25.80%	23.76%	23.29%	12.91%	11.24%
Negative bending	Modulus (GPa)	28.38	32.57	37.72	39.67	51.87
	St. dev (GPa)	2.36	2.28	4.10	2.67	4.18
	CoV (%)	8.31%	7.01%	10.87%	6.74%	8.05%
	Strength (MPa)	150.3	209.5	268.9	371.8	603.9
	St. dev (MPa)	17.0	27.4	32.5	49.0	38.9
	CoV (%)	11.34%	13.09%	12.08%	13.17%	6.44%

When the hybrid plaques were subjected to an axial load, it was found that the effects of the joint size were significant as the complex structure prevents direct characterisation of the material response. The tensile modulus exceeds that of DFC (36.3GPa  $\pm$ 3.3GPa) with an S-T ratio of just 5:1 (step length of 1.5mm). However, the ultimate tensile strengths, **Fig. 6.23** and **Table 6.5**, for the hybrids with stepped joints are significantly lower than the DFC baseline (323MPa  $\pm$ 27MPa). This reduction in strength is the result of the resin rich regions that forms at the end of the surface UD

ply, which are the site for crack initiation, *Fig. 6.24*. However, there is a distinguishable trend with increasing step length as the taper angle reduces, which reduces the stress concentration at the end of each ply and facilitates a more gradual transition from high stiffness to low stiffness material. The peel stress and the associated tensile stress at the end of the UD surface ply decrease with increasing step size. The crack propagates along the resin rich path along the joint interface at the end of each ply step (*Fig. 6.25*).

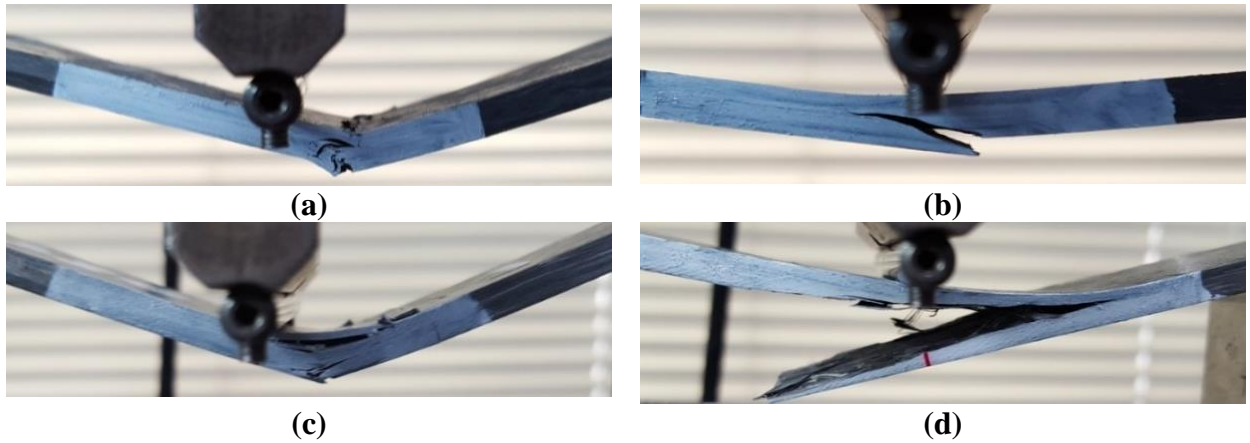


**Figure 6.22.** Photographs of examples of failure mechanisms for step size 5:1 (1.5mm) in positive (a) and negative (b) bending directions, and step size 20:1 (6mm) in positive (c) and negative (d) bending directions.

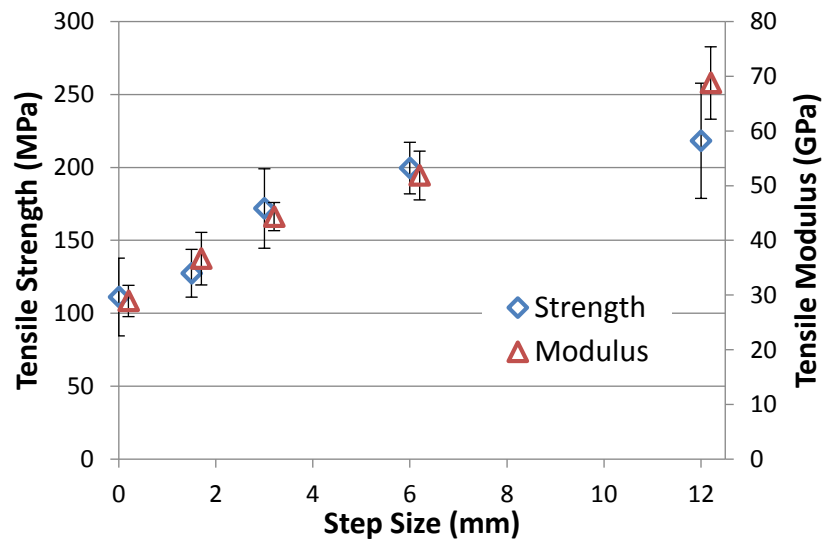


**Figure 6.23.** Tensile strengths and tensile modulus with strain measured by extensometer (with offset step size by +0.2mm) of UD/DFC stepped joints for varying step size.

Out-of-plane strains were evident in the laminate when in-plane tensile loads were applied, due to the asymmetry of the layup. This indicates that the flexural testing, characterising the structural response, is more appropriate for investigating the mechanical performance of joint design. This caused failure at lower tensile strengths than expected, i.e. lower than the tensile strength of the DFC. This was investigated further using electronic speckle pattern interferometry (ESPI).

**Table 6.5.** Tensile properties of UD/DFC stepped joints with the centre of the length of the joint aligned with the centre of the gauge length (50mm from the grips)

Step size:Ply thickness Ratio		No Steps	5:1	10:1	20:1	40:1
Step size (mm)		0	1.5	3	6	12
Tensile properties	Modulus (GPa)	28.92	36.65	44.35	51.85	68.77
	St. dev (GPa)	2.86	4.81	2.58	4.46	6.61
	CoV (%)	9.89%	13.12%	5.81%	8.60%	9.62%
	Strength (MPa)	111.2	127.5	171.8	199.5	218.3
	St. dev (MPa)	26.7	16.4	27.2	17.7	39.5
	CoV (%)	23.98%	12.84%	15.84%	8.86%	18.09%



**Figure 6.24.** Time stepped images of joint specimen (step size = 0mm) showing the specimen at the start of the test (0s), crack initiation (22s), sudden crack propagation (36s) and total failure (47s)

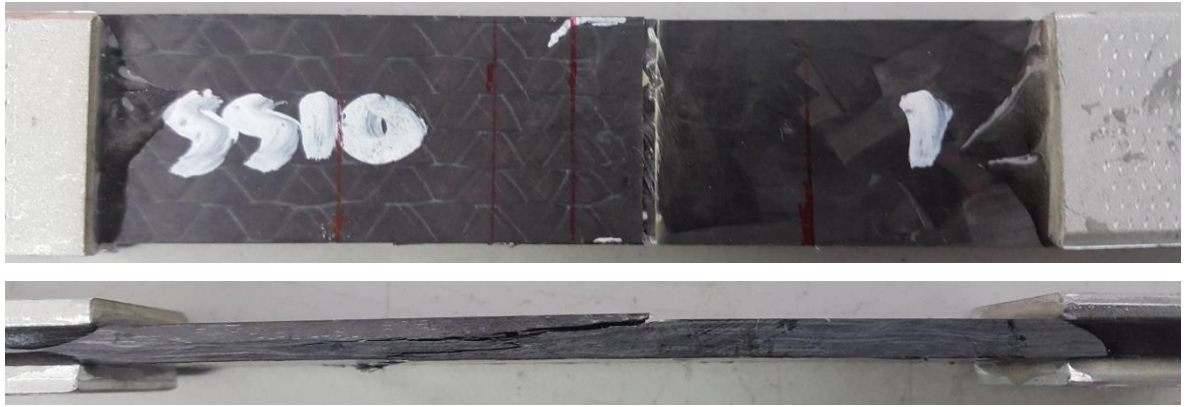


*Figure 6.25. Tensile failure of UD/DFC stepped joint with a 10:1 step size (3 mm).*

### 6.4.3.2 In-plane strain measurement

The first investigation using ESPI was used to analyse the strain distribution to the ‘front’ and ‘back’ planar faces of specimens with a stepped joint, where the ‘front’ face refers to the surface containing the UD fabric. Results are shown in *Fig. 6.26* and *Fig. 6.27*, for the front and back faces respectively. The joint between UD fabric and chopped fibres is clearly visible by a transition from a uniformly distributed strain of the UD material in comparison to the large local variations within the random material. The axial strain distribution experiences both positive and negative variations under the 5kN axial load.

The least uniform axial strain distribution was experienced within the random material. At the mesoscale, these large variations in local strain are the result of interactions between neighbouring short fibre bundles with dissimilar orientations. This produces local stiffness variations in the load direction and therefore shear between fibre bundles which leads to micro-bending of the chopped fibre bundles.

The strain measurements were averaged across the width of the specimen to produce a strain profile along the length of the specimen, shown in *Fig. 6.26 (a)* and *Fig. 6.27 (a)*. The high stiffness of the UD material results in a low average axial strain when observing the front face in contrast, mostly <2 microstrain, to the greater average axial strain on the back face, <8 microstrain, caused by the lower stiffness of the chopped architecture. This difference between front and back surfaces is also shown in *Fig. 6.26 (c)* and *Fig. 6.27 (c)*, respectively. These figures have a magnified scale to increase the

contrast of the image. It can also be noted diamond-like pattern on the back surface strain measurements is the result of the low stiffness stitching material within the UD fabric.

The steps in UD material can also be noted by the strain profile, shown by *Fig. 6.28* which magnifies the average axial strain profile of the front face. The peaks in strain indicate the resin rich regions at the ply ends indicated approximately by the red arrows, the largest of which is shown at the first step between the first and second plies, 7.8 microstrain.

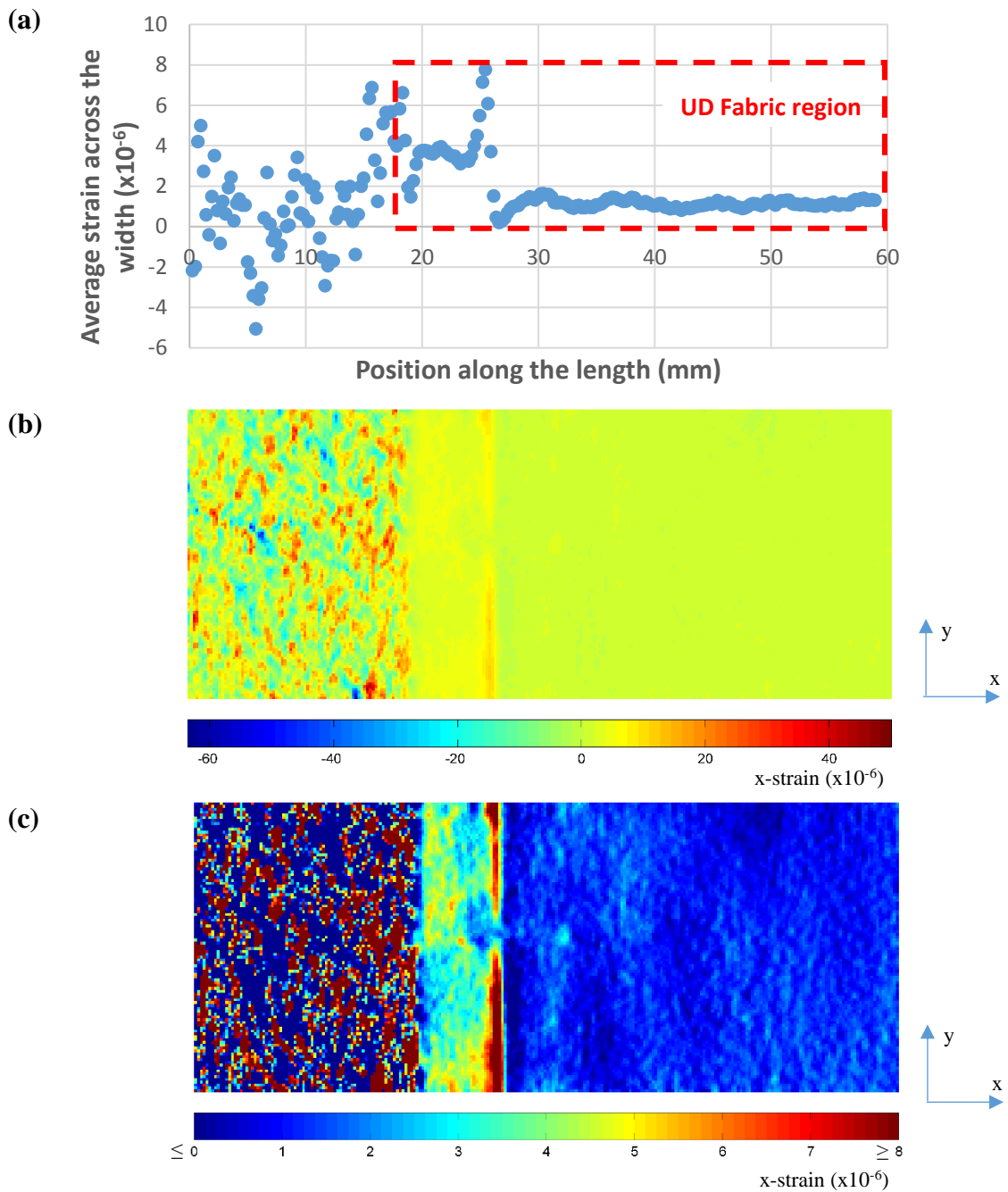


**Figure 6.26.** EPSI axial strain results of DFC/Unidirectional hybrid carbon fibre architecture, stepped joint with a step size to ply thickness ratio of 20:1 (6mm). Images (b and c) are of the front surface of the specimen, where the unidirectional fibres are on the visible surface, under 5kN axial load (x-direction). The field of view of 60mm x 25mm. The graph (a) shows the average axial strain of the data points across the width of the specimen (y-direction) with respects to its position along the length (x-direction). The axial strain distribution (b) is shown with a colour map scale determined by the maximum and minimum axial strain. Distribution (c) uses the range of 0-8  $\times 10^{-6}$  axial strain.

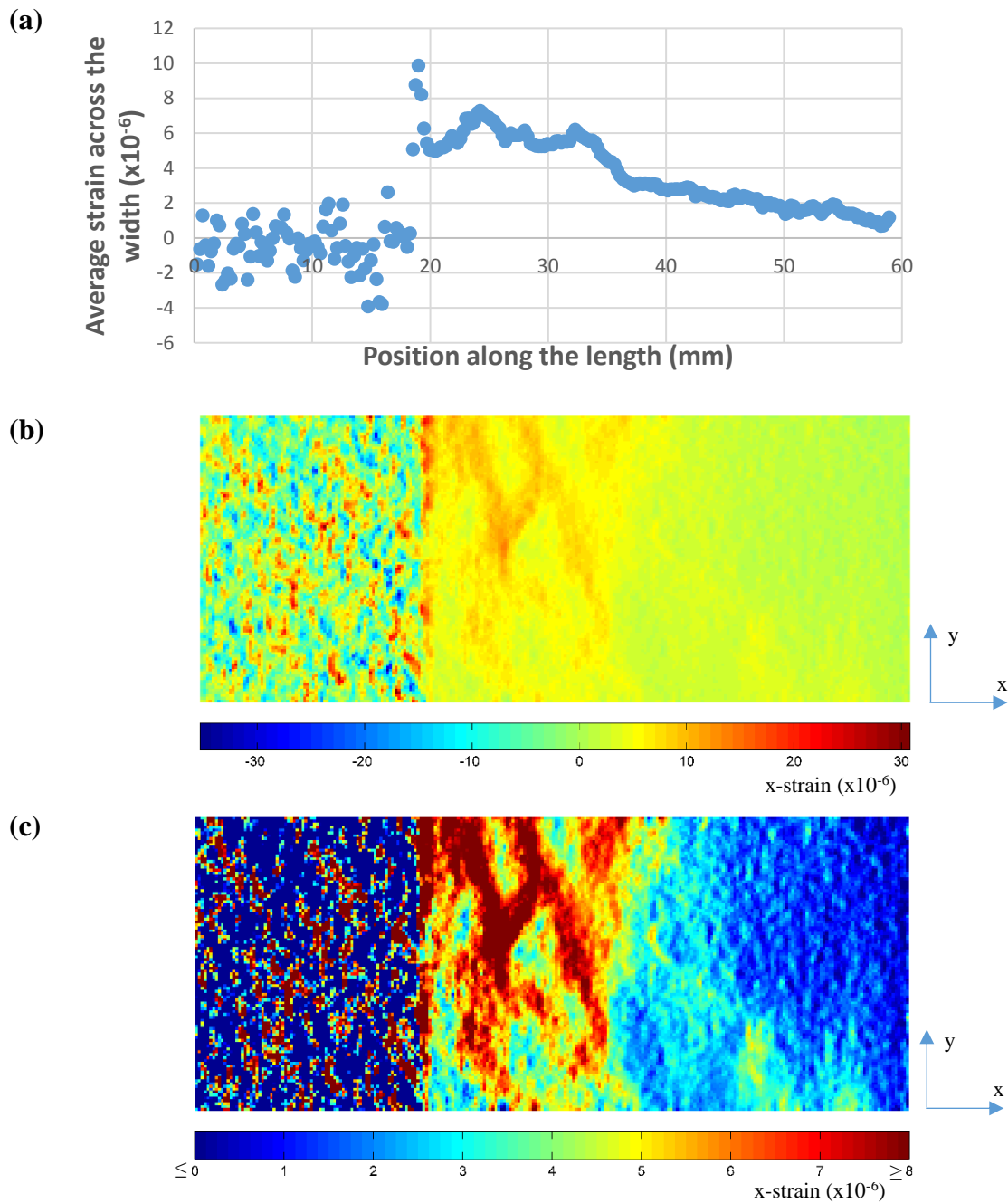


**Figure 6.27.** EPSI axial strain results of DFC/Unidirectional hybrid carbon fibre architecture, stepped joint with a step size to ply thickness ratio of 20:1 (6mm). Images (b and c) are of the back surface of the specimen under 5kN axial load (x-direction). The field of view is 60mm x 25mm. The graph (a) shows the average axial strain of the data points across the width of the specimen (y-direction) with respects to its position along the length (x-direction). The axial strain distribution (b) is shown with a colour map determined by the maximum and minimum axial strain.

Distribution (c) uses the range of  $0-8 \times 10^{-6}$  axial strain.

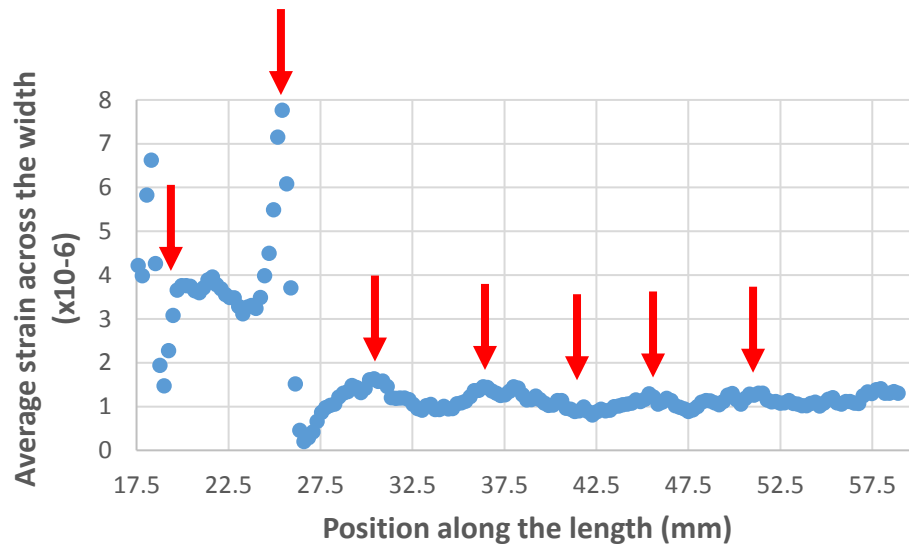


**Figure 6.28.** Average strain across the width of the specimen when looking at the front surface, with the unidirectional fabric on the surface. Results are magnified to show the average strain for the unidirectional fabric section of the fig. 6.27(a) indicated by the red dotted rectangle. Red arrows indicate the approximate locations of the end of each UD ply, indicated by the peaks in axial strain resulting from resin rich regions.

### 6.4.3.3 Out-of-plane characterisation

The dissimilar strains between the front and back faces induces macroscale out-of-plane shear about the joint. The tensile properties in **Fig. 6.23** and **Table 6.5** are therefore artificially low, as the apparatus is unable to apply pure tension over the complete length of the specimen. Continuous-discontinuous joints therefore require further investigation to fully understand their tensile performance. A simple FE model, detailed in *section 3.6*, was produced to understand the axial, normal and shear stress distributions along each ply. However, this does not account for the microstructural variations such as resin richness and local fibre bundle orientation distribution within the DFC material. ESPI tests were therefore performed to experimentally characterise the strains on the out-of-plane surface of the specimens.

**Fig. 6.29** shows examples of the stress distributions along each of the plies using the joints shown in **Fig. 3.30**, where the ply ends were synchronised and with an S-T ratio of 20:1 (6mm step size). It should be noted that the x-position (X) along the specimen,

is the position of the specimen when in its undeformed state as to remove strain variations from the curve. These results have been normalised because there is no depth to the 2D model and does not account for microstructural variations. This was performed by dividing each calculated stress by the average stress across all the plies. This enables visualisation of the stress distribution of each ply to compare the magnitude of stress peaks between each ply.

Across each of the stresses, the concentration of the stress risers through the thickness (from ply 1 to ply 7) reduces as the location of the peaks is dependent on the ply drop locations. The combination of each axial, shear and peel stress concentrations that form at the ply ends suggests that when the cracks propagate from the end of the surface ply and along the interface, they exhibit mode-I and mode-II failure. The peak axial stresses form in the continuous material just before the transition to discontinuous material, *Fig. 6.29*. The axial stress then reduces in the discontinuous region as a result of the reduction in material stiffness. The magnitude of these peaks and reductions in axial stress, relative to the average axial stress, are the smallest of the three stresses investigated.

Peak shear stress forms just before and after the transition between materials when the ply ends are synchronised ( $X=50\text{mm}$ ). However, when steps are introduced the largest shear stresses are observed along the ply centrelines at the location of the neighbouring ply ends, *Fig. 6.29*. For example, the peaks in shear stress along the centreline of ply 4 arise near the ends of ply 3 and ply 5. This increases the distance (in the x-direction) between the positive and negative shear stress risers in each ply (approximately 12mm), in comparison to synchronising all ply ends at one location (approximately 0.5mm). *Fig. 6.30* shows the shear stress distribution of each step size. Stress risers are seen at the upper and lower interfaces of each ply end. However, the peak positive stress of ply 1 (surface) is less than that of end of ply 2, moving peak stresses away from the surface of the composites.

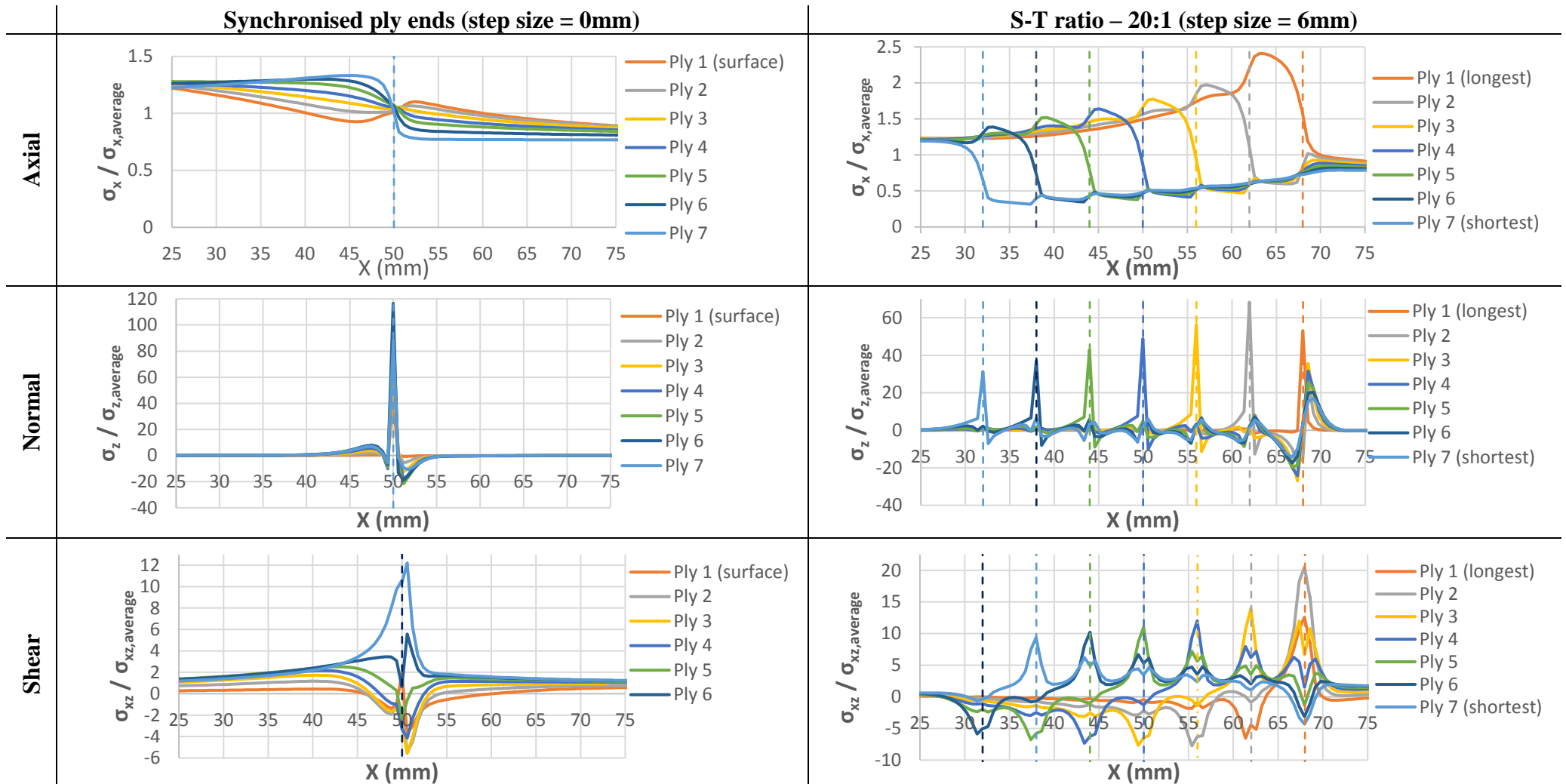


**Figure 6.29.** Normalised axial, normal/peel and shear stress distributions from 25mm to 75mm along the continuous-discontinuous hybrid stepped joints with synchronised ply ends (step size = 0mm) and S-T ratio of 20:1 (step size = 6mm). Stress distribution curves are positioned along the centreline of each ply, where ply 1 is the surface ply/longest ply and ply 7 is positioned at the UD-DFC interface (shortest ply). Each ply end is indicated by the dashed lines.

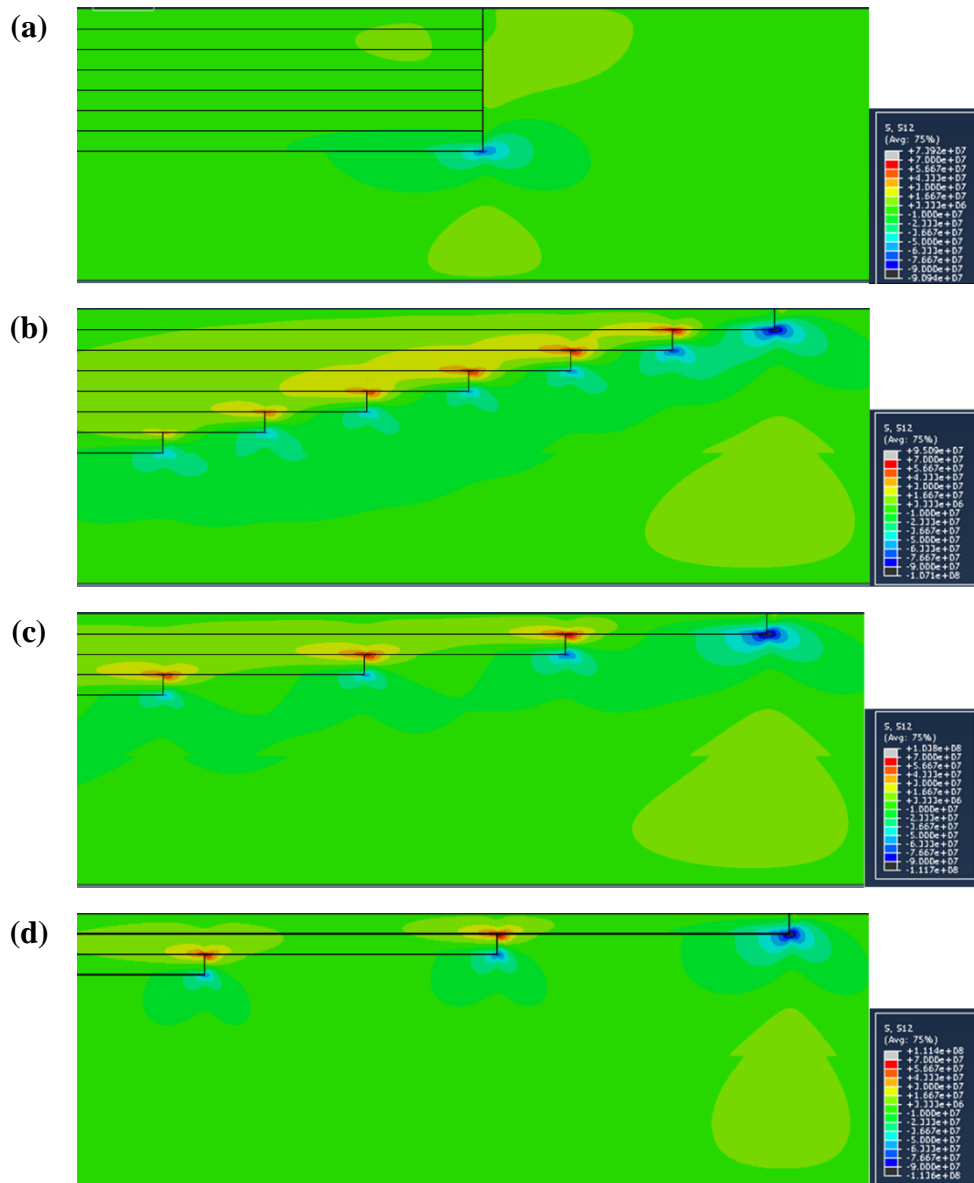


**Figure 6.30.** Shear stress,  $\sigma_{xz}$ , results from the 2D FE models of continuous-discontinuous hybrid joints with increasing step sizes from: (a) no steps (step size = 0mm), (b) 5:1 S-T ratio (step size = 1.5mm), (c) 10:1 S-T ratio (step size = 3mm) and (d) 20:1 S-T ratio (step size = 6mm)

The greatest increase in stress magnitude along the ply centrelines was experienced in the normal direction (peel stress). This forms at the transition between the dissimilar materials of each ply, **Fig. 6.29**. As well as reducing the concentration of the stresses, the magnitude of the peak peel stress is approximately halved by stepping the joint with an S-T ratio of 20:1 rather than synchronising all of the ply ends. **Fig. 6.31** shows that in addition to peel stress risers at the ends of each ply, there are also stress concentrations that form in the DFC material beneath each ply end. When the step sizes

are small (<10:1 S-T ratio), these stress concentrations interact with each other which would provide a plane of weakness once failure initiates. However, this interaction can be reduced or removed by increasing the step size (>10:1 S-T ratio).

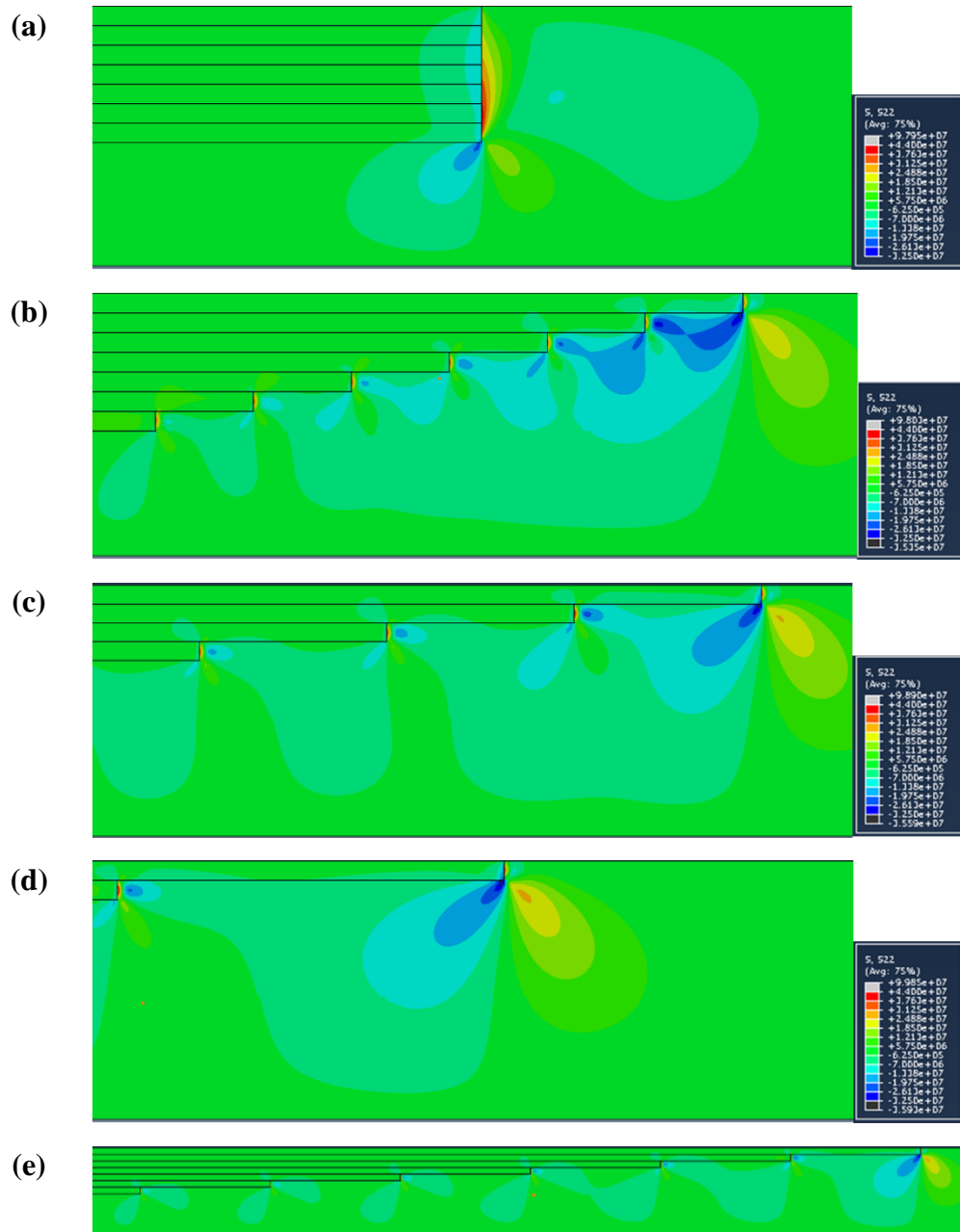


**Figure 6.31.** Normal/Peel stress,  $\sigma_z$ , results from the 2D FE models of continuous-discontinuous hybrid joints with increasing step sizes from: (a) no steps (step size = 0mm), (b) 5:1 S-T ratio (step size = 1.5mm), (c) 10:1 S-T ratio (step size = 3mm) and (d) 20:1 S-T ratio (step size = 6mm). (e) shows a larger field of view of the results for an S-T ratio of 20:1.

From the ESPI results shown in *Fig. 6.32*, the ends of the surface ply experienced a large axial strain because of the resin rich region in this location. This is the reason failure initiates from the surface at the interface between the continuous and discontinuous fibre architecture. The largest of these axial strains is seen within the ‘No Step’ specimen where all ply ends are synchronised *Fig. 6.19 (a)*. *Fig. 6.32* indicates that the size and magnitude of the axial strain at the end of the surface ply reduces dramatically from approximately 33 microstrain to 8 microstrain (for an applied load of 5 kN) as the step size increases from 0 mm to 3 mm (S-T ratio of 10:1). As the step size increases further, the magnitude of the maximum axial strain at the surface remains at approximately 8 microstrain for a 5 kN load. This agrees with the joint design guidelines, which suggest that the joint angle should not exceed  $7^\circ$  [97, 107], supporting the conclusion that the S-T ratio must be greater than 8:1. The FE results also agree that peel stresses at the end of each ply have less interaction between stress concentrations for the step sizes greater than 10:1 S-T ratio.

The specimen asymmetry causes out-of-plane displacement and therefore induces a bending stress when a tensile load is applied. This confirms our conclusion that the tensile strengths are influenced by the stresses that arise from bending producing artificially low results. To obtain correct results for the tensile strengths of hybrid architecture, the joint needs to be symmetrical. This however would be difficult to align joints on opposing surfaces.

When comparing ESPI strain results to the failure locations of the specimens, the axial strains at the end of the plies were the dominate cause of failure when the S-T ratio was less than or equal 10:1 ( $\leq 3\text{mm}$ ), resulting in failure at the joint for every specimen. However, failure within the DFC material commonly occurred for S-T ratios greater than or equal to 20:1 ( $\geq 6\text{mm}$ ), due to through-thickness shear and variability within the discontinuous material, shown in *Fig. 6.32*. This resulted in failure within the DFC component between the joint and the tensile grips. This can be seen in *Fig. 6.33*.

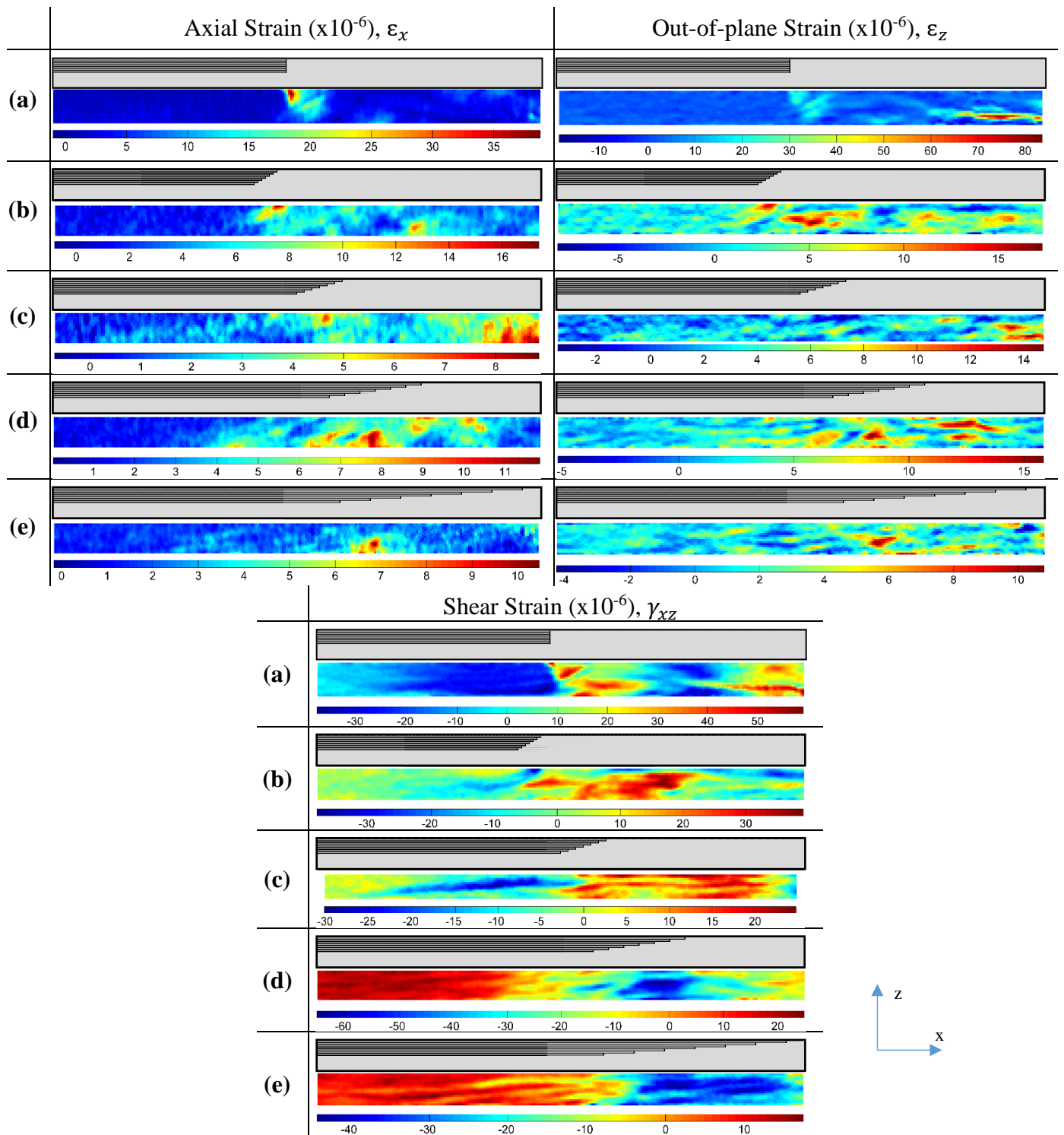


**Figure 6.32.** Through thickness axial ( $x$ -direction), out-of-plane ( $z$ -direction) and shear strain ( $xz$ ) distributions (ESPI results with 60mm x 4mm view window, 5kN axial load) for each of the step size to ply thickness ratio: (a) No step, (b) 5:1, (c) 10:1, (d) 20:1 and (e) 40:1 (ply thickness - 0.3mm) and the schematic diagrams indicate the position of each step



**Figure 6.33.** Failure of a tensile specimen with a step size:ply thickness ratio of 20:1 (6mm), where failure arises within the DFC region

#### 6.4.4 Joint Design: Effect of joint geometry

The design of the joint (stepped, tapered or alternating (*Fig. 6.2*)) was varied to change the position of the ends of the dropped plies in relation to the interface. The aim was to reduce the concentration of ply ends near to the DFC/UD interface to deflect crack growth. The tapered and alternating arrangements only had one and two ply drops at the DFC/UD interface, respectively. The remaining plies were all enclosed by other plies. This can be seen in the micrographs, *Fig. 6.34*, showing the joint geometries. This shows the large, triangular resin rich region that are produced by the enclosed ply drops.

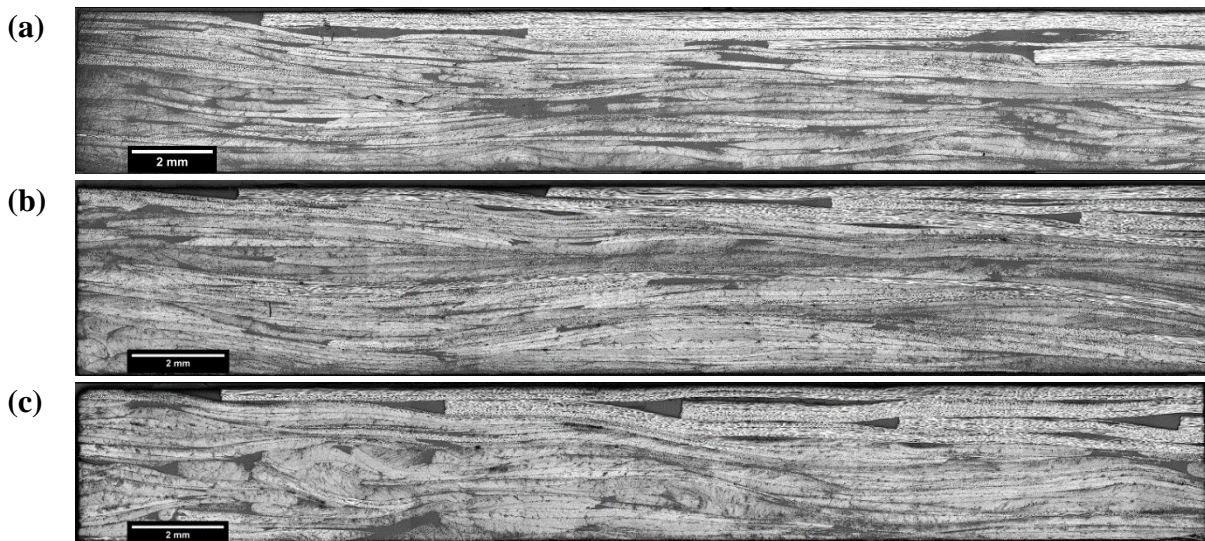


**Figure 6.34.** Micrographs of the tested joint geometries, each with a step size of 20:1 (6mm): Stepped (a), tapered (b) and alternating (c)

The flexural moduli of the tapered and alternating geometries are shown in **Table 6.6** and **Fig. 6.35** and compared to those of the stepped joints. Tapering the joint provides a ‘smoother’ transition for the discontinuous architecture compared to a stepped joint, where the interface is more continuous in comparison to the steep gradients that form at the end of each ply within the stepped joints. Therefore, as the discontinuous fibre bundles flow in the direction of the joint, less out-of-plane misalignment of the fibres is exhibited. This results in a statistically significant ( $p < 1\%$ ) increase in the negative bending modulus from the stepped joint geometry to the tapered or alternating geometries, with a p-value of 0.0019 or 0.0006, respectively. This is less apparent in the positive bending direction, but the trend is still statistically significance ( $p < 5\%$ ), as the tapered joints have a greater flexural modulus than the stepped joints (p-value of 0.0450).

**Table 6.6.** Flexural properties of three UD/DFC joint geometries bent about the centre of the length of the joint during three-point bend testing in the positive and negative bending directions. All joint geometries have a step size to ply thickness ratio of 20:1 (6mm).

Joint Geometry	Stepped		Tapered		Alternating	
	Positive	Negative	Positive	Negative	Positive	Negative
Modulus (GPa)	43.06	39.67	46.63	45.01	45.57	48.07
St. dev (GPa)	3.64	2.67	2.21	2.24	3.22	3.69
CoV (%)	8.44%	6.74%	4.74%	4.98%	7.06%	7.68%
Strength (MPa)	422.5	371.8	411.4	402.6	446.3	436.1
St. dev (MPa)	54.6	49.0	53.6	23.3	40.5	20.3
CoV (%)	12.91%	13.17%	13.02%	5.78%	9.08%	4.65%

According to the ultimate flexural strengths in **Table 6.6** and **Fig. 6.36** joint design did not have a significant affect in positive bending. However, negative bending is largely influenced by crack deflection between the stress risers. All 7 ply ends are positioned at the joint interface for the stepped joint, whereas tapered joints only have one ply end at the joint interface, with the remaining ply ends at least one ply thickness away. The alternating joint contains 2 ply ends at the interface, but the others are up to 0.9mm (3 times the ply thickness) away from the interface. Within the alternating joints, the greatest number of continuous fibres therefore intersect any cracks that grow between the ply ends and the interface, preventing linear crack growth. This resulted in a

statistically significant increase under negative bending ( $p < 5\%$ ) compared with the stepped joints and alternating joints, with a p-value of 0.0200. Changing the geometry of the joint therefore reduces the difference between the positive and negative bending flexural strengths from 50MPa to approximately 10MPa. Additionally, although the increase in strength was small, it was sufficient to increase the flexural strength beyond the 436MPa baseline of the DFC material in both bending directions.

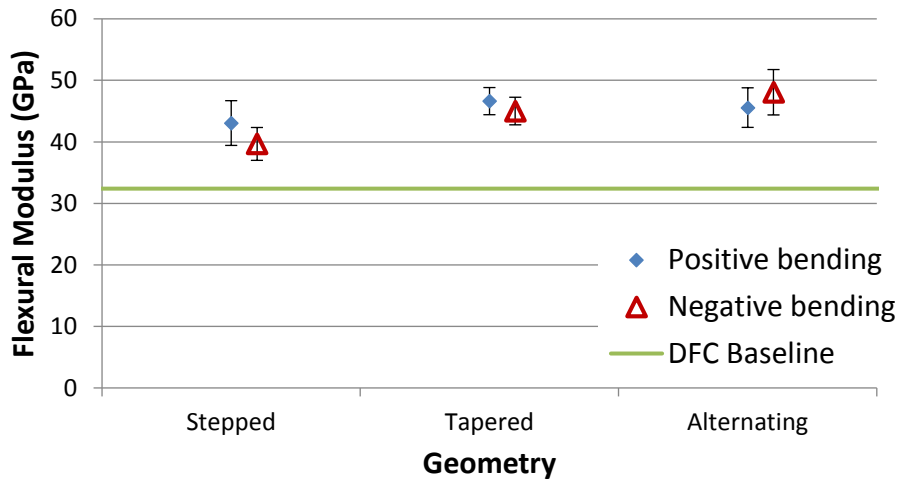


**Figure 6.35.** The flexural modulus of UD-DFC joint with varying geometry compared to the DFC baseline (32.4GPa  $\pm$ 4.6).

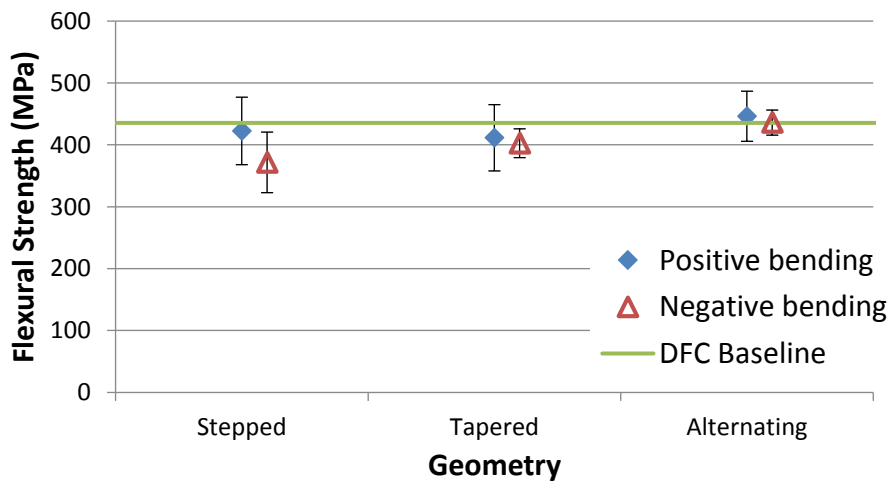


**Figure 6.36.** The flexural strength of UD-DFC joint with varying geometry compared to the DFC baseline (435.5MPa  $\pm$ 60.4)

Inspecting the effect of changing the joint geometry by tensile testing was limited by the variability of the results, because of the discontinuous nature of the material. There

was no significant difference between the tensile moduli for the three geometries. However, although the tensile strength of the stepped joint and the tapered joint showed a statistical increase ( $p < 5\%$ ) as a result of the number of experimental repeats (9 repeats), the error bars overlap considerably, shown in **Fig. 6.37**. Therefore, the 5-11% variations, shown in **Table 6.7**, are considerable enough to negate little observable increase in tensile strength.

As the tensile results showed no clear change in tensile performance, ESPI was used to further inspect the strain distribution to understand effect of the joint geometry. These results show no change in axial strain, 9 microstrain, at the end of the surface ply from stepped to tapered (A1 in **Fig. 6.38**). However, enclosing all ply drops away from the joint interface reduces the axial strain concentration around the resin rich regions by around 50%, 5 microstrain, compared to the stepped equivalent, 10 microstrain, (A2 in **Fig. 6.38**). This reduces the through thickness shear stresses, as shown **Fig. 6.38**.

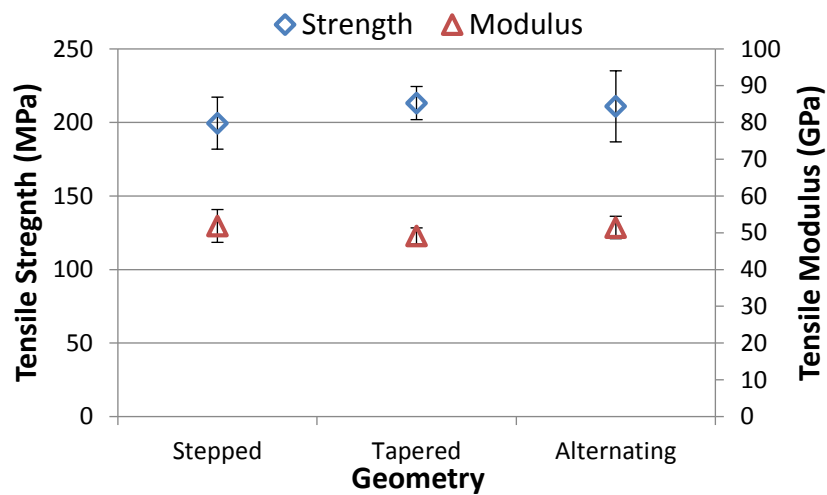


**Figure 6.37.** Tensile strength of different joint geometries and the tensile modulus measured by extensometers

**Table 6.7.** Tensile properties of three UD/DFC joint geometries with centre of the length of the joint positioned 50mm from each grip. All joint geometries have a step size to ply thickness ratio of 20:1 (6mm).

Joint Geometry	Stepped	Tapered	Alternating
Modulus (GPa)	51.85	49.13	51.44
St. dev (GPa)	4.46	2.19	3.05
CoV (%)	8.60%	4.46%	5.93%
Strength (MPa)	199.5	213.2	210.9
St. dev (MPa)	17.7	11.3	24.2
CoV (%)	8.86%	5.28%	11.45%

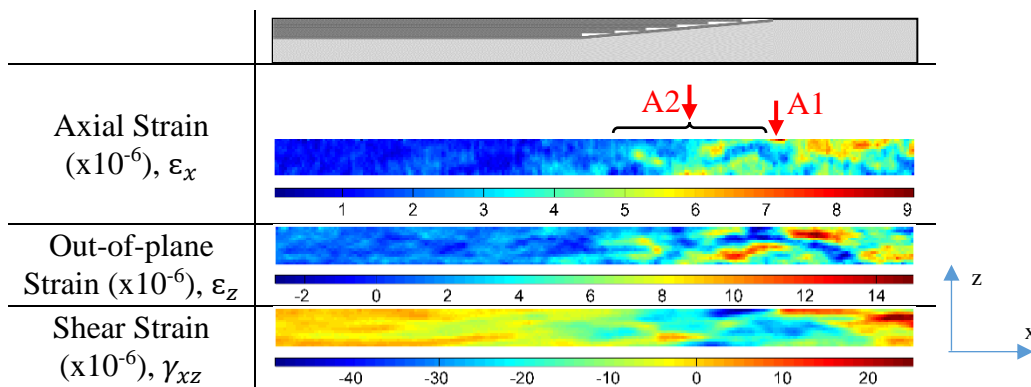


**Figure 6.38.** Through thickness axial, ( $x$ -direction), out-of-plane ( $z$ -direction) and shear strain ( $xz$ ) distributions (ESPI results with 60mm x 4mm view window) for tapered joint geometry with a 20:1 step size to ply thickness ratio (6mm)

#### 6.4.5 Continuous/discontinuous interfacial Analysis

The interfacial properties of the hybrid laminates were analysed by investigating the mode-I fracture toughness by double cantilever beam (DCB) testing. The average crack initiation force was determined from the peak loads. For the non-hybrid benchmarks, the discontinuous material required approximately 34N more than the UD interface to initiate crack growth for the 25mm wide specimens, shown by **Table 6.8**. The non-laminate structure of the discontinuous mesoscale architecture has a high resistance to crack initiation, indicated by the highest peak load recorded of all materials. A characteristic saw-tooth shape in the load-displacement curve is experienced, **Fig. 6.39**, because the random fibre architecture hinders crack propagation by a complex mixed failure mode at the crack front. Failure can occur in any resin rich regions at the interface, leading to sudden drops in load. It is possible for the crack to then encounter

a bridging bundle at the interface, in which case the load rises sharply until bundle failure occurs, shown by *Fig. 6.40 (b)*. The bridging bundles help to sustain high out-of-plane loads, initially minimising the rate of crack propagation [121]. Fibre bridging across the crack therefore results in the largest mode-I fracture toughness,  $G_{IC}$ , over the 100mm crack length (*Table 6.8*).  $G_{IC}$  is 23% higher for the DFC material than for the UD material, shown by *Fig. 6.41* and *Table 6.8*, which has a planar interface with no fibre bridging (*Fig 6.40 (a)*). Energy is therefore released more progressively as the crack propagates at a continuous rate, indicated by the green line on the load-displacement curve (*Fig. 6.39*).

*Table 6.8. Average crack initiation loads and mode-I fracture toughness results from DCB testing*

Interface	DFC	UD	Hybrid Architecture	
			Co-moulded	Pre-cured NCF
Crack Initiation Load (N)	125.33	91.35	105.37	57.99
St. dev (N)	14.37	1.70	13.77	6.75
CoV (%)	11.46%	1.86%	13.07%	11.64%
Mode-I fracture toughness, $G_{IC}$ (J/m <sup>2</sup> )	2689.78	2180.06	1940.85	1169.06
St. dev (J/m <sup>2</sup> )	469.24	143.13	117.71	154.50
CoV (%)	17.45%	6.57%	6.06%	13.22%

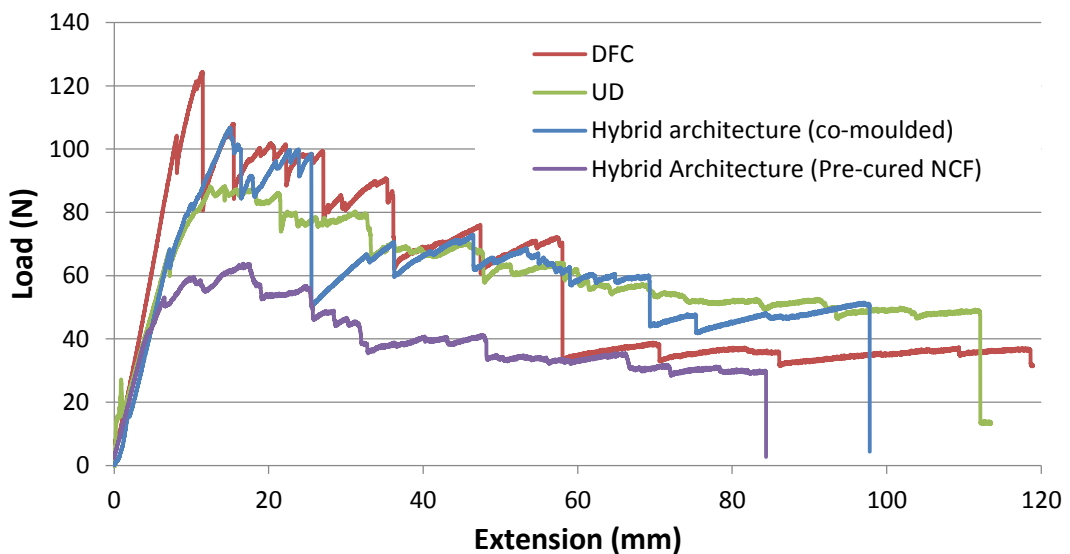


*Figure 6.39. Typical load vs extension graphs of each of the DCB tests for each interface*

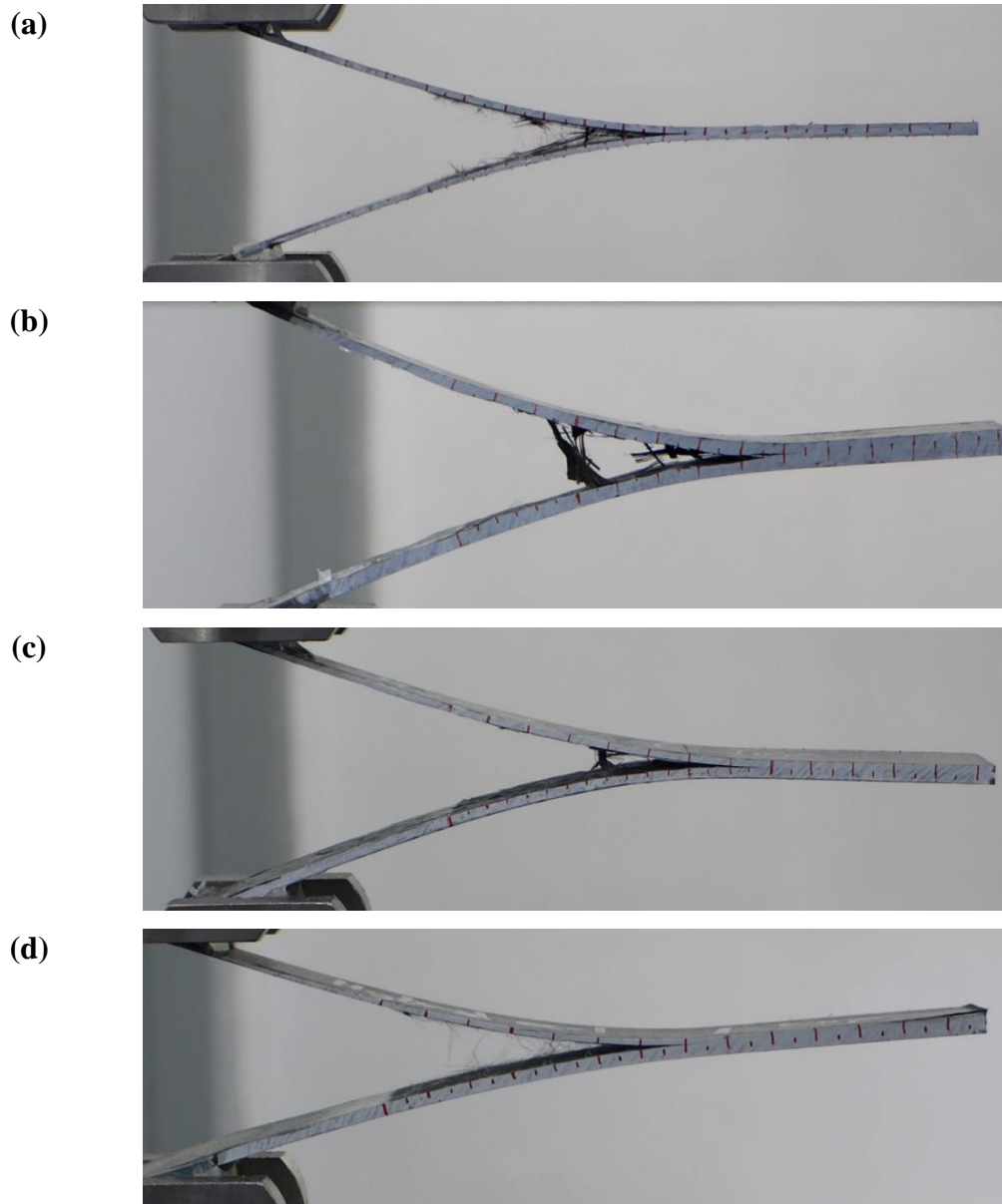


**Figure 6.40.** Photographs during the DCB testing of a UD interface (a), DFC centreline (b), co-moulded UD-DFC hybrid fibre architecture (c) and hybrid fibre architecture where the UD material was pre-cured before compression moulding (d). Red markings are positioned every 5mm from the position of crack initiation.

The crack initiation load for the co-moulded hybrid architecture is between the UD and DFC crack initiation loads, 105N. This implies that there is some interleaving of fibres at the interface, which disrupt the straight path for crack growth. As the bridged fibres fail the sudden release of energy results in high rate crack growth along the linear interface, similar to that observed for the DFC material. This results in a mode-I fracture toughness 11% lower than the UD plaque (*Fig. 6.41* and *Table 6.8*). This interleaving

however is eliminated if the UD material is pre-cured, as resin crosslinking is prevented between each of the materials and there is less disruption to the UD fibre architecture due to the moulding process. This scenario results in the least fibre bridging (*Fig 6.40 (d)*) and therefore exhibits the smallest crack initiation load and mode-I fracture toughness, which are 35% and 40% lower, respectively, than the co-moulded equivalent (*Fig. 6.41* and *Table 6.8*).

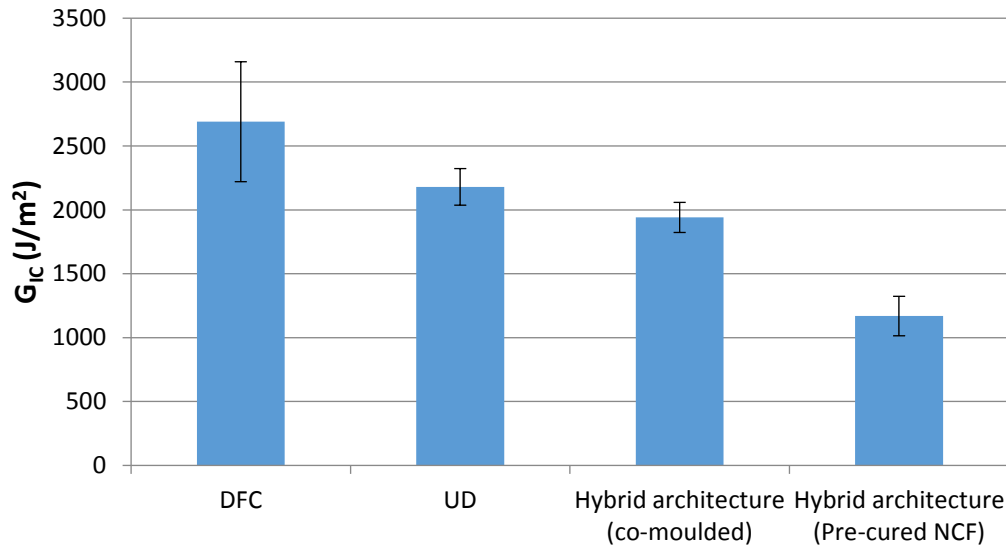


*Figure 6.41. The mode-I fracture toughness,  $G_{1C}$ , over 0-100mm crack length for each fibre architecture interface*

## 6.5 Summary

Some of the potential limitations of hybrid carbon fibre architectures have been explored in this chapter. Tensile testing has shown that the strength and stiffness of symmetrical hybrid laminates (UD/DFC/UD) increase linearly with increasing UD content according to a rule of mixtures relationship. Adding 20% by volume of UD fibres increases the tensile strength and modulus of the hybrid UD-DFC plaque by 110% and 60%, respectively, in the UD fibre direction. The main failure mechanism during axial loading was observed to be sudden delamination. This occurred because of out-of-plane shear due to the asymmetric laminate. Expectedly, in the transverse direction, this relationship showed a linear decrease as the quantity of UD material increases. The microstructure has also been observed for UD material compression moulded with hybrid fibre architecture. As a result of the stitching within the UD

material, this showed resin rich formations around the stitching and also between the some of the laminates as a result of the resin spray deposition onto one surface, relying on mould pressure to produce through thickness resin flow. However, although only one surface of each laminate was sprayed the high mould pressures, 85 bar, was sufficient to maintain a consistently low void content, <0.7%.

A primary limitation of asymmetric hybrid architecture is the result of residual stress formation caused by the through-thickness variation of thermal expansion coefficient between the UD fabric in the transverse orientation to the DFC material. This resulted in warpage during the freestanding cooling of the component proceeding hot demoulding from the compression mould tool. This degree of warpage appeared to peak at approximately 60% UD (by vol). In the future, it may be beneficial to quantify the residual stresses by techniques such as open-hole drill strain measurements, which measures the level of strain in multiple orientations to upon relaxation induced by a drilled hole [112, 174, 175]. Measuring the directionality of the thermal stresses potentially may be used to measure the orientation distribution of the random material. However, this would be limited to a relatively small sample area. Alternatively, the discontinuous material can use its ability to produce complex geometry to position ribs into components to diminish the warpage.

The design of the joint was established to be of a significant factor when transitioning from a UD-DFC hybrid to a DFC only region. Micrographs were used to identify resin rich regions in the vicinity of the dropped ply ends. This was particularly apparent when all ply ends were synchronised, i.e. there was no step at the transition point between the UD and DFC. The shape of the resin rich region was also dependent on the orientation of the contacting bundles, however the smallest resin regions required the compaction of transversely orientated fibre bundles which still produces a 'weak spot'. The DFC material flows turbulently over joints with steep gradients. This induces 'swirling' and out-of-plane misalignment of the fibre bundles reducing mechanical performance unless this gradient is reduced.

Investigating the structural response of the joint designs by three point bend testing, it was found that the flexural strength at failure was ~50MPa greater when bending positively, UD in compression, than bending negatively, UD in tension. Positive

bending often resulted in failure within the DFC region away from the joint, whereas the negative bending failure was dominated by the peel stresses that arose at the end of the surface laminate of the joint and propagated rapidly along the joint interface. This required an S-T ratio greater than 20:1, 6mm, to exceed the strength of DFC only.

Attempts were made to determine the tensile performance of the stepped architecture. However, these results are not representative of exhibiting pure tension because of bending caused by asymmetric stiffness imbalance. This bending prevents uniform axial stresses along the length of the specimen during axial load. The additional unmeasured, off-axis stresses therefore resulted in underestimations in the tensile strength results. A simple 2D FE model demonstrated the stress distributions and ESPI testing was suitable for measuring the strain distributions within the jointed architecture in both axial and out-of-plane orientations when subjected to 5kN axial load. The FE model visually demonstrated the stress concentrations around each other the ply ends, showing that the greatest stress concentration that forms at and interacts between ply ends are the peel stress. The ESPI results then demonstrated the uniform strain distribution experienced by the UD material and high positive and negative strain formations within DFC. Measuring the axial strains across the front and back in-plane surfaces of the stepped joint specimens with 20:1 S-T ratio, the ends of the plies were clearly defined by high strains produced by the resin rich regions. The magnitude of these peaks in strain reduce with each ply step as the local stiffness increases.

This observation was supported by the strain distributions at the interface of the joint during axial loading. The strain concentration at the surface ply decreased by 75% with step size up to an S-T ratio of 10:1 (step length of 3mm) rather than synchronising the ply ends. Greater step lengths exhibited a constant magnitude of strain in this region (approximately 8 microstrain with 5kN axial load) and the greatest strains were then experienced in the DFC part of the plaque. A 10:1 S-T ratio produced a joint angle of  $\sim 6^\circ$ , which agrees with the ply drop design guidelines that suggests that the taper angle should not exceed  $7^\circ$  ( $\sim 8:1$  S-T ratio) [97, 107]. When the S-T ratio was increased greater than 20:1, the greatest strains are within the DFC region. This prevents failure at the joint interface by moving the shear stresses away from the joint.

Changing the joint geometry to move the dropped ply ends away from the joint interface increased the bending strength in the negative direction (UD plies in tension on the underside) from 50MPa to approximately 10MPa. Introducing continuous fibres between the strain concentration at the end of the surface ply and the remaining plies, increased the stiffness of the interface which resulted in a more gradual transition from high to low stiffness materials. This subsequently reduced the out-of-plane strain within the joint region by 20% and therefore the local shear strain by approximately 50%.

Directly comparing the DCB performance of the discontinuous, DFC, and continuous, UD, materials, the results were found to support those obtained by Truss et al. [120]. The interfacial fracture toughness and crack initiation loads during mode-I separation of these hybrid plaques were influenced by the degree of fibre bridging, as a result of the discontinuous fibre bundles in the DFC material. This increases the load required to initiate the crack and the mode-I fracture toughness of the DFC by 37% and 23%, respectively, from that of a UD interface. The co-moulded hybrid architecture experiences a mixture of fibre bridging at regions of the discontinuous fibres interleaving the continuous plies and sudden energy release rates along the resin rich linear interface regions. This results in a crack initiation load between that of the UD and DFC materials but a lower overall fracture energy.

Additionally, co-moulded hybrids were compared to hybrid architectures produced by moulding pre-cured continuous plies. This showed that co-moulding the constituents produced significantly higher fracture performance. This was evident by a higher crack initiation load and mode-I fracture toughness over a 100mm crack length, compared to pre-curing the continuous architecture. Co-moulding dissimilar architecture ensures that the matrix crosslinking forms across the boundary of the constituents, whilst also providing some partial interleaving of the fibre bundles.

# 7. Damage tolerance of hybrid fibre architecture

## 7.1 Introduction

Depending on the design requirements for hybrid architectures, the through thickness position of the continuous fabric plies is important relative to the discontinuous material. Whilst positioning the continuous laminates at the surface enhances the bending properties in the longitudinal fibre direction, design guidelines recommend positioning a suitable number of primary loaded plies away from the surface to protect against damage from low velocity impact [97, 99]. This chapter will investigate the resultant effects of changing the through thickness position of plies within hybrid fibre architecture composites.

When the continuous plies are positioned against the tool surface during moulding they conform to the tool shape, minimising out-of-plane misalignment or waviness. Conversely, continuous plies positioned centrally with the laminate surrounded by discontinuous material results in higher levels of ply waviness because the local fibre volume fraction variations within the discontinuous architecture cause varying levels of ply compaction in the continuous fibres. This misalignment mechanism causes significant degradation of the compressive properties by more than 50% as a result of buckling that prevents pure axial stress transfer along the fibres [144-147]. One method to potentially reduce the degree of waviness will be investigated in this chapter to increase the pre-moulded ply stiffness by partially curing the plies prior to the final compression moulding step.

Compression after impact (CAI) testing is often used to characterise the damage of low velocity out-of-plane impact scenarios. Out-of-plane impacts cause delamination

between plies, which significantly reduces interlaminar shear strength, tensile and compressive stiffness and strength [133]. Random discontinuous architectures can distribute the impact stresses more uniformly in-plane to reduce the degradation experienced in the inter-laminar region compared to UD laminates [130].

## **7.2 Objectives**

This chapter aims to characterise the microstructural benefits of embedding continuous plies within the central through thickness region of the laminate to create a hybrid architecture, whilst trying to control fibre waviness in order to improve the overall damage tolerance of the structure. Laminates designed with a [DFC/0/DFC] layup will be investigated with varying degrees of partial cure of the continuous plies prior to compression moulding. The fibre waviness will be characterised by microscopy using a MATLAB algorithm to measure the out-of-plane angles across each specimen. The damage tolerance will be investigated by CAI to determine the mechanical performance retained post low-velocity impact. The impact damage will be implemented by drop weight impacting at two velocities and in addition to investigating compressive performance, the damage zones are characterised by ultrasound scanning to measure the size of delamination.

## **7.3 Design of Experiments**

### **7.3.1 Cure staging**

A short study was performed to quantify out-of-plane waviness of a NCF ply located centrally through the thickness of a composite, with DFC on the upper and lower surface. The impregnated NCF was partially or fully cured under vacuum pressure to understand the effect of resin staging on the degree of out-of-plane waviness and void entrapment within the fabric.

A preliminary trial was performed to determine the best method to apply heat for partially or fully curing the fabric under isothermal conditions. It was determined that cure was best to be achieved by an aluminium plate in oven. This conclusion was drawn after considering using an autoclave or a hot plate also. These findings are shown in

Appendix A3. **Table 7.1** shows the degrees of cure used for this trial, from the enthalpies calculated by DSC shown in **Table 7.2**.

The out-of-plane waviness of these specimens was quantified in terms of the amplitude, indicated by the range of ply migration from the centre line,  $h$  (mm), and the maximum and minimum waviness angles from the horizontal,  $\alpha_{\max}$  and  $\alpha_{\min}$  ( $^{\circ}$ ). These are demonstrated in **Fig. 7.1**.

**Table 7.1** Dwell times used for the target degrees of cure (from B-stage only) for the 400mm x 400mm impregnated NCF materials for the out-of-plane waviness investigation.

Target degree of pre-cure (%)	Dwell time @100°C (min):	Actual degree of pre-cure from B-stage (%)
No pre-cure	N/A	0
0.25	35	42
0.5	48	56
0.75	67	94
1	240	100

**Table 7.2** Table of enthalpies measured by DSC to show the degree of cure of each partially cured ply. Degrees of cure have been determined that 0% is where only a B-stage has been applied, and 100% is a fully cured ply.

	Repetition/ Target degree of cure	Mass (mg)	Heat (J/g)	Average (J/g)	Degree of Cure (from pre B-stage)	Degree of Cure (from post B-stage)
Before B-staging	1	16.3	346.8	362.25	0	N/A
	2	18.6	377.7			
Uncured (After B-staging)	1	21.2	278.8	282.3	22.07%	0.00%
	2	13.6	285.8			
Pre-cure	25%	11.6	162.8	162.8	55.06%	42.33%
	50%	20.3	124.8	124.8	65.55%	55.79%
	75%	20.8	17.82	17.82	95.08%	93.69%

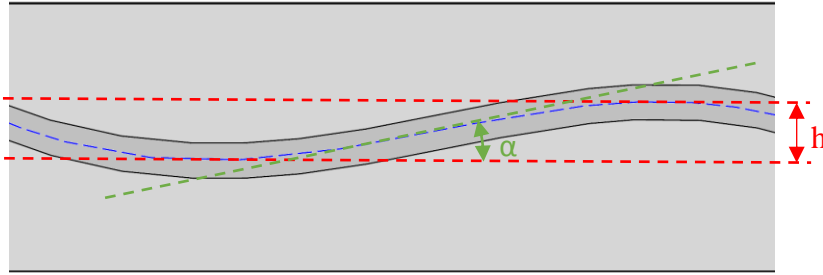


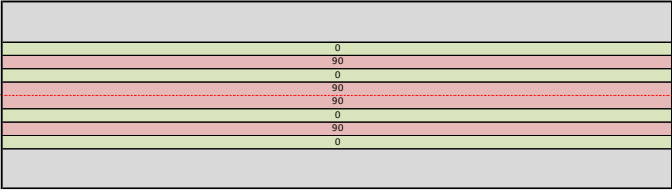
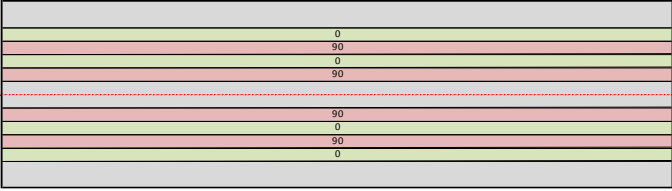
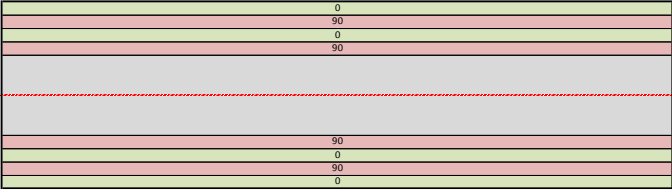
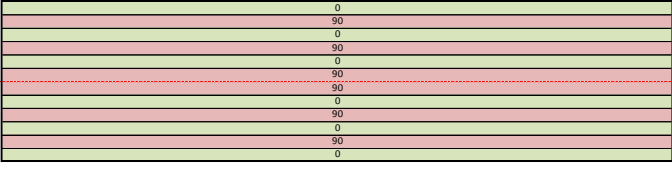
**Figure 7.1.** Figure demonstrating the measurements for the amplitude of ply migration,  $h$ , and waviness angles to the horizontal,  $\alpha$

### 7.3.2 Compression after impact (CAI)

Five different fibre architectures were used to establish the effect of ply position on the damage tolerance of hybrid architectures following low velocity out-of-plane impacts. These are shown in **Fig. 7.2**. Three hybrid architectures were studied containing equal quantities of random chopped carbon fibre bundles with a 12K tow size and fibre length of 25mm, and two stacks of orthogonal UD plies,  $(0/90)_2$ . The through thickness positions of the UD plies were varied by controlling the volume of DFC material in contact with the tool surface (a charge approximately 1.2mm thick). The interspersed arrangement had three 0.8mm thick DFC regions separating the continuous stacks. The final hybrid architecture arrangement was produced by positioning the UD plies at the surface with 2.4mm thick DFC material symmetrically about the centre of the through thickness. These arrangements are shown in **Fig. 7.2**, and were each compression moulded net-shape to prevent inducing flow.

The compressive properties of each architecture were determined prior to impacting. Compression testing was performed in the longitudinal orientation for at least 4 repeats of each arrangement. During this testing, the DFC material had a width of 25mm, whilst the hybrid architectures and cross-ply arrangement used 15mm wide specimens to ensure failure at loads within the 50kN limitation of the testing fixtures. As a result of the small viewing window it was not suitable to measure the strain using strain gauges, therefore a video extensometer was used. However, the large specimen thicknesses, 4-5.5mm, reduced the susceptibility of bending under compression over a 12.7mm gauge length.

Drop weight impacting was performed on each fibre arrangement with two target thickness dependent impact energies: 4.5J/mm and 6.7J/mm. Six repeats were performed on each fibre arrangement for each impact energy. Although the drop height was calculated depending on the thickness of each specimen, the actual impact energy was calculated by the measured velocity of the impactor. Two of each of the impacted panels were cut to produce micrographs within the impact zone. The remaining four of each arrangement were then scanned by ultrasound to produce C-scans to observe the delamination and damage zones before obtaining compressive properties retained by each panel.

Ply position	Arrangement	Schematic
DFC only	DFC	
Centre	[DFC/(0/90) <sub>2</sub> ] <sub>s</sub>	
Intersperse	[DFC/(0/90) <sub>2</sub> /DFC] <sub>s</sub>	
Surface	[(0/90) <sub>s</sub> /DFC] <sub>s</sub>	
Cross-ply	[(0/90) <sub>3</sub> ] <sub>s</sub>	

**Figure 7.2.** List of the investigated hybrid fibre architecture arrangements and schematics of the through thickness arrangements.

## 7.4 Results and Discussion

### 7.4.1 Cure staging

To validate the Matlab algorithm, the out-of-plane laminate waviness of continuous plies were measured from three micrographs produced from a compression moulded composite of 10 UD plies,  $[0_{10}]$ . This was characterised by tracking the centreline and then determining the average through thickness position of each ply. A horizontal line was applied to the average through thickness position of each ply and from the maximum distance of the centreline above and below the horizontal line for each micrograph was determined. This is referred to as the ply deviation. The maximum and minimum waviness angles from the horizontal lines across each micrograph were also obtained. Across the  $[0_{10}]$  composites, the amplitude of waviness was small,  $\pm 0.13\text{mm}$ , just 0.43 times the ply thickness, with a coefficient of variation of 33%. The angle of waviness of these samples was found to be  $< \pm 3^\circ$  on average. The only out-of-plane waviness experienced within this flat structure was induced by the tows within the NCF compressing against the stitching. This is shown by *Point A* in *Fig. 7.3*.

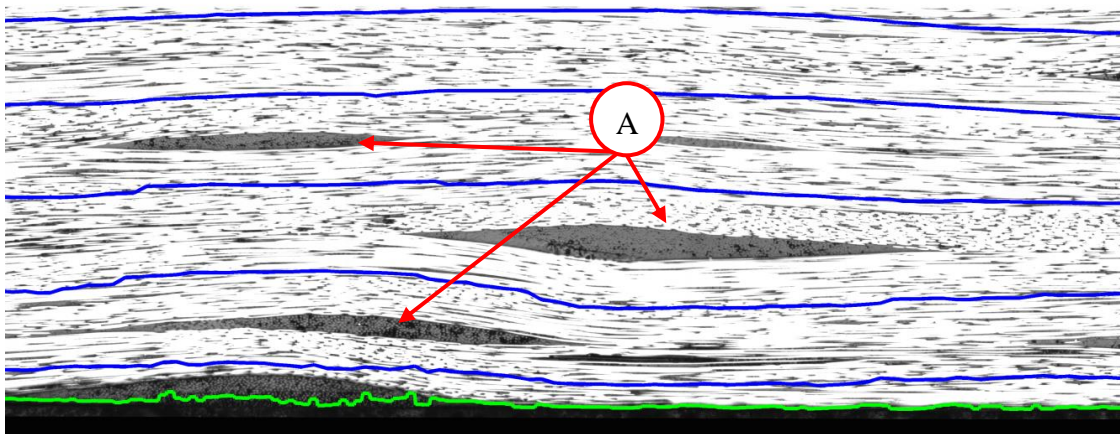


*Figure 7.3. Examples of the ply waviness about NCF stitches using a MATLAB algorithm to track the centreline of each ply*

Co-compression moulding of continuous plies with DFC using the  $[\text{DFC}/0/\text{DFC}]$  layup induces the greatest degree of UD fibre waviness. However, a further consideration had to be made when measuring the amplitude of ply migrations from the centreline. The through-thickness position of the central ply may migrate during moulding as a result of the local thickness and fibre content variations in the DFC material. This is shown

in *Fig. 7.4 (a)*, where the blue line, indicating the centre line of the continuous ply, is below the centreline of the laminate (red line) across the length of the micrograph. The ply deviation is therefore characterised as the range of the highest and lowest through thickness position of the ply. The average ply deviation range about the central horizontal line within the micrographs of the [DFC/0/DFC] with no pre-cure is the largest,  $378\mu\text{m}$ , and the average waviness angles are also the greatest at approximately  $\pm 4.2^\circ$ . This can be reduced by partially pre-curing the continuous ply to increase the stiffness of the ply prior to compression moulding with the discontinuous architecture. Partially pre-curing the continuous ply within [DFC/0/DFC] increases its stiffness prior to compression moulding with the discontinuous material.

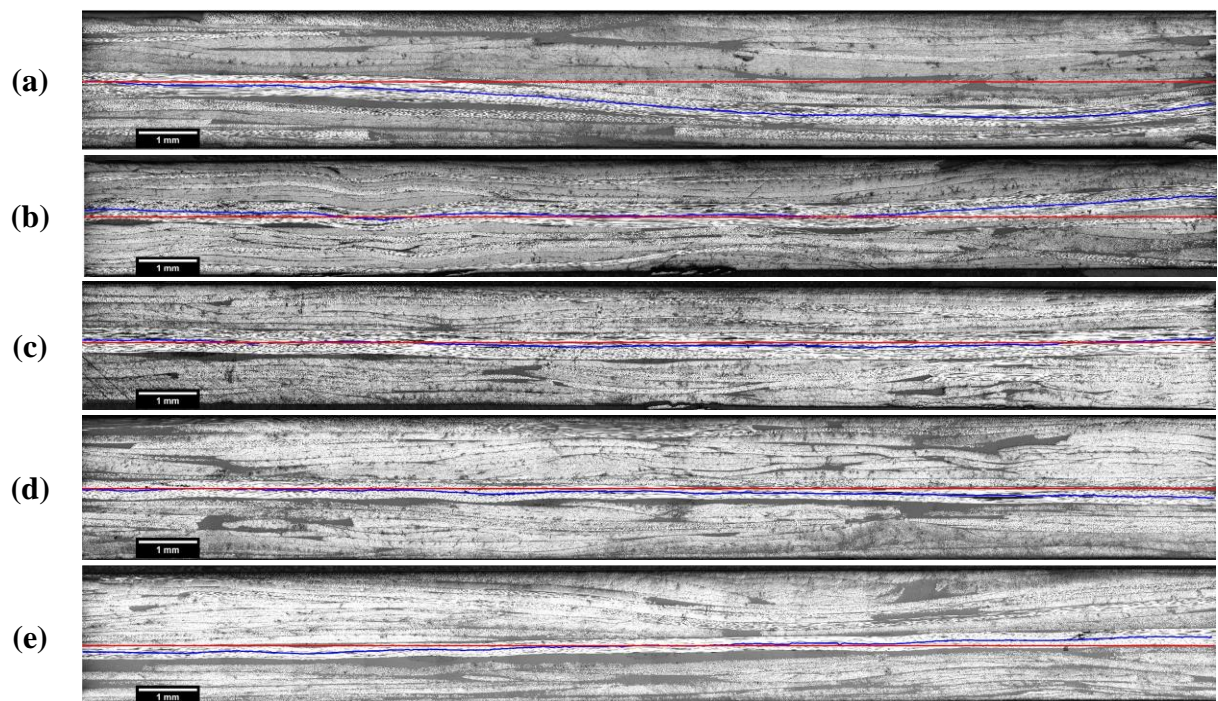


**Figure 7.4.** Example micrographs showing their composite horizontal centreline (red) and ply centreline (blue) for with partial target pre-cures of (a) 0, (b) 0.25, (c) 0.5, (d) 0.75 and (e) full pre-cure

The average ply deviation and out-of-plane waviness angles are shown in *Fig. 7.5* and *Table 7.3*. These were measured to be greater than the target degrees of pre-cure for each of the plies. This was because the rate of cooling of the plies and DSC specimens were slow after removing them from the oven. *Fig. 7.5* shows how both the average amplitude of ply migration from the centreline and out-of-plane waviness angles decrease as the degree of pre-cure increased. However, there are other considerations

to make when pre-curing the plies. It was also observed in the micrographs that as the degree of pre-cure is increased, a thin resin rich layer forms between the continuous ply and the DFC material. This is demonstrated in **Fig. 7.6 (a)** that shows a micrograph, perpendicular to the fabric orientation, of the DFC/0/DFC laminates without pre-cure, where compression of the ply interleave with similarly orientated fibre bundles. This makes it difficult to determine the shape of the continuous-discontinuous interface. In contrast, **Fig. 7.6 (b)** shows a similar location where the continuous ply is fully pre-cured. The increased hardness of the continuous constituent before moulding prevents interleaving of the dissimilar materials, indicated by a resin rich boundary along the interface. This would also reduce the interlaminar shear strength as a result of the reduced crosslinking between the continuous and discontinuous architecture [38].

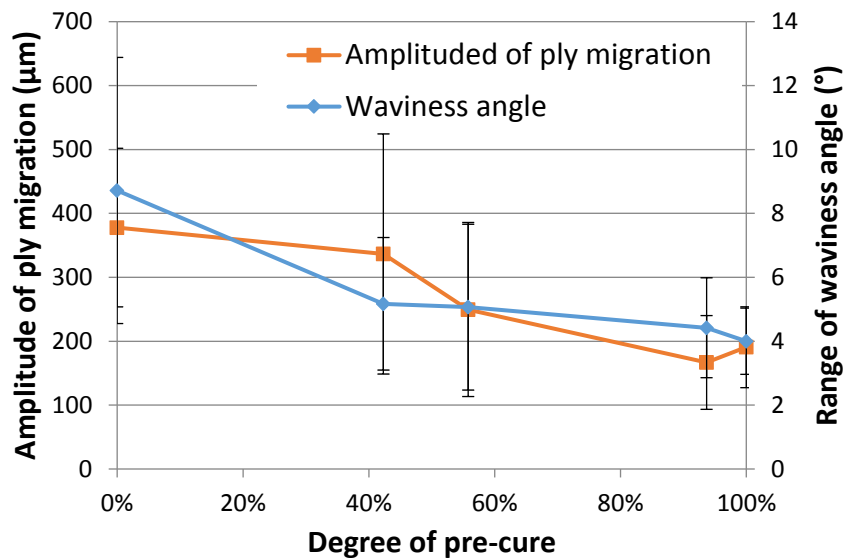


**Figure 7.5.** Average ply migration and waviness angle range across 10 specimens measured by a MATLAB algorithm with varying degrees of pre-cure of the continuous plies within [DFC/0/DFC] composites

**Table 7.3.** The measured degrees of pre-cure for each target degree of pre-cure and the average ranges of ply migration and out-of-plane waviness angle across 10 micrographs of each [DFC/0/DFC] plaque.

Actual degree of cure		Migration*	Waviness angle**		
		Range	Max	Min	Range
		( $\mu\text{m}$ )	( $^{\circ}$ )	( $^{\circ}$ )	( $^{\circ}$ )
0	Average	378	4.17	-4.54	8.72
	St. dev	124	2.58	2.03	4.16
	CoV (%)	32.86%	61.84%	-44.78%	47.78%
0.42	Average	336	2.62	-2.55	5.17
	St. dev	188	1.38	1.63	2.07
	CoV (%)	55.82%	52.63%	-63.92%	40.10%
0.56	Average	250	2.88	-2.18	5.07
	St. dev	136	1.26	1.55	2.59
	CoV (%)	54.57%	43.61%	-71.02%	51.20%
0.94	Average	167	1.89	-2.53	4.42
	St. dev	73	0.78	1.05	1.56
	CoV (%)	44.01%	41.39%	-41.39%	35.37%
1	Average	191	2.01	-1.99	4.00
	St. dev	63	0.60	1.02	1.04
	CoV (%)	33.20%	29.81%	-51.44%	25.94%

\*The range between the maximum distance highest and lowest through thickness position across each 20mm long micrograph

\*\*The angle of out-of-plane misalignment of the centre ply across each micrograph

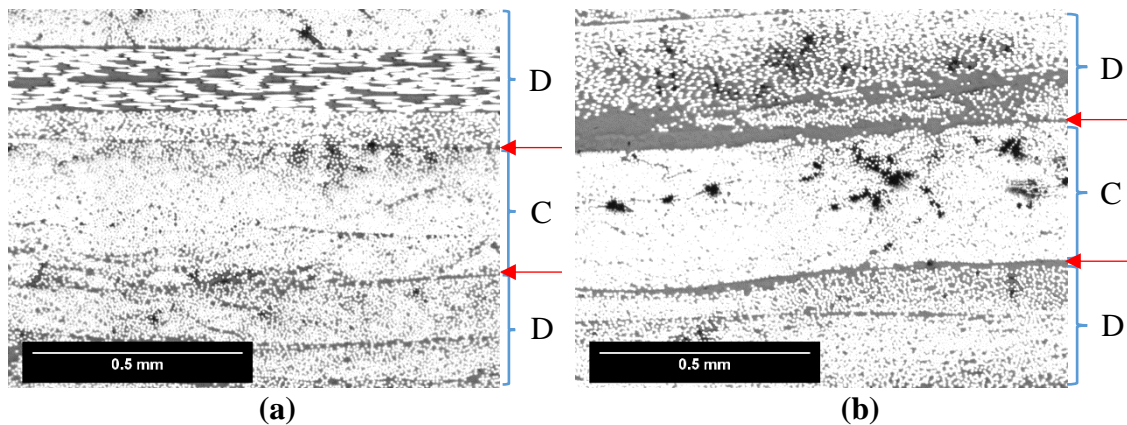


**Figure 7.6.** Micrographs orientated perpendicular to the continuous ply direction

#### 7.4.2 Compressive performance

Prior to drop weight impact testing, the compressive properties were established to provide a baseline performance for each of the tested fibre architectural arrangements. It was shown that there was no statistically significant difference in the compressive

strength and modulus between any of the hybrid architectures, shown in *Fig. 7.7*. Where the ply stack is located at the centre of the through thickness, this suggests that there was insufficient ply waviness to reduce the compressive strength in comparison to the other hybrid arrangements. When observing the failure, it was clear that specimens each failed by crushing of the within the DFC and cross-ply specimens, rather than bending, such as in *Fig. 7.8*. However, although there was no bending within the hybrid fibre architecture specimens, there was also apparent delamination along the interface between the dissimilar architecture, shown in *Fig. 7.8*. This could be the result of failure initiating within the transversely oriented fibre regions or random discontinuous bundles and tracking along the interface before failure of the high strength longitudinal fibres.

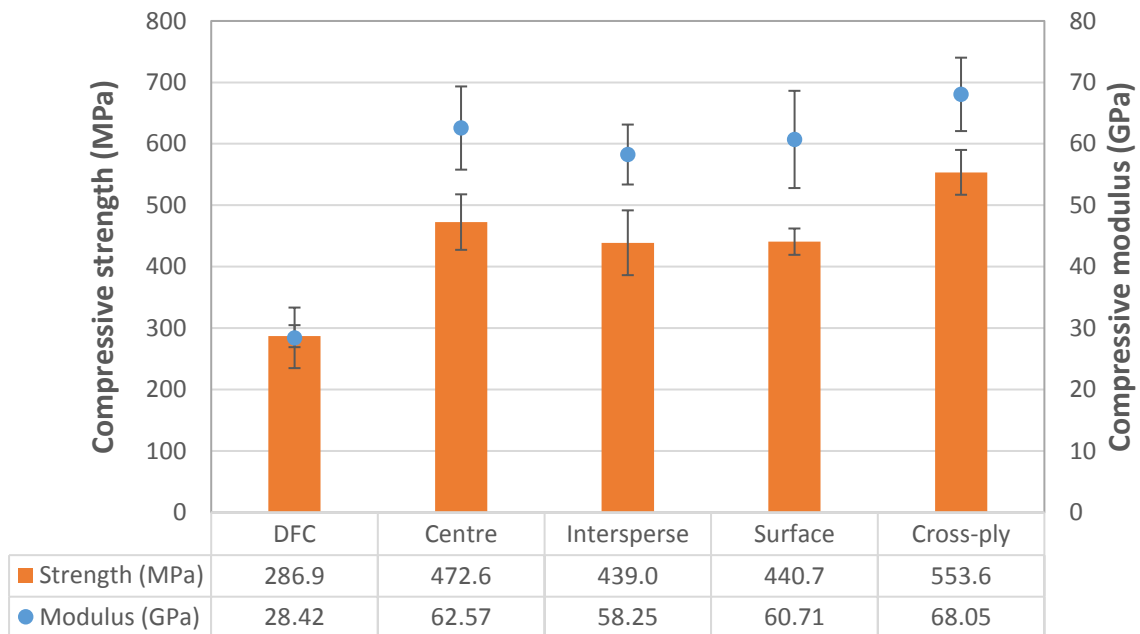


**Figure 7.7.** Compressive strength and stiffness of each of the undamaged continuous (cross-ply), discontinuous (DFC) and hybrid architectures (Centre, Intersperse, Surface)



*Figure 7.8. Typical crush failure of a hybrid architecture specimen with intersperse arrangement exhibiting delamination along the length of the load direction*

### **7.4.3 Impact testing**

Each fibre arrangement was subjected to two different impact energies, 4.5J/mm and 6.7J/mm. Drop heights were calculated prior to testing depending on specimen thickness and impactor mass, 8.641kg. The tables in *Appendix A4* show the impact velocities and actual impact energy calculated. The average lower and upper impact energies were lower than expected, 3.6J/mm and 5.9J/mm respectively. This suggests that friction of the dropped weight reduced the velocity of the impactor.

*Fig. 7.9* shows the depths of each impact zone which were measured by the travel distance of the impactor below the surface of each specimen. This indicates that the impact depth was similar for both DFC and the hybrid fibre arrangements, for both impact energies. There is a small statistically significant ( $p < 0.05$ ) increase in impact depth for the cross-ply laminates in comparison to the other arrangements for low impact velocities. However, no statistical significance is not apparent for the higher impact velocity.

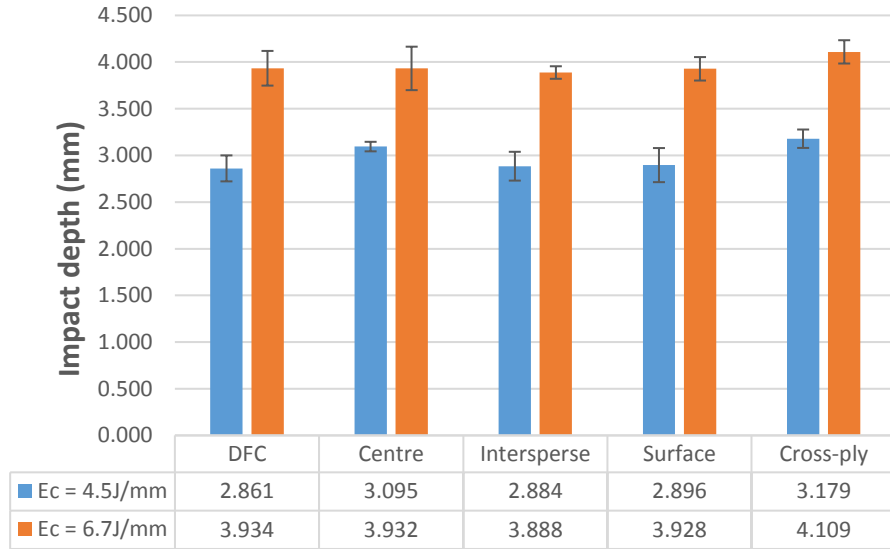


**Figure 7.9.** Impact depths of each architectural arrangement for low and high impact velocities

#### 7.4.4 Damage zones

Ultrasonic C-scans were obtained before and after impact testing. Images of the discontinuous DFC material exhibit a large variability in the amplitude of the return ultrasonic signal as a result of the random fibre bundle structure and resin regions. It should be noted that in **Fig. 7.10 - 7.13** the aspect ratios of the C-scans of the 150mm x 100mm panels is not equal to the actual aspect ratio. Reductions in signal amplitude occur near the corners which result from the pads used to elevate the specimen. Some DFC panels contain some large resin rich regions. **Fig. 7.10** shows an example of an undamaged DFC panel with a resin rich region located approximately 1mm below the surface, evident in the B and D scans. The significant change in material density causes the ultrasound to reflect at the transition between the fibres and the resin region and therefore obscures anything beneath this region. It was observed that the damage zone merged into the resin regions if the impact location was near to these resin regions, as shown in **Fig. 7.11**.

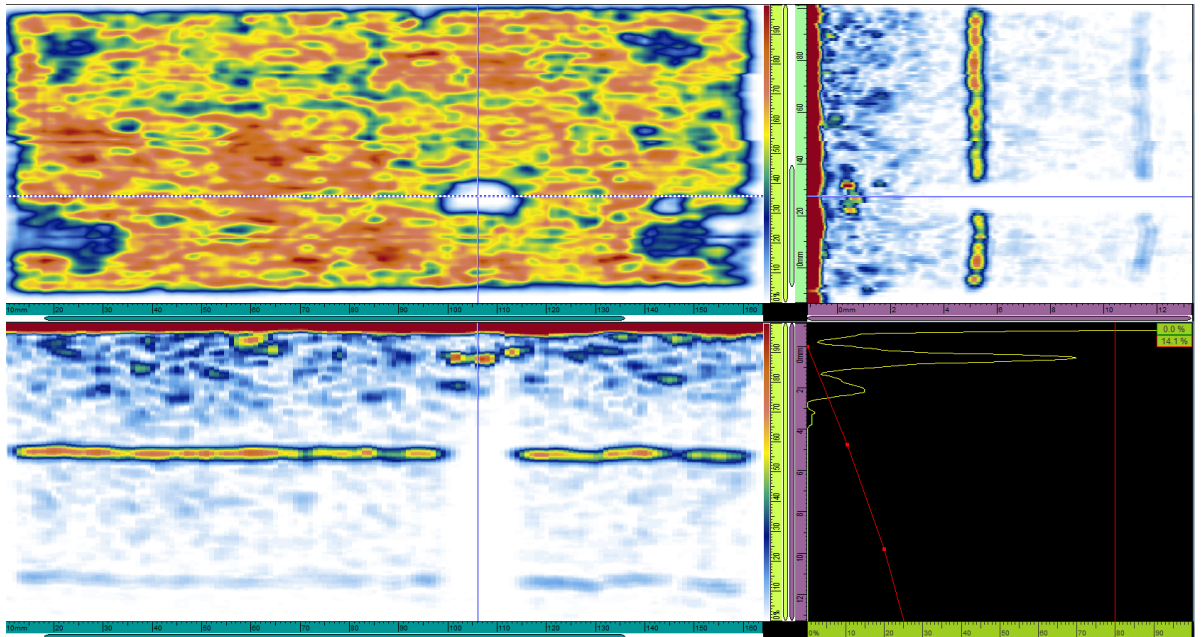


*Figure 7.10. C-scan (top-left), B-scan (top-right), D-scan (bottom-left) and amplitude of return signal versus through-thickness depth (bottom-right) of an undamaged DFC specimen*

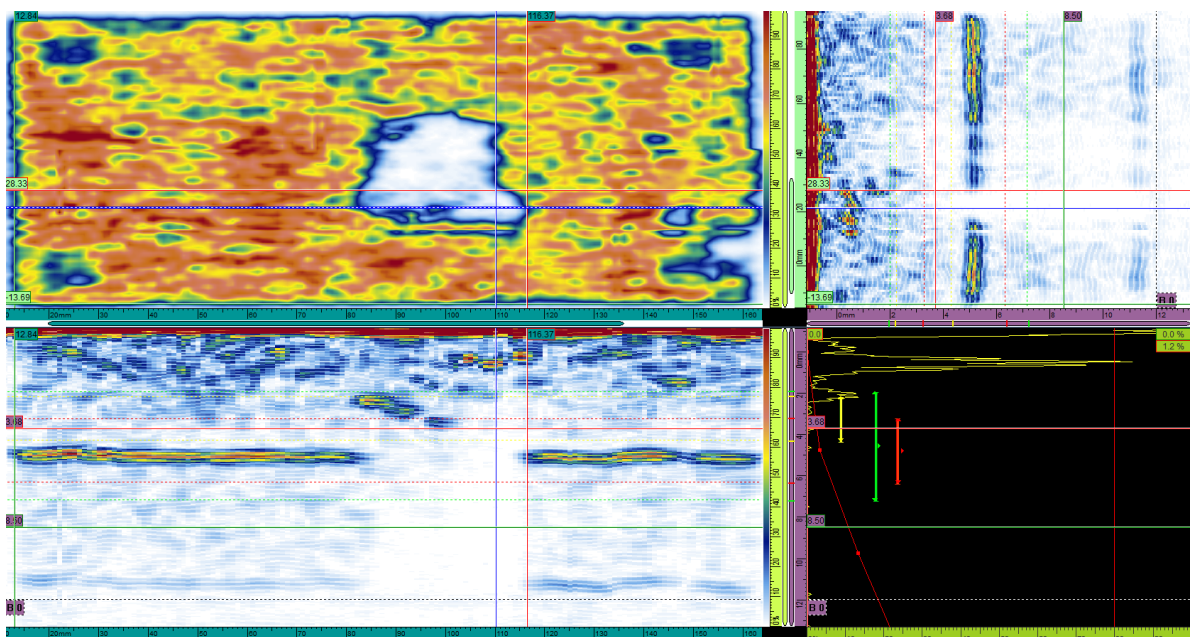


*Figure 7.11. C-scan (top-left), B-scan (top-right), D-scan (bottom-left) and amplitude of return signal versus through-thickness depth (bottom-right) of DFC specimen that has experienced high impact velocity*

Introducing continuous fabrics into the hybrid architecture produced more uniform C-scans, shown in **Fig 7.12**, regardless of the through thickness UD ply position, producing a peak amplitude signal from the back face of the panels. However, the DFC

was still visible, when amplitudes were measured at different through thickness positions. The resolution of the scans did not allow clear distinction between the different fibre architectures.

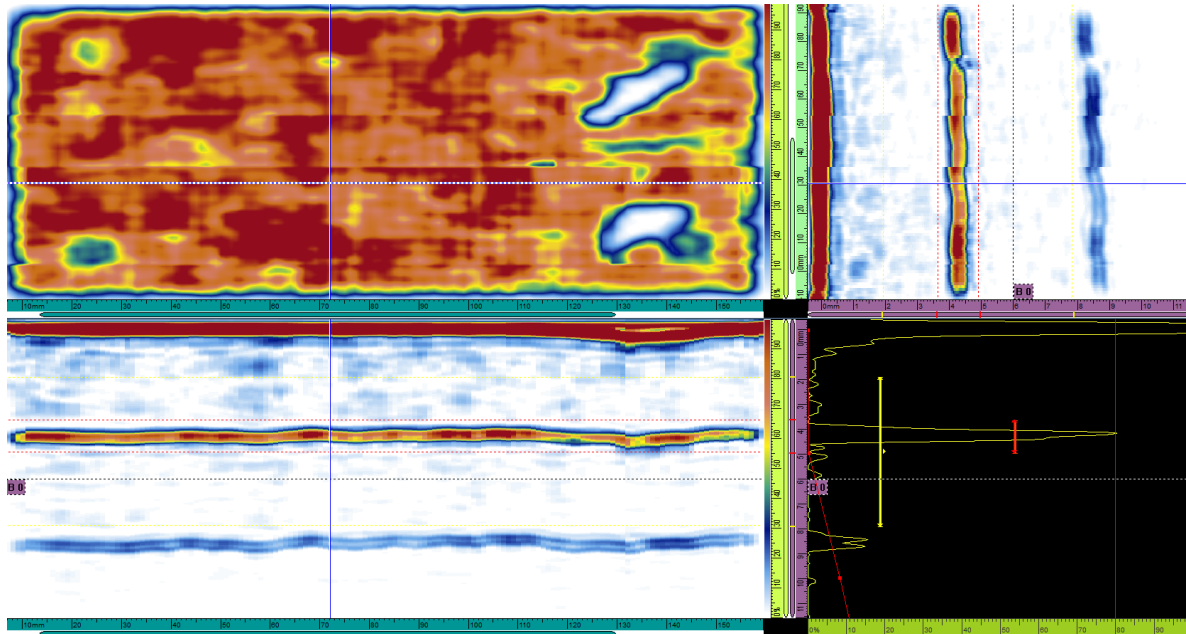


**Figure 7.12.** C-scan (top-left), B-scan (top-right), D-scan (bottom-left) and amplitude of return signal versus through-thickness depth (bottom-right) of an undamaged hybrid architecture specimen with the fabric positioned central of the through thickness,  $[DFC/(0/90)_2]_s$

**Figures. 7.11 & 7.13** demonstrate that the shapes of the C-scanned damage zones were found to be irregular with no distinguishable difference between each of the architectures investigated. The damage zones have therefore been considered to be approximately circular/elliptical to enable the diameter to be determined with regards to the length and width of the damaged zone for each fibre arrangement. The average damage length and width across the four scans were measured to the nearest millimetre and given in **Fig. 7.14** as the damage zone diameter. There was a large degree of variability in the recorded damage zone size, but trends were distinguishable. The size of damage zones caused by low impact energy appear to increase in size as the UD plies are moved closer to the surface of the hybrid plaques: from Centre to Intersperse to Surface.

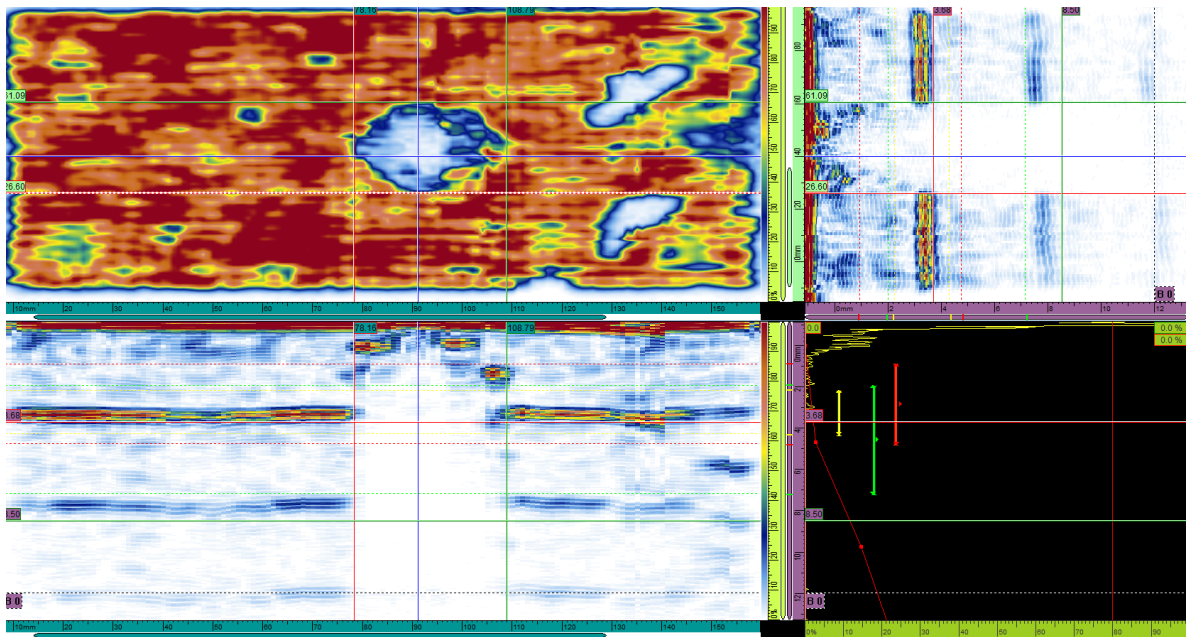


**Figure 7.13.** C-scan (top-left), B-scan (top-right), D-scan (bottom-left) and amplitude of return signal versus through-thickness depth (bottom-right) of hybrid architecture specimen with the fabric positioned central of the through thickness,  $[DFC/(0/90)_2]_s$ , that has experienced low impact velocity

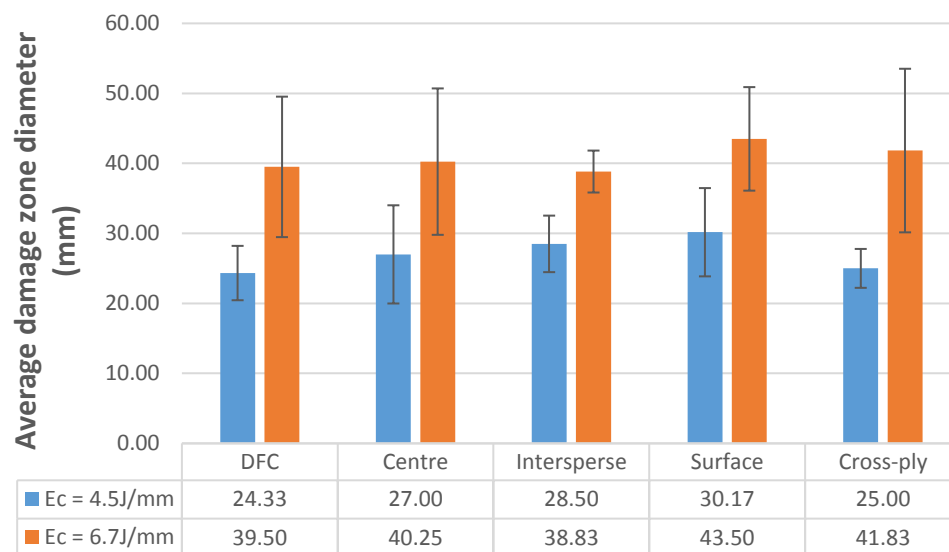


**Figure 7.14.** Average damage zone diameters determined by the length and width of damage zones measured from each C-scan

Micrographs taken through the impact zones in **Fig. 7.15** indicate large amount of delamination between the plies, while shorter cracks form along the length of the discontinuous fibre bundles. Looking at the failure in the cross-ply architecture, the longitudinal plies show delamination along the interface in the fibre direction.

However, fibres orientated normal to the plane of the image show that cracks propagate in the through thickness direction of the ply, connecting the delamination either side of the transverse ply. Within the discontinuous DFC material there appears to be some delamination within fibre bundles. The lengths of these sites are therefore restricted to the length of the bundle itself, so the crack is quickly arrested or diverted around neighbouring fibre bundles.

#### 7.4.5 Compression after impact

Strain gauges determined over three panels, with DFC, centre and intersperse arrangements, the compression fixtures demonstrated that panels experienced less than 10% bending,  $B_y$ , using *equation 7.1*, in accordance to the standards.  $\epsilon_{front}$  and  $\epsilon_{back}$  refer to the strain gauges on the front and back faces of the specimen.

$$B_y = \frac{\epsilon_{front} - \epsilon_{back}}{\epsilon_{front} + \epsilon_{back}}$$

Strains measured by video extensometer found that the compressive moduli of each hybrid fibre arrangement reduced by 15-20% with low velocity impact. The cross-ply arrangement also exhibited a 10% reduction that increased to 17% with high impact velocities. However, there was no further reduction to the compressive modulus of the hybrid fibre arrangement with the high velocity impact. The discontinuous architecture however does not experience this reduction in compressive modulus because of its notch insensitivity. The heterogeneous nature of the meso-structure within the discontinuous architecture obscures the impact defects by the inherent large stress concentrations that form at the ends of the fibre bundles [10]. These stress concentrations arise from the large disparity between the stiffness of the carbon fibre and epoxy matrix in the fibre direction and the synchronisation of the filament ends within the bundles [52].

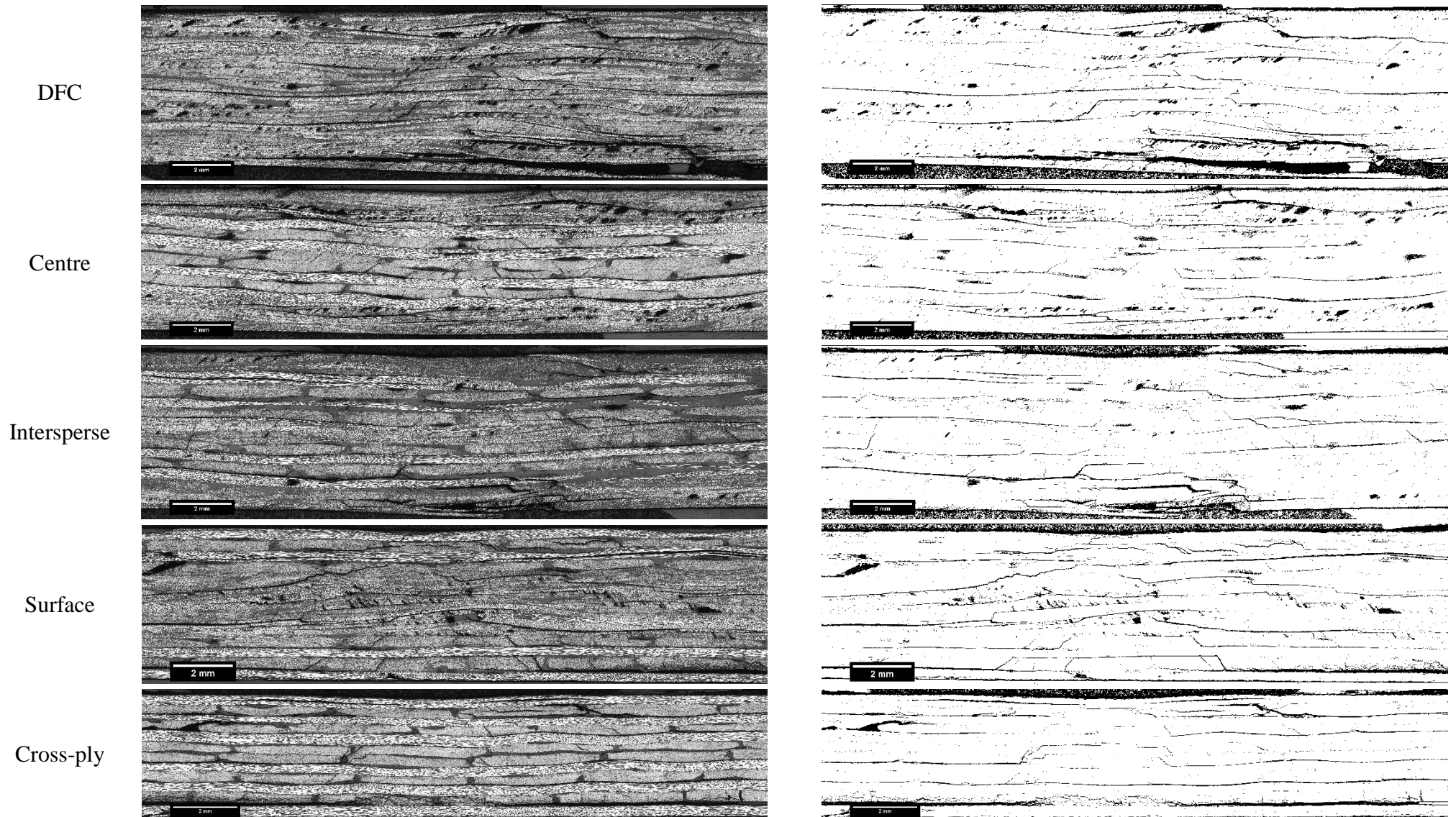


*Figure 7.15. Through thickness micrographs of the damage zone of high velocity impacted specimens (left) and with a threshold applied (right)*

The compressive strengths are shown in **Fig. 7.16**. This shows that low velocity impacts reduced the compressive performances to near equal strengths, regardless of their undamaged compressive performance. This was unexpected, as it appears there is no change in damage tolerance between varying DFC skin thicknesses. This is indicated by **Fig. 7.17** which shows the percentage compressive strength retained post-impact. Following low velocity impacts, the greatest percentage of compressive strength was retained by the discontinuous architecture, 79%, whilst the cross-ply architecture retained only 41%. Increasing the impact velocity, the compressive strength of the cross-ply reduced by a further 50MPa and the DFC by just 20MPa. The post-impact compressive strength of the DFC was therefore higher than the post impact strength of the cross-ply architecture (following a 6.7J/mm impact).

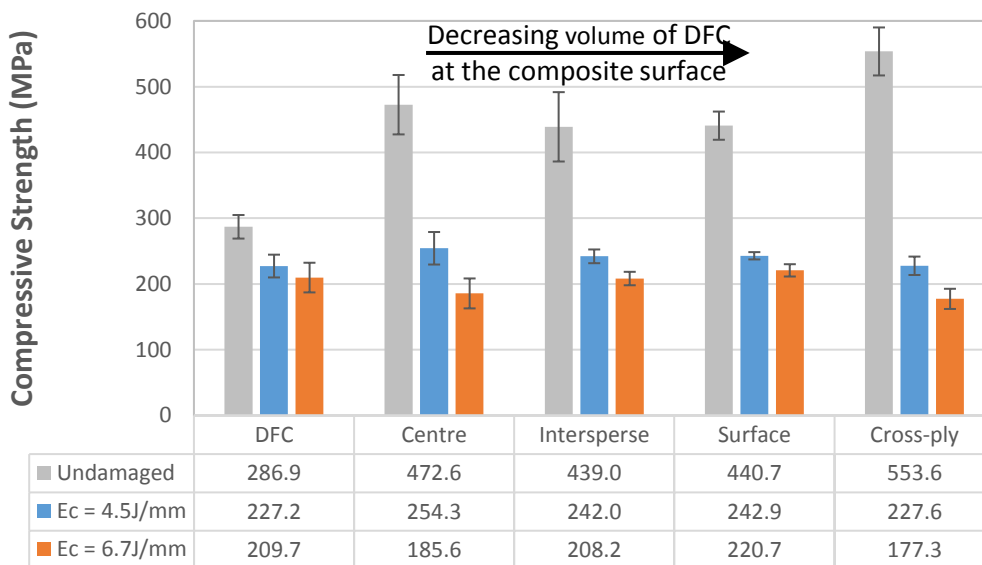


**Figure 7.16.** Compressive strengths of each fibre architecture prior to impact testing and after exhibiting target out-of-plane impacts of 4.5J/mm and 6.7J/mm

Loads are transferred along the fibre direction during the local bending induced by out-of-plane impacts. Within continuous fibre structures, this results in inter-ply shearing and delaminations as cracks propagate in the fibre direction. **Fig. 7.18 (e)** and **(f)** are micrographs of the cross-ply specimen following the high-energy impact located directly beneath the impact location and 7.5mm from the impact centre, respectively. These figures demonstrate the delamination at *point 7* in **Fig. 7.18 (e)** and *point 9* in **Fig. 7.18 (f)**. **Fig. 7.18(a)** and **(b)** are micrographs of the DFC specimens at the centre of the laminate (through thickness) beneath the high-energy impact location and 7.5mm from the impact centre respectively. *Point 1* in **Fig. 7.18 (a)** shows that horizontal

cracks follow the  $0^\circ$  fibre, whilst *point 2* shows that large out-of-plane crack deviates as it interacts with contacting bundles. Small out-of-plane cracks are seen directly beneath the impact in cross-ply specimens at *point 8* in **Fig. 7.18 (e)** through the  $90^\circ$  oriented laminates, however these are not present at a further from the impact location, **Fig. 7.18 (f)**, showing only delamination. **Fig. 7.18 (b)** also shows cracks being arrested in the longitudinal orientation at *point 3*. These multi-directional short, non-linear cracks enable the DFC material to retain higher stiffness and strength values compared to the long, continuous delaminations along the load direction of the cross-ply architecture.

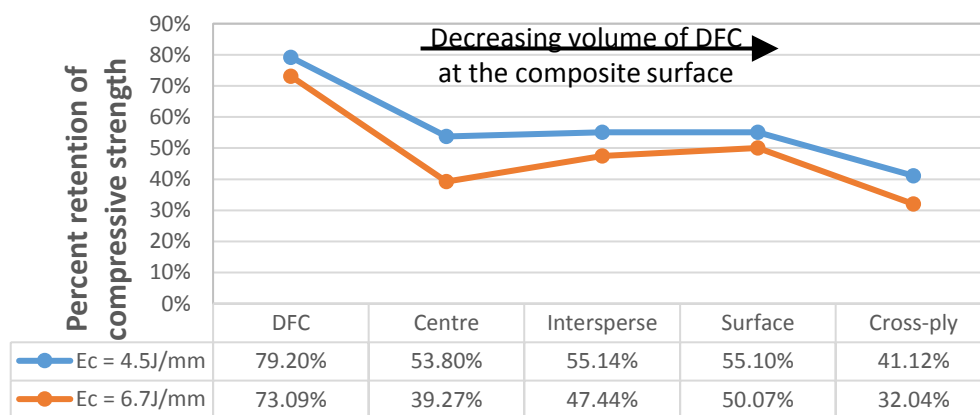


**Figure 7.17.** The percentage of compressive strengths retained after exhibiting a low impact energy (4.5J/mm) and high impact energy (6.7J/mm) in comparison to the undamaged compressive strengths

Also shown in **Fig. 7.16** and **7.17**, there was no distinguishable difference in the compressive strength and percentage strength retained for the hybrid fibre architectures, following the low energy impact. These specimens retained 53-55% of their compressive strength post impact. Increasing the impact energy, it was found that there was no difference between the compressive strength retained by the surface and intersperse fibre arrangements whereas the compressive strength of the centre arrangement retained approximately 10% less. This indicates that the dominating factor between the impact behaviour of these hybrid architectures is the thickness of the continuous region. Intersperse and surface arrangements contain stacks of 4 plies through the thickness separated by DFC material, whereas positioning the continuous plies at the centre creates an 8 ply thick stack. This thick continuous region has smaller interfacial contact with the random fibres, meaning less energy is dissipated at the interface in multiple directions and therefore the frequency of delaminations increase.

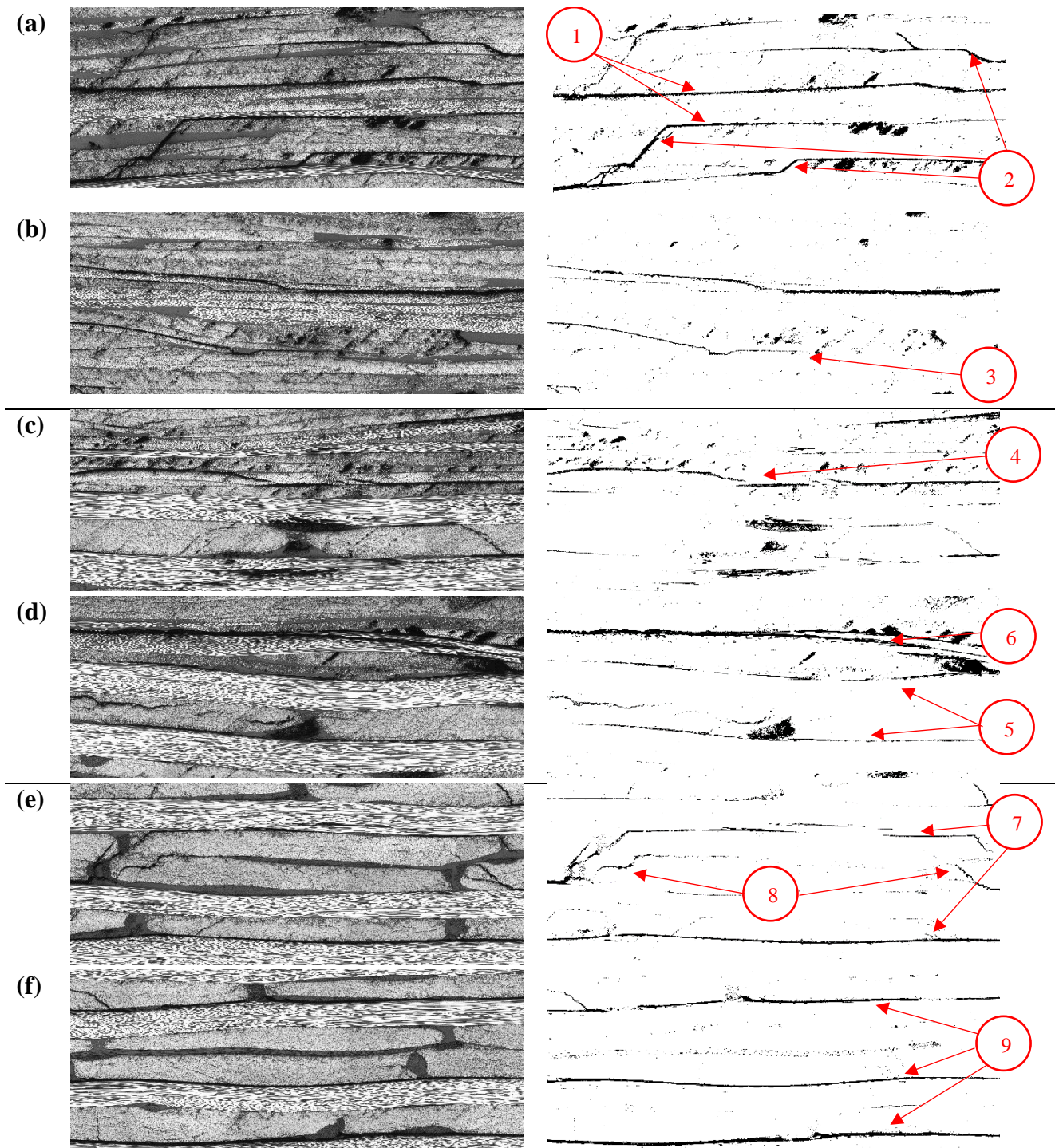


**Figure 7.18.** Micrographs (5mm x 2mm) or regions within impacted specimens ( $J_c = 6.7\text{J/mm}$ ). Images (a) and (b) are DFC specimens, (c) and (d) have the centre arrangement and (e) and (f) are cross-ply specimens. For each of these, the former is positioned centrally in the through thickness direction and with the centre of the impact aligned with the centre images, and the latter are positioned centrally in the through thickness direction but with the centre of the image located 7.5mm in the longitudinal direction from the centre of the impact.

Increasing the number of continuous plies within a stack, increases the likelihood of delamination along the ply-ply interfaces as a result of lower resistance to damage than thinner laminates [21, 51, 76, 81, 176]. This can be seen in the micrograph 7.5mm away from the impact within a centre arrangement hybrid specimen showing delamination at *point 5* of **Fig. 7.18 (d)**. However, there is still crack propagation along the multi-directional chopped fibres that can be seen at *point 4* in **Fig. 7.18 (c)** and *point 6* in **Fig. 7.18 (d)**.

## 7.5 Summary

This chapter has determined that it is possible to reduce the degree of out-of-plane ply misalignment by approximately 50% with respects to both the waviness angle and the amplitude of ply migration, when pre-curing the continuous laminate within a net mould shape [DFC/0/DFC] arrangement. This design would however only suit a component that exhibits pure in-plane loading that would be limited by out-of-plane misalignment [144-147]. The inter-laminar shear strength is significantly affected by partially curing the laminates [38], would limit the out-of-plane performance. However, if out-of-plane loading was a priority, it would be beneficial to locate the continuous plies closer to the surface to reduce out-of-plane misalignment of the UD plies, as they conform to the shape of the tool without being influenced by the local fibre volume fraction variation within the fibre discontinuous moulding compound.

The initial reasoning behind moving plies oriented in the primary load direction towards the centre of the composite was to improve the damage tolerance of the structure. Hybridising the fibre architecture improved the damage tolerance, retaining approximately a further 20% of the compressive strength than cross-ply structures when exhibiting a high impact energy, 6.7J/mm. However, results indicate that surface or intersperse hybrid architectures retained the most compressive strength post-impact (approximately 50% after an impact energy of 6.7J/mm). Whilst positioning the ply stack near the centre, with the thickest DFC skin, retained only 39% compressive strength after a 6.7J/mm impact. This is a consequence of the different damage mechanisms for discontinuous and continuous fibre materials. There are short, non-linear cracks visible within the discontinuous architecture and long, linear delaminations exhibited between the continuous plies. Therefore stacking 8 plies

together is increasingly likely to increase delamination around the primarily loaded longitudinal plies than by dividing into two 4 ply stacks with greater ability to transfer energy into the multi-directional fibre bundles capable of retaining a greater percentage of strength post impact. It is widely known that thinner plies exhibit greater damage resistance and exhibiting larger damage zones than thick plies [21, 51, 76, 81, 176]. Microcracks form at lower strains within the matrix of transverse lamina of greater thickness. The thickness of a continuous stack within a hybrid arrangement has great influence over the damage resistance even though they maintain equal in-plane stiffness, total thickness, and continuous-discontinuous material ratios (by volume). An additional influence of positioning the continuous plies at the centre would be the effect of out-of-plane waviness. This would however reduce the overall compressive performance rather than the retention of strength between and impacted and non-impacted specimen.

# 8. Demonstrator components

The suitability of directed fibre compounds for producing complex geometries containing ribs and metallic inserts is demonstrated within this chapter. The primary focus was to maintain the high-volume capability of DFC whilst adding some unidirectional reinforcement to further improve the structural performance whilst maintaining a suitable Takt time. This is the culmination of the research presented in *Chapters 5-7*, including the methods established for enhancing the mechanical properties by introducing flow induced fibre alignment, introducing local continuous fibre plies and the design guidelines established for improving both damage tolerance and creating effective joints in the material transition zones within the hybrid architectures.

## 8.1 Demonstrator Components

To demonstrate the capability to produce complex geometries using the discontinuous and/or continuous architecture, 3D structures have been moulded: a compression moulded ribbed panel and a compression moulded brake pedal component.

### 8.1.1 Ribbed panel

An upper mould tool was developed in-house to introduce complex features to the existing 405mm x 405mm flat plaque mould tool. This was used to add stiffening features within regions of varying thicknesses, ranging from 3-20mm, detailed in *Fig. 8.1 (a)*. It incorporated ribs, high detailed areas with low radius corners, a concave geometry (3mm at the centre, 10mm at the edges) and a mounting in the upper mould tool to incorporate an M8 BigHead fastener, which is encapsulated by the composite charge during moulding (shown in *Fig. 8.1 (b)*).

**Fig. 8.2** and **Fig. 8.3** show the ribbed panels moulded with 100% and 50% areal mould coverage, respectively, with uniform charge thickness. The 50% coverage panels were produced from compounds that filled the width of the mould and half of the length, positioned centrally, to encourage flow in a single planar dimension. When moulding with 100% charge coverage, the out-of-plane flow pushed the fibre bundles into the ribs. However, out-of-plane flow has poor fibre carrying capabilities resulting in resin rich regions in the ribs where insufficient mould pressure was exhibited, shown in **Fig. 8.2 (a)**. These out-of-plane flow regions are also visible on the opposing surface as a result of the turbulent flow within this region, **Fig. 8.2 (c-d)**. Also, variations in the local fibre content do not exhibit sufficient flow for the fibre bundles to conform. This results in resin rich regions around the low radii, detailed sections, shown in **Fig. 8.2 (b)**.

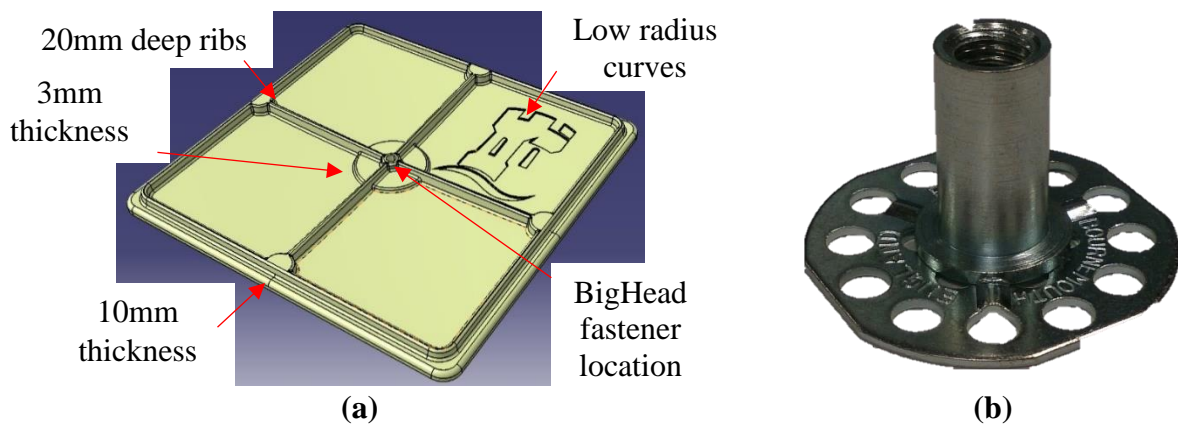


**Figure 8.1.** CAD drawing of the 400mm x 400mm ribbed panel design (a) and BidHead fastener that can be inserted during compression moulding at the centre of the panel

The 50% mould coverage panels significantly reduced the resin rich formations that formed in the net mould coverage panels, as the increased flow improves the fibre conformity under compaction. This can be seen in **Fig. 8.3** where there are significantly fewer resin rich regions. This is also evident when looking at micrographs of the rib cross-section for the 100% and 50% mould coverage plaques, **Fig. 8.4**. This shows that the fibre bundles in the 100% mould coverage plaque are pushed into the ribs from the out-of-plane direction, **Fig. 8.4 (a)**. These fibres conform into a series of U-shapes as they are bent into the rib geometry. It is also shown that the fibre bundles were unable to fully conform at the tip of the rib causing resin richness. When compared to the 50%

mould coverage panels, *Fig. 8.4 (b)*, the fibre bundles flow along the rib direction, which results in aligned fibres conforming fully to the structure of the ribs. This would further enhance the stiffness and strength of the ribs in that direction.

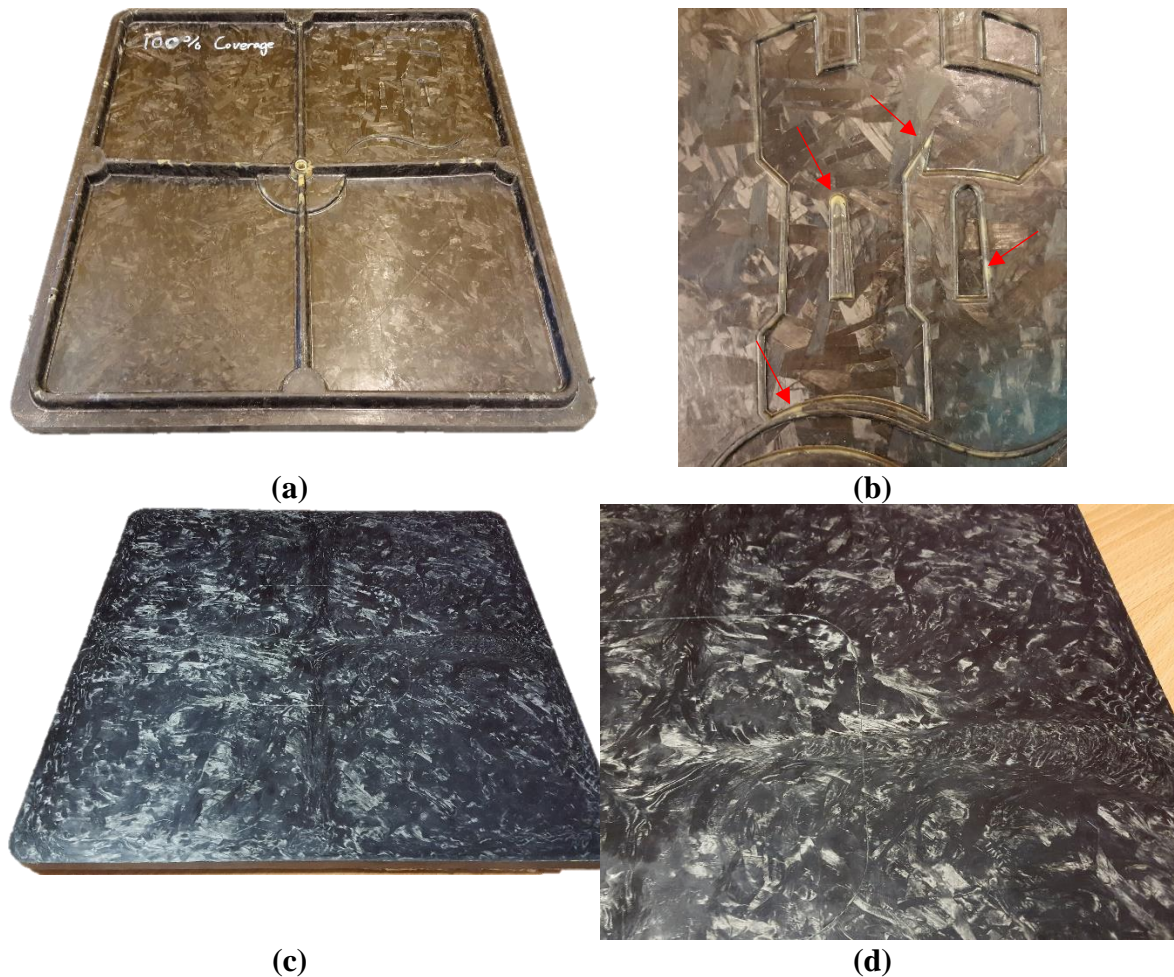
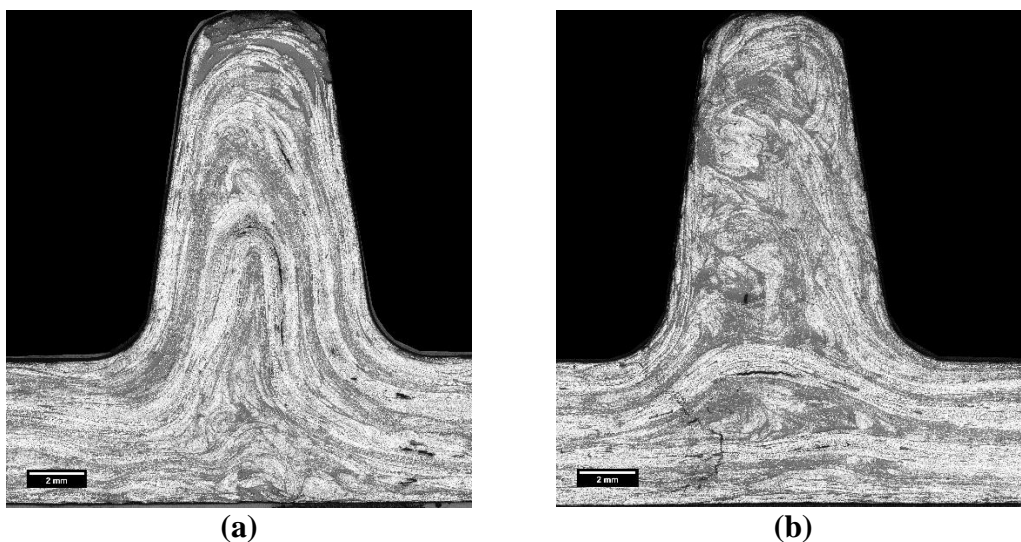


**Figure 8.2.** 3D ribbed panels produced in-house by 100% mould coverage charge viewing the top surface (a), close-up image of the small radius details (b), the bottom surface (c) and a close-up of the bundle swirling on the reverse surface of the ribbed regions



**(a)** **(b)**  
**Figure 8.3.** 3D ribbed panels produced in-house by 50% mould coverage charge (a), close-up image of the small radius details (b)

In-mould flow is important for the encapsulation of metallic fasteners. When moulding with 100% mould coverage, the flat flange of the fastener is difficult to push through the compound as a result of the large surface area. This results in fibre-matrix separation as the resin flows around the fastener causing fibre to fail to fill this region, as shown in **Fig. 8.5 (a)**. One option was to reduce the charge coverage to increase the amount of in-plane flow, or the charge design could be modified by placing a small patch of fibres initially above the insert, as shown in **Fig. 8.5 (b)**. A cross section showing successful fibre filling around the anchor is presented in **Fig. 8.6**, which indicates deformation in the base of the anchor caused by the high moulding pressure.



**(a)** **(b)**  
**Figure 8.4.** Cross-sectional micrographs of 100% mould coverage (a) and 50% mould coverage with flow in the image out-of-plane direction (b)



**Figure 8.5.** Photographs of the resin richness around the fastener moulded with 100% mould coverage (a) and using a small patch of DFC to prevent this (b)

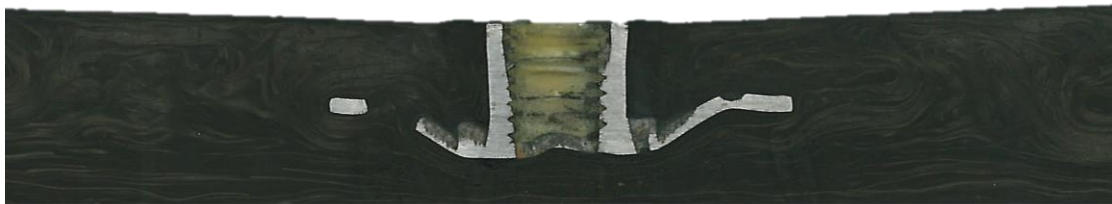


**Figure 8.6.** Cross-sectional image of a successful moulding of the BigHead fastener

When introducing continuous fibres to form a hybrid architecture, large distortions of the UD plies were observed when using small charges, consisting of 150mm x 150mm and 75mm x 150mm charges, shown in *Fig. 8.7 (a)*. These distortions can be seen in *Fig. 8.7 (b)*, which were caused by the flow of the discontinuous material dragging the continuous fabric. However, this can be significantly reduced by placing a net-shaped layer of DFC in contact with the fabric to reduce the shear forces between the continuous plies and the flowing DFC. This prevented distortion in the continuous plies while charge flow on the opposing surface was sufficient to fill the ribs, shown by *Fig. 8.7 (c-d)*.

### 8.1.2 Integrally stiffened pedal

A generic pedal geometry was used to demonstrate a complex component with integrally stiffened ribs and a cylindrical metallic insert encapsulated by the DFC compound. The component was 355mm long with a width ranging from 30-50mm and a part thickness tapering from 30mm to 6mm consisting of rib/wall thickness from 2-3mm, shown in *Fig. 8.8 (a)*. This geometry was produced from 175g of DFC with 50%

Vf and fibre length of 25mm. A successfully moulded DFC pedal, at 60 bar mould pressure, is pictured in *Fig. 8.8 (b-c)*.

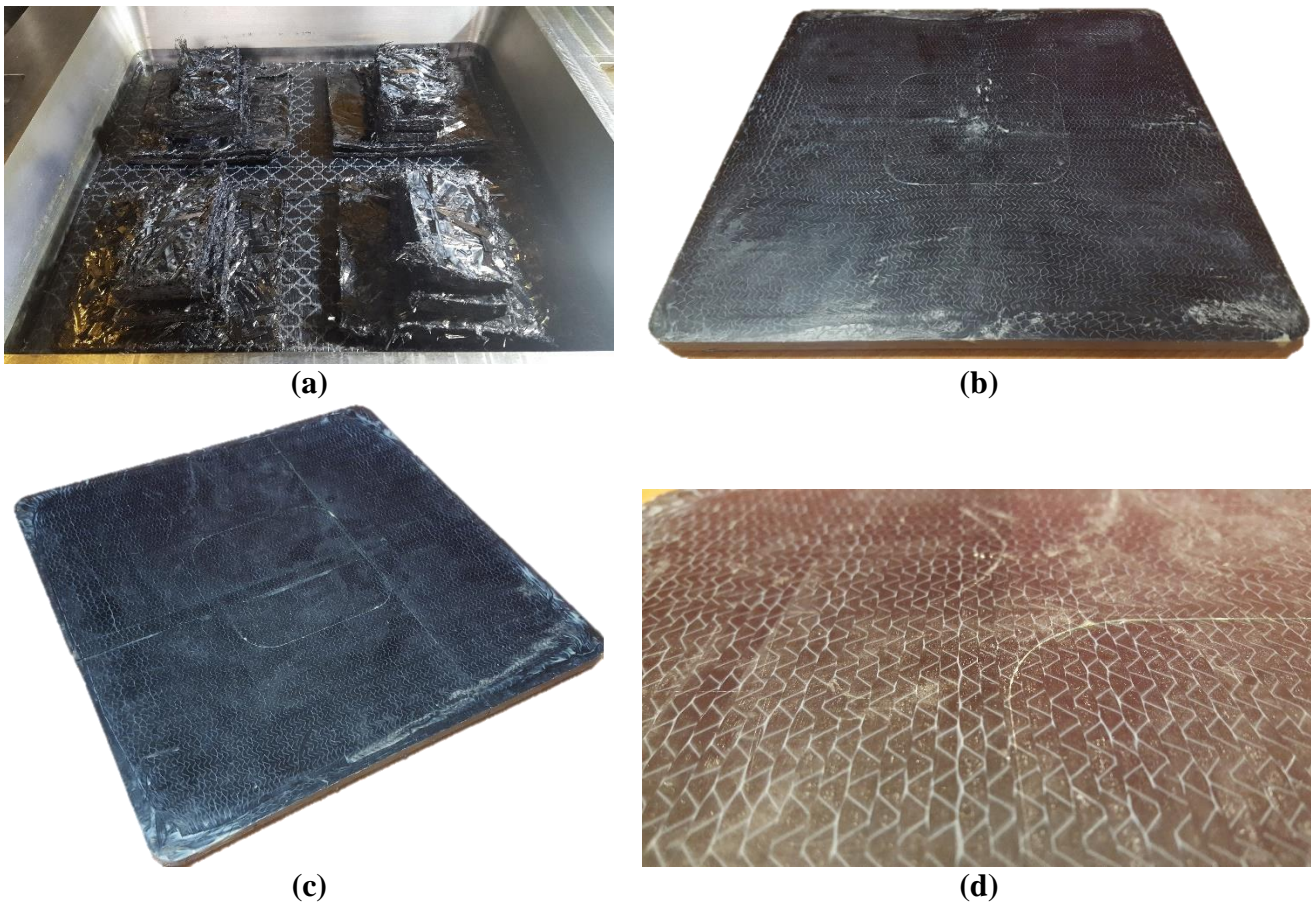


**Figure 8.7.** *Introducing two UD plies, 0/90 arrangement, to the ribbed panel geometry with separate charges of DFC to induce flow (a), the distortion created as a result of this flow (b), a panel with reduced distortion as a result of 100% mould coverage of the contacting layer of DFC to fabric (c) and a close-up image of the straight, undistorted surface layer of fabric (d)*

Trials were performed using DFC material only to ensure that complete filling of the mould could be achieved depending on the layup strategy, such as that shown in *Fig. 8.9* which produced the successful moulding. There were three key areas of interest in this strategy that were required for the successful compression moulding of this component, labelled in the figure. A long base layer, near component length, indicated by *point A* was required to prevent fibre-matrix separation as a result of the reducing thickness of the component. A thick layer was required to overhang the insert, *point B*, to produce sufficient mould pressure all around this component, shown in *Fig. 8.10 (a)*,

with loading from the press only acting in a singular dimension (downwards). Having a large quantity of material near to the insert, *point C*, encouraged flow within the ribs of varying thickness along the length of the pedal, shown in *Fig. 8.10 (b)*.

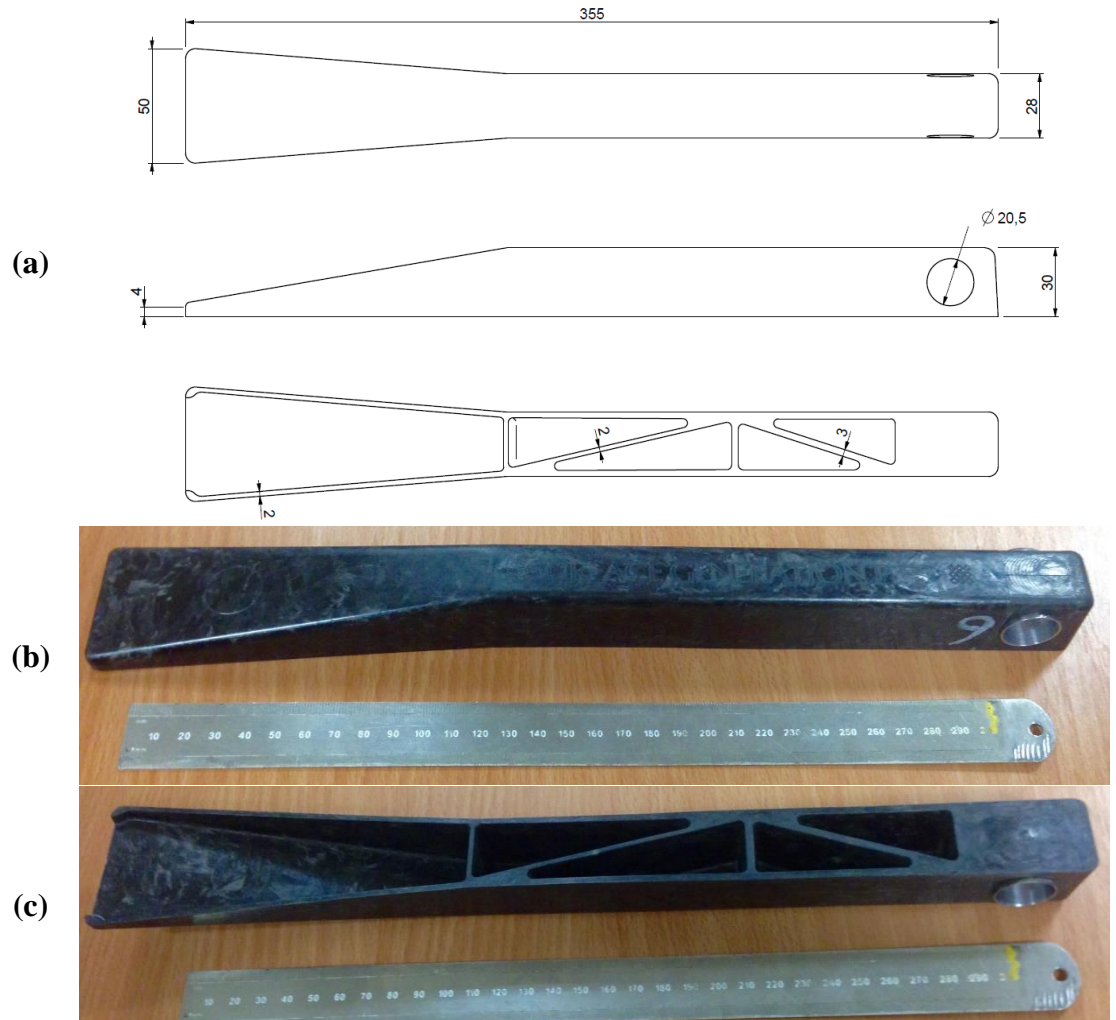


**Figure 8.8.** Schematic of brake pedal dimensions (a) and a successfully moulded DFC brake pedal top surface (a) and bottom surface (b)

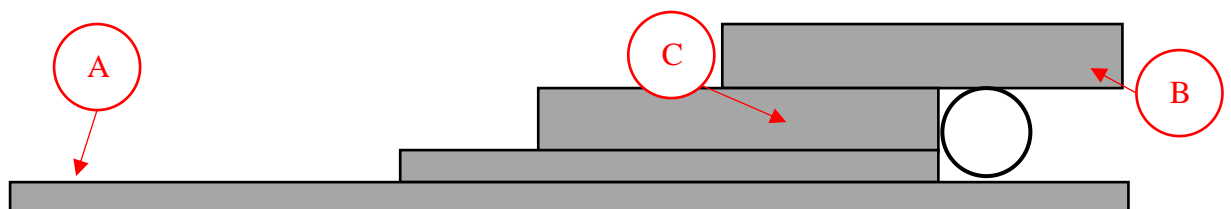


**Figure 8.9.** Side view schematic of the DFC charge layup strategy around the metallic insert



**Figure 8.10.** Close-up images of the metallic insert (a) and the ribs of varying thickness (b)

Two UD layers were then placed onto the top surface of the composite coupled with the ribbed feature to further increase the stiffness of the component in the length dimension. This part is shown in **Fig. 8.11**.



**Figure 8.11.** DFC brake pedal stiffened by hybrid architecture and integrally by ribs

### **8.1.3 Demonstrator conclusions**

Unfortunately, there was insufficient equipment availability to perform any mechanical testing between the DFC and hybrid architectures 3D geometries. However, this has successfully demonstrated their ability to produce hybrid architecture with complex with 50% fibre volume fraction within the discontinuous material and a target of 60% within the continuous plies. These were each produced without increasing the layup time in comparison to producing the complex geometries with DFC only. The rib features have shown an integrally stiffened design, that would be difficult (or impossible) to produce from continuous fabrics with two methods of metallic inserts integrated into each component during the moulding process: an anchored fastener and a plain bush.

# 9. Thesis conclusions

## 9.1 Investigation conclusions

### 9.1.1 Manufacturing process

This project has successfully demonstrated a new manufacturing process to produce carbon low cost fibre-epoxy moulding compounds from low cost constituents. This process enables discontinuous/continuous hybrid carbon fibre architectures to be manufactured quickly (5 minute Takt time), which are suitable for high-volume structural applications. Deriving advanced sheet moulding compounds from UD prepreg, which can cost in excess of £75/kg [6], is prohibitively expensive because it relies on expensive intermediate materials that are chopped into chips using secondary processes to create randomly distributed bundled materials. DFC eliminates the need for these intermediate processes, as impregnation occurs during fibre deposition and charges are produced just-in-time to avoid expensive transportation and storage costs. Material costs alone are therefore reduced by approximately 78% (£16.50/kg) whilst achieving similar mechanical performance.

The mechanical properties of the DFC have been obtained experimentally and compared to commercially available systems such as HexMC (a prepreg derived carbon/epoxy mould compound) and a carbon/vinyl-ester moulding compound. The tensile modulus and strength of DFC,  $36\text{GPa} \pm 3.3\text{GPa}$  and  $320\text{MPa} \pm 27\text{MPa}$  respectively, were found to be equivalent to the prepreg derived moulding compound,  $38\text{GPa}$  and  $300\text{MPa}$  respectively [11]. This resulted from impregnating each individual bundle during deposition to achieve good interfacial adhesion between the fibre and matrix. Additionally, DFC can achieve 50%  $V_f$  as a result of thickening the compound chemically rather using fillers. Comparing to a carbon/vinyl-ester mould compound that used filler, the modulus was 17% lower in the carbon/vinyl-ester compound because of a lower fibre volume fraction (40%). The strength of the carbon/vinyl-ester

compound were also 72% lower than DFC as exhibited matrix-dominated fracturing as a result of the poor interfacial fibre-matrix bonding, either by resin type or poor wet-out during the manufacturing process (i.e. pressing the fibres into a resin film).

### **9.1.2 In-mould flow characterisation**

Tow-based moulding compounds such as DFC can enhance mechanical properties by introducing flow induced alignment. Flow alignment orientates fibres parallel to the direction of flow. The mechanical property distribution across each of the tested panels showed global uniformity, suggesting that fibre-matrix separation was prevented within the compression moulding of charges as low as 40% charge coverage. Where the Takt time is governed by the slowest stage of the manufacturing process, the DFC Takt time is dependent on the rate of material deposition, with constant charge lay down and mould times. Therefore, the degree of flow by the area coverage of the charge has no influence on Takt time, regardless of geometry complexity, because the quantity of deposited material remains constant. However, DFC enables charge geometry to be optimised to enhance the directional properties without influencing Takt time.

Material parameters such as the fibre bundle length and the mould pressure influenced the mechanical performance when flow induced alignment was introduced. Whilst shorter fibre lengths (<25mm) improved the areal mass distribution, they experienced greater fragmentation during chopping than longer fibre lengths and result in increased loft/charge thickness. This increases the out-of-plane fibre orientation variation and prevents adequate compaction during moulding and also caused fibre tangling. The friction created by the fibre-fibre interactions prevented the short fibres (<25mm), from flowing, resulting in fibre-matrix separation. No fibre matrix separation was experienced as the fibre length increased (>25mm), fibre bundles exhibited greater degrees of bundle waviness because of in-mould flow. An analytical model for predicting the stiffness of discontinuous compounds was reverse engineered to produce an orientation tensor, and demonstrated that there was greater out-of-plane misalignment as the fibre length increased.

When moulding net-shaped compounds the highest mechanical properties were achieved when the moulding pressure was increased to 85 bar. For a compound

manufactured with a 25mm fibre length ( $V_f$ -50%) moulded at 85 bar, the tensile strength and modulus were 323MPa and 36GPa, respectively. By increasing the fibre length to 75mm and reducing the mould pressure to 20bar, the greatest properties achieved by flow (50% mould coverage) were 480MPa and 48GPa, respectively. Composites manufactured by this method maintained low void content throughout at approximately 0.3%, relying on in-mould flow to remove trapped air within the compound. The 49% and 33% increases in directional strength and modulus, respectively, and change in void formation mechanisms demonstrate how the geometry and fibre length can be locally tailored within a single DFC charge depending on the mould geometry. High pressure regions within the mould, such as flat surfaces perpendicular to the compression direction, will be capable of isotropic planar mechanical performance with uniform areal density distribution by using short fibres (<25mm) with low void content. However, regions that exhibit low pressure, such as increases in part thickness or surfaces orientated parallel to the compression direction, will require flow to remove voids. These regions will also require greater fibre lengths (>25mm) to flow without fibre-matrix separation, whilst stiffening features such as ribs will also benefit from longer fibres flowing along the length of the ribs to increase the stiffness by fibre alignment.

### **9.1.3 Hybrid carbon fibre architecture**

It was established that very little literature was available for hybrid carbon fibre architecture and consequently there are no design guidelines or testing standards for these materials. Therefore, appropriate continuous or discontinuous test methodology has been used to understand how similarly laminate or joint design guidelines can be used understand hybrid fibre architecture.

In-plane mechanical testing of symmetrical hybrid laminates (UD/DFC/UD) established that the strength and stiffness properties follow a linear trend by volume of continuous to discontinuous material within the composite. This allows the ‘rule of mixtures’ equations to predict the tensile properties depending on the quantity of each constituent. The experimental data showed adequate goodness of fit, where the  $R^2$  values of the longitudinal strength and modulus were both greater than 0.96, whilst the transverse properties had  $R^2$  values greater than 0.75. Additional consideration is also

required when moulding asymmetric hybrid laminates. These exhibited great degrees of warpage as a result of the imbalance of coefficient of thermal expansion in each orientation between UD fibres and the random material.

However, patches of ply stacks may be added to localised regions where laminate ends are introduced as the plies transition from continuous/discontinuous hybrid to a purely discontinuous architecture. It was immediately apparent that resin rich formations are produced at the end of each laminate to produce stress concentrations. Failure often initiated where this resin richness is located at the surface under axial and bending loads. ESPI demonstrated that these stress concentrations formed greatest at the end of the surface laminate of the joint. Under 5kN axial load, strain concentrations in this location reduced by 75% by increasing the step-size from 0mm to 3mm (10 times the ply thickness). Greater than this step size maintained this strain under the same loading, and therefore support the ply-drop and joint guidelines for composite materials [97, 99-101, 107]. These state that the taper angle should not exceed  $7^\circ$  and tapering joints to minimise the peel stresses that arise at the end of the surface ply. However, the bending results showed that the joint strength remained lower than the DFC baseline until a step size 20 times the ply thickness was used. Step sizes greater than this experienced greater axial strains within the DFC region than the end of the surface laminate, resulting in failure away from the joint interface.

An alternative method of moving the high strain concentrations from the joint interface was to taper the interfacial ply to conceal the ply-drops. This increased the stiffness of the interfacial region under axial loading and provided a gradual transition from high to low stiffness material, reducing the shear stresses at the interfacial region by 50%.

#### **9.1.4 Discontinuous/continuous damage tolerance**

The interface of these joints was also successfully characterised by DCB testing, with dissimilar thicknesses of each constituent to ensure equal bending stiffness and achieve horizontal crack fracture along the interface. It demonstrated that the fracture toughness of DFC was greatest because of the non-linear crack growth during mode-I separation and the degree of fibre bridging increased across the interface. Continuous material provided a linear, delamination path that reduced the fracture toughness. However, the

variability in rate of crack growth of hybrid architecture provided a mixture of the two; with localised regions of high fracture toughness and sudden delamination along interfacial regions of resin richness.

A short study with regards to the through thickness position of continuous material within hybrid architecture, demonstrated that if positioned centrally (DFC/UD/DFC), the variability of the fibre volume fraction within the discontinuous material introduces out-of-plane misalignment to the plies. This could be reduced by partially pre-cure the continuous ply/plies prior to compression moulding. However, the DCB testing showed that this significantly reduced the fracture toughness of the continuous/discontinuous interface by preventing both matrix crosslinking and fibrous interleaving across the interface.

An impact study investigated the damage retention following low velocity impact damage. This showed that the impacts resulted in dissimilar microcracking mechanisms as the loads were transferred along the fibre directions. This suggests that continuous plies are only capable of transferring load in a singular orientation and resulting in large delamination in this orientation. Discontinuous fibres however are able transfer load in multiple directions, propagating microcracks in the orientation of fibre bundles before interacting with neighbouring bundles to prevent linear crack propagation. This enables the discontinuous fibre architecture to retain greater mechanical properties post-impact than continuous arrangements. Within hybrid fibre architectures, it was evident that the thickness of the continuous ply stacks, separated by DFC, effected the size of the delaminations. The larger the ply stack the more susceptible the composite is to large delamination.

The overall damage tolerance performance of the hybrid architecture containing 50% continuous material and 50% DFC was shown to retain approximately 55% and 45% of the compressive strength following low and high energy impacts, respectively. These values are approximately an average between the compressive strengths retained by the monolithic DFC and continuous results. This therefore shows that introducing discontinuous material to continuous material can enhance the damage tolerance of a continuous carbon fibre composite.

## 9.2 Summary of thesis conclusions

This thesis has completed the aim and objectives detailed in Section 1.4 as follows:

- The directed fibre compounding process has been developed. This is a low cost automated manufacturing technique (approximately €19/kg material cost) produces discontinuous carbon fibre compounds by using a robot arm to direct the simultaneous deposition of fibre and matrix material. This process has shown the feasibility of achieving a 5 minute Takt time, as demonstrated in *Chapter 4*, although this would require further optimisation of the resin blend to suitable for high volume manufacturing.
  - A tow size of 12K was selected that achieved similar tensile properties to the 3K as a result of the induced fragmentation during the fibre chopping. A toughened epoxy matrix was used with multiple hardeners for B-staging and room temperature storage capabilities. This enables the ability to elevate the temperature initially to reduce viscosity during resin spray before using the B-stage to thicken the compound. The need to use fillers is therefore eliminated and can achieve fibre volume fractions of up to 55% and void content less than 1%.
- The material response of the DFC has been characterised in *Chapter 5* and shows similar performance to prepreg derived carbon fibre-epoxy moulding compounds. The in-mould flow capabilities were also demonstrated, showing the flow induced alignment ability of the material as low as 40% mould coverage. This additionally demonstrated the change in air removal mechanisms which enabled low pressure moulding (20 bar) to obtain low void content (<0.3%). Reducing the mould pressure further reduced the degree of out-of-plane fibre misalignment, which was demonstrated by reverse engineering a stiffness prediction model for tow based discontinuous composites from the experimental results.
- In *Chapter 6 and 7*, the liquid resin spray was used to impregnate non-crimp fabrics for compression moulding.
- The mechanical performance of co-compression moulded continuous and discontinuous hybrid composites was compared in *Chapter 6* to the monolithic architectures. This showed a linear relationship between increasing the UD

content and the tensile modulus and strength. In the longitudinal direction, increased from the modulus and strength of pure DFC (38GPa  $\pm$ 3GPa and 333MPa  $\pm$ 22MPa, respectively) to that of UD (147GPa  $\pm$ 9GPa and 1849MPa  $\pm$ 145MPa, respectively). The mechanical properties of hybrid architecture can therefore be predicted by applying these values, and the volume fraction of each constituent, to the rule of mixtures.

- *Chapter 6* has also investigated the microstructure surrounding the joints between continuous and discontinuous architectures. This shows the resin rich formations at ply ends and ‘swirling’ behaviour of the discontinuous material as the DFC thickness changes. These features result in weakening at the end of the joints. This is also location of peel stress risers under loading. The flexural properties, investigating the structural response of the specimen, indicated that a greater step size than 10:1 S-T ratio was required to reduce impact of the peel stress riser.
  - The strain distributions in the through thickness plane have been quantified by ESPI testing and a simple model has been used to visualise the stress risers in their given orientation.
- Additionally in *Chapter 6*, the fibre bridging has been observed during mode-I separation to show interleaving across the interface. This shows how loads may continue to transfer across the interface in the surrounding areas of the crack.
  - There was an increase in crack initiation load during mode-I in DFC and DFC-UD interfaces compared to UD-UD, however the UD fracture performance is still dominant in terms of the overall mode-I fracture toughness of DFC-UD interfaces.
- In *Chapter 7*, the multi directionality of the random fibres within hybrid fibre architectures has demonstrated improved damage tolerance performance by CAI compared to cross-ply laminates.
- Demonstrator parts have been successfully manufactured, in *Chapter 8*, to incorporate complex features such as ribs and metallic inserts.

### 9.3 Potential future work

Further developments are planned to produce low cost pre-impregnated fabrics by liquid resin spray. Further observations were made throughout this project that would benefit from further study:

Fabric distorts within the hybrid carbon fibre architectures with the flow of the discontinuous material. This would affect the mechanical performance of the composites significantly and has been shown that waviness of the fibres affects mechanical performance. Therefore, optimisation of the orientations of the continuous plies would improve formability when producing complex 3D, minimising fibre misalignment and defect formation.

To develop a forming model for predicting the orientation and stiffness distribution of tow based moulding compounds. This requires understanding of the bundle tow size and length effects and how they interact between each other, align and bend within three-dimensional structures. Flow models of DFC would utilize the ability to locally vary the fibre length and fibre volume fractions to tailor the friction behaviour to encourage variable flow rates within the mould to optimise mould filling. With the introduction of continuous material to compression moulding compounds, this would incorporate optimisation to determine the pressure distribution and flow characteristics. This would enable the prediction of ply migration and misalignment to reduce the shear forces at the hybrid interface.

The liquid resin spray technology may also be developed further. A rheology and through thickness permeability study would determine the potential of impregnating low cost NCF within alternative applications. This thesis has only impregnated individual plies with low areal density (<400gsm). However, understanding the through-thickness permeability with various fabric structures could determine whether multiply or high-density plies could be impregnated at high volumes. LRS impregnation would also be suitable for 3D woven applications to use the out-of-plane orientated tows to enhance through-thickness permeability to impregnate high density fabric (such as 5000gsm).

Additionally, work has already commenced using this production method to produce resin films for automated dry tow placement. This technique combined with discontinuous fibre material will enhance the current DFC/fabric composite manufacturing and will help to further reduce fabric waste. This will also enable the fabric orientations within hybrid carbon fibre architecture to be optimised to minimise tow distortions during preforming and compression moulding to produce high quality complex geometry at high volume production rates. This will require further investigation to understand the resin rheology and tack characteristics in order to deposit dry tows. The B-stage characteristics will also be investigated further to ensure a low Takt time is maintained.

# APPENDIX

## A1 – List of Publications

The following papers have been produced as a result of this work:

1. “Flow Characteristics of Directed Carbon Fibre Compounds”,  
A.D. Evans, C.C. Qian, L.T. Harper, N.A. Warrior,  
Oral Presentation at International Conference on Manufacturing  
Advanced Composites (ICMAC) 2015, Bristol, UK, 24<sup>th</sup>-25<sup>th</sup> June  
2015
2. “Flow Characteristics of Carbon Fibre Sheet Moulding Compounds”,  
A.D. Evans, C.C. Qian, L.T. Harper, N.A. Warrior, P. Brookbank, L.  
Savage,  
Oral Presentation and paper at 20<sup>th</sup> International Conference on  
Composite Materials, Copenhagen, Denmark, 19<sup>th</sup>-24<sup>th</sup> July 2015
3. “Flow characteristics of carbon fibre moulding compounds”,  
A.D. Evans, C.C. Qian, T.A. Turner, L.T. Harper, N.A. Warrior,  
Journal Paper, Composites: Part A, Vol. 90, 2016, pg. 1-12
4. “Joint Design of Continuous/Discontinuous Hybrid Carbon Fibre  
Composites”,  
A.D. Evans, L.T. Harper, T.A. Turner, N.A. Warrior,  
Oral Presentation and paper at 21<sup>st</sup> International Conference on  
Composite Materials, Xi’an, China, 20<sup>th</sup>-25<sup>th</sup> August 2017

The following journal papers are expected to be submitted for review in the near future:

1. “Joint Design of Continuous/Discontinuous Hybrid Carbon Fibre  
Composites”,  
A.D. Evans, L.T. Harper, T.A. Turner, N.A. Warrior.
2. “Damage tolerance of hybrid carbon fibre architecture”,  
A.D. Evans, L.T. Harper, T.A. Turner, N.A. Warrior

## A2 - Cost Model Estimation for DFC compared to other processes modelled in [6]

A. Table A2.A – Information used in referenced cost modelling [6]

Material	Feedstock Price	Feedstock utilised	Preparation Method	Moulding Process	Auto-cutting time	Layup time	Cure Time	Process time	Feedstock cost	Tooling cost	Labour cost	Plant cost	Total cost
	(\$/kg)	(%)			(min)			(min)	(\$/part)				(\$/part)
UD thermoplastic - Diaphragm formed	150	55	Auto-cut hand layup	Diaphragm formed	22	1476	90	90	1418	50	737	118	2323
UD prepreg - Autoclave	100	60	Auto-cut hand layup	Autoclave	16	800	480	480	806	40	610	502	1958
Towpreg - Autoclave	50	90	Tow place	Autoclave	12	727.8	480	480	560	40	553	586	1739
Woven fabric - Autoclave	45	70	Auto-cut hand layup	Resin Infusion/ Autoclave	10.4	650	480	480	402	40	518	484	1444
GMT - Thermoformed	90	90	Stamped Blanks	Thermo-formed	N/A	N/A	2	2	1336	16	23	20	1395
Woven fabric - Vabcag	45	70	Auto-cut hand layup	Resin Infusion/ Oven Vabcag	10.4	650	180	180	402	40	468	73	983
Woven fabric - LP RTM	45	70	Auto-cut hand layup	LP-RTM	11.2	560	120	120	425	80	394	63	962
Woven fabric - HP RTM	45	70	Auto-cut hand layup	HP-RTM	11.2	560	60	60	425	60	369	62	916
SMC ( $V_f = 40\%$ ) - Compression Mould	80	90	Stamped Blanks	Isothermal Press	N/A	N/A	6	6	518	10	38	27	593

**B. Table A2.B – Estimated values for DFC compression moulding ( $V_f = 50\%$ )**

Material	Feedstock Price	Feedstock utilised	Preparation Method	Moulding Process	Auto-cutting time	Layup time	Cure Time	Process time	Feedstock cost	Tooling cost	Labour cost	Plant cost	Total cost
	(\$/kg)	(%)			(min)			(min)	(\$/part)			(\$/part)	
DFC ( $V_f = 50\%$ ) - Compression moulding	50 [6]	97 [5]	DFC near net shape deposition	Isothermal Press	-	-	23 [9]	23 [9]	314.5	5.11	19.42	13.8	352.83
									[Section A1-C]				

**C. Explanation of values generated in Table A2.B**

To produce a comparison against the other manufacturing processes in **Table A2.A**, the same work schedule and other assumptions are used as in study [6]:

- 250 days per year
- One work shift = 8 hours
- Assumed to have one mould tool for each process
- All processes operate as 1 shift per day, except for GMT thermoforming and SMC compression moulding which operate as 3 shifts per day

For DFC, the mould preparation method, directed spray deposition, and moulding, isothermal press, are known. To ensure that the prices are comparative to those in the cost model found in the literature, the feedstock price for roving and resin used for pultrusion, \$50 /kg, was used from this study [6]. DCFP spray deposition closely resembles the fibre deposition method used for DFC compression moulding and therefore similar wastage of <3% by mass [5] can be assumed, hence 97% feedstock utilised. The process time is assumed to be limited by the cure time of 23 minutes [9] however this could be improved in industry by faster curing resins.

Assuming that DFC has the same triple work shift schedule as SMC the production rate for the stated 23min process time can be calculated, for a single mould tool:

$$Production\ rate = \frac{250 \times (3 \times 8) \times 60}{23} = 15652\ parts\ per\ annum$$

The mass of each part can be estimated from the other discontinuous carbon fibre part, SMC, which has a mass of 9.32kg when it's Young's Modulus was 27Gpa [6]. However, it has a Young's modulus of approximately 40GPa has been tested, *Chapter 4* and therefore the mass required for an equivalent stiffness part can be estimated to be:

$$m_{DFC} = m_{SMC} \times \left( \frac{E_{SMC}}{E_{DFC}} \right) = 9.32 \times \left( \frac{27}{40} \right) = 6.29kg$$

Giving a feedstock cost per part:

$$Feedstock\ cost = 50 \times 6.29 = \$314.50 /part$$

Using the tooling, labour and plant costs of SMC in *Table A2.A*, which has a production rate in this model of 8000 parts per annum for this component and single mould [6], the tooling, labour and plant costs per part can be estimated:

$$Tooling\ cost = 10 \times \left( \frac{8000}{15652} \right) = \$5.11 /part$$

$$Labour\ cost = 38 \times \left( \frac{8000}{15652} \right) = \$19.42 /part$$

$$Plant\ cost = 27 \times \left( \frac{8000}{15652} \right) = \$13.80 /part$$

Negating the initial investments for robot apparatus for DFC.

### A3 – Determining the process to partial cure a fabric ply

For determining the best method of partially curing fabric with control over the degree of cure, curing in an oven under vacuum, autoclave and curing on a hot plate were considered. An autoclave was deemed too costly, both expense and time consuming for this test. Therefore, a temperature profile was established on the surface of an aluminium plate heated by a hot plate and in the oven. Starting from ambient conditions, temperature was elevated and held at 100°C. One thermocouple was placed at the centre of the plate and a second 200mm away to establish the uniformity of the heat transfer over the area of the 400mm x 400mm of the fabric.

The temperature profile of the surface heated by the hot plate, *Fig. A3.1 (a)*, showed an overshoot and oscillations in temperature as a result of the controller's zero proportional band. It was also noticed that there was a large temperature difference between the thermocouple located at the centre and 200mm away, >5°C. However, a larger proportional band and convection heat transfer in the oven allowed for constant temperature and uniform heat distribution across the surface of the aluminium plate, *Fig. A3.1 (b)*. It was also demonstrated, at 110 minutes, that when opening the oven door for 3 minutes that the temperature reached its constant temperature within a short time, ~5 minutes, as to cause no significant effect to the degree of cure 100°C.

Once the impregnated fabric had been B-staged, the aluminium plaques were preheated to 100°C. They were removed where the fabric was placed on release film to avoid using release agent and sealed in vacuum bagging. The vacuum pressure was maintained and for a dwell time until a target degree of cure is reached, shown in *Table 7.1*, based on the cure model in *Chapter 4.3*. The enthalpies are shown in *Table 7.2*. Upon completion of the partial or full cure, the fabric is rapidly cooled by removing it from the vacuum and placed onto a cool metallic surface. A sample of partially cured resin was also taken at this point for testing by DSC to measure the actual degree of cure, comparing to the data collected in *Chapter 4*. The degree of cure is calculated from the resin enthalpy post B-stage. Once at room temperature, it is sandwiched between two DFC charges of equal size. The charges and fabric are then co-compression moulded to full cure under normal compression moulding conditions for a net-shape charge.

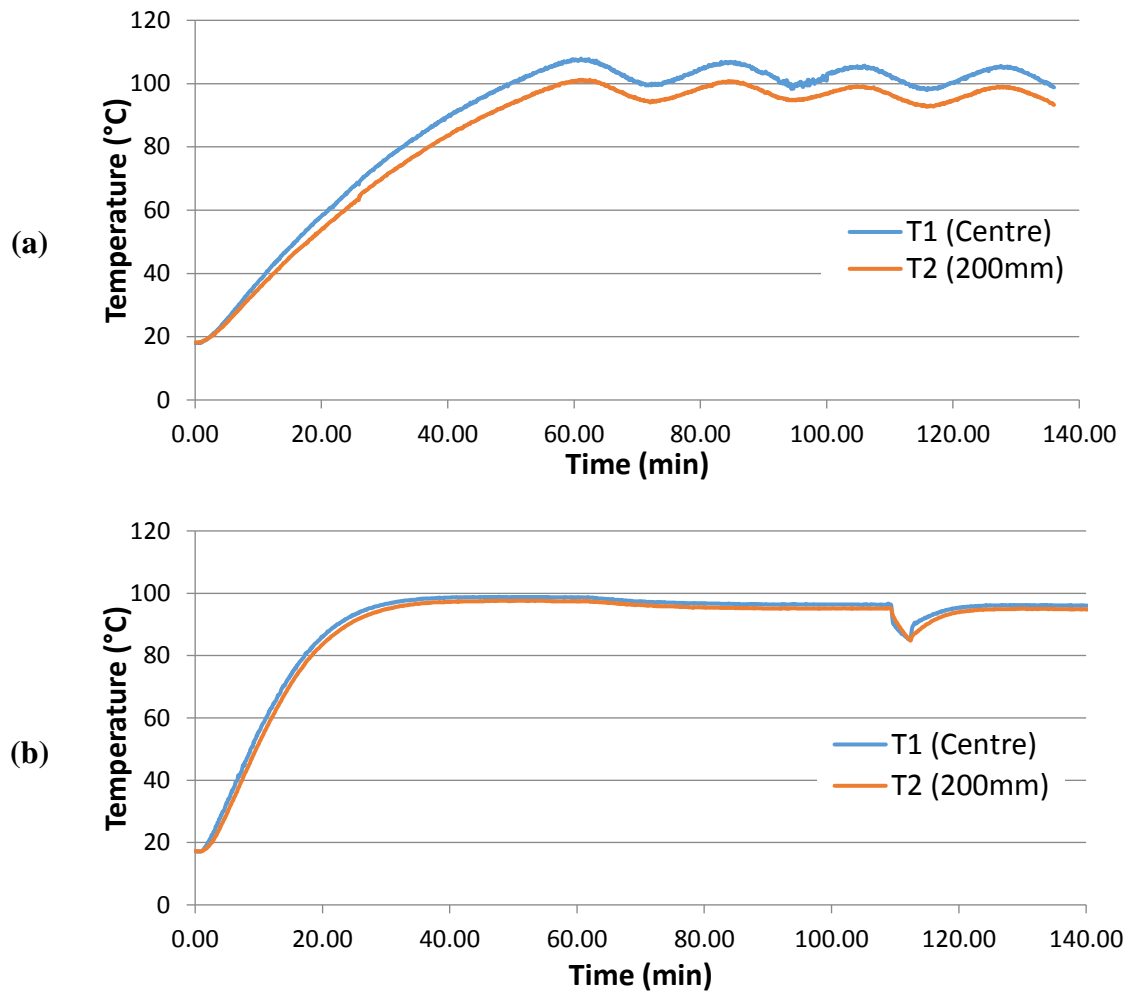


**Figure A3.1** Temperature profiles of an aluminium plate heated to 100°C using conduction through a hot plate (a) and convection oven (b). It should also be noted that at 110minutes, the oven door was opened to simulate for placing the impregnated NCF onto the aluminium plate and sealing in a vacuum.

## A4 – Calculated and actual impact energies

The impactor had a mass of 8.641kg impactor.

Target impact energy:  $E_c = 4.5\text{J/mm}$ :

	Repeat	Calculations			Actual		
		Thickness	Impact energy	Drop height	Impact velocity	Impact energy	$E_c$
		mm	J	m	m/s	J	J/mm
<b>DFC only</b>	1	5.35	24.09	0.28	2.13	19.69	3.68
	2	5.01	22.55	0.27	2.03	17.81	3.55
	3	5.45	24.53	0.29	2.16	20.15	3.70
	4	5.27	23.72	0.28	2.07	18.53	3.52
	5	5.83	26.24	0.31	2.20	20.83	3.57
	6	5.35	24.08	0.28	2.15	20.00	3.74
						Avg.	3.63
						St. dev	0.09
						CoV	2.49%
<b>Centre</b>	1	5.05	22.71	0.27	2.07	18.59	3.68
	2	4.81	21.65	0.26	1.97	16.80	3.49
	3	5.83	26.24	0.31	2.28	22.40	3.84
	4	5.67	25.50	0.30	2.14	19.76	3.49
	5	4.23	19.01	0.22	1.88	15.19	3.60
	6	4.58	20.62	0.24	1.97	16.71	3.65
						Average	3.62
						St. dev	0.13
						CoV	3.67%
<b>Intersperse</b>	1	5.12	23.02	0.27	2.05	18.12	3.54
	2	4.88	21.95	0.26	2.00	17.22	3.53
	3	5.30	23.86	0.28	2.11	19.21	3.62
	4	5.09	22.91	0.27	2.00	17.29	3.40
	5	6.12	27.52	0.32	2.25	21.87	3.58
	6	5.71	25.70	0.30	2.17	20.41	3.57
						Average	3.54
						St. dev	0.08
						CoV	2.18%

	Repeat	Calculations			Actual		
		Thickness	Impact energy	Drop height	Impact velocity	Impact energy	$E_c$
		mm	J	m	m/s	J	J/mm
<b>Surface</b>	1	5.79	26.07	0.31	2.19	20.76	3.58
	2	5.53	24.86	0.29	2.18	20.50	3.71
	3	4.88	21.95	0.26	2.01	17.49	3.59
	4	5.29	23.82	0.28	2.08	18.76	3.54
	5	5.20	23.41	0.28	2.12	19.36	3.72
	6	5.72	25.74	0.30	2.17	20.27	3.54
						Average	3.62
						St. dev	0.08
						CoV	2.22%
<b>Fabric only</b>	1	3.61	16.26	0.19	1.70	12.52	3.47
	2	3.62	16.30	0.19	1.71	12.64	3.49
	3	3.99	17.94	0.21	1.80	14.00	3.51
	4	4.03	18.12	0.21	1.81	14.09	3.50
	5	4.55	20.45	0.24	1.93	16.14	3.55
	6	4.77	21.44	0.25	1.98	16.98	3.56
						Average	3.51
						St. dev	0.04
						CoV	1.08%

Target impact energy:  $E_c = 6.7\text{J/mm}$ :

	Repeat	Calculations			Actual		
		Thickness	Impact energy	Drop height	Impact velocity	Impact energy	$E_c$
		mm	J	m	m/s	J	J/mm
<b>DFC only</b>	1	5.30	35.51	0.42	2.72	32.08	6.05
	2	5.05	33.84	0.40	2.59	29.06	5.76
	3	5.67	37.96	0.45	2.83	34.69	6.12
	4	5.11	34.25	0.40	2.66	30.62	5.99
	5	5.84	39.11	0.46	2.87	35.51	6.08
	6	5.53	37.02	0.44	2.75	32.70	5.92
						Avg.	5.99
						St. dev	0.13
						CoV	2.25%
<b>Centre</b>	1	4.88	32.71	0.39	2.61	29.46	6.03
	2	4.77	31.94	0.38	2.57	28.49	5.98
	3	6.02	40.33	0.48	2.93	37.05	6.15
	4	5.50	36.87	0.43	2.77	33.10	6.02
	5	4.46	29.87	0.35	2.48	26.58	5.96
	6	4.30	28.83	0.34	2.45	25.85	6.01
						Avg.	6.03
						St. dev	0.07
						CoV	1.13%
<b>Intersperse</b>	1	4.92	32.96	0.39	2.62	29.68	6.03
	2	4.80	32.14	0.38	2.58	28.67	5.98
	3	5.35	35.85	0.42	2.75	32.58	6.09
	4	4.98	33.38	0.39	2.59	28.90	5.80
	5	6.14	41.10	0.48	2.95	37.51	6.11
	6	5.78	38.69	0.46	2.82	34.33	5.94
						Avg.	5.99
						St. dev	0.11
						CoV	1.91%

	Repeat	Calculations			Actual		
		Thickness	Impact energy	Drop height	Impact velocity	Impact energy	$E_c$
		mm	J	m	m/s	J	J/mm
<b>Surface</b>	1	5.68	38.06	0.45	2.84	34.83	6.13
	2	5.44	36.43	0.43	2.76	33.02	6.07
	3	5.22	34.97	0.41	2.67	30.84	5.91
	4	5.02	33.62	0.40	2.65	30.41	6.06
	5	5.39	36.08	0.43	2.76	32.92	6.11
	6	5.49	36.80	0.43	2.78	33.40	6.08
						Avg.	6.06
						St. dev	0.08
						CoV	1.31%
<b>Fabric only</b>	1	3.57	23.90	0.28	2.11	19.17	5.37
	2	3.70	24.79	0.29	2.20	20.95	5.66
	3	4.12	27.62	0.33	2.36	23.96	5.81
	4	3.86	25.86	0.31	2.18	20.49	5.31
	5	4.79	32.11	0.38	2.55	28.20	5.88
	6	4.35	29.15	0.34	2.38	24.38	5.60
						Avg.	5.61
						St. dev	0.23
						CoV	4.11%

# REFERENCES

- 1 . V. Mollon, J. Bonhomme, J. Vina and A. Arguelles, *Fracture and Failure Mechanisms for Different Loading Modes of Unidirectional Carbon Fibre/Epoxy Composites*. Advanced Composite Materials for Automotive Applications: Structural Integrity and Crashworthiness. Somerset, NJ, USA John Wiley & Sons. Ltd.; 2014. pp. 229-56.
- 2 . *BMW formally launches i3 manufacture and assembly*, Composites World, 2013, [www.compositesworld.com](http://www.compositesworld.com).
- 3 . J. Starke, Carbon Composites in Automotive Structural Applications, *EuCIA: Composites and Sustainability*, Brussels, 2016, Website: <http://www.eucia.eu/userfiles/files/Starke-Eucia%202016-V4-Druck%20b.pdf>, accessed on: 24/5/2017
- 4 . P. Mårtensson, D. Zenkert and M. Åkermo, Effects of manufacturing constraints on the cost and weight efficiency of integral and differential automotive composite structures. *Composite Structures*. **134**, 2015, 572-8.
- 5 . L. T. Harper, T. A. Turner, N. A. Warrior, J. S. Dahl and C. D. Rudd, Characterisation of random carbon fibre composites from a directed fibre preforming process: Analysis of microstructural parameters. *Composites Part A: Applied Science and Manufacturing*. **37**, 2006, 2136-47.
- 6 . M. G. Bader, Selection of composite materials and manufacturing routes for cost-effective performance. *Composites Part A: Applied Science and Manufacturing*. **33**, 2002, 913-34.
- 7 . A. Wheatley, D. Warren and S. Das, Development of Low-Cost Carbon Fibre for Automotive Applications. *Advanced Composite Materials for Automotive Applications: Structural Integrity and Crashworthiness*. **1**, 2014, 51-73.
- 8 . X. Cui, H. Zhang, S. Wang, L. Zhang and J. Ko, Design of lightweight multi-material automotive bodies using new material performance indices of thin-walled beams for the material selection with crashworthiness consideration. *Materials & Design*. **32**, 2011, 815-21.
- 9 . L. T. Harper, A. Dodworth, R. Luchoo and N. A. Warrior, Automated spray deposition for net-shape carbon/epoxy compression moulding, *17th International Conference on Composite Materials (ICCM17)*, Edinburgh, UK, 2009, 1-10.
- 10 . C. Qian, L. T. Harper, T. A. Turner and N. A. Warrior, Notched behaviour of discontinuous carbon fibre composites: Comparison with quasi-isotropic non-crimp fabric. *Composites Part A: Applied Science and Manufacturing*. **42**, 2011, 293-302.
- 11 . *HexMC (M77) User Guide*. 2014, [http://www.hexcel.com/Resources/UserGuides/HexMC\\_User%20Guide.pdf](http://www.hexcel.com/Resources/UserGuides/HexMC_User%20Guide.pdf), Hexcel Corporation, accessed on: 16/04/2014
- 12 . U. Beier, F. Fischer, J. K. W. Sandler, V. Altstädt, C. Weimer and W. Buchs, Mechanical performance of carbon fibre-reinforced composites based on stitched preforms. *Composites Part A: Applied Science and Manufacturing*. **38**, 2007, 1655-63.
- 13 . K. Mason, *Compression molding with structural carbon SMC*. 2005, <http://www.compositesworld.com/articles/compression-molding-with-structural-carbon-smc>, Composites World, accessed on: 7-5-15

- 14 . *Technical Data Sheet: Forged Composites*. [https://www.lamborghini.com/en-en/sites/en-en/files/DAM/lamborghini/forged/Forged%20composites\\_EN.pdf](https://www.lamborghini.com/en-en/sites/en-en/files/DAM/lamborghini/forged/Forged%20composites_EN.pdf), Lamborghini, accessed on: 24/5/2017
- 15 . L. Orgéas and P. J. J. Dumont, *Sheet Moulding Compounds*. In: L. Nicolais, A. Borzacchiello, S. M. Lee, editors. *Wiley Encyclopedia of Composites*. 2nd ed. New Jersey, United States: Wiley-Blackwell; 2012. pp. 2683-718.
- 16 . M. Revellino, L. Saggese and E. Gaiero, 2.22 - *Compression Molding of SMCs*. In: A. Kelly, C. Zweben, editors. *Comprehensive Composite Materials*. Oxford: Pergamon; 2000. pp. 763-805.
- 17 . *menzolit CarbonSMC 1100*. 2014, <http://menzolit.com/wp-content/uploads/2014/06/Menzolit-PI-CarbonSMC-1100-en.pdf>, Menzolit, accessed on: 1-5-2015
- 18 . *Quantum Lytex 4197*. 2013, <http://www.quantumcomposites.com/pdf/datasheets/lytex/Quantum-Lytex-4197.pdf>, Quantum Composites, accessed on: 6/5/2014
- 19 . L. T. Harper, T. A. Turner, N. A. Warrior and C. D. Rudd, Characterisation of random carbon fibre composites from a directed fibre preforming process: The effect of fibre length. *Composites Part A: Applied Science and Manufacturing*. **37**, 2006, 1863-78.
- 20 . C. Qian, L. T. Harper, T. A. Turner and N. A. Warrior, Structural optimisation of random discontinuous fibre composites: Part 1 – Methodology. *Composites Part A: Applied Science and Manufacturing*. **68**, 2015, 406-16.
- 21 . K. Johanson, L. T. Harper, M. S. Johnson and N. A. Warrior, Heterogeneity of discontinuous carbon fibre composites: Damage initiation captured by Digital Image Correlation. *Composites Part A: Applied Science and Manufacturing*. **68**, 2015, 304-12.
- 22 . D. Trent, *Lamborghini Huracan Performante - Geneva 2017*. 2017, <https://www.pistonheads.com/news/ph-eurocars/lamborghini-huracan-performante--geneva-2017/35870>, PistonHeads, accessed on: 12/7/2017
- 23 . P. Dumont, S. Le Corre, L. Orgéas, D. Favier, C. Gaborit and P. Lory, Finite element implementation of a two-phase model for compression molding of composites. *Revue Européenne des Éléments*. **14**, 2005, 885-902.
- 24 . P. Dumont, L. Orgéas, D. Favier, P. Pizette and C. Venet, Compression moulding of SMC: In situ experiments, modelling and simulation. *Composites Part A: Applied Science and Manufacturing*. **38**, 2007, 353-68.
- 25 . M. Gruskiewicz and J. Collister, Analysis of the thickening reaction of a sheet molding compound resin through the use of dynamic mechanical testing. *Polymer Composites*. **3**, 1982, 6-11.
- 26 . R. Saito, W.-M. J. Kan and L. James Lee, Thickening behaviour and shrinkage control of low profile unsaturated polyester resins. *Polymer*. **37**, 1996, 3567-76.
- 27 . O. Guiraud, P. J. J. Dumont, L. Orgéas and D. Favier, Rheometry of compression moulded fibre-reinforced polymer composites: Rheology, compressibility, and friction forces with mould surfaces. *Composites Part A: Applied Science and Manufacturing*. **43**, 2012, 2107-19.
- 28 . B. Mitchell. *An Introduction to Materials Engineering and Science For Chemical and Materials Engineers*. New Jersey: Wiley Interscience; 2004.
- 29 . T. R. Shives and W. A. Willard. *Advanced Composites: Design and Applications : Proceedings of the 29th Meeting of the Mechanical Failures*

- Prevention Group, Held at the National Bureau of Standards, Gaithersburg, Maryland, May 23-25, 1979: The Bureau; 1979.*
- 30 . C. Kjelgaard, *Challenges in composites*, Aircraft Technology Engineering & Maintenance, 2012, UBM Aviation Publications, **116**, pp. 52-7.
  - 31 . K. Akiyama, *Development of PCM (Prepreg Compression Molding) Technology*. 2011,  
[http://www.speautomotive.com/SPEA\\_CD/SPEA2011/pdf/ET/ET2.pdf](http://www.speautomotive.com/SPEA_CD/SPEA2011/pdf/ET/ET2.pdf), SPE Automotive Division, accessed on: 02/01/2014
  - 32 . D. M. Corbridge, L. T. Harper, D. S. A. De Focatiis and N. A. Warrior, Compression moulding of composites with hybrid fibre architectures. *Composites Part A: Applied Science and Manufacturing*. **95**, 2017, 87-99.
  - 33 . G. Nilakantan and S. Nutt, Reuse and upcycling of aerospace prepreg scrap and waste. *Reinforced Plastics*. **59**, 2015, 44-51.
  - 34 . M. Cabrera-Ríos and J. M. Castro, An economical way of using carbon fibers in sheet molding compound compression molding for automotive applications. *Polymer Composites*. **27**, 2006, 718-22.
  - 35 . M. Bruderick, D. Denton, M. Shinedling and M. Kiesel, Applications of carbon/fiber SMC for the 2003 Dodge Viper, *Second SPE Automotive Composites Conference*, Michigan, USA, 2002, 10.
  - 36 . I. Verpoest. *Micromechanics of Continuous and Short Fibre Composites*. Katholieke Universiteit, Belgium: Department of Metallurgy and Materials Engineering; 2009.
  - 37 . *The Advantages of Epoxy Resin versus Polyester in Marine Composite Structures*.  
<http://www.amtcomposites.co.za/sites/default/files/media/howto/Advantages%20of%20Epoxy%20over%20Polyester.pdf>, SP Systems, accessed on: 16/04/2014
  - 38 . C. A. Harper. *Modern Plastics Handbook*: Mcgraw-hill; 2000.
  - 39 . D. Hull and T. W. Clyne. *An introduction to composite materials*. 2nd ed. Cambridge, UK: Cambridge University Press; 1996.
  - 40 . T. Johnson, *Selecting Composite Materials - Comparing and Choosing Composite Materials*. 2014,  
<http://composite.about.com/od/whatsacomposite/a/Selecting-Composite-Materials.htm>, About.com, accessed on: 16/04/2014
  - 41 . Fibers, Resin Sprayed All at Once. *Chemical & Engineering News Archive*. **36**, 1958, 54-5.
  - 42 . C. Plueddeman, *Deja Vu: A time-warped study of the fiberglass family runabout*, Boating, Jan 1988, pp. 121-36.
  - 43 . D. Gerr. *The Elements of Boat Strength: For Builders, Designers and Owners*: McGraw-Hill Professional; 1999.
  - 44 . L. T. Harper, T. A. Turner, N. A. Warrior and C. D. Rudd, Characterisation of random carbon fibre composites from a directed fibre preforming process: The effect of tow filamentisation. *Composites Part A: Applied Science and Manufacturing*. **38**, 2007, 755-70.
  - 45 . L. T. Harper, *Discontinuous Carbon Fibre Composites for Automotive Applications*, PhD Thesis: University of Nottingham; 2006.
  - 46 . G. Estrada, C. Vieux-Pernon and S. G. Advani, Experimental Characterization of the Influence of Tackifier Material on Preform Permeability. *Journal of Composite Materials*. **36**, 2002, 2297-310.

- 47 . S. Bickerton, Q. Govignon and P. Kelly, 7 - *Resin infusion/liquid composite moulding (LCM) of advanced fibre-reinforced polymer (FRP) A2* - Bai, Jiping. *Advanced Fibre-Reinforced Polymer (FRP) Composites for Structural Applications*: Woodhead Publishing; 2013. pp. 155-86.
- 48 . A. Endruweit, L. T. Harper, T. A. Turner, N. A. Warrior and A. C. Long, Random discontinuous carbon fibre preforms: Permeability modelling and resin injection simulation. *Composites Part A: Applied Science and Manufacturing*. **39**, 2008, 1660-9.
- 49 . A. Endruweit, L. T. Harper, T. A. Turner, N. A. Warrior and A. C. Long, Random discontinuous carbon fiber preforms: Experimental permeability characterization and local modeling. *Polymer Composites*. **31**, 2010, 569-80.
- 50 . D. O'Regan and M. Akay, The distribution of fibre lengths in injection moulded polyamide composite components. *Journal of Materials Processing Technology*. **56**, 1996, 282-91.
- 51 . S. Mathurosemontri, P. Uawongsuwan, S. Nagai and H. Hamada, The Effect of Processing Parameter on Mechanical Properties of Short Glass Fiber Reinforced Polyoxymethylene Composite by Direct Fiber Feeding Injection Molding Process. *Energy Procedia*. **89**, 2016, 255-63.
- 52 . K. G. Swift and J. D. Booker, *Chapter 5 - Plastics and Composites Processing*. *Manufacturing Process Selection Handbook*. Oxford: Butterworth-Heinemann; 2013. pp. 141-74.
- 53 . *Injection moulding of lightweight parts: Less weight thanks to solutions with multi material design*. 2016, [https://www.arburg.com/fileadmin/redaktion/mediathek/prospekte/arburg\\_lightweight\\_parts\\_681230\\_en\\_gb.pdf](https://www.arburg.com/fileadmin/redaktion/mediathek/prospekte/arburg_lightweight_parts_681230_en_gb.pdf), Arburg, accessed on: 6-7-2017
- 54 . V. P. McConnell, SMC has plenty of road to run in automotive applications. *Reinforced Plastics*. **51**, 2007, 20-5.
- 55 . J. Wulfsberg, A. Herrmann, G. Ziegmann, G. Lonsdorfer, N. Stöß and M. Fette, Combination of Carbon Fibre Sheet Moulding Compound and Prepreg Compression Moulding in Aerospace Industry. *Procedia Engineering*. **81**, 2014, 1601-7.
- 56 . P. Feraboli, E. Peitso, F. Deleo, T. Cleveland and P. B. Stickler, Characterization of Prepreg-Based Discontinuous Carbon Fiber/Epoxy Systems. *Journal of Reinforced Plastics and Composites*. **28**, 2009, 1191-214.
- 57 . J. Aubry, HexMC — bridging the gap between prepreg and SMC. *Reinforced Plastics*. **45**, 2001, 38-40.
- 58 . Boeing 787 features composite window frames. *Reinforced Plastics*. **51**, 2007, 4.
- 59 . I.-C. Kim and T.-H. Yoon, Enhanced interfacial adhesion of carbon fibers to vinyl ester resin using poly(arylene ether phosphine oxide) coatings as adhesion promoters. *Journal of Adhesion Science and Technology*. **14**, 2000, 545-59.
- 60 . F. Vautard, L. Xu and L. Drzal, *Carbon Fiber—Vinyl Ester Interfacial Adhesion Improvement by the Use of an Epoxy Coating*. In: I. M. Daniel, E. E. Gdoutos, Y. D. S. Rajapakse, editors. *Major Accomplishments in Composite Materials and Sandwich Structures*: Springer Netherlands; 2010. pp. 27-50.
- 61 . *Lytex Properties*. <http://www.hycompinc.com/PDFs/Lytex%20Properties.pdf>, Quantum Composites, accessed on: 6/5/2014

- 62 . *Quantum Lytex 9063 BK-E*. 2013, <http://www.quantumcomposites.com/pdf/datasheets/lytex/Quantum-Lytex%209063%20-E.pdf>, Quantum Composites, accessed on: 6/5/2014
- 63 . R. F. Eduljee, R. L. McCullough and J. W. Gillespie Jr, The influence of aggregated and dispersed textures on the elastic properties of discontinuous-fiber composites. *Composites Science and Technology*. **50**, 1994, 381-91.
- 64 . H. Li, W.-X. Wang, Y. Takao and T. Matsubara, New designs of unidirectionally arrayed chopped strands by introducing discontinuous angled slits into prepreg. *Composites Part A: Applied Science and Manufacturing*. **45**, 2013, 127-33.
- 65 . S. F. M. de Almeida and Z. d. S. N. Neto, Effect of void content on the strength of composite laminates. *Composite structures*. **28**, 1994, 139-48.
- 66 . Ghiorse, Sr., Effect of void content on the mechanical properties of carbon/epoxy laminates. *SAMPE Quarterly*. **24**, 1993, 54-9.
- 67 . M.-S. Kim, W. I. Lee, W.-S. Han and A. Vautrin, Optimisation of location and dimension of SMC precharge in compression moulding process. *Computers & Structures*. **89**, 2011, 1523-34.
- 68 . C. H. Park, W. I. Lee, Y. E. Yoo and E. G. Kim, A study on fiber orientation in the compression molding of fiber reinforced polymer composite material. *Journal of Materials Processing Technology*. **111**, 2001, 233-9.
- 69 . B. A. Davis. *Compression Molding*. Munich: Hanser Publishers; 2003.
- 70 . D.-K. Kim, H.-Y. Choi and N. Kim, Experimental investigation and numerical simulation of SMC in compression molding. *Journal of Materials Processing Technology*. **49**, 1995, 333-44.
- 71 . G. Kotsikos and A. G. Gibson, Investigation of the squeeze flow behaviour of Sheet Moulding Compounds (SMC). *Composites Part A: Applied Science and Manufacturing*. **29**, 1998, 1569-77.
- 72 . P. Neto and N. Mendes, Direct off-line robot programming via a common CAD package. *Robotics and Autonomous Systems*. **61**, 2013, 896-910.
- 73 . J. E. Lindhagen and L. A. Berglund, Application of bridging-law concepts to short-fibre composites Part 1: DCB test procedures for bridging law and fracture energy. *Composites Science and Technology*. **60**, 2000, 871-83.
- 74 . A. Kelly and W. R. Tyson, Tensile properties of fibre reinforced metals—II. Creep of silver-tungsten. *Journal of the Mechanics and Physics of Solids*. **14**, 1966, 177-84.
- 75 . M. R. Piggott, Mesostructures and their mechanics in fibre composites. *Advanced Composite Materials*. **6**, 1996, 75-81.
- 76 . P. D. Soden, M. J. Hinton and A. S. Kaddour, Lamina properties, lay-up configurations and loading conditions for a range of fibre-reinforced composite laminates. *Composites Science and Technology*. **58**, 1998, 1011-22.
- 77 . T. A. Turner, L. T. Harper, N. A. Warrior and C. A., Energy Absorption Performance of Meso-Scale Discontinuous Fibre Composites. *International Journal of Vehicle Structures and Systems - Special Issue on Structural Impact & Crashworthiness: Part 1*. **3**, 2011, 80-6.
- 78 . G. C. Jacob, J. M. Starbuck, J. F. Fellers and S. Simunovic, Effect of fiber volume fraction, fiber length and fiber tow size on the energy absorption of chopped carbon fiber-polymer composites. *Polymer Composites*. **26**, 2005, 293-305.

- 79 . P. T. Odenberger, H. M. Andersson and T. S. Lundström, Experimental flow-front visualisation in compression moulding of SMC. *Composites Part A: Applied Science and Manufacturing*. **35**, 2004, 1125-34.
- 80 . M. Rabinovich, K. L. Olsavsky, B. Leach, M. Cabrera-Ríos and J. M. Castro, Sheet molding compound characterization using spiral flow. *Journal of Applied Polymer Science*. **109**, 2008, 2465-71.
- 81 . T. H. Le, P. J. J. Dumont, L. Orgéas, D. Favier, L. Salvo and E. Boller, X-ray phase contrast microtomography for the analysis of the fibrous microstructure of SMC composites. *Composites Part A: Applied Science and Manufacturing*. **39**, 2008, 91-103.
- 82 . K. S. Christensen, B. Hutchinson, M. E. Sun, A. T. Osswald and A. B. Davis, Fiber-Matrix Separation in Ribbed SMC and BMC Parts, *Annual Technical Conference '97 - ANTEC : Society of Plastics Engineers Annual Technical Papers*, 1997, 6.
- 83 . M. Rabinovich, *Sheet Molding Compound (SMC) Processing: Spiral Flow Test and Physical Properties*: Ohio State University; 2004.
- 84 . L. Kacir, M. Narkis and O. Ishai, Oriented short glass fiber composites. I. Preparation and Statistical Analysis of Aligned Fibre Mats. *Polymer Engineering and Science*. **15**, 1975, 525-31.
- 85 . E. R. Trambauer, J. R. Hellman and L. E. Jones, Orientated microchannel membranes via oxidation of carbon-fiber-reinforced glass composites. *Carbon*. **30**, 1992, 873-82.
- 86 . A. E. Scott, M. Mavrogordato, P. Wright, I. Sinclair and S. M. Spearing, In situ fibre fracture measurement in carbon–epoxy laminates using high resolution computed tomography. *Composites Science and Technology*. **71**, 2011, 1471-7.
- 87 . P. Wright, X. Fu, I. Sinclair and S. M. Spearing, Ultra High Resolution Computed Tomography of Damage in Notched Carbon Fiber—Epoxy Composites. *Journal of Composite Materials*. **42**, 2008, 1993-2002.
- 88 . B. X. Bie, J. Y. Huang, D. Fan, T. Sun, K. Fezzaa, X. H. Xiao, M. L. Qi and S. N. Luo, Orientation-dependent tensile deformation and damage of a T700 carbon fiber/epoxy composite: A synchrotron-based study. *Carbon*. **121**, 2017, 127-33.
- 89 . N. Q. Nguyen, M. Mehdikhani, I. Straumit, L. Gorbatikh, L. Lessard and S. V. Lomov, Micro-CT measurement of fibre misalignment: Application to carbon/epoxy laminates manufactured in autoclave and by vacuum assisted resin transfer moulding. *Composites Part A: Applied Science and Manufacturing*. **104**, 2018, 14-23.
- 90 . A. R. Aziz, M. A. Ali, X. Zeng, R. Umer, P. Schubel and W. J. Cantwell, Transverse permeability of dry fiber preforms manufactured by automated fiber placement. *Composites Science and Technology*. **152**, 2017, 57-67.
- 91 . F. Prade, F. Schaff, S. Senck, P. Meyer, J. Mohr, J. Kastner and F. Pfeiffer, Nondestructive characterization of fiber orientation in short fiber reinforced polymer composites with X-ray vector radiography. *NDT & E International*. **86**, 2017, 65-72.
- 92 . Y. Li, S. Pimenta, J. Singgih, S. Nothdurfter and K. Schuffenhauer, Experimental investigation of randomly-oriented tow-based discontinuous composites and their equivalent laminates. *Composites Part A: Applied Science and Manufacturing*. **102**, 2017, 64-75.

- 93 . *HexPly M77 Snap Cure Prepreg*. 2015,  
<http://www.hexcel.com/products/industries/isnap-cure>, Hexcel, accessed on:  
 1-5-2015
- 94 . K. Akiyama, *Development of Particle-Core Compression Molding*. 2013,  
[http://www.speautomotive.com/SPEA\\_CD/SPEA2013/pdf/CF/CF7.pdf](http://www.speautomotive.com/SPEA_CD/SPEA2013/pdf/CF/CF7.pdf), SPE  
 Automotive Division, accessed on: 17/04/2014
- 95 . M. Fette, M. Hentschel, F. Köhler, J. Wulfsberg and A. Herrmann, Automated  
 and Cost-efficient Production of Hybrid Sheet Moulding Compound Aircraft  
 Components. *Procedia Manufacturing*. **6**, 2016, 132-9.
- 96 . M. Belhaj, M. Deleglise, S. Comas-Cardona, H. Demouveau, C. Binetruy, C.  
 Duval and P. Figueiredo, Dry fiber automated placement of carbon fibrous  
 preforms. *Composites Part B: Engineering*. **50**, 2013, 107-11.
- 97 . AMT Composites, AMTS Standard Workshop Practice, *Composite design  
 Section 2 of 3: Composite design guidelines*, Technology Innovation Agency,  
 2011
- 98 . *Laminate Design Rules*. 2002,  
<http://www.compositesworld.com/articles/laminate-design-rules>, accessed on:  
 2/7/2014
- 99 . J. A. Bailie, R. P. Ley and A. Pasricha, *A summary and review of composite  
 laminate design guidelines*. 1997,  
[http://www.abbottaerospace.com/download/reference\\_data/composites/faa\\_nasa\\_composite\\_papers/NASA-NAS1-19347.pdf](http://www.abbottaerospace.com/download/reference_data/composites/faa_nasa_composite_papers/NASA-NAS1-19347.pdf), Northrop Gruman, accessed  
 on: 12-2-2016
- 100 . F. X. Irisarri, A. Lasseigne, F. H. Leroy and R. Le Riche, Optimal design of  
 laminated composite structures with ply drops using stacking sequence tables.  
*Composite Structures*. **107**, 2014, 559-69.
- 101 . A. Mukherjee and B. Varughese, Design guidelines for ply drop-off in  
 laminated composite structures. *Composites Part B: Engineering*. **32**, 2001,  
 153-64.
- 102 . B. P. Adamson and B. L. Fox, An evaluation of the performance of advanced  
 melded composite joints. *Composite Structures*. **92**, 2010, 2071-6.
- 103 . P. Vannucci, On Bending–Tension Coupling of Laminates. *Journal of  
 elasticity and the physical science of solids*. **64**, 2001, 13-28.
- 104 . Z. Jiang, S. Wan, T. Keller and A. P. Vassilopoulos, Two-dimensional  
 analytical stress distribution model for unbalanced FRP composite single-lap  
 joints. *European Journal of Mechanics - A/Solids*. **66**, 2017, 341-55.
- 105 . R. D. S. G. Campilho, *Repair of composite and wood structures*, PhD thesis:  
 Porto University; 2009.
- 106 . L. F. M. da Silva and R. D. S. G. Campilho. *Advances in Numerical Modeling  
 of Adhesive Joints*: Springer Berlin Heidelberg; 2011.
- 107 . A. S. Mosallam. *Design Guide for FRP Composite Connections*. American  
 Society of Civil Engineers (ASCE); 2011.
- 108 . B. R. Vidyashankar and A. V. Krishna Murty, Analysis of laminates with ply  
 drops. *Composites Science and Technology*. **61**, 2001, 749-58.
- 109 . T. Brien, *Residual Thermal and Moisture Influences on the Analysis of Local  
 Delaminations*. 1992.
- 110 . R. P. Theriault, T. A. Osswald and J. M. Castro, Processing induced residual  
 stress in asymmetric laminate panels. *Polymer Composites*. **20**, 1999, 493-509.

- 111 . W. Xiaojun and D. D. L. Chung, Residual stress in carbon fiber embedded in epoxy, studied by simultaneous measurement of applied stress and electrical resistance. *Composite Interfaces*. **5**, 1997, 277-81.
- 112 . A. S. Maxwell, W. Broughton and M. Lodeiro. *Measurement of residual stresses and strains in carbon fibre composites*. Teddington: National Physical Laboratory; 2009.
- 113 . A. I. Selmy, A. R. Elsesi, N. A. Azab and M. A. Abd El-baky, Interlaminar shear behavior of unidirectional glass fiber (U)/random glass fiber (R)/epoxy hybrid and non-hybrid composite laminates. *Composites Part B: Engineering*. **43**, 2012, 1714-9.
- 114 . Fibre-reinforced plastic composites - Determination of apparent interlaminar shear strength by short beam method, *BS EN ISO 14130*, London, UK, 1998
- 115 . S. L. Bai, V. Djafari, M. Andréani and D. François, In situ study of short-beam shear tests for composite materials. *Composites Science and Technology*. **55**, 1995, 343-8.
- 116 . D.-J. Lee and I. Palley, Simple model to predict the interlaminar shear strength of laminate composites. *Journal of Composite Materials*. **46**, 2012, 1357-65.
- 117 . D. Adams, *Through-the-thickness tensile strength testing using a curved beam*. 2008, <https://www.compositesworld.com/articles/through-the-thickness-tensile-strength-testing-using-a-curved-beam>, accessed on: 17/10/2017
- 118 . Standard Test Methods for Mixed Mode I-Mode II Interlaminar Fracture Toughness of Unidirectional Fiber Reinforced Polymer Matrix Composites, *ASTM Standards D6671/D6671M-13*, West Conshohocken, PA, 2013 (originally published in 2001)
- 119 . A. B. Pereira and A. B. de Moraes, Mixed mode I+II interlaminar fracture of carbon/epoxy laminates. *Composites Part A: Applied Science and Manufacturing*. **39**, 2008, 322-33.
- 120 . R. W. Truss, P. J. Hine and R. A. Duckett, Interlaminar and intralaminar fracture toughness of uniaxial continuous and discontinuous carbon fibre/epoxy composites. *Composites Part A: Applied Science and Manufacturing*. **28**, 1997, 627-36.
- 121 . B. D. Manshadi, E. Farmand-Ashtiani, J. Botsis and A. P. Vassilopoulos, An iterative analytical/experimental study of bridging in delamination of the double cantilever beam specimen. *Composites Part A: Applied Science and Manufacturing*. **61**, 2014, 43-50.
- 122 . R. C. Østergaard, B. F. Sørensen and P. Brøndsted, Measurement of Interface Fracture Toughness of Sandwich Structures under Mixed Mode Loadings. *Journal of Sandwich Structures & Materials*. **9**, 2007, 445-66.
- 123 . J. G. Ratcliffe, Sizing single cantilever beam specimens for characterizing facesheet/core peel debonding in sandwich structure, *NASA Technical Publication*, NASA-TP 2010-216169, 2010.
- 124 . J. G. Ratcliffe and J. R. Reeder, Sizing a single cantilever beam specimen for characterizing facesheet–core debonding in sandwich structure. *Journal of Composite Materials*. **45**, 2011, 2669-84.
- 125 . Standard Test Methods for Notched Bar Impact Testing of Metallic Materials, *ASTM Standards E23-07*, West Conshohocken, PA, 2007 (originally published in 1933)

- 126 . Standard Test Method for Determining the Charpy Impact Resistance of Notched Specimens of Plastics, *ASTM Standards D6110-10*, West Conshohocken, PA, 2010 (originally published in 1997)
- 127 . D. F. Adams, *Impact testing of composite materials*. 2012, <http://www.compositesworld.com/articles/impact-testing-of-composite-materials>, accessed on: 17/10/2017
- 128 . E. V. González, P. Maimí, J. R. Sainz de Aja, P. Cruz and P. P. Camanho, Effects of interply hybridization on the damage resistance and tolerance of composite laminates. *Composite Structures*. **108**, 2014, 319-31.
- 129 . R. S. Choudhry, S. F. Hassan, S. Li and R. Day, Damage in single lap joints of woven fabric reinforced polymeric composites subjected to transverse impact loading. *International Journal of Impact Engineering*. **80**, 2015, 76-93.
- 130 . M. A. Pérez, X. Martínez, S. Oller, L. Gil, F. Rastellini and F. Flores, Impact damage prediction in carbon fiber-reinforced laminated composite using the matrix-reinforced mixing theory. *Composite Structures*. **104**, 2013, 239-48.
- 131 . E. V. González, P. Maimí, P. P. Camanho, A. Turon and J. A. Mayugo, Simulation of drop-weight impact and compression after impact tests on composite laminates. *Composite Structures*. **94**, 2012, 3364-78.
- 132 . A. M. Amaro, P. N. B. Reis, M. F. S. F. de Moura and M. A. Neto, Influence of multi-impacts on GFRP composites laminates. *Composites Part B: Engineering*. **52**, 2013, 93-9.
- 133 . P. N. B. Reis, J. A. M. Ferreira, F. V. Antunes and M. O. W. Richardson, Effect of interlayer delamination on mechanical behavior of carbon/epoxy laminates. *Journal of Composite Materials*. **43**, 2009, 2609-21.
- 134 . L. Walker, M.-S. Sohn and X.-Z. Hu, Improving impact resistance of carbon-fibre composites through interlaminar reinforcement. *Composites Part A: Applied Science and Manufacturing*. **33**, 2002, 893-902.
- 135 . M. Sayer, N. B. Bektaş and O. Sayman, An experimental investigation on the impact behavior of hybrid composite plates. *Composite Structures*. **92**, 2010, 1256-62.
- 136 . G. Kirupanantham, *Characterisation of discontinuous carbon fibre preforms for automotive applications*, PhD thesis: University of Nottingham; 2013.
- 137 . D. Ghelli and G. Minak, Low velocity impact and compression after impact tests on thin carbon/epoxy laminates. *Composites Part B: Engineering*. **42**, 2011, 2067-79.
- 138 . J. S. Lightfoot, M. R. Wisnom and K. Potter, Defects in woven preforms: Formation mechanisms and the effects of laminate design and layup protocol. *Composites Part A: Applied Science and Manufacturing*. **51**, 2013, 99-107.
- 139 . P. Hallander, M. Akermo, C. Mattei, M. Petersson and T. Nyman, An experimental study of mechanisms behind wrinkle development during forming of composite laminates. *Composites Part A: Applied Science and Manufacturing*. **50**, 2013, 54-64.
- 140 . M. P. F. Sutcliffe, S. L. Lemanski and A. E. Scott, Measurement of fibre waviness in industrial composite components. *Composites Science and Technology*. **72**, 2012, 2016-23.
- 141 . J. Y. Shu and N. A. Fleck, Microbuckle initiation in fibre composites under multiaxial loading. *Proceedings of the Royal Society of London Series A: Mathematical, Physical and Engineering Sciences*. **453**, 1997, 2063-83.

- 142 . M. Duhovic, P. Mitschang and D. Bhattacharyya, Modelling approach for the prediction of stitch influence during woven fabric draping. *Composites Part A: Applied Science and Manufacturing*. **42**, 2011, 968-78.
- 143 . R. Joffe, Performance of non-crimp fabric composites in shear. *Key Engineering Materials: Trends in Composite Materials and their Design*. **425**, 2010, 45-60.
- 144 . B. Budiansky and N. A. Fleck, Compressive failure of fibre composites. *Journal of the Mechanics and Physics of Solids*. **41**, 1993, 183-211.
- 145 . D. Liu, N. A. Fleck and M. P. F. Sutcliffe, Compressive strength of fibre composites with random fibre waviness. *Journal of the Mechanics and Physics of Solids*. **52**, 2004, 1481-505.
- 146 . H. M. Hsiao and I. M. Daniel, Effect of fiber waviness on stiffness and strength reduction of unidirectional composites under compressive loading. *Composites Science and Technology*. **56**, 1996, 581-93.
- 147 . R. F. Elhajjar and S. S. Shams, Compression testing of continuous fiber reinforced polymer composites with out-of-plane fiber waviness and circular notches. *Polymer Testing*. **35**, 2014, 45-55.
- 148 . P. Davidson, A. M. Waas, C. S. Yerramalli, K. Chandraseker and W. Faidi, Effect of fiber waviness on the compressive strength of unidirectional carbon fiber composites, *Structural Dynamics and Materials Conference 2012*, Honolulu, HI; United States, 2012.
- 149 . P. Feraboli, T. Cleveland, M. Ciccu, P. Stickler and L. DeOto, Defect and damage analysis of advanced discontinuous carbon/epoxy composite materials. *Composites Part A: Applied Science and Manufacturing*. **41**, 2010, 888-901.
- 150 . J. E. Lindhagen and L. A. Berglund, Application of bridging-law concepts to short-fibre composites Part 2: Notch sensitivity. *Composites Science and Technology*. **60**, 2000, 885-93.
- 151 . Resin XU 3508 / Aradur 1571 / Accelerator 1573 / Hardener XB 3403. *Huntsman Advanced Materials*. July 2012.
- 152 . Resin XU 3508 / Aradur 1571 / Accelerator 1573 / Hardener XB 3471. *Huntsman Advanced Materials*. October 2009.
- 153 . R. Luchoo, L. T. Harper, M. D. Bond, N. A. Warrior and A. Dodworth, Net shape spray deposition for compression moulding of discontinuous fibre composites for high performance applications. *Plastics, Rubber and Composites*. **39**, 2010, 216-31.
- 154 . L. T. Harper, R. Luchoo, M. D. Bond, N. A. Warrior and A. Dodworth, Automated charge placement for structural molding compounds, *International SAMPE Symposium and Exhibition*, Seattle, WA; United States, 2010.
- 155 . G. F. C. Rogers and Y. R. Mayhew. *Thermodynamic and Transport Properties of Fluids*: Wiley; 1995.
- 156 . T. Mori and K. Tanaka, Average stress in matrix and elastic energy of materials with misfitting inclusions. *Acta Metallurgica*. **21**, 1973, 571-4.
- 157 . Y. P. Qiu and G. J. Weng, On the application of Mori-Tanaka's theory involving transversely isotropic spheroidal inclusions. *International Journal of Engineering Science*. **28**, 1990, 1121-37.
- 158 . S. G. Advani and C. L. Tucker III, The use of tensors to describe and predict fiber orientation in short fiber composites. *Journal of Rheology*. **31**, 1987, 751-84.

- 159 . L. T. Harper, T. A. Turner, J. R. B. Martin and N. A. Warrior, Fiber alignment in directed carbon fiber preforms - Mechanical property prediction. *Journal of Composite Materials*. **44**, 2010, 931-51.
- 160 . N. Sbirrazzuoli and S. Vyazovkin, Learning about epoxy cure mechanisms from isoconversional analysis of DSC data. *Thermochimica Acta*. **388**, 2002, 289-98.
- 161 . A. Atarsia and R. Boukhili, Relationship between isothermal and dynamic cure of thermosets via the isoconversion representation. *Polymer Engineering & Science*. **40**, 2000, 607-20.
- 162 . P. J. Flory. *Principles of Polymer Chemistry: Paul J. Flory*: Cornell University; 1953.
- 163 . J. K. Stevenson, Free radical polymerization models for simulating reactive processing. *Polymer Engineering & Science*. **26**, 1986, 746-59.
- 164 . M. R. Keenan, Autocatalytic cure kinetics from DSC measurements: Zero initial cure rate. *Journal of Applied Polymer Science*. **33**, 1987, 1725-34.
- 165 . G.-l. Zhu, Y.-p. Xiao, Y.-x. Yang, J. Wang, B.-d. Sun and R. Boom, Degradation behavior of epoxy resins in fibre metal laminates under thermal conditions. *Journal of Shanghai Jiaotong University (Science)*. **17**, 2012, 257-62.
- 166 . R. Luchoo, L. T. Harper, N. A. Warrior and A. Dodworth, Automated charge placement for structural molding compounds. *SAMPE Journal*. **46**, 2011, 6-21.
- 167 . A. Tezvergil, L. V. J. Lassila and P. K. Vallittu, The effect of fiber orientation on the polymerization shrinkage strain of fiber-reinforced composites. *Dental Materials*. **22**, 2006, 610-6.
- 168 . W. F. Zoetelief, L. F. A. Douven and A. J. I. Housz, Residual thermal stresses in injection molded products. *Polymer Engineering & Science*. **36**, 1996, 1886-96.
- 169 . M. R. Wisnom, Size effects in the testing of fibre-composite materials. *Composites Science and Technology*. **59**, 1999, 1937-57.
- 170 . P. Feraboli, E. Peitso, T. Cleveland, P. B. Stickler and J. C. Halpin, Notched behavior of prepreg-based discontinuous carbon fiber/epoxy systems. *Composites Part A: Applied Science and Manufacturing*. **40**, 2009, 289-99.
- 171 . G. Subramanian and D. L. Koch, Inertial effects on fibre motion in simple shear flow. *Journal of Fluid Mechanics*. **535**, 2005, 383-414.
- 172 . T. S. Lundström, Measurement of void collapse during resin transfer moulding. *Composites Part A: Applied Science and Manufacturing*. **28**, 1997, 201-14.
- 173 . L. J. Hart-Smith, Analysis and design of advanced composite bounded joints. *NASA Technical Reports*. 1974, 1-60.
- 174 . G. S. Schajer, Advances in Hole-Drilling Residual Stress Measurements. *Experimental Mechanics*. **50**, 2010, 159-68.
- 175 . O. Sicot, X. L. Gong, A. Cherouat and J. Lu, Determination of Residual Stress in Composite Laminates Using the Incremental Hole-drilling Method. *Journal of Composite Materials*. **37**, 2003, 831-44.
- 176 . P. Latil, L. Orgéas, C. Geindreau, P. J. J. Dumont and S. Rolland du Roscoat, Towards the 3D in situ characterisation of deformation micro-mechanisms within a compressed bundle of fibres. *Composites Science and Technology*. **71**, 2011, 480-8.